Quasi-Monte Carlo computation of radiative heat transfer in coupled Large Eddy Simulation of a swirled premixed flame

Lorella Palluotto

NNT : 2019SACLC034

Prédiction du transfert radiatif au sein d'une flamme prémélangée swirlée à l'aide d'une méthode Quasi-Monte Carlo couplée à la simulation aux grandes échelles

Thèse de doctorat de l'Université Paris-Saclay et ULB
préparée à CentraleSupélec et à l'ULB

École doctorale n°579 Sciences mécaniques et énergétiques, matériaux et géosciences (SMEMAG)
Spécialité de doctorat : Combustion

Thèse présentée et soutenue à Gif-sur-Yvette, le 04/07/2019, par

Lorella Palluotto

Composition du Jury :

Thierry Schuller Professeur, Institut de Mécanique des Fluides de Toulouse	Président
Florent Duchaine Chercheur Senior, CERFACS	Rapporteur
Mouna El Hafi Professeur, École des Mines Albi	Rapporteur
Antonio Andreini Professeur, Università degli studi di Firenze	Examinateur
Axel Coussement Professeur, Université Libre de Bruxelles	Examinateur
Olivier Gicquel Professeur, CentraleSupélec (EM2C – UPR 288)	Directeur de thèse
Alessandro Parente Professeur, Université Libre de Bruxelles	Directeur de thèse
Ronan Vicquelin Maître de Conférences, CentraleSupélec (EM2C – UPR 288)	Co-Directeur de thèse
Bernard Labegorre Ingénieur de recherche, Air Liquide	Invité

Thèse de doctorat

Remerciements

Dans un premier temps, je tiens à remercier tous les membres du jury qui a évalué ma thèse. Mes soutenances ayant été logistiquement compliquées, je vous remercie de vous être déplacés pour mes deux soutenances, à Bruxelles et à Paris. Je tiens à remercier tout particulièrement les rapporteurs de ma thèse, Florent Duchaine et Mouna El Hafi, pour avoir pris le temps de lire et d'annoter mon manuscrit et pour leurs remarques enrichissantes concernant mon travail de thèse. Je remercie également Thierry Schuller d'avoir accepté d'assumer le rôle de président du jury de ma soutenance publique, ainsi que pour tous les échanges intéressants qu'on a pu avoir sur Oxytec. De même, je remercie Axel Coussement d'avoir accepté la présidence de ma soutenance privée. Merci également à Antonio Andreini d'avoir accepté son rôle d'examinateur. Je tiens enfin à remercier Bernard Labegorre pour sa bienveillance et pour m'avoir donné l'opportunité d'effectuer un stage très constructif chez Air Liquide.

Dans un second temps, je remercie grandement mes directeurs de thèse pour leur encadrement tout au long de mon doctorat. Olivier, merci pour tes conseils toujours très pragmatiques et formateurs. Alessandro, merci de m'avoir accueilli et de m'avoir permis de m'intégrer avec aisance à cette grande famille qu'est l'ULB. Et enfin Ronan, je te remercie parce que tu n'as pas été un simple co-encadrant comme mentionné sur la première page de ce manuscrit, mais un vrai directeur de thèse. Tu as toujours été présent, disponible et à l'écoute, pour moi comme pour tous tes doctorants. Merci parce que tu as su me guider et m'encourager tout au long de mon doctorat, parce que j'ai énormément appris à tes côtés, et puis parce que sans ton apport scientifique et ton soutien moral ce travail n'aurait pas été le même.

Je souhaite ensuite remercier toutes les belles personnes que j'ai eu la chance de rencontrer au laboratoire EM2C, et qui m'ont accompagnées pendant ces trois ans et demi de thèse. Tout d'abord merci au secrétariat, Noï, Nathalie et Brigitte d'avoir été toujours disponibles et prêtes à m'aider au moindre besoin. Et puis merci à tous mes collègues, surtout ceux qui sont devenus des amis très proches : Abi, Amanda, Théa, Livia, Arthur, Giampi, Léo, Jan, Stefano, Giunio, Pedro, Nicolas, Davy, Quentin et tous les autres que je n'ai pas cités car la liste serait trop longue ! Vous avez beaucoup compté pour moi pendant ces an-

nées de thèse et votre compagnie a rendu les situations stressantes plus légères et supportables. Je n'oublierai jamais les moments passés au labo, à Châtenay avant et à Saclay après, les heures de sport, les voyages ensemble, les journées passées à travailler et les soirées à rigoler :) Je tiens à remercier également mes collègues de l'ULB, en compagnie desquels j'ai passé des mois très agréables et des moments très drôles. Merci aussi à ma petite famille italienne à Paris : Alfredo (perché siamo inseparabili), Giampi (sì, ti ringrazio di nuovo altrimenti non basta), Nicola (sperando che torni presto a trovarci), Lydia, Petra e tanti altri parce que la vie à Paris n'aurait pas été aussi agréable sans votre présence et parce que mes soirées n'auraient pas été aussi rigolotes sans votre amitié.

E dulcis in fundo, il più grande ringraziamento va alla mia famiglia: mamma, papà, Maria Grazia e Carmelo, per essermi stati accanto anche se lontani. Grazie per avermi sostenuto, per aver sempre mostrato fiducia in quello che faccio e per avermi dato la forza e la serenità necessarie per arrivare fin qui. Ringrazio inoltre i miei nonni, per la loro gioia ogni volta che torno a casa, e perché insieme ai miei zii e cugini mi hanno sempre fatto sentire come se fossi a due passi da casa.

Grazie di cuore.

Abstract

Numerical simulations represent an important tool for the design of combustion chambers. The prediction of wall fluxes is a significant aspect in the life cycle of combustors, since it allows to prevent eventual wall damages. For a correct quantification of wall thermal loads, radiative fluxes have to be taken into account, since the heat transfer from flame to the walls is driven, apart from convection, also by radiation of burnt gases inside the chamber. Wall heat losses depend on the temperature distribution inside the combustor, and the flow temperature field is, in turn, strongly modified by radiation from hot gases. In order to correctly account for both convective and radiative contributions to wall fluxes, the simultaneous solution of the radiative transfer equation (RTE) and the governing equations for reactive flows is required. Nowadays, coupled simulations involving combustion and radiative heat transfer are more and more used and targeted. Thanks to the increase in computing power and advances in numerical algorithms and solver scalability, the use of accurate Monte Carlo (MC) methods in 3D unsteady simulations, such as Direct Numerical Simulations (DNS) and Large Eddy Simulations (LES), has become affordable and enables high-fidelity of the described radiative heat transfer. However, such coupled and multi-physics simulations remain very costly, and additional efforts are necessary to make MC methods more efficient. The purpose of this study is then to investigate improvements of MC methods, by using an alternative sampling mechanism for numerical integration usually referred to as Quasi-Monte Carlo (QMC) integration: a method which has barely been studied for the numerical resolution of thermal radiation. In the present study, QMC is assessed on several practical 3D configurations and compared to MC. The efficiency improvement achieved by QMC, makes such method a perfect candidate for coupled high-fidelity simulations based on LES or DNS. In the present work, an interesting 3D application has been retained for the assessment of QMC methods in coupled simulations: the Oxytec chamber, experimentally investigated at the EM2C laboratory. Two atmospheric swirled premixed flames have been experimentally studied during the Oxytec campaign: a methane-air flame (Flame A) and a CO_2-diluted oxy methane flame (Flame B). Despite their different composition, such flames share a lot of common characteristics, like thermal power, adiabatic temperature and wall fluxes distribution. The first numerical simulations of the Oxytec chamber are carried out in this thesis

work: a QMC approach enabling to solve the RTE with detailed radiative properties of gases and confining viewing windows is coupled to the LES solver, for the simulation of the Flame A. LES and LES-QMC simulations are carried out, by imposing measured wall temperature on the solid parts of the combustor. The comparison between coupled and non-coupled simulations with experimental data shows that thermal radiation has an impact on both flow and flame topology. Moreover, heat transfer results highlight that radiative heat losses account for the 20% of the flame thermal power and that around 35% of radiative power inside the combustor is transmitted to the exterior, through the quartz windows. Finally, a good agreement is found in the numerical wall heat flux compared to experimental data. In the last part of this thesis, attention is focused on the Flame B, where the high CO_2 concentration of burnt gases is expected to enhance the radiative heat transfer. It is first shown that the presence of a strong absorber, such as CO_2, in the fresh mixture increases the laminar flame speed by a factor which depends on the size of the investigated configuration. Then, first results issued from LES of Flame B are shown and preliminary results on radiative heat transfer are discussed and compared to the ones obtained from coupled simulations of Flame A.

Résumé

La simulation numérique représente un outil important pour la conception des systèmes de combustion. La prédiction des flux aux parois joue un rôle déterminant dans le cycle de vie des chambres de combustion, car elle permet de prédire la fatigue thermique des parois et d'augmenter ainsi la durée de vie des équipements. Le transfert de chaleur de la flamme aux parois est entraîné, outre la convection, également par le rayonnement des gaz chauds au sein de la chambre. Pour évaluer les transferts thermiques aux parois il faut donc tenir compte des flux radiatifs. Les pertes thermiques aux parois dépendent de la répartition de la température à l'intérieur de la chambre de combustion, et le champ de température est, à son tour, fortement modifié par le rayonnement des gaz brûlés. Afin d'intégrer les contributions convectives et radiatives au flux pariétal dans des simulations numériques, il est nécessaire de résoudre simultanément l'équation de transfert radiatif et les équations régissant l'écoulement réactif. De nos jours, les simulations couplées impliquant combustion et transfert de chaleur radiatif sont de plus en plus utilisées et ciblées. Grâce à l'augmentation de la puissance de calcul et aux progrès des algorithmes numériques et de la scalabilité des codes, l'utilisation des méthodes de Monte Carlo (MC) dans des simulations 3D instationnaires, telles que les simulations numériques directes (DNS) et les simulations aux grandes échelles (LES), est devenue abordable et permet une résolution haute-fidélité des transferts radiatifs. Cependant, de telles simulations couplées et multi-physiques restent très coûteuses, et des efforts supplémentaires sont nécessaires afin d'améliorer l'efficacité des méthodes de MC. L'objectif de cette thèse est donc d'investiguer une technique pour améliorer l'efficacité de la méthode MC, basée sur un mécanisme alternatif d'échantillonnage et généralement appelé intégration Quasi-Monte Carlo (QMC). Cette méthode a rarement été utilisée pour la résolution numérique du rayonnement thermique. Dans cette étude, la méthode QMC est appliquée sur plusieurs configurations 3D et comparée à celle de MC. L'amélioration de l'efficacitéé obtenue par QMC fait de cette méthode un candidat idéal pour des simulations haute-fidélité couplées avec des simulations LES ou DNS. Au cours de cette thèse, la méthode QMC a pu être appliquée à une configuration où le rayonnement joue un rôle important : la chambre Oxytec, étudiée expérimentalement au laboratoire EM2C. Deux flammes prémélangées swirlées à pression atmosphérique ont été étudiées expérimentalement : une flamme méthane-air

(Flamme A) et une oxy-flamme de méthane diluée en CO2 (Flamme B). Malgré leur composition différente, ces flammes partagent de nombreuses caractéristiques communes, telles que la puissance thermique, la température adiabatique de flamme et la distribution des flux thermiques aux parois. Les premières simulations numériques de la chambre Oxytec sont réalisées dans ce travail de thèse : une approche QMC, permettant de résoudre l'équation de transfert radiatif avec des propriétés radiatives détaillées des gaz et des parties solides de la chambre, est couplée au solveur LES pour la simulation de la flamme A. Des simulations couplées LES-QMC sont effectuées en imposant la température mesurée aux parties solides de la chambre de combustion. La comparaison entre les simulations couplées et non couplées avec les données expérimentales montre que le rayonnement thermique a un impact sur la topologie de l'écoulement et de la flamme. De plus, les résultats montrent que les pertes radiatives représentent le 20% de la puissance thermique de la flamme et qu'environ 35% de la puissance radiative émise et absorbée au sein de la chambre de combustion est transmise à l'extérieur à travers les fenêtres en quartz. Enfin, un bon accord est trouvé entre le flux de chaleur pariétal prédit par la simulation et les données expérimentales. Dans la dernière partie de cette thèse, l'étude se concentre sur la flamme B, où l'on s'attend que la concentration élevée de CO2 dans les gaz brûlés augmente le transfert de chaleur radiatif. Il est d'abord montré que la présence d'une espèce absorbante telle que le CO2 dans les gaz frais augmente la vitesse laminaire de flamme d'un facteur qui dépend de la taille de la configuration étudiée. Ensuite, les premiers résultats issus des calculs LES de la Flamme B sont présentés : les résultats préliminaires sur le transfert radiatif sont discutés et comparés à ceux obtenus à partir des simulations couplées de Flamme A.

Contents

List of Tables

List of Figures

Chapter 1

Introduction: coupled thermal radiation and turbulent combustion

This chapter provides an introduction to coupled simulations where combustion and radiation are both taken into account. Theory on thermal radiation is presented through the radiative transfer equation. Modeling strategies to account for spectral properties of participating gas are presented.
Existing approaches for the simulation of turbulent reacting flows are also summarized, focusing the attention on the Large Eddy Simulation, which is the approach used in this thesis.
Moreover, a literature review of works about coupled combustion-radiation simulations is done with a state-of-the-art about approaches and models most frequently used.
The motivation of accounting for radiative heat transfer in combustion systems is highlighted in some new combustion technologies.
Finally the approaches and models used in this study are justified, and the originality and objectives of this thesis are presented.

Contents

1.1 Introduction

This thesis work is part of the CLEAN-Gas project, a European Joint Doctorate program funded by the European Community through the Horizon 2020 Actions.
CLEAN-Gas is an acronym for Combustion for Low Emission Applications of Natural Gas. The interest in natural gas comes from the fact that it represents a key parameter in the European Union energy policy while being responsible for the production of greenhouse gases and pollutants emissions. One of the possible strategies of intervention is the development of advanced experimental and numerical tools, which would provide a better knowledge about the new combustion processes, and aim at limiting pollutants formation. The new combustion technologies investigated in the course of the project are: flameless combustion and oxy-combustion.
Both Computational Fluid Dynamics (CFD) simulations and experimental investigations are of a paramount importance in the combustion community. If on one hand, experiments are necessary to the physical observation of the phenomena involved in combustion processes, on the other hand numerical simulations

are fundamental for their capacity to predict the behavior of systems . Nevertheless, experiments and simulations always go hand to hand, as one is used to validate the other.
The present work is inserted in the context of CFD simulations of turbulent combustion systems. Particular attention is given, in this work, to thermal radiation. In the past, in numerical simulations of turbulent combustion systems, radiative heat transfer was often neglected or accounted for with very simplistic assumptions such as the 'optically thin' and 'gray gas' models, despite the fact that radiation is often the dominant mode of heat transfer in this kind of systems.
The reason for which little attention was paid to the accurate modeling of radiative heat transfer could be on one hand the extra-difficulty, added to an already complicated problem such as turbulent reacting flows, in accounting for a phenomenon which is highly non linear to variables like temperature, pressure and species concentration. Consequently, accurate calculations would require instantaneous spatially resolved information regarding temperature and species composition fields.
On the other hand one should consider also the extra-cost of accurate radiation modeling since it is governed by a complex integro-differential equation which is time consuming to solve. An accurate thermal radiation modeling could be prohibitive in the past, especially if coupled to accurate calculations of turbulent combustion systems. However, nowadays, thanks to the increase in computing power, facing accurate problems becomes more realistic and accurate calculations get more and more affordable.
Moreover, in a real combustion application, several phenomena are involved, such as combustion, radiation and wall heat transfer. Accounting for all the phenomena simultaneously through multi-physics simulations, becomes necessary if one wants to predict the different heat transfer mechanisms taking place during the combustion process. In the present work, attention is mainly focused on the coupling between combustion and thermal radiation.
In the context of coupled combustion-radiation simulations, in the next sections, numerical approaches for both combustion and radiation are presented, through their governing equations. A literature review of the main works about combustion simulations coupled with radiation is also given.
The motivation of accounting for radiative heat transfer in combustion systems is shown in some of the new combustion technologies. Finally, the objectives of the thesis are presented and the approaches used in this work are justified.

1.2 Thermal radiation

1.2.1 Radiative Transfer Equation

When thermal radiation is considered, some difficulties arise, due to the fact that, compared to other mechanisms transferring energy which are present in

combustion processes, such as conduction and convection, radiation is transferred by electromagnetic waves involving long-range interactions. To determine the radiative flux onto a surface, spectral radiative intensity for all the directions and wavenumbers must be solved. And in order to obtain the spectral radiative intensity I'_ν corresponding to an energy ray travelling at wavenumber ν along a path ds in the direction $\mathbf{u}$, for a medium that emits, absorbs and scatters radiation, an energy balance needs to be done. The result of this balance leads to the *Radiative Transfer Equation* (RTE) which is an integro-differential equation in six independent variables:

$$\begin{aligned}\frac{\mathrm{d}I'_\nu}{\mathrm{d}s} =& -\kappa_\nu I'_\nu - \sigma_\nu I'_\nu + \kappa_\nu n^2 I^\circ_\nu + \\ &+ \frac{\sigma_\nu}{4\pi}\int_{4\pi} p_\nu(\mathbf{u}', \mathbf{u}, s) I'_\nu(\mathbf{u}', s) d\Omega'\end{aligned} \tag{1.1}$$

where n is the refractive index of the medium (in the following $n = 1$), κ_ν its absorption coefficient, σ_ν the scattering coefficient, Ω the solid angle and $p_\nu(\mathbf{u}', \mathbf{u}, s)$ the phase function, representing the probability that a ray coming from $\mathbf{u}'$ is scattered towards $\mathbf{u}$.
I°_ν is the spectral intensity emitted by a blackbody and is described by Planck's law:

$$I^\circ_\nu(T) = \frac{2hc_0^2\nu^3}{(e^{\frac{h\nu}{k_b T}} - 1)} \tag{1.2}$$

where c_0 is the speed of light in vacuum and h and k_b are, respectively, the Planck's and Boltzmann's constants. Three energy mechanisms are involved in Eq. (1.1): emission, absorption and scattering. Local thermodynamic equilibrium has been assumed in the reported RTE where the medium emmision term is expressed as $\kappa_\nu n^2 I^\circ_\nu$.
The RTE then states that the radiative intensity along a path s can be augmented by emission ($\kappa_\nu n^2 I^\circ_\nu$) and received scattering (last term on the RHS), i.e. scattering from other directions into the direction of propagation, and it can be decreased by absorption ($\kappa_\nu I'_\nu$) and scattering ($\sigma_\nu I'_\nu$), i.e. scattering away from the direction of propagation. In the case of absence of scattering, assumed in this thesis, the last term in Eq. (1.1) disappears and the RHS of the RTE is reduced to the difference between local emission and local absorption:

$$\frac{\mathrm{d}I'_\nu}{\mathrm{d}s} = -\kappa_\nu I'_\nu + \kappa_\nu I^\circ_\nu \tag{1.3}$$

The radiative intensity $I'_\nu(\mathbf{u}, s)$ allows to obtain the radiative heat flux $\mathbf{q}^R$ defined as:

$$\mathbf{q}^R = \int_{\nu=0}^{\infty} \mathbf{q}^R_\nu d\nu = \int_{\nu=0}^{\infty} d\nu \int_{4\pi} I'_\nu(\mathbf{u}, s)\mathbf{u} d\Omega \tag{1.4}$$

Knowing $\mathbf{q}^R$ one can obtain the radiation source term P^R which appears in the energy equation:

$$P^R = -\nabla \cdot \mathbf{q}^R = \int_{\nu=0}^{\infty} d\nu \int_{4\pi} div[I'_\nu(\mathbf{u}, s)\mathbf{u}]d\Omega \tag{1.5}$$

Using Eq. (1.3), the radiative power is expressed as:

$$P^R = \int_{\nu=0}^{\infty} \int_{4\pi} \kappa_\nu I'_\nu d\Omega d\nu - 4\pi \int_{\nu=0}^{\infty} \kappa_\nu I^\circ_\nu d\nu \tag{1.6}$$

where the first term represents the absorbed radiative power and the second term the emitted one.
Finally the wall radiative flux ϕ^R writes:

$$\phi^R = \mathbf{q}^R \cdot \mathbf{n} = \int_{\nu=0}^{\infty} \mathbf{q}^R_\nu d\nu = \int_{\nu=0}^{\infty} d\nu \int_{4\pi} I'_\nu(\mathbf{u}, s)\mathbf{n} \cdot \mathbf{u} d\Omega \tag{1.7}$$

where $\mathbf{n}$ is the unity vector normal to the wall.

1.2.2 Gas radiative properties

Participating gases usually present in combustion applications are CO_2, H_2O, CO and CH_4. One of the biggest difficulties introduced by thermal radiation is the presence, in the RTE, of the absorption coefficient κ_ν of gases, which strongly varies with the wavenumber ν. Accounting for such properties is not an easy task and in the past several models have been developed. In the following, the way these radiative properties can be described is illustrated and the existing strategies are grouped in three main families in descending order of accuracy: line-by-line databases, band models and global models.

Spectral line-by-line

Participating gases emit, absorb and scatter radiation. Such phenomena cause the transition between energy states leading to the formation of thousands of emission and/or absorption spectral lines. Informations about location, strength and width of spectral lines are collected in several line-by-line spectral database. The first one is the HITRAN database (acronym for HIgh-resolution TRANsmission molecular absorption database) (Rothman et al. 2009) which, in the upgrated versions, includes detailed information on 39 species. However the first versions of HITRAN were not adequate at elevated temperatures. Thus, ameliorations have been made to include, through theoretical calculations, data for water vapor (Riviere et al. (1995), Partridge and Schwenke (1997), Jørgensen et al. (2001), Barber et al. (2006)) and carbon dioxide (Scutaru et al. (1993), Tashkun and Perevalov (2011)) . All the extensions have finally been integrated in the HITEMP (HIgh-TEMPerature molecular spectroscopic database) (Rothman et al. 2010), designed for temperatures up to 3000 K.

Using such databases allows to have a high spectral resolution and a reference solution; however such an approach is excessively time-consuming and becomes unaffordable for most practical problems. For this reason special attention has been given in the past to the development of less expensive models, like band models and global models summarized in the following.

Band models

Since gas absorption coefficient varies much more strongly across the spectrum than other variables, like the blackbody intensity, it is possible to replace the actual absorption coefficient by values averaged over a narrow spectral range. This is the principle of the traditional narrow band models, such as Elsasser and statistical models detailed in Modest (2013).
Moreover, since it is observed that over a narrow spectral range a given value of the absorption coefficient repeats many times, it is possible to reorder it thus making the spectral integration very straightforward. Such model is called 'correlated k-distribution' and is part of the narrow band models.
Another category of band models is the one of 'wide band models', whose correlations are found by integrating narrow band results across an entire band. In the following, only narrow band k-distribution models are presented, since they are the ones used in this thesis work.

Narrow band k-distribution models

The concept at the base of the correlated-k model is to consider frequency bands sufficiently small (few tens of cm^{-1} of wavenumber) where Planck function remains constant. If one looks at the absorption coefficient over the wavenumber η (Fig. 1.1), it can be seen that κ_η attains the same value many times inside this small spectral range.
For this reason the absorption coefficient is reordered to have a smooth monotonically increasing function so that each intensity field calculation is performed just once. This is the correlated-k or ck method (Goody et al. 1989) and it is based on the observation that over a narrow spectral range the radiative transfer is insensitive to the exact placement of spectral lines within the interval. Then, reordering the lines within the interval should not affect the radiative transfer.
Any spectral quantity which depends only on the gaseous absorption coefficient can be averaged over a narrow band and written in terms of a k-distribution $f(k)$, which is the fraction of $\Delta\nu$ for which the absorption coefficient κ_ν takes values between k and $k+dk$. The transmittivity $\bar{\tau}_\nu(X)$ over the band $\Delta\nu$ of a uniform column of size X writes:

$$\bar{\tau}_\nu = \frac{1}{\Delta\nu}\int_{\Delta\nu} e^{-\kappa_\nu X} d\nu = \int_0^\infty f(k) e^{-kX} dk \tag{1.8}$$

Thus, in the k-distribution method the integral over the wavenumber ν is re-

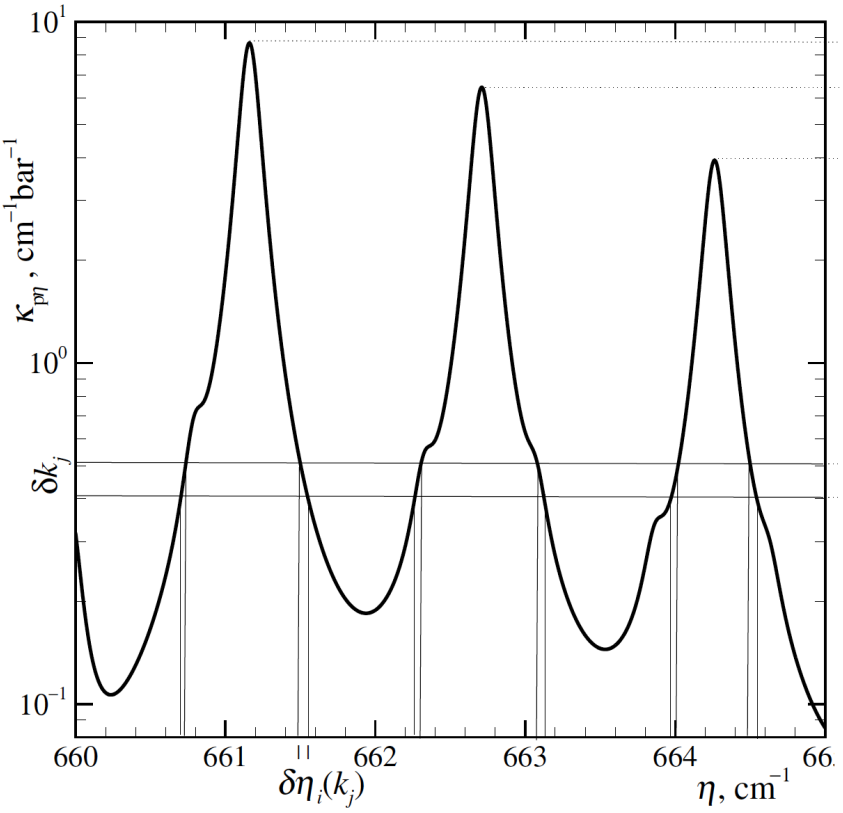

Figure 1.1: *Absorption coefficient across a small portion of the CO_2 band as a function of the wavenumber η (p = 1.0 bar, T = 296 K). Extracted from Modest (2013).*

placed by an integration over the values taken by κ_ν.
Mathematically $f(k)$ can also be written as the sum of the points where $\kappa_\nu = k$:

$$f(k) = \frac{1}{\Delta\nu}\int_{\Delta\nu}\delta(k-\kappa_\nu)d\nu \tag{1.9}$$

However, the k-distribution function can have a very erratic behavior, specially in non-uniform media where spectral lines are very dynamic. For this reason the cumulative k-distribution function $g(k)$ is introduced, which is defined as:

$$g(k) = \int_0^k f(k)dk \tag{1.10}$$

The function $g(k)$ represents the probability that the absorption coefficient takes a value lower than k. It is a monotonic increasing function, then it exists a reciprocal function $k(g)$ representing the reordered absorption coefficient and

its advantage lies in the fact that more robust integration methods can be used. With the $c-k$ method the average transmissivity of a nonuniform column at a point s of the medium is then written as:

$$\bar{\tau} = \frac{1}{\Delta\nu}\int_{\Delta\nu} e^{-\int_0^X \kappa_\nu(s)ds} d\nu \approx \int_0^1 e^{-\int_0^X k(g,s)ds} dg \tag{1.11}$$

In combustion applications, species like CO_2 and H_2O absorb simultaneously in the same spectral bands. In this case, it is assumed that the spectra of these species are uncorrelated over each narrow band and the mean transmissivity of a mixture column in a given narrow band can be approximated by the multiplication of the mean transmissivities of the species sharing the same narrow band.
The $correlated-\kappa$ model by Goody et al. (1989) based on updated parameters due to Rivière and Soufiani (2012) is retained in this work. These parameters have been generated for a temperature range of $300-4000\ K$ and for atmospheric pressure applications; they are based on the CDSD-4000 database for the absorption spectra of CO_2 (Rothman et al. 2010) and on HITEMP 2010 for the ones of H_2O (Tashkun and Perevalov 2011). The whole considered spectrum spans from 150 to 9200 cm^{-1}. 44 spectral bands are considered for H_2O, whose width varies from 50 to 400 cm^{-1}. CO_2 spectrum overlaps the H_2O one and CO_2 absorbs in only 17 of the 44 bands.
To perform the integration, a Gaussian-type quadrature is used with seven quadrature points per band of each gaseous component. The calculation cost is proportional to the power of the number of participating species: a N^m-points quadrature would be needed for m species. For this reason, only two species, CO_2 and H_2O, are considered, which are the main participating species in combustion applications. This leads to a total of 1022 quadrature points: 7^2 quadrature points for each of the 17 bands where both species absorb plus 7 quadrature points for the remaining 27 bands where only H_2O participates.

Global models

The principle of global models is to spectrally integrate radiative properties of participating gases, before solving the RTE. In the following, some of the most commonly used global models are presented.

Weighted-Sum-of-Gray-Gases Model This method was first proposed by Hottel (Hottel and Sarofim 1972) with the aim to simulate emission and absorption of non-gray gas through a sum of gray gases. In this approach a few bands with uniform absorption coefficients are considered, and each band corresponds to a gray gas.
According to this principle, the total emissivity of a non-gray iso-thermal gas

may be approximated by a weighted sum of the emittances of k gray gases:

$$\epsilon(T,s) = \sum_{k=0}^{K} \omega_k(T)(1 - e^{-\kappa_k s}) \tag{1.12}$$

where s is the optical path length, T the temperature and ω_k the weight of the k^{th} gray gas which is function of temperature. The property that these weights have to respect is that the emittance is equal to one:

$$\sum_{k=0}^{K} \omega_k(T) = 1 \tag{1.13}$$

Usually $K = 2$ or 3 gives satisfactory results.
The corresponding total radiative intensity $I(s)$ is then calculate as the sum of the solutions to the RTE for each gray gas:

$$I'(s) = \sum_{k=0}^{K} I'_k(s) \tag{1.14}$$

This method benefits of great popularity since it is easy to implement and it is also computationally affordable. Moreover it may lead to acceptable accuracy which can be improved if accurate gray-gas coefficients are used, as it is done in the Spectral-Line-based WSGG.

Spectral-Line-based WSGG The idea proposed by Denison and Webb (1995a), Denison and Webb (1993), Denison and Webb (1995b) is to generate WSGG models directly from line-by-line spectra. In this approach the weights ω_k are function of Absorption Line blackbody Distribution Functions (ALBDF) F_s:

$$\omega_k(T) = F_s(C_{abs,k}, T_b, T_g, P, Y_s) - F_s(C_{abs,k-1}, T_b, T_g, P, Y_s) \tag{1.15}$$

and they depend on the blackbody source temperature T_b, gas temperature T_g, total pressure P, species mole fraction Y_s and molar absorption cross section C_{abs} which is related to the absorption coefficient. An ALDF, or F_s is defined as *the fraction of the blackbody energy in the portions of the total spectrum where the high-resolution spectral molar absorption cross section of the gas $C_{abs,\eta}$ is less than a prescribed value C_{abs}* (Howell et al. 2010) and it is expressed as:

$$F_s(C_{abs}, T_b, T_g, P, Y_s) = \frac{\pi}{\sigma T_b^4} \sum_i \int_{\Delta_\eta \in (C_{abs,\eta} < C_{abs})} I_{b\eta}(T_b) d\eta \tag{1.16}$$

In other words the weight factors are simply the sum of $I_{b\eta}\Delta\eta$ for all the spectral intervals of integration Δ_η, and they are normalized by I_b.
Calculations performed with SLW-WSGG show that very accurate results can

be obtained for homogeneous gas mixtures, using only three or four spectral calculations and, to a lesser extent, also in mixtures with varying temperature and concentrations (Modest 2013). In Solovjov and Webb (2011) it is shown that SLW method yields the exact solution in an isothermal and homogeneous medium if the number of gray gases tends to infinity.

Absorption Distribution Function method The Absorption Distribution Function (ADF) is very similar to the SLW-WSGG; it was applied to extended applications, such as air plasma under high temperature gradients in Riviere et al. (1996) and a 1D mixture of water vapor and carbon dioxide for a wide range of temperature and concentrations in Pierrot et al. (1999).
This approach is also extended to the case of strong temperature inhomogeneities, where the gas is separated into a number of 'fictitious gases' (ADFFG: Absorption Distribution Function Fictitious Gases) (Pierrot et al. 1999) and spectral lines are grouped according to the values of their lower level energies.

Full-Spectrum k-distribution method (FSK) This method was developed by Modest and Zhang (2002) and Modest and Zhang (2000) and it shares some common considerations with the SLW and the narrow band distributions. Like the narrow band k-distribution, the absorption coefficient is reordered into a monotonically increasing function to facilitate the spectral integration. And the cumulative k-distribution used in FSK is very similar to the ALBDF associated with the SLW.
Indeed, methods like SLW and ADF perform the spectral integration over absorption cross section using discrete subdivisions, while the FSK method integrates over the Planck-weighted function using Gaussian quadrature. More details about similarities between SLW and FSK methods are given in Solovjov and Webb (2011).
The accuracy of the FSK depends on the fidelity of the Planck-weighted spectral line distribution function and from the accuracy of the quadrature scheme which is used for the integration over the distribution function.

1.2.3 Solution methods

The RTE (Eq.1.1) is an integro-differential equation in 6 dimensions: 3 in coordinates space, 2 in direction (polar and azimuthal angle) and 1 frequency, and its resolution is quite challenging. Over the course of the years, several solution methods have been developed and the most commonly used ones are illustrated in the following in order of increasing accuracy.

Optically thin approximation

An approach widely used in the past thanks to its ease and low computational cost consists in considering the medium optically thin for all wavelengths. This

means that the mean free path of a photon is very big compared to the dimensions of the retained system.
When a medium is optically thin the absorption phenomenon is neglected. As a consequence the radiative power is expressed as:

$$P^R = -4\kappa_P \sigma T^4 \tag{1.17}$$

where κ_P is the Planck mean absorption coefficient defined as:

$$\kappa_P = \frac{\int_0^\infty \kappa_\nu I_\nu^\circ(T) d\nu}{\int_0^\infty I_\nu^\circ(T) d\nu} = \frac{\int_0^\infty \kappa_\nu I_\nu^\circ(T) d\nu}{\sigma/\pi T^4} \tag{1.18}$$

This approach has been widely adopted in the past in the context of combustion applications, however it does not give reliable predictions since reabsorbed radiative power from burnt gases is not negligible for all the wavelengths.

The Spherical Harmonics Method: P_1 approximation

A more accurate approach is the Spherical Harmonics P_N approximation. Actually such a method is potentially more accurate than the Discrete Ordinates Method presented hereafter; however high-order P_N are rarely used because of their complexity in mathematics and implementation. Thus one of the most extensively used approximation is the lowest order P_1 approximation.
This method consists in expanding the radiative intensity into a series of spherical harmonics decoupling spatial and directional dependency through a series of Legendre polynomials in distance and an orthogonal set of spherical harmonics in solid angle:

$$I(\mathbf{r}, \mathbf{u}) = \sum_{r=0}^{\infty} \sum_{m=-l}^{+l} A_{l\nu}^m(\mathbf{r}) Y_l^m(\mathbf{u}) \tag{1.19}$$

where $A_{l\nu}^m(\mathbf{r})$ are position-dependent coefficients and $Y_l^m(\mathbf{u})$ the angularly dependent normalized spherical harmonics. More details about the Spherical Harmonics Method (SHM) can be found in Modest (2013) and Howell et al. (2010).
When the number l of terms in the series tends to infinity, the spherical harmonics approximation is exact. However the expansion is often truncated to a $l = 1$ (P_1 approximation) or $l = 3$ (P_3 approximation). The main drawback of this approach is indeed the computational cost which drastically increases with the increase of the accuracy. Therefore, high-order approximation are often limited to one-dimensional problems. On the contrary, the P_1 approximation is computationally cheap but it can be inaccurate when strong directional variations are involved.

The Discrete Ordinates Method

In the Discrete Ordinates Method (DOM) spatial and angular variables are discretized. The integrals over the directions, i.e. solid angle, are replaced by numerical quadratures:

$$\int_{4\pi} f(\mathbf{u})d\Omega \simeq \sum_{i=1}^{n} \omega_i f(\mathbf{u}_i) \tag{1.20}$$

where ω_i are the quadrature weights associated to the directions $\mathbf{u}_i$.
The discrete ordinates representation of RTE for an absorbing-emitting gray medium can then be written as:

$$\mathbf{u_i} \cdot \nabla I(\mathbf{u_i}, s) = \kappa(s) I^{\circ}(s) - \kappa(s) I(\mathbf{u_i}, s) \tag{1.21}$$

Eq. 1.21 is then a system of first-order partial differential equations with as many equations as there are directions $\mathbf{u}_i$, $i = 1, 2, ..., n$.
The DOM can be easily implemented and is present in most of the CFD codes. For this reason it is very popular, however it suffers from a few drawbacks such as *ray effects* (Coelho 2001), consequence of angular discretization, and *false scattering*, consequence of spatial discretization.

Monte Carlo methods

An alternative approach consists in solving the RTE in a statistical way, tracing the history of a statistically meaningful random sample of photons emitted accordingly to probability density functions for directions and wavelength.
The main advantage of this method is its high accuracy and the possibility to estimate the committed error, together with the fact that its cost does not increase with the integration dimensions. Its main drawback is its computational cost due to its slow convergence rate.
Such methods are detailed in Chapters 2 and 3.

Ray tracing

The most accurate method to solve the RTE is the deterministic ray tracing where directions and wavelength are discretized, and photons are emitted for each direction and wavelength. However such approach is not affordable for real applications, for this reason it is used only for 1D or 2D applications.

1.3 Turbulent combustion

1.3.1 Conservation equations

Reacting turbulent flows are described by a system of partial differential equations, called *Navier-Stokes equations*. A gas-phase reacting system of N_S chemical species is governed by the equations of conservation of mass, species mass

fractions, momentum and energy which are:

$$\frac{\partial \rho}{\partial t} + \frac{\partial \rho u_i}{\partial x_i} = 0 \tag{1.22}$$

$$\frac{\partial \rho Y_k}{\partial t} + \frac{\partial}{\partial x_i}(\rho Y_k u_i) = -\frac{\partial}{\partial x_i}(J_{k,i}) + \dot{\omega}_k \quad (k = 1, 2, ..., N_S) \tag{1.23}$$

$$\frac{\partial \rho u_j}{\partial t} + \frac{\partial}{\partial x_i}(\rho u_i u_j) = -\frac{\partial p}{\partial x_j} + \frac{\partial \tau_{ij}}{\partial x_i} + \rho g_j \tag{1.24}$$

$$\frac{\partial \rho E}{\partial t} + \frac{\partial}{\partial x_i}(\rho E u_i) = -\frac{\partial}{\partial x_i}(u_i p) + \frac{\partial}{\partial x_i}(\tau_{ij} u_j) - \frac{\partial}{\partial x_i} q_i + \dot{\omega}_T + P^R \tag{1.25}$$

ρ is the mass density, u_i the i^{th} component of velocity, Y_k the mass fraction of the species k and E the energy per unit mass (sensible + kinetic).
In the species conservation equation (Eq. 1.23), $\dot{\omega_k}$ is the species chemical source term while $J_{k,i}$ is the i-component of the diffusion flux of species k.
In the momentum equation (Eq. 1.24) τ_{ij} is the ij-component of the viscous stress tensor, p the pressure and g_j the j-component of the gravity vector. In the energy conservation equation several terms appear:

- q_i is the conductive heat flux composed by the two contributions: the heat diffusion in the mixture, expressed by Fourier law, and the heat flux due to species enthalpy diffusion.
- $\dot{\omega}_T$ is the heat release rate from chemical reaction, which is computed from species reaction rates present in species equation and the species mass enthalpy of formation $\Delta h^0_{f,k}$:

$$\dot{\omega}_T = -\sum_{k=1}^{N} \dot{\omega}_k \Delta h^0_{f,k} \tag{1.26}$$

- P^R is a non-chemical source term, for instance the one due to radiation.

1.3.2 Computational approaches

Numerical simulation is a powerful tool to solve this set of equations on a discrete mesh, in some cases with the help of specific models.
If all the turbulent scales need to be resolved, from the biggest ones up to the smallest dissipative scales, the computational grid has to be very refined, since the size of the elements constituting the mesh determines the threshold of the structures that will be captured.
A very refined computational grid would allow to explicitly capture all the scales of the turbulence without modeling issues and the corresponding method is called *Direct Numerical Simulations* (DNS). However temporal and spatial scales involved in turbulent combustion systems span a so wide range that it becomes unaffordable to fully resolve them on practical 3D applications. With

the computational resources available nowadays, DNS remains accessible just for academic configurations.
In order to reduce the range of the solved scales and overcome the computational cost issue of DNS, other modeling frameworks have been developed. The *Reynolds-averaged Navier-Stokes* (RANS) method models all turbulent length scales and focuses on the resolution of averaged quantities of the flow. This approach is often used for the simulation of industrial configurations thanks to the low amount of computational resources needed; however only averaged quantities are available for stationary flows. Moreover, the introduction of all the models needed in this approach results in a limited accuracy.
An intermediate alternative is the *Large Eddy Simulation* (LES) which is more and more popular; it aims to solve only the largest scales (those ones larger than the filter scale), while the smallest one are modeled through subgrid scale models. More details are given in the next section. This approach lowers the computational cost compared to a DNS simulation and provides time resolved solution and a good estimation of the spatial correlation in the simulation domain.
The difference between RANS and LES can be appreciated below, on the simulations results of a laboratory-scale combustion chamber. The burner is the target application of this thesis work and it is detailed in the dedicated chapter. RANS simulations have been performed during an internship at AirLiquide, with the commercial code ANSYS Fluent.
Figure 1.2 shows the axial velocity field of a turbulent reacting flow obtained in RANS and LES simulations. It can be seen that only mean quantities are accessed in RANS simulations, while time resolved solution are available from LES, for which an instantaneous field is shown in Fig. 1.2.

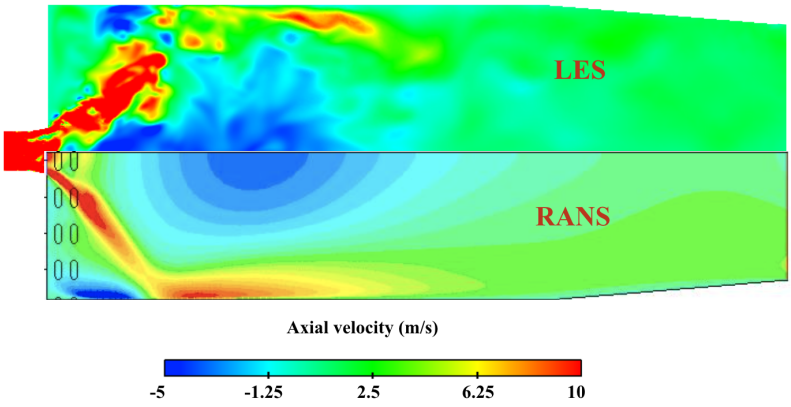

Figure 1.2: *Axial velocity fields from LES (top) and RANS (bottom) on a longitudinal plane of a laboratory scale burner.*

1.3.3 Large Eddy Simulation governing equations

As already mentioned, LES aims at solving the largest turbulent structures that can be explicitly captured by the LES grid and at modeling the smallest one that cannot be resolved on the LES grid through subgrid models. This concept is qualitatively shown in Fig. 1.3 where the turbulent energy spectrum is plotted against the wavenumber. The role of RANS and DNS is also represented. In LES a cut-off value k_c represents the threshold beyond which modelization is needed. In LES, in order to solve the Navier-Stokes equations governing

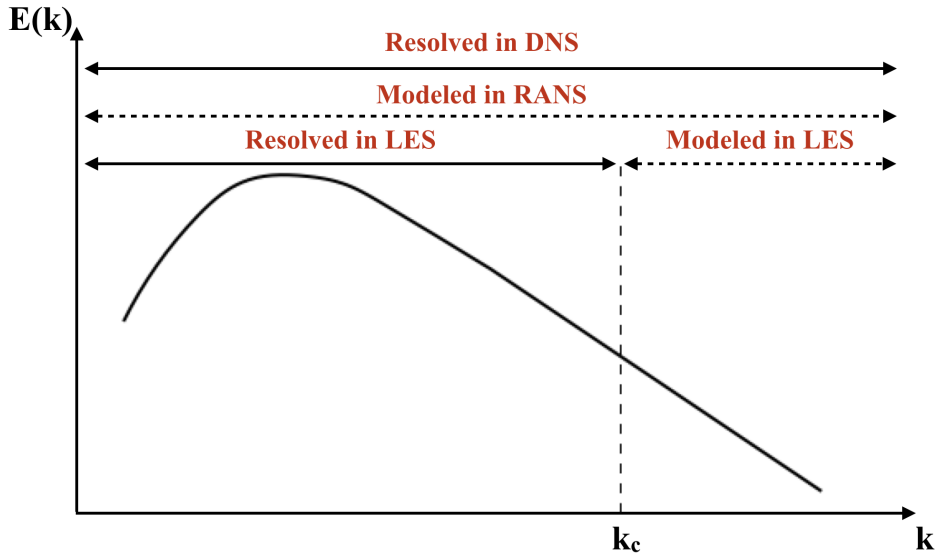

Figure 1.3: *Turbulent energy spectrum as a function of the wavenumber k, where k_c is the cut-off value. Computed and resolved scales from DNS, RANS and LES are also highlighted.*

the evolution of the larger scales (those larger than Δ), a spatial filter G_Δ of characteristic size Δ is applied, while the effects of smaller scales on the resolved fields are represented by subfilter-scale models. The local spatially filtered value $\bar{\Phi}$ of a physical quantity Φ is defined as:

$$\bar{\Phi} = \int \Phi(\mathbf{x}')G_\Delta(\mathbf{x} - \mathbf{x}')d\mathbf{x}' \tag{1.27}$$

The spatially filtered value $\bar{\Phi}$ thus depends on the filter function G_Δ and on the filter size Δ. In practice, the filter size is usually taken to be equal or proportional to the local CFD mesh size.
The physical variable Φ in a turbulent flow can be decomposed in the filtered part $\bar{\Phi}$ and the subgrid scale part Φ'.
In variable-density flows, the density-weighting is useful and it is done in a

procedure similar to the Favre average (Favre 1965):

$$\bar{\rho}\widetilde{\Phi} = \overline{\rho\Phi} = \int \rho(\mathbf{x}')\Phi(\mathbf{x}')G_\Delta(\mathbf{x}-\mathbf{x}')d\mathbf{x}' \tag{1.28}$$

Applying the spatial filter operation to Eqs. 1.22, 1.23, 1.24 and 1.25 leads to:

$$\frac{\partial\overline{\rho}}{\partial t} + \frac{\partial\overline{\rho}\widetilde{u_i}}{\partial x_i} = 0 \tag{1.29}$$

$$\frac{\partial\overline{\rho}\widetilde{Y_k}}{\partial t} + \frac{\partial}{\partial x_i}(\overline{\rho}\widetilde{Y_k}\widetilde{u_i}) = -\frac{\partial}{\partial x_i}(\overline{J_{k,i}}) + \overline{\dot{\omega}_k} - \frac{\partial}{\partial x_i}(J^t_{k,i}) \tag{1.30}$$

$$\frac{\partial\overline{\rho}\widetilde{u_j}}{\partial t} + \frac{\partial}{\partial x_i}(\overline{\rho}\widetilde{u_i}\widetilde{u_j}) = -\frac{\partial\overline{p}}{\partial x_j} + \frac{\partial\overline{\tau_{ij}}}{\partial x_i} + \frac{\partial\tau^t_{ij}}{\partial x_i} + \overline{\rho}g_j \tag{1.31}$$

$$\frac{\partial\overline{\rho}\widetilde{E}}{\partial t} + \frac{\partial}{\partial x_i}(\overline{\rho}\widetilde{E}\widetilde{u_i}) = -\frac{\partial}{\partial x_i}(\overline{pu_i}) + \frac{\partial}{\partial x_i}(\overline{\tau_{ij}u_i}) + \tag{1.32}$$

$$- \frac{\partial}{\partial x_i}\overline{q_i} + \overline{\dot{\omega}_T} + \overline{P^R} - \frac{\partial}{\partial x_i}q^t_i \tag{1.33}$$

In this system of equations three new terms appear:

- the subgrid-scale (SGS) species fluxes $J^t_{k,i}$:

$$J^t_{k,i} = \overline{\rho}(\widetilde{Y_k u_i} - \widetilde{Y_k}\widetilde{u_i}) \tag{1.34}$$

- the SGS Reynolds stress τ^t_{ij}:

$$\tau^t_{k,i} = -\overline{\rho}(\widetilde{u_i u_j} - \widetilde{u_i}\widetilde{u_j}) \tag{1.35}$$

- the SGS energy fluxes q^t_i:

$$q^t_i = \overline{\rho}(\widetilde{E u_i} - \widetilde{E}\widetilde{u_i}) \tag{1.36}$$

Since these three unresolved subgrid-scale terms are not known, closure models are used. Approximations and closure models for such terms are listed here:

- the pressure velocity term $\overline{Pu_i}$ is usually approximated by $\overline{P}\widetilde{u_i}$ (Poinsot and Veynante 2005);
- the laminar filtered stress tensor $\overline{\tau_{ij}}$ is approximated as:

$$\tau_{i,j} = \bar{\mu}\left(\frac{\partial u_i}{\partial x_j} + \frac{\partial u_j}{\partial x_i}\right) - \frac{2}{3}\mu\frac{\partial u_k}{\partial x_k}\delta_{ij} \tag{1.37}$$

$$\approx \bar{\mu}\left(\frac{\partial u_i}{\partial x_j} + \frac{\partial u_j}{\partial x_i}\right) - \frac{2}{3}\bar{\mu}\frac{\partial\widetilde{u_k}}{\partial x_k}\delta_{ij} \tag{1.38}$$

- the diffusive species flux vector $\overline{J_{k,i}}$ is expressed as:

$$\overline{J_{k,i}} = \overline{\rho Y_k V_k, i} \approx -\overline{\rho}\left[\overline{D_k}\frac{W_k}{W}\frac{\partial\widetilde{X}_k}{\partial x_i} - \widetilde{Y}_k\widetilde{V}^c_i\right] \tag{1.39}$$

- the filtered heat flux $\overline{q_i}$ is written:

$$\overline{q_i} = -\overline{\lambda \frac{\partial T}{\partial x_i} + \sum_{k=1}^{N_S} J_{k,i} h_{s,k}} \tag{1.40}$$

$$\approx -\overline{\lambda} \frac{\partial \widetilde{T}}{\partial x_i} + \sum_{k=1}^{N_S} \overline{J_{k,i}} \widetilde{h}_{s,k} \tag{1.41}$$

- the SGS Reynolds stresses $\tau_{i,j}^t$ becomes:

$$\tau_{i,j}^t = -\overline{\rho}(\widetilde{u_i u_j} - \widetilde{u}_i \widetilde{u}_j) \approx \overline{\rho} \nu_t \left(\frac{\partial \widetilde{u}_i}{\partial x_j} + \frac{\partial \widetilde{u}_j}{\partial x_i} \right) - \frac{2}{3} \overline{\rho} \nu_t \frac{\partial \widetilde{u}_k}{\partial x_k} \delta_{ij} \tag{1.42}$$

- the SGS species fluxes $J_{k,i}^t$ is expressed as a function of the SGS turbulent viscosity ν_t, the turbulent Schmidt number Sc_k^t, $D_k^t = \nu_t / Sc_k^t$ and $V_i^{c,t} = \sum_{k=1}^{N_S} D_k^t \frac{W_k}{W} \frac{\partial \widetilde{X}_k}{\partial x_i}$:

$$J_{k,i}^t = \overline{\rho}(\widetilde{u_i Y_k} - \widetilde{u}_i \widetilde{Y_k}) \approx -\overline{\rho} \left(D_k^t \frac{W_k}{W} \frac{\partial \widetilde{X}_k}{\partial x_i} - \widetilde{Y}_k \widetilde{V}_i^{c,t} \right) \tag{1.43}$$

- finally the SGS energy fluxes q_i^t is approximated as:

$$q_i^t = \overline{\rho}(\widetilde{u_i E} - \widetilde{u}_i \widetilde{E}) \approx -\lambda^t \frac{\partial \widetilde{T}}{\partial x_i} + \sum_{k=1}^{N_S} J_{k,i}^t \widetilde{h_{s,k}} \tag{1.44}$$

  where $\lambda^t = \mu^t \bar{C}_P / Pr^t$ and $\mu^t = \bar{\rho} \nu^t$.

1.4 State of the art of coupled simulations of turbulent flows with thermal radiation

In order to predict heat fluxes at the walls, coupling of radiation and combustion is needed. Moreover, coupling fluid solver and radiation solver allows to increase the accuracy in combustion calculations (Coelho 2007), as radiation impacts the temperature distribution and the wall heat fluxes. And since the chemistry of polluting species is sensitive to temperature, radiation can also have an indirect impact on species formation.
In this section, advances made in last years in coupling radiation modelling with turbulent combustion are reviewed. In Tab. 1.1 selected works carried out in the last two decades are summarized and sorted according to the increasing precision of fluid solver (from RANS to DNS). The type of radiation solver and the model for radiative properties of gases as well as the kind of combustion application which is simulated are highlighted.
Several observations can be done. First it can be noticed that the first studies

Reference	Fluid-radiation	Gas model	Application
Adams and Smith (1995)	RANS-DOM	Grey	Confined turbulent sooting flame
Coelho et al. (2003) Habibi et al. (2007) Wang et al. (2008) Bertini et al. (2018)	RANS-DOM	Glob	Turb. jet flame Industrial furnace Turb. Jet flame Aeronautical combustor
Snegirev (2004) Mehta et al. (2009)	RANS-MC	Glob	Turb. flame Turb. sooting flame
Tessé et al. (2004)	RANS-MC	CK	Turb. sooting flame
Zhao et al. (2013)	RANS-MC	LBL	Oxy-combustion
Poitou et al. (2012) Berger et al. (2016)	LES-DOM	Glob	Confined turb. flame Helicopter combustor
Jones and Paul (2005)	LES-DOM	Grey	Gas turbine combustor
Gupta et al. (2013)	LES-MC	LBL	Turb. jet flame (1 M cells)
Koren et al. (2017) Rodrigues et al. (2018)	LES-MC	CK	Laboratory-scale combustor
dos Santos et al. (2008)	LES-RT	CK	2D burner
Wu et al. (2005)	DNS-MC	Grey	3D DNS of statistically 1D flame
Zhang et al. (2013)	DNS-MC	CK	Turb. channel flow

Table 1.1: *Short literature review of advances in coupled combustion-radiation simulations with RANS, LES and DNS. Gas radiative properties are described as: Gray Gas (Grey), Global model (Glob.), narrow-band CK model (CK), Line-By-Line (LBL). The type of radiation solver is also highlighted: Discrete-Ordinates Method (DOM), Monte Carlo (MC), Ray tracing (RT).*

on radiation-combustion coupling were carried out in RANS simulations. The reason is the low computational cost of such an approach, which is a constraint if one considers the computing power available at that time. RANS simulations have been coupled, over the course of the years, with both DOM and MC for a variety of applications and using several gas models. Several works about RANS-DOM simulations using global models are available in literature. The first work found in literature uses a gray gas approximation in order to simulate a turbulent sooting flame of natural gas inside an industrial scale furnace. Many works have used, instead, global models for gases in RANS-DOM simulations such as WSGG (Coelho et al. (2003), Habibi et al. (2007), Bertini et al. (2018)) and full-spectrum k-distribution (FSK) (Wang et al. 2008). In spite of the advantage in terms of computational cost, RANS simulations do not benefit of accurate instantaneous spatially resolved information, therefore Turbulence-Radiation Interaction (TRI) modelling is required.
A significant alleviation of accuracy and modeling issues can be obtained by fully resolving in time and space the turbulent flow field trough DNS simulations. However, due to the prohibitive cost of such simulation, in the past DNS have been coupled with MC solvers only to study radiation effects on statistically 1D flames (Wu et al. 2005), or in an academic test case with a non-reacting mixture of burnt gases (Zhang et al. 2013).
Therefore an intermediate choice is to use LES instead of DNS, providing time resolved solution and a good estimation of the spatial correlation in the simulation domain. Moreover LES enables to avoid most of the modelling issues of Turbulence-Radiation Interaction (TRI) which must be considered in RANS simulations. For this reason, several works on LES coupled with radiative transfer can be found in literature. DOM methods for radiation are used in Jones and Paul (2005) with a gray gas approximation and in Poitou et al. (2012) and Berger et al. (2016) with the help of global models for the simulation of combustion chambers. One work about LES coupled with a deterministic ray tracing can also be found in literature (dos Santos et al. 2008), however it is applied to a 2D application. More recently, thanks to the increase in computing power, LES are also coupled with MC methods. Very accurate methods and models are applied in the simulation of a turbulent jet flame in Gupta et al. (2013) on a 1 million cells mesh. High fidelity simulations of semi-industrial burners become nowadays affordable and examples can be found in the most recent works of Koren et al. (2017) and Rodrigues et al. (2018), where LES-MC is applied with a narrow-band model.

1.5 The importance of radiation in combustion systems

During the past, several works have shown the importance of including radiation in combustion applications (Viskanta and Mengüç (1987), Modest and

Haworth (2016)). Moreover, nowadays there is an increasing interest towards new combustion technologies which aim to reduce pollutants emissions; some examples are oxy-combustion and flameless combustion. In such applications radiation plays a very important role, since the wall radiative fluxes can be very high and could affect the design and material choice of components.
In order to show the motivation to this thesis study, in the following some of the more recent works carried out at the EM2C laboratory are presented. The first example constitute the background of this thesis work, while the second and third example deal with applications investigated during this thesis.

1.5.1 Confined turbulent CH4-H2-Air premixed flame

The configuration illustrated in this section and studied by Guiberti et al. (2015) is a semi-industrial burner typical of industrial furnaces used in the steel industry. The fuel is a mixture of CH_4 and H_2 (60% and 40% in volume, respectively) and the corresponding flame thermal power is 4 kW.
This combustion system is simulated by Koren et al. (2017) through a multi-physics approach combining large-eddy simulation, conjugate heat transfer and radiative heat transfer with the objective of predicting the wall temperature field in order to retrieve flame stabilization and wall heat losses without any prior knowledge from experimental data. Accurate Monte Carlo methods are used to solve the radiative heat transfer. Figure 1.4 shows temperature and radiative power fields computed in Large Eddy Simulations on a longitudinal section of the combustion chamber.
In this specific application, radiative and convective fluxes are of the same order of magnitude ($\approx$ 1 kW each) and the importance of including an accurate radiation solving is shown in Fig. 1.5 where measured wall temperature from Mercier et al. (2016) is compared to the computed wall temperature field in a case where radiation is neglected (left) and in the case of multiphysics simulation (right). The gap between computed and measured temperature fields becomes very small when thermal radiation is included.

1.5.2 Flameless combustion

The work presented in this section has been carried out during the thesis secondment spent at the Université Libre de Bruxelles as part of the CLEANGas project. The application studied is a 20 kW flameless burner fed with natural gas, studied by Ferrarotti et al. (2017).
Over the last decades, flameless combustion or 'Moderate or Intense Low Oxygen Dilution' (MILD) combustion has attracted considerable attention because of its capability of targeting both high thermal efficiency and reduced NO_x emissions. The furnace, made of stainless steel and insulated with ceramic fiberboards, is a squared chamber with an internal section of 70 cm and it is represented in Fig. 1.6. The chamber has been designed with the goal to rep-

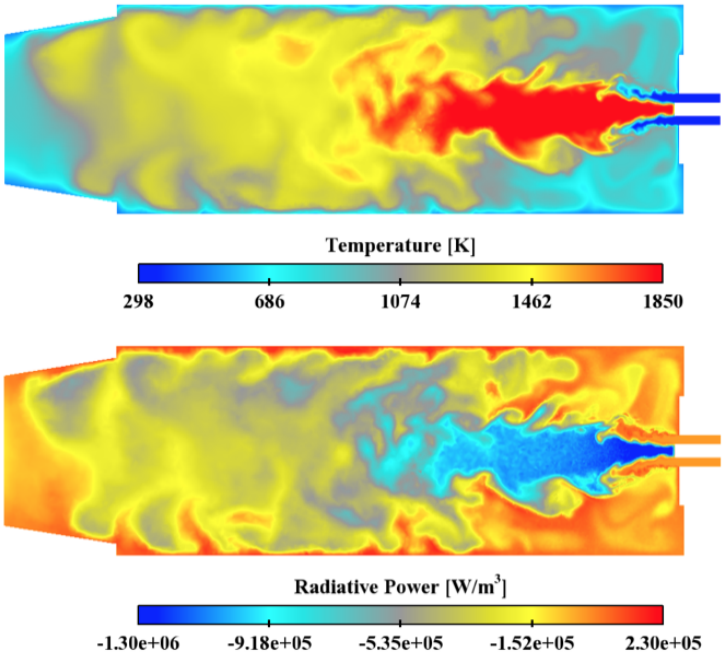

Figure 1.4: *Instantaneous fields of temperature (top) and radiative power (bottom) on a longitudinal section of the burner (Koren et al. 2017).*

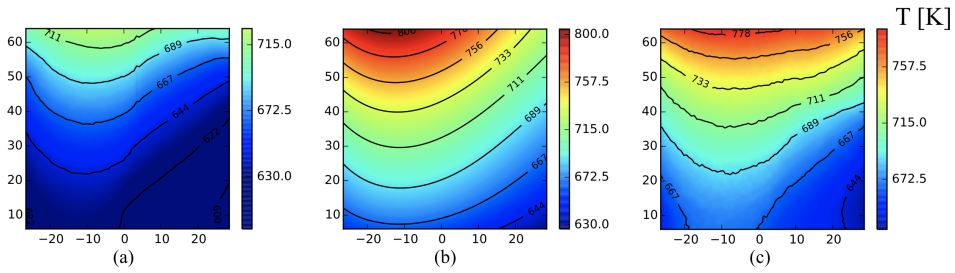

Figure 1.5: *Wall temperature over the measurements zone (lengths in mm). (a): numerically computed wall temperature without radiation. (b) experimentally measured temperature (Mercier et al. 2016). (c): numerically computed wall temperature with radiation (Koren et al. 2017).*

resent realistic conditions faced in industry in terms of air excess, fuel and air velocity and internal load.

MILD furnaces usually operate with a high recirculation degree k_R, representing the fraction of the mass flow rate of the exhaust gases recirculating into the reaction zone over the total fuel and air mass flow rates fed to the burner. For this configuration k_R is equal to 15.3, as a consequence a high dilution of reactants and flame products is created. Reactants, natural gas and air in this case, are pre-heated above their self-ignition temperature by burnt gases.

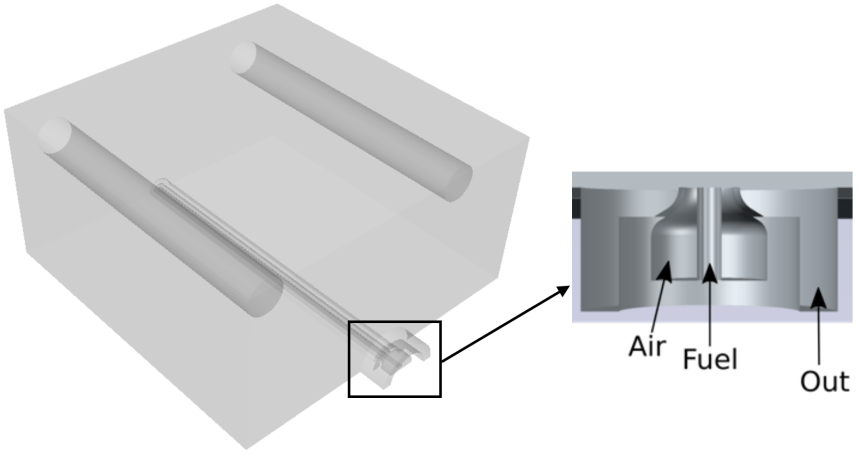

Figure 1.6: *Numerical domain of the 20 kW flameless burner on the left; sketch of injector on the right.*

Such a system is characterized by a more uniform temperature field than in traditional combustion, and by the absence of high temperature peaks, thus suppressing NO formation through thermal mechanism. Figure 1.7 shows the fields of temperature and CO_2 molar fractions extracted from RANS calculations (Ferrarotti et al. 2017) and used for non-coupled radiative heat transfer simulations performed in this study.

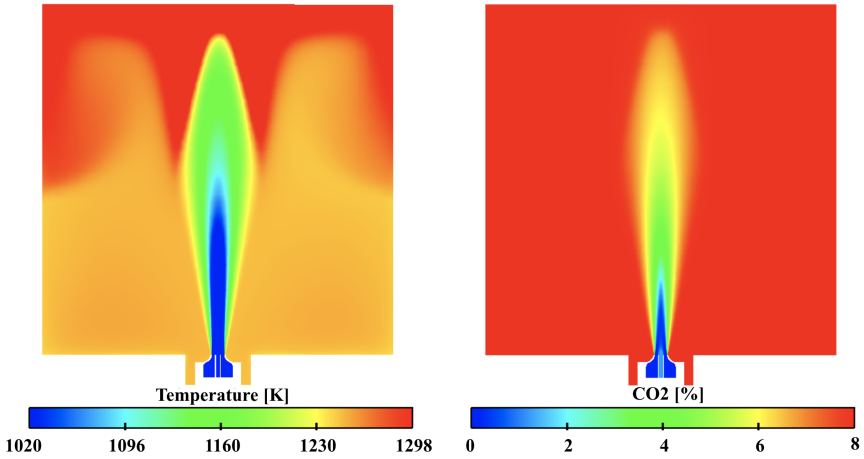

Figure 1.7: *Computed fields of temperature (left) and CO_2 molar concentration (right).*

The corresponding radiative power field, obtained with an accurate Monte Carlo method combined with an accurate model for the radiative properties of gases, is shown in Fig. 1.8 (c) together with the radiative power field obtained in a case where the optically thin assumption is considered (a) and a case where the

Discrete Ordinate Method is used with a gray gas model with the commercial software Fluent.

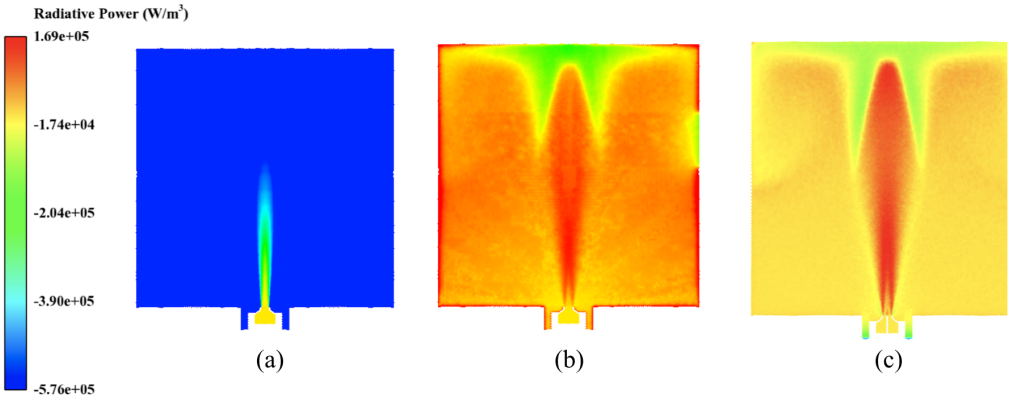

Figure 1.8: *Numerical radiative power fields obtained in case of optically thin assumption (a), solved with a Discrete Ordinates Method using a gray gas model (b) and solved with a Monte Carlo method with a narrow band model (c).*

It is worth noticing that the commonly used Optically Thin approach (Fig. 1.8 (a)) leads to false information about thermal power field: when the radiative power absorbed by participating gases is neglected, the corresponding predicted radiative fluxes could be very high since all the volume is characterized by high negative values of radiative power.
On the contrary, when the gray gas approximation is applied (b), spectral radiative properties of gases are neglected and this could lead to an overestimation of the radiative power field inside the combustion chamber, which results in a higher absorption compared to accurate results (c). As a consequence the radiative fluxes predicted by RANS simulations (6 kW = 30% of flame power P^{th}) in Ferrarotti et al. (2017) are overestimated compared to the ones predicted by more accurate methods (2.4 kW = 12% of P^{th}).
Two main conclusions can be drawn by the presented study: the first one is that radiative fluxes cannot be neglected in the investigated flameless burner, since 12 % of the thermal power is lost through wall radiative fluxes; the second one is that simplistic approximations like optically thin media or gray gas may give a misleading quantification of radiative power field which in turns affect the temperature field in coupled simulations.

1.5.3 Oxy-combustion

Oxy-combustion is a relatively recent combustion technology which has gained a significant interest in industry because it is characterized by several advantages. In an oxy-combustion process, the reactant air is replaced by pure oxygen O_2. This allows to easily capture CO_2 from burnt gases, which are mainly composed by CO_2 and water vapor. In order to keep burnt gas temperature low,

oxy-combustion is often operated in CO_2 and H_2O dilution. Since N_2 is absent, an other big advantage of oxy-combustion is the reduction of NO_x emissions. However, industrial furnaces are designed for air-fuel flames. It could be then very interesting to better understand the effects of this process in order to retrieve conditions similar to ones obtained in air fuel flames and make industrial furnaces versatile to the oxy-combustion without doing many modifications.
All these observations motivated the creation of the Oxytec project dedicated to OXY-combustion and heat transfers for the new energy TEChnologies, with the cooperation of Air Liquide, CentraleSupélec and CNRS.
In this context, an experimental device has been developed at the EM2C laboratory, the Oxytec chamber, shown in Fig. 1.9. Methane-Air flames and oxy-methane flames with high CO2-dilution have been experimentally investigated by Jourdaine et al. (2017). The studied flames, which are different in composition, share lot of common features, such as flame topology, adiabatic temperature and heat fluxes through the walls.

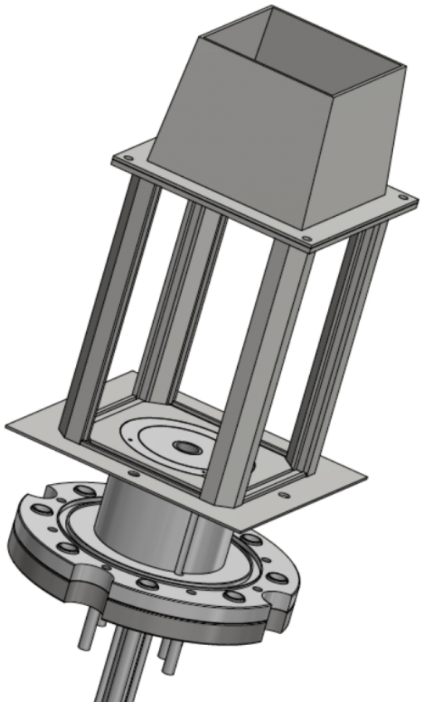

Figure 1.9: *Sketch of the Oxytec chamber.*

A first quantification of thermal radiation inside the Oxytec chamber in these two flame configurations can be made. Thus, a radiative heat transfer simulation is performed in a configuration where the chamber is filled with an homogeneous mixture of burnt gases at adiabatic temperature, which is the same for both the configurations. A value of temperature T_w= 1000 K has been imposed on the chamber walls, as well as a value of global emissivity

equal to 0.75.
The burnt gases mass concentration for both the investigated flames is summarized in Tab. 1.2. CO_2 concentration is around 6 times higher in the oxy-flame compared to the methane-air one and this let think that radiative fluxes may be significant in the oxy-flame.

Flame	CO_2 [-]	H_2O [-]	N_2 [-]
A	0.14	0.12	0.73
B	0.83	0.12	-

Table 1.2: *Mass fraction of burnt gases in the investigated Methane/Air flame (A) and CO_2-diluted oxy-methane flame (B) .*

Results of preliminary studies provide the instantaneous radiative flux on the chamber walls which is shown in Fig. 1.10 for both the configurations A and B. This is a rough approximation since, in reality, wall heat losses are present and consequently burnt gas temperature is not homogeneous inside the chamber, and lower than the adiabatic flame temperature far from the flame region. Moreover wall temperature is not uniform and quartz windows are not opaque to radiation but characterized by radiative properties which vary depending on the frequency. Nevertheless if the ratio of radiative fluxes in both the studied cases is considered, it can be deduced that in a CO2-diluted oxy-methane flame radiation is very important and its impact may be 1.4 bigger than a traditional Methane-Air flame.

The Oxytec chamber represents a very interesting opportunity to numerically investigate one of the key combustion technologies, the oxy-combustion, allowing to meet the objectives of the CLEAN Gas project. For this reason, it is retained as the target configuration for the numerical simulations envisaged in this thesis work.

1.6 Approaches and models used in this thesis

In the precedent sections, main principles on radiative heat transfer and combustion of turbulent reacting flows are given. Starting from the conclusions drawn during the description of the several approaches available in literature, methods and models used in the simulations performed in this thesis work can be justified.
The main methods and models reviewed in this chapter are summarized in Fig. 1.11. For each phenomenon (combustion, radiation and gas radiative properties) three approaches are listed and classified in order of accuracy and CPU cost.

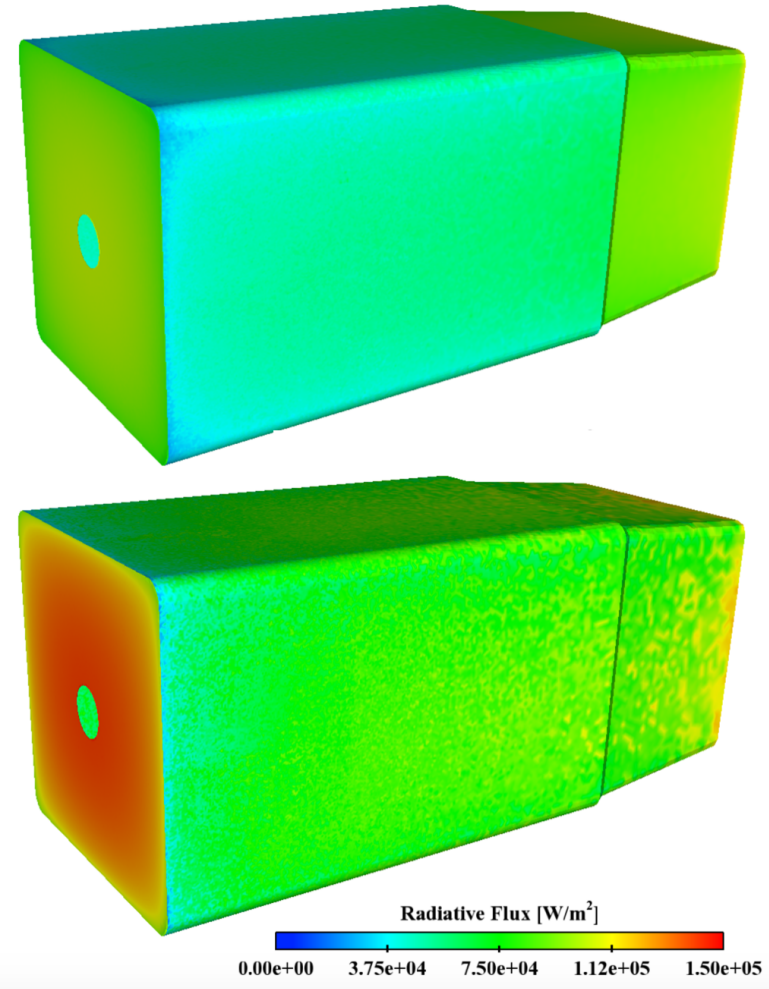

Figure 1.10: *Instantaneous radiative heat flux on chamber walls for the two flames A (top) and B (bottom), corresponding to an homogeneous composition of burnt gases at adiabatic temperature.*

1.6.1 Turbulent combustion

As already mentioned, accounting for radiative heat transfer in turbulent reacting flows is not an easy task, since local radiative intensity is strongly correlated to the instantaneous medium distribution in the spatial domain. Furthermore it also shows a highly non-linear response to temperature and species concentrations. Therefore accurate calculation of radiative transfer requires an instantaneous spatially resolved information regarding temperature and species composition fields. DNS is the best approach to face this problem because it fully resolves in time and space the flow field. However DNS simulations remain prohibitive for use in large-scale applications, such as the laboratory scale combustion chamber targeted in this study.

Combustion	Radiation	Gas radiative properties
DNS	MC	LBL
LES	DOM	Narrow band
RANS	P1	Global models

Accuracy

CPU cost

Figure 1.11: *List of the principal approaches used for the simulation of turbulent reacting flows, radiative heat transfer and radiative properties of participating gases in order of accuracy and computational cost.*

On the other side, carrying out RANS simulations, which are characterized by a low computational demand, do not provide information resolved in space and time, since only average quantities are calculated. Then accounting for Turbulence-Radiation Interaction (TRI) (Coelho (2007), Coelho (2012)) in such configurations requires TRI modelling, and the incertitude linked to these models also has to be taken into account. While deriving such models is still an ongoing research domain, an intermediate choice is to use LES instead of RANS, providing time resolved solution and a good estimation of the spatial correlation in the simulation domain. The subgrid-scale TRI effects are nonetheless strictly not negligible and modeling efforts are ongoing (Soucasse et al. (2014), Gupta et al. (2013)).
RANS and LES simulations of the target application can be qualitatively compared in Fig. 1.12 (left), where the mean axial velocity field issued from LES is compared to the axial velocity field of RANS simulations. Compared to

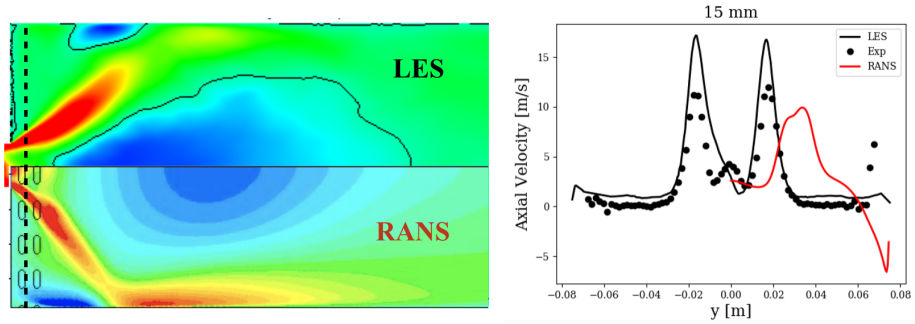

Figure 1.12: *On the left: mean axial velocity field from LES (top) and RANS (bottom) on a longitudinal plane of a laboratory scale burner. On the right: mean axial velocity profiles on a transvere at a height of 15 mm from the chamber inlet represented in dashed line. — LES results; – RANS results; • : Experimental data.*

Fig. 1.2 where instantaneous field from LES is shown, Fig. 1.12 adds one more information showing that even if one is interested only to averaged quantities, RANS simulations may lead to erroneous results when complex turbulent flows are targeted. For example, the axial velocity field in RANS is just qualitatively comparable to the LES one: the negative axial velocity regions predicted by LES can be found also in RANS, as well as the velocity peaks; however, if velocity profiles are compared (Fig. 1.12 right), it can be seen that the quantitative results from RANS simulations are significantly different from LES.
All the aforementioned reasons justify the choice of a LES approach for coupled and non-coupled simulations of the target application.

1.6.2 Radiation and gas radiative properties

For the resolution of the RTE several methods have been presented. The most frequently used are listed in the Fig. 1.11. The $P1$ approximation is the less computationally demanding, however, as already discussed, it results in lack of accuracy. The DOM is often used and is often a good compromise between accuracy and CPU cost, however it may leads to some issues linked to ray effect and false scattering. The most accurate method in Fig. 1.11 is the Monte Carlo (MC) method. The main advantage of this method is that the cost of a simulation does not depend on the integration dimensions (such as directions and wavelength). However its convergence rate is low and high computational resources are needed.
For the simulation of combustion chambers, DOM has been widely used leading to acceptable results. But, in order to get rid of the uncertainty of thermal radiation computations, the method which is finally chosen for the set-up of non-coupled radiative simulations and for coupled combustion-radiation simulations is the MC method. The main advantages of MC are:

- possibility to statistically estimate the precision of a computation
- CPU cost does not increase with the number of the problem dimensions
- possibility to account for detailed radiative properties without any major additional cost contrary to other methods
- possibility to easily tackle complex geometry configurations

It is also recognized that computational cost of MC is generally very high. In order to increase the efficiency of the classical MC, an improvement is applied in this thesis, through the use of Quasi-Monte Carlo methods which are presented in the following chapters.
Concerning the modeling of gas radiative properties, LBL may be very expensive when applied to real configurations, for this reason in literature its application is limited to low-dimensions cases. A good compromise between LBL and global models, allowing to account for the spectral dependency of the radiative properties of participating gases, is the $c-k$ method. It is here cho-

sen for its facility of implementation, its accuracy, and its relatively reasonable cost when only two absorbing gaseous species are considered (CO_2 and H_2O). Another big advantage of narrow-band distribution models is the possibility to easily account for spectral radiative properties of confining walls, which is not possible when global models are used. Thanks to this approach, spectral dependency of the radiative properties of quartz windows confining the flame is taken into account in the coupled simulations of this thesis work and its effect is shown in Chap. 5.

1.7 Thesis objectives and organisation of the manuscript

This thesis is inserted in the context of multi-physics simulations involving thermal radiation and combustion. Thermal radiation is known to play an important role in some combustion processes, such as the ones involved in the new combustion technologies. The Oxytec chamber, experimentally investigated to disseminate the knowledge about oxy-combustion, is retained as target application for the numerical simulations envisaged in this thesis.
In order to accurately account for thermal radiation, Monte Carlo methods are retained, which, on the other hand, are known to be computationally demanding. Indeed, the use of MC methods can make a coupled simulation even 10 times more expensive than an only-combustion simulation.

The objective of this thesis is to make coupled simulations of real combustion systems computationally affordable, while accounting for accurate modelling of thermal radiation. For this reason, an alternative family of methods, known as Quasi-Monte Carlo methods (QMC), is investigated. QMC have been applied, in the past, only to simple 1D or 2D configurations. In this work they are, for the first time, applied to real 3D configurations. Attention is focused on the efficiency improvement obtained with QMC compared to MC. QMC are finally retained in a coupled combustion-radiation simulation of the target application, the Oxytec chamber.

Chapter 2 is dedicated to Monte Carlo methods (MC) in radiative heat transfer. Monte Carlo principles are first presented with a mathematical approach; attention is focused on the importance sampling, one of the existing methods for variance reduction. An alternative method to improve the MC efficiency is briefly introduced: the Quasi-Monte Carlo methods (QMC). Successively, a state-of-the-art is carried out about the application of MC and QMC methods to radiative heat transfer, in terms of methodologies and applications.

In **Chapter 3**, the principles and properties of Quasi-Monte Carlo method, introduced in Chapter 2, are illustrated on a simple numerical integration prob-

lem. In order to get the error estimation of MC, a randomization is needed, leading to Randomized-QMC (RQMC). RQMC and MC are first compared on a two dimensional integral, and then assessed in simulations of radiative heat transfer in three practical 3D combustion applications which combine several degrees of complexity (high pressure, presence of soot, gas-wall interactions). Efficiency of MC and QMC methods is finally discussed.

Chapter 4 presents results of Large eddy simulation (LES) of the target application, the Oxytec chamber where a swirled premixed methane-air flame (Flame A) is investigated. The numerical set-up is presented. In a first step, LES of non-reacting flow are considered: typical features from swirling flows are retrieved. In a second step, the reactive case is studied, accounting for isothermal boundary conditions at walls. Simulations are validated using the available experimental data. The high residence time characterizing the Oxytec chamber makes necessary defining some convergence criteria for the establishment of the steady flow.

Before presenting coupled simulations, the concepts of the coupling between LES fluid solver, AVBP, and Monte Carlo radiation solver, Rainier, are introduced in **Chapter 5**. Due to the computational cost of a coupled LES-MC simulation, an analysis is carried out in terms of accuracy and computational cost. Two main parameters are retained in such an analysis: the size of the computational grid used for radiation simulations and the coupling frequency between fluid and radiation solver. Their impact on the computational cost of a coupled simulation is derived and several scenarios are defined. The numerical set-up of coupled simulation is then described. Attention is focused on boundary conditions imposed in Rainier, specifically to the treatment of semi-transparent windows.

In **Chapter 6**, Large Eddy Simulations of the premixed methane-air flame are coupled with thermal radiation. The radiative transfer equation is solved using a Quasi-Monte Carlo method with a ck model for gas radiative properties. Spectral radiative properties of the viewing windows confining the flame are considered and their impact on wall radiative flux is shown. The impact of radiative heat transfer on the different variables fields of the swirled premixed flame of methane and air is investigated. The comparison with the LES without radiation allows to highlight the radiation effects on velocity and temperature fields, wall fluxes distribution and flame shape.

In **Chapter 7**, Oxy-combustion is approached, through the CO_2-diluted oxy-methane flame (Flame B) experimentally investigated in the Oxytec experimental campaign. Attention is given to the effects of CO_2-dilution in a combustion process, from the point of view of radiation absorption operated from fresh gases. Results highlight a big impact of CO2 re-absorption on the laminar

flame speed but also a high dependence on the domain size used in the simulation. In the final part of the chapter, first 3D simulations of the Flame B are presented; their numerical-set up is discussed and, while being not converged, encouraging results are shown. Finally, a preliminary study on radiative heat transfer taking place in Flame B is carried out, and a comparison with the Flame A is performed.

Acknowledgments

This project has received funding from the European Union's Horizon 2020 research and innovation programme under the Marie Sklodowska-Curie grant agreement No 643134. This work was also supported by the Air Liquide, CentraleSupélec and CNRS Chair on oxy-combustion and heat transfer for energy and environment and by the OXYTEC project, grant ANR-12-CHIN-0001 of the French Agence Nationale de la Recherche.
The numerical study was carried out thanks to the HPC resources of CINES under the allocations 2016-020164, 2017-A0022B10159 and 2018-A0042B10159 made by GENCI, and the HPC resources from the "Mésocentre" computing center of CentraleSupélec and École Normale Supérieure Paris-Saclay supported by CNRS and grants from Ministry of Research via the Contrat Plan État-Région.

Chapter 2

Monte Carlo methods in radiative heat transfer

The goal of this chapter is to present the state-of-the-art about Monte Carlo (MC) methods. Their principles are first presented from a mathematic point of view, leading to the definition of the MC error. If one one hand, MC methods are considered as reference methods thanks to their high accuracy, on the other hand they are characterized by a slow convergence.
Some methods to accelerate MC convergence and used in the context of the radiative heat transfer are presented and discussed, such as the strategy of the importance sampling. A state-of-the-art about the MC formalisms used in radiative heat transfer is given, together with the one about the models used to treat the radiative properties of participating gases.
Another family of methods, called Quasi-Monte Carlo methods and known to improve the MC convergence, are introduced and a literature review about their applications is presented.

Contents

2.1 Introduction

The idea to use a statistical approach to approximate mathematical solutions to physical problems is not recent. During the early years of the twentieth century many notable scientists such as Lord Rayleigh, Courant, Kolmogorov and many others used statistical procedures to approximate the solutions of differential equations. Any method of solving a mathematical problem with a statistical sampling technique is commonly referred to as a Monte Carlo method (MC). The first developments of MC date back to the 1930s-1940s, when experiments for the development of nuclear weapons were difficult and their potential behavior wanted to be accurately analyzed. Indeed one of the early simulations dealt with the investigation of statistical approaches to the behavior of neutrons diffusion for the development of the atomic bomb during World War II. The first paper on the MC was published by Metropolis and Ulam (1949), and the method's name was chosen in homage to Monte Carlo, a city known for its gambling casinos in Monaco (where Ulam used to gamble very often). Since then, the Monte Carlo method was applied to several fields (graphics, biology,

finance and so on) and in this chapter the attention is focused on the application of the Monte Carlo method to problems involving the radiative heat transfer. First, an introduction about MC and some concepts of statistical theory is given. Then Quasi-Monte Carlo method's principles are illustrated, and finally a state of the art about methods, convergence improvements, gas properties models and applications is presented.

2.2 Cubature Monte Carlo methods

Monte Carlo is a statistical numerical method which simulates mathematical relations through random processes. It allows for numerically estimation of the value of an integral and its theory is based on the theory of probability.

It is worth mentioning that the Monte Carlo technique is perhaps the most attractive method when different complexities are combined to the same problem, while for trivial problems a conventional numerical technique might be more appropriate. However, the complexity of the formulation and the CPU cost is not increased too much when the complexity of the problem increases, which is not the case for conventional methods (see Fig. 2.1). For this reason, MC has

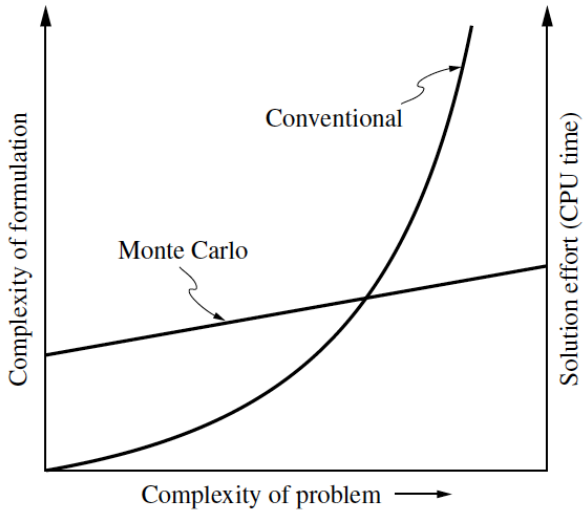

Figure 2.1: *Comparison between Monte Carlo and other techniques conventionally used for the RTE solutions (extracted from Modest (2013)).*

been extensively used since the mid 1900s. The main disadvantage of MC is its large demand of computer time. With the advent of faster and faster computer resources, this challenge is becoming surmountable so that the popularity and the use of MC are increasing.

2.2.1 Monte Carlo principles

When a statistical approach is used to solve mathematical problems, random numbers are required. Random numbers are numerical quantities that substitute random variables and that have the same statistical properties as the random variables. Having truly random numbers on conventional computers seems impossible since their generation is simulated by deterministic algorithms that aim to reproduce numbers whose behavior is very close to that of truly random ones. So the most useful method for obtaining random numbers for computer use is a *pseudorandom* number generator: an algorithm that generates sequences of numbers that have the same statistical behavior as if they were sampled from a sequence of random variables. The pseudo-random number generator used in this thesis work is L'Ecuyer's Multiple Recursive Generator MRG32k3a (L'ecuyer 1999).
As stated above, the MC is a statistical approach for a general multivariate integration problem where the goal is to estimate:

$$I(f) = \int_{[0,1]^d} f(\mathbf{u}) d\mathbf{u} \tag{2.1}$$

where f is a bounded real valued function and $\mathbf{u}$ a d-dimensional vector in $[0,1]^d$. The idea of MC is to use a random sample of N independent and identically distributed points uniform over $[0,1]^d$ to construct the Monte Carlo estimator for the integral $I(f)$:

$$Q(N) = \frac{1}{N} \sum_{i=1}^{N} f(\mathbf{u}_i) \tag{2.2}$$

The approximation is obtained by taking a weighted average of n function evaluatons of f made at the n chosen points, where the weights are all set to $1/n$.
It is possible to compute the expectation of $Q(N)$ and verify that it is equal to $I(f)$:

$$E[Q(N)] = \frac{1}{N} \sum_{i=1}^{N} E(f(\mathbf{u}_i)) = \int_{[0,1]^d} f(\mathbf{u}) d\mathbf{u} = I(f) \tag{2.3}$$

where the second equality follows because the vector $\mathbf{u}$ is uniformly distributed over $[0,1]^d$ and thus its pdf is 1.
The *Strong Law of Large Numbers* (LLN) states that $Q(N)$ converges to $I(f)$ almost surely with N. In other words, if N is large enough, the approximation $Q(N)$ can become arbitrarily close to the desired quantity $I(f)$ with probability 1.

2.2.2 Error estimation

Unfortunately, the LLN does not give any information about the convergence rate, or in other words about how the sample needs to be in order for the estimate to be close to the exact value. Moreover, the knowledge of the convergence rate is important to determine when MC is more efficient than conventional algorithms.
The *Central Limit Theorem* provides such a characterization, and it shows that:

$$\frac{Q(N) - I(f)}{\sigma/\sqrt{N}} \Rightarrow N(0,1), \tag{2.4}$$

where $\Rightarrow$ means convergence in distribution and σ is the standard deviation of $f(\mathbf{u})$. Hence the probabilistic error of the Monte Carlo estimator is in $O(1/\sqrt(n))$ and it is independent of the considered dimension d. The variance of the estimator $Q(N)$, $\sigma[Q(N)]^2$, can be estimated as:

$$\sigma[Q(N)]^2 \simeq \frac{\hat{\sigma}^2}{N} = \frac{1}{N(N-1)} \sum_{i=1}^{N} (f(\mathbf{u}_i) - Q(N))^2 \tag{2.5}$$

where $\hat{\sigma}$ is an approximate of the intrinsic standard deviation. Such a characterization is useful when the MC is compared to other (stochastic) integration methods.

Another methodology to estimate the error, equivalent to the one illustrated above, consists in breaking up the samples resulting in $Q(N)$ into M subsets. For each subset $i \in [1, M]$, a MC estimate $Q_i(P)$ can be computed where $P = N/M$ is the number of samples in the subset. The MC estimations from the total number N of samples is simply related to the MC estimates in the subsets as

$$Q(N) = \frac{1}{M} \sum_{i=1}^{M} Q_i(P). \tag{2.6}$$

The M subsamples $Q_i(P)$ are independent estimations of the same quantity $Q(P)$ whose expectation is $I \approx Q(N)$. The standard deviation of estimates $Q_i(P)$ can then be estimated as

$$\sigma[Q(P)]^2 \approx \frac{1}{M-1} \sum_{i=1}^{M} [Q_i(P) - Q(N)]^2. \tag{2.7}$$

The CLT theorem states that $\sigma[Q(N)]^2 \approx \frac{1}{M}\sigma[Q(P)]^2$ which finally yields an alternative estimation of the standard deviation of the MC estimate from all samples (Modest 2013; Lemieux 2009):

$$\sigma[Q(N)] \approx \widehat{\sigma}_{Q,2}(N) = \left(\frac{1}{M(M-1)} \sum_{i=1}^{M} [Q_i(P) - Q(N)]^2 \right)^{1/2} \tag{2.8}$$

The accuracy of a MC calculation is proportional to the variance $\widehat{\sigma}^2$ and inversely proportional to the number of samples as $N^{-1/2}$. A possibility to accelerate the Monte Carlo convergence rate as a function of N consists in the use of alternative samplings such as low-discrepancy sequences. The resulting quadrature method is called Quasi-Monte Carlo (QMC) and it is introduced in the next section.

2.2.3 Quasi-Monte Carlo methods

Acceleration in Monte Carlo convergence can be obtained by using alternative samplings, the *quasi-random sequences*, which replace the random variables of MC. Such sequences are introduced in the following.

Quasi-random sequences

As the Monte Carlo method, the QMC is a numerical method to compute high-dimensional integrals, and the integral of a function f defined in $[0,1]^d$ is approximated by:

$$\int_{[0,1]^d} f(\mathbf{u}) d\mathbf{u} \approx \frac{1}{N} \sum_{i=1}^{N} f(\mathbf{u_i}) \tag{2.9}$$

with the difference that in MC the points u_i of $[0,1]^d$ are realizations of a sequence of uniform and independent random variables, while in QMC methods the random sequences are replaced by a deterministic alternative, the quasi-random sequences. Such sequences are constructed to minimize a measure of their deviation from uniformity. The uniformity of a sequence is measured in terms of its discrepancy, for this reason the quasi-random sequences are also called *low-discrepancy sequences*.
The discrepancy of a quasi-random sequence enters into QMC via the *Koksma-Hlawka inequality* (Hlawka 1961) which states that for any sequence $\{u_n\}$ and any bounded function f defined in $[0,1]^d$ with variation in the sense of Hardy-Krause, $V[f]$; the integration error ϵ is bounded as:

$$\epsilon[f] = \left| \int_{[0,1]^d} f(\mathbf{u}) d\mathbf{u} - \frac{1}{n} \sum_{i=1}^{n} f(\mathbf{u}_i) \right| \leq V[f] D_n^*(\mathbf{u_1}, ..., \mathbf{u_n}) \tag{2.10}$$

where $V[f]$ is the variation (in the Hardy-Krause sense) of f which, for a function of a single variable, is defined as:

$$V[f] = \int_0^1 \left| \frac{df}{fy} \right| dt \tag{2.11}$$

and D_n^* is the discrepancy of the set of points $\mathbf{u}_i$ $1 \leq i \leq n$.
In order to minimize the error ϵ, the discrepancy D_n^* should be as low as possible.

The discrepancy D_n^* of the points set $\mathbf{u}_i$ $1 \leq i \leq n$ is defined as:

$$D_n^*(\mathbf{u_1}, ..., \mathbf{u_n}) = \sup_{\nu \subset [0,1]^d} \left| \frac{\#\{i : \forall j, x_{i,j} \leq \nu_j\}}{n} - \prod_{j=1}^{d} \nu_j \right|. \tag{2.12}$$

A widely conjecture, still not proved for $d \geq 3$ is that the lowest possible bound attainable for the discrepancy D_n^* is:

$$D_n^*(\mathbf{u_1}, ..., \mathbf{u_n}) \geq C \frac{(log\ n)^{d-1}}{n} \tag{2.13}$$

where C and d are constants and independent of n.
Sequences of points achieving this bound are referred to as low-discrepancy sequences.
The original construction of quasi-random sequences was related to the van der Corput sequence (Niederreiter 1992), which is a one-dimension quasi-random sequence. Following that, Halton (1960) generalized the van der Corput sequence to d dimensions. The Halton sequence D_n^{*H} is bounded by

$$D_n^{*H} \leq C_d \frac{(log\ n)^d}{n} \tag{2.14}$$

where the constant C_d depend on the dimension d.
More details about the way these sequences are built is given in Lemieux (2009). Several algorithms have been proposed for the generation of such sequences, and the Halton, Sobol and Fauvre sequences are most commonly applied to QMC methods. Morokoff and Caflisch (1995) demonstrated that the Halton sequence outperforms when the integral dimensionality is lower than six. More recent constructions, like the Sobol sequence (Sobol' 1976) or Faure (Faure 1982), have much better constants C_d. Among them, the Sobol one outperforms in higher dimensions.
Figure 3.4 illustrates a pseudo-random sequence and a quasi-random sequence (Sobol) in two dimensions. It is possible to clearly see the clumping that occurs in pseudo-random sampling, leaving regions with a few samples, thus making the convergence slower compared to the quasi-random sampling where points are more uniformly distributed in the space.

Unlike for random sampling, points are not independent. In fact, the sample is completely deterministic. Since there is no Central Limit Theorem for quasi-random sequences, there is, however, no corresponding error estimate for quasi-Monte Carlo.
A practical method to obtain error estimates for QMC is based on the randomization of QMC methods. More details about the Randomized Quasi-Monte Carlo methods will be given in the next chapter.

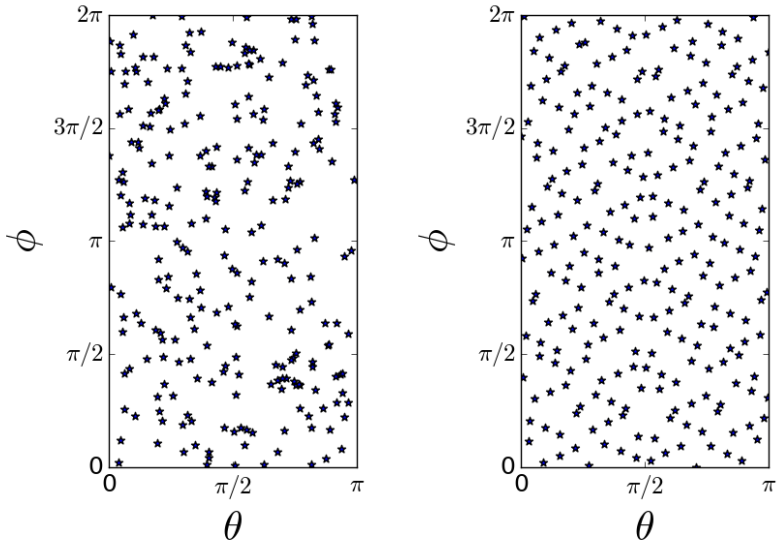

Figure 2.2: *A quasi-random sampling of two variables (θ and ϕ) using a pseudo-random sequence (left) and a Sobol sequence (right).*

2.3 Applications of Monte Carlo methods to radiative heat transfer problems

Since Metropolis original work in 1949, MC have been extensively used in radiative transfer. Indeed, radiation problems possess a form ideally suited for Monte Carlo applications. From a physical point of view energy travels in discrete parcels (photons) over relatively long distances. Thus, applying a Monte Carlo method to a thermal radiation problem is equivalent to trace the history of random samples of photons along their optical path. From a mathematical point of view, the radiative transfer equation is a high-dimensional integral equation depending on various parameters, such as wavelength, direction, point of emission, and this make its solution extremely difficult. This challenge led to an increasing interest towards Monte Carlo methods which are ideal candidates to numerically evaluate high dimensional integrals with relative ease.

The reason of the large diffusion of MC in radiative heat transfer is mainly due to its advantages, such as the possibility to handle complicated systems and to account for physical effects, such as anisotropic scattering, spectral dependence of wall and medium properties, their directional dependence, without any assumption and a large increment of computational effort. Moreover, the statistical features of the results of MC allows the system error, represented by the standard deviation, to be computed. However, the drawback is the need of a large number of realizations in order to obtain statistically meaningful results.

In fact, the standard deviation tends to be proportional to $1/\sqrt{N}$, where N is the total number of bundles.

Several methods have been developed over the years; the most straightforward application of MC models the radiative transfer process simulating photons histories starting at emission point and ending at the absorption point, determining how much power is transferred from one region to another (Forward MC). Other methods start at a termination point and track back the ray in the reverse direction, determining how much power emitted along the path is incident on the detector point (Reverse or Backward MC). Other methods directly compute the radiation transfer exchanges between two computational cells from a traced ray (Reciprocal MC). In the following sections these methods are presented and discussed, together with the approach of hybrid methods.
The aforementioned methods can use different ray-tracing procedures and catch different information from it to provide their results. Two procedures are presented in this section: the standard ray tracing or collision-based method and the energy-partitioning (or path-length based) method.

2.3.1 Classical and reciprocal methods

Three MC formulations for the calculation of the radiative power are here presented. Forward and Backward MC methods are first described before introducing reciprocal methods.

Forward MC

In order to model the radiative transfer process, in the conventional or forward MC (FM), a large number of photon bundles carrying a fixed amount of radiative energy are emitted in the system and their history is traced until the carried energy is absorbed at a certain point in the participative medium or at the wall, or until it exits the system.
Its formulation can be illustrated by dividing the computational domain into N_v and N_f isothermal finite cells.The radiative power in the cell i is the sum of the radiative power emitted by all the cells j of the domain and absorbed by the cell i, P_{ji}^{ea}, minus the power emitted by the cell i, P_i^e:

$$P_i^{FM} = \sum_{j=1}^{N_v+N_f} P_{ji}^{ea} - P_i^e \tag{2.15}$$

P_{ji}^{ea} designates the energy emitted by a differential volume dV_j, transmitted by the media and absorbed by $dA_i \times ds_i$ and it is expressed by:

$$P_{ji}^{ea} = \int_{\nu=0}^{+\infty} P_{\nu,ji}^{ea} d\nu = \int_{\nu=0}^{+\infty} 4\pi\kappa_\nu(T_j) I_\nu^0(T_j) dV_j \times \left(\frac{dA_i}{4\pi r^2}\right) \times \tau_{\nu,r} \times \kappa_\nu(T_i) ds_i \, d\nu$$

(2.16)

where $I^0_\nu(T_j)$ is the equilibrium spectral intensity at temperature T_j, r the distance between the two differential volume cells, κ_ν the spectral absorption coefficient and $\tau_{\nu,r}$ the transmissivity of the column between dV_i and dV_j.
The departure point, propagation direction and spectral frequency of the ray are independently and randomly chosen according to given distribution functions.

Backward or reverse MC

The intuitive physical interpretation given by Collins et al. (1972) to the Backward MC (BMC) was to trace the photon histories from a receiver point backward to the source position (thus the term "Backward") in order to calculate the scattered light intensity at a point receiver located within the earth's atmosphere due to a plane source. This approach is particularly advantageous for those problems where the solution is desired for only a portion of the solid angle, or equivalently only for differential areas, allowing to take all the samples within the solid angle of interest, or equivalently only the areas of the source plane that have the greatest possibility of contributing to the scattered intensity at the receiver position. In these cases the forward MC can be very inefficient. In the application, changing the variable of integration in terms of the source position demonstrated to give the same solution of the Forward formalism but in a more economical way.
Walters and Buckius (1992) and Walters and Buckius (1994) provided the fundamental framework reversing the Monte Carlo paths including a proof of the reciprocity principle presented by Case (1957) and illustrated in the following. They developed this method considering an anisotropically scattering inhomogeneous absorbing and emitting medium, with boundaries that incorporate a bidirectional reflectivity and spectrally dependent properties as in Fig. 2.3.
The reverse paths are initiated from surface dA_k and considered as a line-of-sight from the black walls back to the source point. The history is followed until the point of origin is reached.
M uniform cells with homogeneous temperature and properties are considered along the total path L that reaches a black boundary at temperature T_w. The intensity reaching dA_k from sample n is:

$$\begin{aligned} I_{\lambda,i,k} =& I_{\lambda b}(T_w) exp\left[-\int_{l=0}^{L} \kappa_\lambda(l)dl\right] \\ &+ \sum_{m=1}^{M}\left(I_{\lambda b}(T_m)\left\{exp\left[-\int_{l=l_{m,out}}^{L} \kappa_\lambda(l)dl)\right] - exp\left[-\int_{l=l_{m,in}}^{L} \kappa_\lambda(l)dl)\right]\right\}\right) \end{aligned} \tag{2.17}$$

The integrals of (2.17) may be replaced by summations over the M homoge-

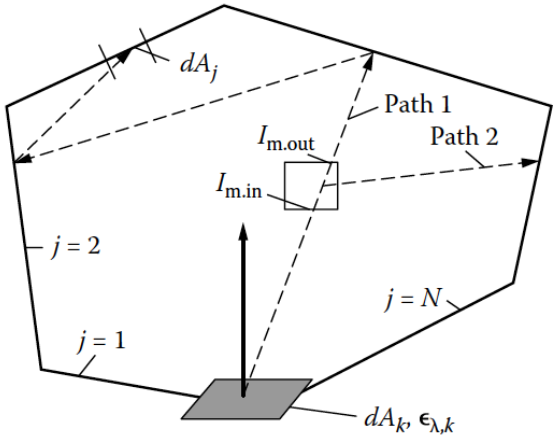

Figure 2.3: *Enclosure containing inhomogeneous spectrally absorbing, emitting and anisotropically scattering medium (Howell)*

neous path elements, becoming:

$$I_{\lambda,i,k} = I_{\lambda b}(T_w) exp\left[-\sum_{m=1}^{M} \kappa_{\lambda,m}(l_{m,out} - l_{m,in})\right] + \sum_{m=1}^{M}\left(I_{\lambda b}(T_m)\left\{exp\left[-\sum_{p=m,out}^{M} \kappa_{\lambda,p}(l_p - l_{p-1})\right] - exp\left[-\sum_{p=1}^{m,in} \kappa_{\lambda,p}(l_p - l_{p-1})\right]\right\}\right) \tag{2.18}$$

m, in is the point where the ray enters the cell m while m, out is the point where it leaves. The overall path length L is made up of the various segments of length $l_{m,out} - l_{m,in}$. If N total samples are considered, the radiative flux incident upon the surface dA_k, q_k, is given by:

$$q_k = \frac{\pi}{N}\sum_{n=1}^{N} I_{\lambda,i,k,n} \tag{2.19}$$

If the boundary is not black, reflection is taken into account and the path is continued according to a given tracing procedure, or terminated otherwise. If the initiating element for the reverse path is a volume element of medium rather than a boundary element, the methodology is the same.

In the BMC, optical paths are generated only from the cell i and the radiative power of a cell i is given by the radiative power emitted by the cells j crossed

by the optical path leaving i and absorbed by i minus the power emitted by i:

$$P_i^{BM} = \sum_{j=1}^{N_v+N_f} P_{ji}^{ea} - P_i^e \tag{2.20}$$

The difference with the FM is that the optical paths are all originated by the cell i of interest. Indeed in BMC tracing ray paths is equivalent to a time-reversal tracking of photons contributing to the desired solution, hence only the rays having a contribution to the solutions are followed, and this greatly enhances the efficiency.
The BMC has been used by several investigators even before Walters and Buckius (1992): Blättner et al. (1974) used this method to analyze twilight phenomena, Adams and Kattawar (1978) for studies in spherical shell atmosphere, Gordon (1985) applied it in the field of seas and oceans. Other applications are found in Nishita et al. (1987), Sabella (1988) and Edwards (1983).
All the cited works using BMC are limited in scope and a large radiation source is required, making a backward simulation straightforward. Modest (2003) presents a more comprehensive formulation for BMC simulations in the area of radiative heat transfer extending its use to the treatment of emitting, absorbing and scattering media with diffuse or collimated irradiation, and cases where the source comes from a very small surface or a point (point and line source). He presents this formulation in terms of both standard ray tracing and energy partitioning method and comparing BMC and FMC simulations.
The reverse MC has been extensively used in the 2000s for several applications: (Ruan et al. 2002) in non-gray medium through spectral radiative exchange factors, (Shuai et al. 2005) used the BMC to analyse the radiation from high-temperature free-stream flow including particles, (Lu and Hsu 2005) applied it to transient radiative transfer, (Wang, Modest, Haworth, and Wang 2008) jet flames, (Sun and Smith 2010) to extreme non-homogeneous media, Tessé et al. (2002) compared it to the FM in 1D systems, Maurente et al. (2008) applied it to a cylindrical combustion chamber and (Dupoirieux et al. 2006) to media with non-homogeneous optical thickness.

Direct Exchange Monte Carlo or Reciprocal Monte Carlo

The conventional and Backward Monte Carlo methods implementation become inefficient in optically thick media, where the photon mean free paths are short and most bundles do not travel far enough from their emission point prior to be absorbed. This means that only a very few bundles participate to distant radiative transfer. Even if this problem can be mitigated by using the energy partitioning method, as seen in Wong and Mengüç (2002), another limitation should be considered, that arises in the treatment of near-isothermal systems where emission and absorption of a hot cell can be orders of magnitude bigger

than the net heat transfer between two cells. Thus, a small uncertainty in emitted and/or absorbed energies may lead to huge errors in the energy balance. To face these problems, Cherkaoui et al. (1996) developed a net-exchange formulation for MC methods, also called Reciprocal MC (RM), who intrinsically fulfills the reciprocity principle.

Reciprocity Principle The radiative power of a cell i can be written as the sum of the exchanged powers P_{ij}^{exch} between i and all the other cells j:

$$P_i = \sum_{j=1}^{N_v+N_f} P_{ij}^{exch} = -\sum_{j=1}^{N_v+N_f} P_{ji}^{exch} \tag{2.21}$$

where P_{ij}^{exch} is defined as:

$$P_{ij}^{exch} = P_{ji}^{ea} - P_{ij}^{ea} = \int_{\nu=0}^{+\infty} (P_{\nu,ji}^{ea} - P_{\nu,ij}^{ea}) d\nu \tag{2.22}$$

Equation (2.16) can be recast as:

$$\frac{P_{\nu,ij}^{ea}}{I_\nu^0(T_i)} = \tau_{\nu,r}\kappa_\nu(T_i)\kappa_\nu(T_j)\frac{dV_i dV_j}{r^2} \tag{2.23}$$

In a similar way $P_{\nu,ji}^{ea}$ is expressed as:

$$\frac{P_{\nu,ji}^{ea}}{I_\nu^0(T_j)} = \tau_{\nu,r}\kappa_\nu(T_i)\kappa_\nu(T_j)\frac{dV_i dV_j}{r^2} \tag{2.24}$$

Since the right sides of (2.24) and (2.24) are identical, it is possible to obtain the *reciprocity principle*:

$$\frac{P_{\nu,ij}^{ea}}{I_\nu^0(T_i)} = \frac{P_{\nu,ji}^{ea}}{I_\nu^0(T_j)} \tag{2.25}$$

Thus the ratio between $P_{\nu,ij}^{ea}$ and $P_{\nu,ji}^{ea}$ is equal to the corresponding equilibrium spectral intensity ratio. The reciprocity principle enables to rewrite the exchanged power $P_{\nu,ij}^{exch}$ as:

$$P_{\nu,ij}^{exch} = P_{\nu,ji}^{ea} - P_{\nu,ij}^{ea} = \tau_{\nu,r}\kappa_\nu(T_i)\kappa_\nu(T_j)[I_\nu^0(T_j) - I_\nu^0(T_i)]\frac{dV_i dV_j}{r^2} \tag{2.26}$$

If $d\Omega_i = \frac{dV_j}{r^2 ds_j}$ is the solid angle at which dA_j is seen from dV_i, Equation (2.26) can be recast as:

$$P_{\nu,ij}^{exch} = \tau_{\nu,r}\kappa_\nu(T_i)\kappa_\nu(T_j)ds_j[I_\nu^0(T_j) - I_\nu^0(T_i)]dV_i d\Omega_i \tag{2.27}$$

In order to obtain P_{ij}^{exch}, Equation (2.27) is integrated over all the optical paths originated by i and crossing the cell j and over all the frequencies:

$$P_{ij}^{exch} = \int_0^{+\infty} \kappa_\nu(T_i)[I_\nu^\circ(T_j) - I_\nu^\circ(T_i)] \int_{V_i} \int_{4\pi} A_{ij\nu} d\Omega_i d\nu \tag{2.28}$$

where $A_{ij\nu}$ accounts for all the paths between emission from the cell i and absorption in any point m of the N_p crossing cells j, after transmission, scattering and possible wall reflections along the paths:

$$A_{ij\nu} = \sum_{m=1}^{N_p} \tau_\nu(BF_m)\alpha_{jm\nu} \tag{2.29}$$

$\tau_\nu(BF_m)$ is the spectral transmissivity between the source point B in the cell i and the inlet point F_m of the cell j, while $\alpha_{jm\nu}$ is the spectral absorptivity defined as:

$$\alpha_{jm} = 1 - exp[-\kappa_\nu(T_j)l_{jm}] \tag{2.30}$$

where l_{jm} is the length of the column m.
As the RM does not compute the difference between two very close approximates values in the case of nearly isothermal configurations, it is characterized by a better accuracy than FM and BM methods, in which the reciprocity principle is only statistically verified. This method was first introduced by Cherkaoui et al. (1996) for a one-dimensional slab of a non-scattering medium showing that CPU requirements were orders of magnitude lower than for standard Monte Carlo and that it was much less sensible to the optical thickness. Tessé et al. (2002) have conceptually extended the method to non-scattering media in one dimensional systems, and then applied it to 3D cases (Tessé, Dupoirieux, and Taine 2004). De Lataillade et al. (2002) used this method with some path sampling procedures to ensure satisfactory convergence even for large optical thicknesses.

Emission based Reciprocity Method (ERM) Among the reciprocal Monte Carlo methods, the Emission Reciprocity Method (ERM) developed by Tessé et al. (2002) is retained in this thesis. The general organization of the radiation model, based on a reciprocal Monte Carlo approach, has been detailed by Tessé et al. (2002). The principles of this method are briefly summarized here; in this approach, as for the BM, only the optical paths issued from the cell of interest are accounted for. The exchanged power P_{ij}^{exch} between the cell i and all the other cells j crossed or encountered by the optical paths originating from the cell i of the discretization domain is expressed as in (2.28) and the radiative power of the cell i is expressed as:

$$P_i^{ERM} = \sum_{j=1}^{N_+N_f} P_{ij}^{exch} \tag{2.31}$$

As in a Monte Carlo method propagation direction $\Delta(\theta,\phi)$ and wave-number ν of the photon bundles emitted are determinated randomly according to a Probability Density Function (PDF) $f_i(\Delta(\theta,\phi),\nu)$, that will be written as $f_i(\Delta,\nu)$, introducing the emitted power $P_i^e(T_i)$ per unit volume, Eq. (2.28) can be written as

$$P_{ij}^{exch} = P_i^e(T_i)\int_0^{+\infty}\left[\frac{I_\nu^\circ(T_j)}{I_\nu^\circ(T_i)}-1\right]\int_{4\pi}A_{ij\nu}f_i(\Delta,\nu)d\Omega_i d\nu, \tag{2.32}$$

where the PDF is expressed as

$$f_i(\Delta,\nu)d\Omega_i d\nu = f_{\Delta i}(\Delta)d\Omega_i f_{\nu i}(\nu)d\nu \tag{2.33}$$

$$= \frac{1}{4\pi}d\Omega_i\frac{\kappa_\nu(T_i)I_\nu^\circ(T_i)}{\int_0^{+\infty}\kappa_\nu(T_i)I_\nu^\circ(T_i)d\nu}d\nu. \tag{2.34}$$

The frequency distribution function of the photon bundles in the ERM is chosen accordingly to the emitting cell temperature, i.e. on the local spectral emitted power.
The use of the reciprocity principle ensures that the power exchanged by two cells at the same temperature is rigorously null, while in the FM this property is only statistically fulfilled. However, the ERM convergence may become difficult in those situations where absorption spectra of cold absorbing regions are very different compared to the emission spectra of the originating emitting regions of the photons.

Tessé et al. (2002) developed the ERM to face the limit of Monte Carlo methods when applied to real complex configurations, where a complete reciprocal computation based on the determination of all the exchanged radiative powers between all the couples of cells of the domain, is not affordable. Moreover the ERM allows accurate calculation of the radiative power on one cell by allocating a large number of optical paths starting from this cell. Thus, the main advantage of the ERM is to shooting photon bundles only from the points where results are wished.
In its work, Tessé et al. (2002) showed that this method is more performant than the FM for optically thick and quasi-isothermal media and it is well adapted to calculate the radiative power in high temperature regions.

Absorption Reciprocity Method Another exemple of reciprocal MC is the Absorption Reciprocity Method (ARM) developed by Tessé et al. (2002). In this approach the radiative power in the cell i, which is crossed or encountered by the optical paths coming from all the other cells j including the cell i, is calculated as:

$$P_i^{ARM} = -\sum_{j=1}^{N_v+N_f} P_{ji}^{exch}. \tag{2.35}$$

Absorption calculation is done like in the FM method, while emission is calculated using reciprocity. As in ERM, the use of the reciprocity principle ensures that the exchange power between two cells at the same temperature strictly vanishes. However, the big drawback of the ARM is that, unlike the ERM, to have an accurate calculation of the radiative power, a large number of optical paths issuing from all the cells of the entire domain is required.

Optimized Reciprocity Method (ORM) The ERM is efficient for high temperature regions while the ARM is better adapted for low temperature regions; however in cases of moderate optical thickness and high temperature gradients (as in combustion chambers) none of these methods is efficient in the whole computational domain; moreover the method to calculate wall fluxes is in general different from the one adapted to calculate radiative powers (Tessé et al. 2002). Thus Dupoirieux et al. (2006) developed an optimized reciprocity method (ORM) by selecting for each power exchange between two cells the best approach between ERM and ARM, i.e. the one that gives the lowest standard deviation. The ORM performs better than ARM and ERM for all the analyzed optical thicknesses, both in the center of the medium and close to the walls, however only 1D results were reported. More recently, Le Corre et al. (2014) used the ORM in a 2D application of radiative heat transfer in glass sagging, while Boulet et al. (2014) to calculate the response of a 3-cm-thick polymer sample subject to an externally incident radiation.

2.3.2 Hybrid methods

Other computational improvements have been made to make a Monte Carlo simulation more efficient for large optical thicknesses considering that some methods like P-N or diffusion methods are quite accurate in these conditions. Thus, the idea is to follow a hybrid technique that uses one of this methods in the optically thick portions of the spectrum or geometry and a Monte Carlo method in the optically intermediate to thin regions. Farmer and Howell (1994) introduced a hybrid method by using the diffusion approximation for optically thick elements and a standard MC for the rest. Feldick et al (2011) proposed a similar hybrid method, dividing the spectrum in thick and thin regions employing the P1 method for the former and a MC for the latter.
However, such hybrid algorithms have some limitations related to the definition of criteria to switch from one model to the other.

2.3.3 Ray-tracing procedures

The methods detailed above can use several procedures to trace the path that a ray follows. The most commonly used ones are presented in the following.

Standard ray-tracing

In this approach, also called *collision-based method*, a ray is emitted with a given energy content E_r and is assumed to travel undisturbed until a collision event, where it is either absorbed or scattered. The distance traveled by the photon is determined by the probability of a photon traveling a distance S before colliding. If the mean free path is used, the distance from an initial emission location to the point of absorption or scattering can be determined from:

$$S = -\frac{1}{\beta} ln R_s \tag{2.36}$$

where β is the extinction coefficient and R_s is a random number uniform in [0,1].
A simple example of application can be given by considering a medium characterized by a Planck mean absorption coefficient, a_p. A given ray can either be absorbed by a surface or by the medium itself.
If N_w and N_m represent, respectively, the number of the rays that are absorbed by the wall and by the medium, at the end of the simulation, the net radiative energy transfer rates for the surface and the medium are derived by:

$$Q_{net-w} = \epsilon E_b dA - N_w E_r \tag{2.37}$$

$$Q_{net-m} = 4 a_p E_b dV - N_m E_r \tag{2.38}$$

where ϵ is the surface emissivity, E_b the blackbody emissive power and E_r is the power contained in each ray.

This method is easy to implement but it has a weakness: a ray that is scattered or absorbed only contributes to the statistics of the region where the collision occurs; as a consequence, a large number of optical paths is required if the solution is desired in more or all the regions of the domain.
In the standard ray tracing, a ray with a fixed energy content is followed until it is absorbed or it leaves the domain. However, in an open configuration or in the presence of highly reflective walls and/or a very optically thin medium, this method could be extremely inefficient since a number of bundles could be reflected many times before leaving the domain; this means that only a fraction of traced rays would be statistically meaningful, wasting computational time in tracing the "meaningless" rays.

Other techniques have been developed in order to reduce the variance of this approach, such as the *forced collision* (Walters and Buckius 1994), whose basis idea is to force a collision to occur, for instance by scaling the extinction coefficient to a larger value, and adjusting the weight of the photon accordingly to the probability that the collision would occur, as done in Iwabuchi (2006).
An alternative to face the limits of the collision-based method is the *absorption*

suppression (Walters and Buckius 1994) which is very similar to the energy partitioning method described in the next section.

Energy partitioning method

In the conventional ray tracing illustrated above, rays are followed until collision occurs, and the energy associated to each ray is kept constant.
Shamsundar et al. (1973) introduced the *energy partitioning method* for a specific problem: a medium in an isothermal walled cavity characterized by an aperture. The problems consisted at finding the radiant energy crossing the aperture. The author based the method on the observation that the energy content of an emitted bundle, after each event in the path, could be split into two portions: the first, which leaves the domain without interacting with the walls, can be evaluated from geometrical factors; the second one also exits the opening, but only after experiencing one or more reflections at the walls cavity (in case the ray is not absorbed by the wall).

Modest (2003) extended the partitioning concept in a more general way and compared it to the standard ray tracing scheme.
As seen in the previous section, in the conventional tracing procedure, a random number is drawn to decide whether a bundle is absorbed or not. On the contrary, in the energy partitioning method, the energy of each bundle hitting a detector, is not absorbed at a single point, but rather it is gradually attenuated along its path by a factor of $exp(-\kappa l)$ (path-based), where l is the path that the bundle travels before hitting the detector. For this reason, such a method is also called *path-length method*, as in Farmer and Howell (1998). The bundle is then traced until it either leaves the enclosure or until its energy is reduced below a certain fraction of the original energy content.

The average CPU time spent for tracing a single ray is often lower in the conventional method than the energy-partitioning method, however the energy-partitioning method allows to accounting all the traced rays to the statistical sample thus leading to a smaller standard deviation compared to the conventional method. The advantage in saving CPU time is very high especially for enclosure configurations with open areas and highly reflective surfaces, but also for very thin media.
Because of such advantages, the energy partitioning method is retained in this thesis work.

2.4 Variance reduction methods

The purpose of Monte Carlo simulations is to obtain an estimate of the expected value of a random variable, and the measure of the accuracy is the standard deviation of the obtained estimate.

As the results of the MC intrinsically possess statistical behavior, many studies have been carried out on the statistical characteristics of MC. Haji-Sheikh and Sparrow (1969) cover the fundamentals of probability distributions and error estimates for Monte Carlo solutions of radiation heat transfer problems.
As emerged from Section 2.2, when N samples are used to determine the mean of a random variable, the accuracy of a Monte Carlo estimation, depends on both $\widehat{\sigma}$ and N:

$$\sigma[Q(N)] = \widehat{\sigma}/\sqrt{N} \tag{2.39}$$

Improvements in the accuracy of MC simulation results can be made by either decreasing $\widehat{\sigma}$ or increasing N.
If N is increased, improvements are typically expensive to obtain: to decrease the error by a factor ten, the number of samples must be increased by a factor 100, which leads to longer calculation times.
Thus, other methods are usually preferred, able to decrease the statistical fluctuations of MC calculations without increasing the number of photons histories, and they are known as *variance reduction techniques*.

Numerous variance reduction strategies exist in literature, which may used to make MC calculations more efficient. Haghighat and Wagner (2003) classify them into three categories: modified sampling methods (e.g: source biasing, implicite capture, forced collisions and exponential transformation), population control methods (splitting/roulette, weight windows and stratification) and semi-analytic methods.
Among the existing methods to reduce the variance, only the more common techniques used in radiative heat transfer problems are approached in this section and these are: splitting/Russian roulette, implicit capture, exponential transformation and importance sampling. A more accurate description of these methods is available in Haghighat and Wagner (2003) and Dupree and Fraley (2012).

2.4.1 Implicit Capture

Implicite capture (Kahn and Harris 1951), also called survival biasing or absorption by weight reduction, is a variance reduction method which modifies the tracking process.
This technique is used in presence of highly absorbing media. In such cases, it could be reasonable to avoid spending computational effort in tracking particles that do not contribute to sample the regions where the results are desired (for instance a particle that do not hit a detector). Without biasing, a particle track is terminated by absorption. This means that a particle that has been tracked for many collisions could be terminated and lost to the calculation.

The objective of the implicit capture is to avoid that a ray path terminates in a capture event. To do that, the absorption events are removed from the tracking procedure and replaced by scattering events. To do that, a distance to a scattering event is needed, rather than a distance to absorption. When this technique is used, the particle that collides is followed with a weight proportional to its weight before the collision multiplied by the non-absorption probability.

The main advantage of the implicit capture is the reduction of computational time spent in following rays which do not contribute to the result (because they are captured before reaching the score). However, the removal of absorption events makes rays path longer; moreover high computational time may be spent by tracking particles with very small weights and therefore giving small contributions to the results.
For this reason, a criterion to cleverly end the ray histories is needed. Implicit capture is often associated with mechanism killing the rays, as the ones introduced in the next paragraph.

2.4.2 Russian roulette

It is reasonable to spend more computational effort in tracking particles that contribute to the desired results, rather than in following light-weight particles. The principle of the Russian roulette, developed by von Neumann and Ulam in 1945, is to reduce the simulation time by killing unimportant particles while the total weight of the tracked particles is conserved; that is, the weight of the killed particles is assigned to the surviving ones. This is generally done by generating a random number and determining whether it is greater or less than a specified survival probability. If the number is lower than the threshold, the particle loses the roulette and can be killed with some kill probability. While, surviving particles are assigned a new increased weight, which is compared to the threshold and if it is higher than the lower weight limit, its random walk can continue.

2.4.3 Splitting

In an analogous point of view, splitting can help preventing the weights of surviving particles be extremely large and above a maximum value. When a ray has a very large weight, it is split in several rays of lower weight.
Splitting is often used in combination with the Russian roulette thus defining Weight Windows (Booth 1983).

A weight window is characterized by. a lower weight limit and an upper weight limit, to control that the weights of the particles lie between them (see Fig. 2.4). Among the variance reduction techniques, the transport biasing method of split-

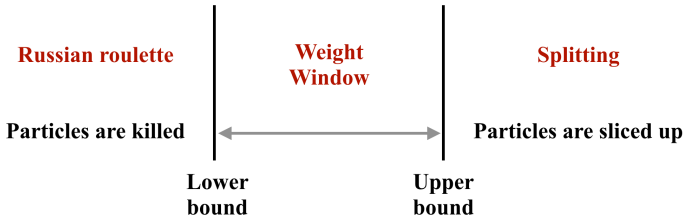

Figure 2.4: *Representative scheme of Weight Windows.*

ting/roulette has been the most effective and widely used approach for reducing the variance of Monte Carlo calculations. The main drawback of both splitting and Russian roulette, is the requirement of the definition of thresholds parameters. More details about this topic can be found in Dupree and Fraley (2012).

2.4.4 Exponential Transformation

The exponential transformation, or path stretching, is a technique to stretch the distance between collisions in the direction toward the area of interest (for exemple, the detector), while reducing that distance in the direction of little interest. The interest is the increasing of computer effort to sample the more important regions of phase space. The particle weight is adjusted in order to preserve in any point the expected weight. This technique work best in highly absorbing media. An example of application can be found in Baes et al. (2016).

2.4.5 Importance Sampling

Among numerous methods of biasing, importance sampling has been popular in the study of radiative heat transfer. The basis idea is to draw the sample from a proposal distribution and re-weight the integral using importance weights so that the correct distribution is targeted.

Mathematical formulation

Its mathematical formulation, is here introduced by considering the energy emitted by a group of photons E; it can be written as:

$$E = \int_{-\infty}^{\infty} w(\xi) f(\xi) d\xi \tag{2.40}$$

where ξ is a vector with components $\xi_1, \xi_2, ...$ (for instance frequency and direction: ν, θ, ϕ), and $f(\xi)$ is the probability density function standing for $f_1(\xi_1) f_2(\xi_2) ... f_k(\xi_k)$. If the probability density function is arbitrarily chosen, this can have consequences in terms of numerical convergence.
The importance sampling is the technique to optimize these probability density functions in order to get smaller standard deviations with a limited number of sampled events. Equation 2.40 may be rewritten as:

$$E = \int_{-\infty}^{\infty} \frac{w(\xi) f(\xi)}{f^*(\xi)} f^*(\xi) d\xi \tag{2.41}$$

where $f^*(\xi)$ is the new probability density function of ξ, also called *importance function*. Equation 2.41 may be rewritten as:

$$E = \int_{-\infty}^{\infty} w^*(\xi) f^*(\xi) d\xi \tag{2.42}$$

This means that the optimized probability density functions f^* are now used for sampling of ξ instead of the original $f(\xi)$ and that the old weight $w(\xi)$ is multiplied by the ratios of the original pdf to the optimized one, thus $w^*(\xi) = w(\xi) f(\xi) / f^*(\xi)$ is the new weighting function.

Applications

One example of application to radiative heat transfer problems may be given by a case where the surface properties have a strong dependence on the wavelength within narrow bands. If no biasing is applied, only a small fraction of bundles will have wavelengths within these narrow bands, wasting computer time. In these cases it is therefore convenient biasing the selection of energy bundles towards the desired wavelengths.
Another example is a configuration with an optically thick medium, which is problematic for MC applications, because most photons will not travel outside of the emitting cell and, thus, make no contributions to the statistics. Mitigating approaches to problems with extreme optical thickness have been proposed in the past.

In a time where the computing power was limited, House and Avery (1969) proposed some solutions to improve the efficiency of calculation through the

"biasing", the technique to distort the probability density function of an event to force the selection of a random variable into a more desirable category, keeping the physics of the process correct by introducing appropriate correction weights.
They applied this technique to distort the wavelength dependence of the emission coefficient in a way to select more photons with wavelength in the line wings, and fewer photons in the line center where the mean free paths are shortest. They also applied a biasing technique in order to choose better distributions for collision distances.
Various techniques for biasing direct Monte Carlo results in reducing variance, along with methods for computing expected variance, are discussed in Haji-Sheikh and Howell (1988).

One of the most widespread applications of importance sampling is the technique of the *forced scattering* (Cashwell and Everett (1959), Mattila (1970), Witt (1977), Iwabuchi (2006)). Sometimes a high variance may result from an extremely low interaction probability, such as the problems of radiative transfer in small optical depth regimes. Thus, an acceleration technique has been developed to deal with this limit, in order to prevent that photons leave the system without having any interactions. Different strategies can be adopted: only the first interaction after the photon emission can be forced (this is the forced first scattering), or forced scattering can be applied throughout the simulation (that is sometimes called eternal forced interaction).
Another direct application of importance sampling is found in Juvela (2005), in the context of cloudy atmospheres. Importance sampling is applied in order to bias photons directions (for instance, to send photons towards preferential directions), emission position (to emit photons close to the cell boundaries in optically thick clouds) or still scatter directions. Feldick et al. (2011) also employed an approach based on importance sampling in wavelength space in order to sample from wavelengths which have larger impact on the heat transfer calculation, and consequently reducing statistical variation and calculation time. The objective was to select lines most often in the line wings, where photon bundles are most likely to leave the cell. A similar concept is used in Jonsson (2006) with the polychromatic algorithm, where photon packages containing photons of different wavelengths are used.
The problems encountered in optically thick regions have often been addressed by importance sampling: De Lataillade et al. (2002) worked on the formulation choice and pdf adaptations to deal with optically thick conditions. PDF for emission points and bundles directions are chosen on the base of the optical depth. Concerning the frequency, random absorption coefficients are generated instead of random frequencies.

Importance sampling is undoubtedly a powerful technique to make Monte Carlo simulations more efficient, but it also has a potential danger: the possible

appearance of large weight factors. The weight function w^* can be larger than unity in some parts of the domain thus becoming source of noise. This is the reason why the choice of the biased pdf, f^*, is a delicate job: on the one hand it should promote those parts of the domain that are desired, and on the other hand it should also be such that the new weighting factor w^* is never boosted to very high values. This problem is tackled in Baes et al. (2016), where a technique called *composite biasing* is introduced and applied to the path stretching. The basis principle is to build a new pdf as a linear combination of the original pdf and the desired biased one, through the introduction of a parameter ζ that sets the relative importance of the desired pdf:

$$q^*(\xi) = (1-\zeta)f(\xi) + \zeta f^*(\xi) \tag{2.43}$$

The advantage is that the new weight factor w^{**}, expressed by the ratio of the original pdf and the one biased in a composite way:

$$w^{**}(\xi) = \frac{f(\xi)}{q^*(\xi)} = \frac{1}{(1-\zeta) + \zeta f^*(\xi)/f(\xi)} \tag{2.44}$$

is always bounded by a finite value, controlled by the parameter ζ. The composite biasing in Baes et al. (2016) is applied to a radiative transfer problem in presence of an optically thick medium, where a random optical depth is generated from an exponential distribution, and it has been combined with the forced interaction, obtaining a gain in efficiency which is many orders of magnitude higher even for higher optical depths.
Importance sampling has been widely investigated also in the context of cloudy atmospheres (Iwabuchi (2006), Buras and Mayer (2011)), in continuum radiative transfer (Juvela 2005), in concentrated solar applications (Delatorre et al. 2014).

The main limitation of the importance sampling is the fact that it should be done based on considerations about the physics of the problem, thus whether or not biasing is beneficial is not always obvious to predict.
Indeed, a universal solution, which fits for all applications, does not exist, because this "clever" sample originates from considerations on the physics of the retained problem and therefore requires experience. Booth (1983) state: "The selection [of parameters] is more art than science, and typically, the user makes a few short trial runs and uses the information these trials provide to better guess the parameters; that is, the user learns to adjust parameters on the basis of previous experience". Thus, the choice of the optimal sampling strongly depends on the retained problem.
One of the approach of importance sampling used in this thesis work is the Optimized Emission Based reciprocity method developed by Zhang et al. (2012) and it is briefly presented in the following paragraph.

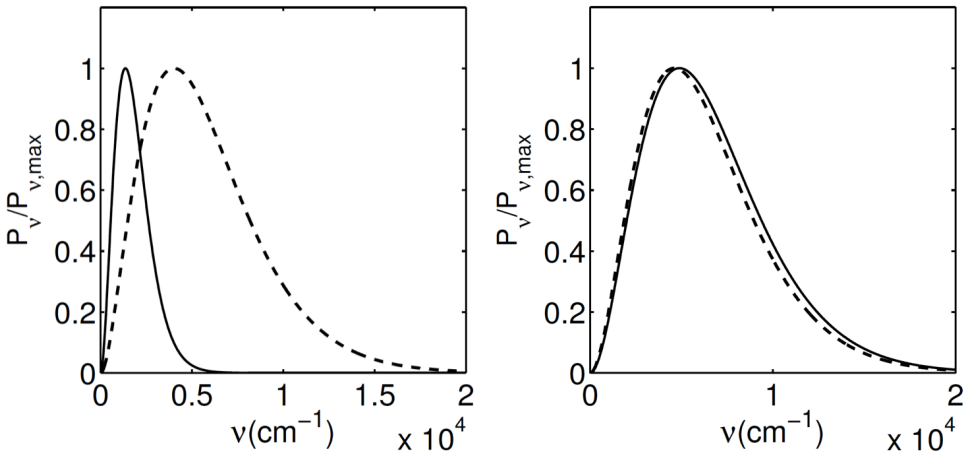

Figure 2.5: *Spectral emitted and absorbed power for a cell of temperature 700K (left) and 2500 K (right); —: P_ν^e; - - : P_ν^{abs}.*

Optimized-ERM

In some situations the convergence of the ERM, introduced in 2.3.1, may become slow.
Zhang et al. (2012) analyzed a configuration of homogeneous non-reacting $CO_2 - H_2O - N_2$ gaseous mixture characterized by heterogeneities in temperature (from 950 to 2050 K) and for two values of pressure (1 and 40 bar). In regions dominated by both absorption and emission, spectral emitted and absorbed power have been analyzed in a hot and a cold cell of the computational domain. The absorbed and emitted spectral power of cold gases are plotted in Fig. 2.5 (left), highlighting that the emitted power is characterized by small frequencies while the absorbed one covers a wider range of frequencies. As a consequence, if the frequency pdf is chosen as in the ERM, i.e. based on the local emission as in (2.34), there will be a few samples in the high frequencies regions. That means slow convergence in the estimation of the absorbed power. If the spectral absorbed and emitted power for a hot cell are analyzed, it can be noticed that the spectra almost overlap and they cover a wide range of frequency (Fig. 2.5 (right)). Consequently if the frequency pdf is chosen accordingly to the power emitted by a hot cell, a greater amount of samples will be characterized by higher frequency compared to the previous case. That is due to the observation that the power absorbed by a cold gas of the computational domain has been mainly due to the emission by hot gases.

Then a method to face the limits of the ERM was proposed, named Optimized Emission-based Reciprocity Method OERM, which in fact corresponds to importance sampling. It uses a frequency distribution function of the photon bundles that is no longer based on the local emission, but rather associated to

the maximum temperature T_{max} encountered within the system:

$$f_{\nu i}^{OERM}(\nu, T_{max}) = \frac{\kappa_\nu(T_{max}) I_\nu^0(T_{max})}{\int_0^\infty \kappa_\nu(T_{max}) I_\nu^0(T_{max}) d\nu} \tag{2.45}$$

If such a frequency distribution function is used, a corrective factor has to be applied in order to rigorously obtain the emission distribution at local temperature and the equation (2.32) becomes:

$$P_{ij}^{exch} = P_i^e(T_{max}) \int_0^{+\infty} \frac{\kappa_\nu(T_i) I_\nu^\circ(T_i)}{\kappa_\nu(T_{max}) I_\nu^\circ(T_{max})} \left[\frac{I_\nu^\circ(T_j)}{I_\nu^\circ(T_i)} - 1 \right] \tag{2.46}$$

$$\int_{V_i} \int_{4\pi} A_{ij\nu} f_{\Delta_i}(\Delta) d\Omega_i f_{\nu i}^{OERM} d\nu \tag{2.47}$$

This approach has been validated by comparison with an analytical reference solution and ERM in Zhang et al. (2012); the results show that the OERM improves the efficiency of the ERM specially in cold regions, where the ERM is inaccurate, while the two models agree in hot regions.
The OERM has been retained for the radiative heat transfer simulations of this thesis work.

2.5 Models for radiative properties of gases used in MC simulations

The irregular variation of the absorption coefficient of gaseous participating media across the spectrum, if accurately represented, requires high computational cost and memory requirements.
For this reason, until the 1990, most of radiative heat transfer simulations (Howell and Perlmutter (1964); Steward and Cannon (1971)) involved gray participating media; nevertheless, several modern studies still employ this assumption. These are the Gray Gas (GG) models, based on total emittance correlations (Hottel and Sarofim (1965); Leckner (1972)), and they consider the absorption coefficient to be independent of the wavenumber. The Radiative Transfer Equation with the GG model becomes:

$$\frac{dI}{ds} = -\kappa I + \kappa I_b \tag{2.48}$$

The use of the gray gas assumption in simulations of radiative heat transfer is justified by low computational demand. However the assumption that the absorption coefficient does not vary with the wavenumber is a strong simplification and yields large errors in the solution (Liua et al. (1998), Johansson et al. (2010), Wang et al. (2014), Meulemans (2016), Nguyen et al. (2017)).

At the top of spectral accuracy, there are the Line-By-Line (LBL) calculations which use spectral database (such as Rothman et al. (2009)) providing detailed

high-resolution spectra of several gaseous species. Unfortunately, computing radiation for all the lines is excessively time-consuming and such an approach is not affordable for most practical problems. This is the reason why not so many studies have been performed in radiative heat transfer with very accurate models in the past. MC methods are applied jointly with LBL approach to take into account the line structure of an absorption spectrum and are successfully demonstrated in Surzhikov and Howell (1998) for simple configurations. Tang and Brewster (1999) also used LBL combined to MC with spectral integrations for a one dimensional medium. Soucasse et al. (2013) used high resolution spectra for CO_2 and H_2O in MC simulations of a 3D configuration of quasi-isothermal participating media. Wang and Modest (Wang and Modest 2007) developed random-number relations for LBL-MC calculations in the context of an atmospheric-pressure methane-air jet flame, where only CO_2 and H_2O species were considered. More recently, Ren and Modest (2019) included CO_2, H_2O, CO, CH_4, C_2H_4, and soot in LBL-MC simulation.

Because of the computational demand of LBL calculations, gases models constitute an important research field and between the two extremes, LBL and GG, there is a vast literature about spectral models, such as: Weighted Sum of Gray Gases (WSGG) first proposed by Hottel and Sarofim (1972), that models the entire spectrum considering a few bands with uniform absorption coefficients, each band corresponding to a gray gas, the Spectral Line Weighted-sum-of-gray-gases (SLW) or the correlated-κ-distribution model (Goody et al. (1989), Lacis and Oinas (1991), Riviere et al. (1992), Riviere et al. (1995)), that have been developed in order to find a compromise between accuracy and computational cost.
Concerning the models that in the past have been used in Monte Carlo simulations of radiative heat transfer, the literature presents several works that demonstrate the application of the Monte Carlo to spectrally dependent properties.

One of the pioneers who applied Monte Carlo to deal with spectrally dependent properties is Modest (1992). A statistical narrow band model, described by Tien (1969), is applied to obtain random-number relations giving the wavenumber for emission and the distance traveled before absorption. It is pointed out that the narrow band model may be applied successfully to MC after comparison to two wide band models: the Tien and Lowder model (Tien and Lowder 1966) and the exponential wide-band model of Edwards (1976)) on a uniform slab, under the assumption of a spatially constant absorption coefficient, thus non-uniformities of temperature and species concentrations are not considered. Liu and Tiwari (1994) applied a statistical narrow band model with an exponential-tailed-inverse intensity distribution (Malkmus 1967) to investigate the radiative wall heat fluxes in non isothermal and non homogeneous molecular gas between infinite parallel plates. The same statistical model (Malkmus 1967) is used in

Cherkaoui et al. (1996) in benchmark configurations of quasi-isothermal media with a net-exchange formulation of MC.
MC method using statistical narrow-band correlated k-distribution method is used to provide a benchmark solution for a 2D problem in Coelho et al. (2003).

Non homogeneous media are considered in Snegirev (2004), where the WSGG is retained in MC simulations of buoyant turbulent diffusion flames. Results are compared to ones obtained with two gray gas models, one based on a total emissivity computed as a weighted sum of gray gases using the coefficients from Smith et al. (1982) and the other one based on the Planck mean absorption coefficient. Results show that the difference between gray and non gray models in the prediction of maximum radiative heat fluxes does not exceed 20%.
Maurente et al. (2008) compares WSGG and the SLW models in the computation of radiation heat transfer in a cylindrical enclosure with the aid of the MC method. The considered temperature and the species concentrations are representative of those found in the combustion of methane and fuel oil. Results show that the WSGG solution over-predict the heat transfer compared to the SLW, moreover its application is limited to homogeneous media. Wang et al. (2007) integrates the Full-Spectrum κ-distribution (FSK) method (Modest and Zhang 2002) in MC simulations, which is a re-ordering of absorption coefficients into smooth κ-distributions over the whole spectrum. The FSK/MC is implemented in a three-dimensional CFD code and verified on one-dimensional layers of non-isothermal and inhomogeneous mixtures and compared to the analytical solution formulated with an LBL approach.
Tessé et al. (2002) and Tessé et al. (2004) coupled MC with parametrized narrow band c-k model (Goody et al. 1989) using more than 1000 pseudo-spectral points. Results are first validated on benchmark 1D solutions and, successively, MC/ck simulations of a turbulent ethylene-air diffusion flame are performed. More recent MC simulations including a correlated k-distribution model can be found in Zhang et al. (2013) the context of a turbulent channel flow filled by a non reacting mixture of combustion burnt gases, and also in Koren et al. (2017) and Rodrigues et al. (2018) in numerical simulation of semi-industrial combustion chambers.

2.6 Quasi-Monte Carlo methods in radiative heat transfer

As already mentioned, a well known disadvantage of MC methods is the slow convergence: the statistical error of the integrals estimation scales as $N^{-1/2}$. It has been shown in section 2.2.3 that using an alternative sampling allows to reduce this error. However the QMC technique has rarely been used in the radiative transfer community.

To the author knowledge, one of the first works on QMC in radiative heat transfer is Sarkar and Prasad (1987), where pseudo-random and quasi-random sequences (Halton and Faure) are compared on one-dimensional slab with scattering. It is highlighted the higher accuracy of QMC compared to MC for low-dimensional problems associated with small thicknesses, as well as the same behavior of the Halton and Faure sequences for the studied tests.
In O'Brien (1992), tests are performed on slabs with multiple scattering and a varying optical thickness. Results show that the greater advantage of QMC integration of the RTE occurs for low collisions number, thus in optically thin media.
A more practical application of QMC methods in radiative heat transfer problems can be found in Kersch et al. (1994) where rapid thermal processing is simulated in the context of the production of semiconductor devices. Results are presented for only the Halton sequence, since the results obtained with the Sobol sequence were generally the same, except for some occasions where the Halton sequence appeared slightly better. The Halton sequence used in the QMC method is compared to a pseudo-random sequence of a standard Monte Carlo approach in terms of error size. Results show that the advantage of using a quasi-random sequence is clear, since the error associated with using a quasi-random sequence is at least as small as in the standard MC approach, and frequently it can be reduced up to a factor 6.
Integration problems with varying number of dimensions are investigated by Morokoff and Caflisch (1995); in this study, the Sobol sequence is compared to Halton, Faure and pseudo-random sequences. Results show that the Halton sequence is the most performant in low-dimensional problems (up to a dimension of the integration space equal to 6), the Sobol sequence gives the best results for higher dimensions, while the Faure sequence, characterized by the best theoretical bound, has the worst behavior among the investigated sampling methods, but generally better than the random sequence. In Evans (1998), QMC method is applied to give a reference solution in order to validate a spherical harmonics discrete ordinate method in the context of cloudy atmospheres.

This literature review shows that QMC in radiative heat transfer has been investigated since the 90's. However, all the works found in literature are limited to simple 1D or 2D applications. Even though the advantage of using a quasi-random sequence has been clearly shown in the past, no work about the use of QMC applied to radiative heat transfer in more realistic applications can be found in literature.

2.7 Conclusions

Monte Carlo methods are often used in radiative heat transfer because of their capability to handle complex geometries and account for various physical ef-

fects, but especially for the possibility to obtain an error estimation, the reason why they are considered as reference solutions.

MC principles have been first shown from a mathematical point of view, and the big drawback that has emerged is their slow convergence which scales as $\sigma/\sqrt{N}$. One generic approach to improve the accuracy of MC methods is the use of variance reduction methods. The most commonly used strategies in radiative heat transfer have been reviewed in this chapter, and special attention has been given to the technique of the importance sampling. In the context of radiative heat transfer, the most common ray tracing procedures and formalism to compute the radiative power have been illustrated.

Another possible approach to reduce the Monte Carlo error consists in the use of quasi-random or law-discrepancy sequences in place of the usual pseudorandom ones. The introduction of quasi-random sequences in MC leads to quasi-Monte Carlo methods. The state-of-the-art on QMC methods confirms the strength of these methods in increasing the convergence rate of MC methods, but also highlights the fact that such methods have never been applied to real configurations. The next chapter details their use for radiative heat transfer simulations in configurations relevant to this thesis work.

Chapter 3

Assessment of randomized Quasi-Monte Carlo method efficiency in radiative heat transfer simulations

The present study focuses on the assessment of QMC methods to solve radiative heat transfer in comparison with MC methods. This is done in several configurations (turbulent channel flow, jet flame, confined premixed flame) with instantaneous 3D solution fields obtained from DNS or LES. The considered cases are characterized by several degrees of complexity: high pressure, presence of soot and finally a confined flame in a combustion chamber. This enables to study the impact of QMC methods in practical 3D cases and to anticipate its benefits in coupled high-fidelity simulations based on LES or DNS.
The principle and properties of Quasi Monte Carlo method and its randomized variant (RQMC) are illustrated on a simple numerical integration problem. Moreover, the Monte Carlo solver in charge of describing the radiative transfer and computing the radiative power fields with MC or QMC methods is detailed. The three application cases are then presented in this section. The accuracy and efficiency of the retained randomized QMC method are finally studied.

This chapter will be submitted to the Journal of Quantitative Spectroscopy & Radiative Transfer.

Contents

3.1 Monte Carlo and Quasi-Monte Carlo integration

3.1.1 Definition of a simple test case and Monte Carlo integration

In a general multivariate integration problem, the goal of MC methods is to estimate:

$$I = \int_V f(\mathbf{x}) d\mathbf{x} \tag{3.1}$$

where f is a real-valued function defined over the given state-space volume V. In order to illustrate the properties of MC and QMC methods, the following simple 2-D integral is considered in this section:

$$I = \int_0^{2\pi} \int_0^{\pi} F(\theta, \phi) \frac{\sin(\theta)}{2} d\theta \frac{1}{2\pi} d\phi. \tag{3.2}$$

I is then expressed as the expectation of $F(\theta, \phi)$, $I = \mathrm{E}[F]$, based on the probability density functions $p_\theta(\theta) = \sin(\theta)/2$ and the uniform distribution $p_\phi(\phi) = 1/(2\pi)$ on the interval $[\,0\,,\,2\pi\,]$. The Monte Carlo estimate for the integral is then defined as

$$Q(N) = \frac{1}{N}\sum_{i=1}^{N} F(\mathbf{x}_i), \tag{3.3}$$

where $\mathbf{x}_i$ are samples from the random vector $\mathbf{x} = (\theta, \phi)$ whose components follow the probability density functions $p_\theta(\theta)$ and $p_\phi(\phi)$, respectively. The samples $\mathbf{x}_i = (\theta_i, \phi_i)$ are determined through two independent random numbers R_ϕ and R_θ uniform between 0 and 1 as

$$\phi = 2\pi R_\phi \tag{3.4}$$

$$\theta = \cos^{-1}(1 - 2R_\theta) \tag{3.5}$$

The function $F(\theta, \phi)$ to integrate is chosen as:

$$F(\theta, \phi) = \sin^2(\phi/2)\sin(\theta) \tag{3.6}$$

and the exact result for the integral in Eq. (3.2) corresponds to $I = \pi/8$. The intrinsic standard deviation is defined as $\sigma_{int}^2 = \mathrm{E}\left[(F - I)^2\right]$. Its exact value corresponds here to $\sigma_{int}^2 = \frac{1}{4} - \left(\frac{\pi}{8}\right)^2 \approx 0.31$.

The MC results for the integral defined in Eq. (3.2) and (3.6) are shown for 900 000 realizations in Fig. 3.1. The convergence $Q(N)$ towards the expected value $\pi/8$ (red dashed line) illustrates the law of large numbers where MC methods are rooted. Additionally, the Central Limit Theorem allows for deriving error estimates of the computed value from the samples standard deviation $\widehat{\sigma}$ computed as

$$\widehat{\sigma} = \frac{1}{\sqrt{N-1}}\left[\sum_{i=1}^{N}\left((F(\mathbf{x}_i) - Q(N))^2\right)\right]^{1/2}. \tag{3.7}$$

The standard deviation $\widehat{\sigma}$ is an approximate of the intrinsic standard deviation σ_{int} and the probability density function of $Q(N)$ tends toward a normal distribution centered in I with a standard deviation equal to $\sigma_{int}/N^{1/2} \approx \widehat{\sigma}/N^{1/2}$. This property provides straightforwardly confidence intervals for the estimate $Q(N)$. These confidence intervals are also shown in Fig. 3.1. They are seen to decrease with N, which allows to control the number iterations necessary to reach a given accuracy.
The error $\varepsilon(N) = |Q(N) - I|$ is plotted in Fig. 3.2. Although the curve is polluted by noise inherent to the statistical estimation of the result, the error is seen to decrease with N approximaltively at a constant rate in this logarithmic

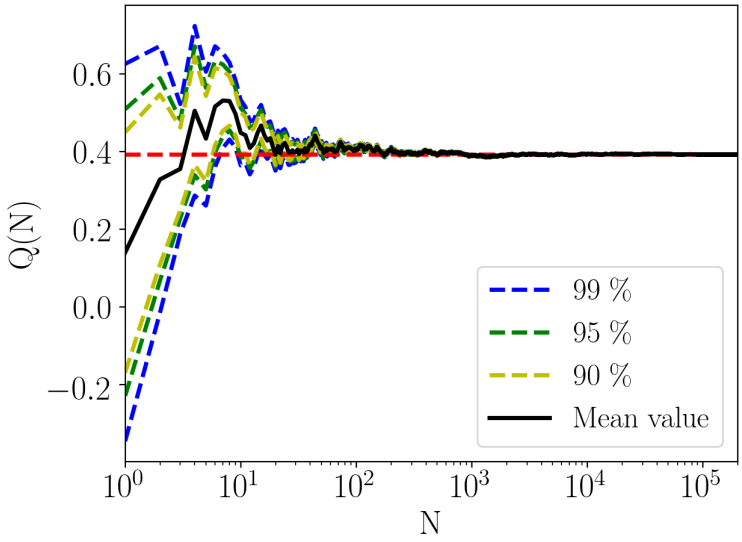

Figure 3.1: *Evolution of the MC result Q(N) as a function of the number of realizations N. Red horizontal dashed line: the exact value of the integral. Confidence intervals at 90%, 95% and 99% are denoted by yellow, green and blue dashed lines, respectively.*

plot. This is expected and can be consistently characterized by considering a statistical moment of the error to get rid of statistical noise. In particular, the standard deviation of the MC estimate $\sigma[Q(N)] = \left(\mathrm{E}\left[(Q(N) - I)^2\right]\right)^{1/2}$ is directly related to the quadratic mean of the error, $\left(\mathrm{E}\left[\varepsilon(N)^2\right]\right)^{1/2}$. $\sigma[Q(N)]$ is computed from 100 independent Monte Carlo simulations and is also shown in Fig. 3.2. After several dozens of realizations, the asymptotic Central Limit Theorem (CLT) becomes valid and $\sigma[Q(N)]$ closely follows the plotted law $\sigma_{int} N^{-1/2}$. The statistical error of the MC estimate $Q(N)$ decreases then according to $1/\sqrt{N}$. Therefore, in order to decrease the error by a factor ten, the number of samples must be increased by a factor 100. This well-known feature of slow convergence is the main drawback of MC methods.

Nevertheless, the error estimate,

$$\sigma[Q(N)] \approx \widehat{\sigma}_{Q,1}(N) = \widehat{\sigma} N^{-1/2}, \tag{3.8}$$

allows for a control of the accuracy of the computed value I from the sample values, which is very appreciable. Another methodology to estimate the error, equivalent to this first one, consists in breaking up the samples resulting in $Q(N)$ into M subsets. For each subset $i \in [1, M]$, a MC estimate $Q_i(P)$ can be computed where $P = N/M$ is the number of samples in the subset. The MC estimations from the total number N of samples is simply related to the MC

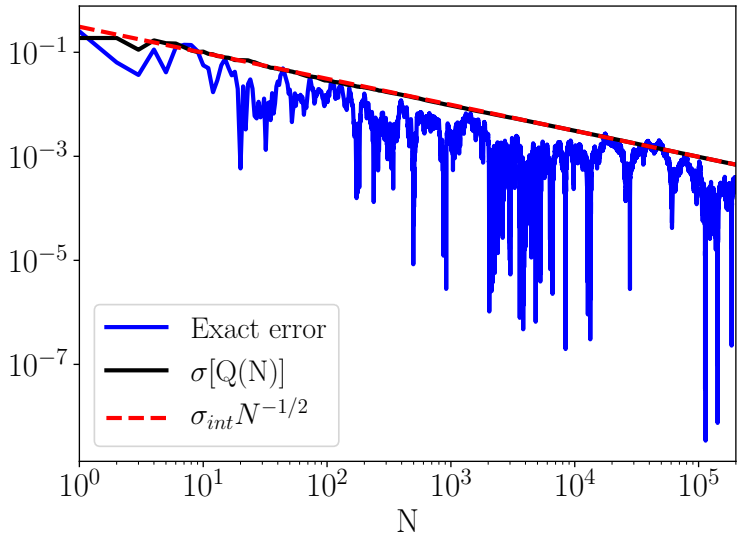

Figure 3.2: *Evolution of deterministic error $\varepsilon(N)$ (blue plain line) and mean quadratic error $\sigma[Q(N)]$ (black plain line) as a function of the number of realizations N. The red dashed line is the theoretical convergence rate $\sigma_{int}N^{-1/2}$.*

estimates in the subsets as

$$Q(N) = \frac{1}{M}\sum_{i=1}^{M} Q_i(P). \tag{3.9}$$

The M subsamples $Q_i(P)$ are independent estimations of the same quantity $Q(P)$ whose expectation is $I \approx Q(N)$. The standard deviation of estimates $Q_i(P)$ can then be estimated as

$$\sigma[Q(P)]^2 \approx \frac{1}{M-1}\sum_{i=1}^{M}[Q_i(P) - Q(N)]^2. \tag{3.10}$$

The CLT theorem states that $\sigma[Q(N)]^2 \approx \frac{1}{M}\sigma[Q(P)]^2$ which finally yields an alternative estimation of the standard deviation of the MC estimate from all samples (Modest 2013; Lemieux 2009):

$$\sigma[Q(N)] \approx \widehat{\sigma}_{Q,2}(N) = \left(\frac{1}{M(M-1)}\sum_{i=1}^{M}[Q_i(P) - Q(N)]^2\right)^{1/2} \tag{3.11}$$

The two estimates for the MC accuracy that are $\widehat{\sigma}_{Q,1}(N)$ and $\widehat{\sigma}_{Q,2}(N)$ are plotted in Fig. 3.3 as a function of the total number of samples N. For the second estimate, $\widehat{\sigma}_{Q,2}(N)$ is evaluated from a fixed number $M = 1\,000$ of subsets. Results for $\widehat{\sigma}_{Q,2}(N)$ are then available for $N = 1\,000$ $(P = 1)$, $N = 2\,000$ $(P = 2)$,

..., up to $N = 1\,000\,000$ corresponding to a number $P = 100$ of samples per subset. For each N, the MC result $Q(N)$ is identical. Only the error estimate of $\sigma[Q(N)]$ differs. Figure 3.3 shows that both formulations in Eqs. (3.11) or (3.8) are equivalent in the retained conditions (large N and large M). As expected, both MC error estimates decreases with the square root of the number of realizations N, following of the law of large numbers.

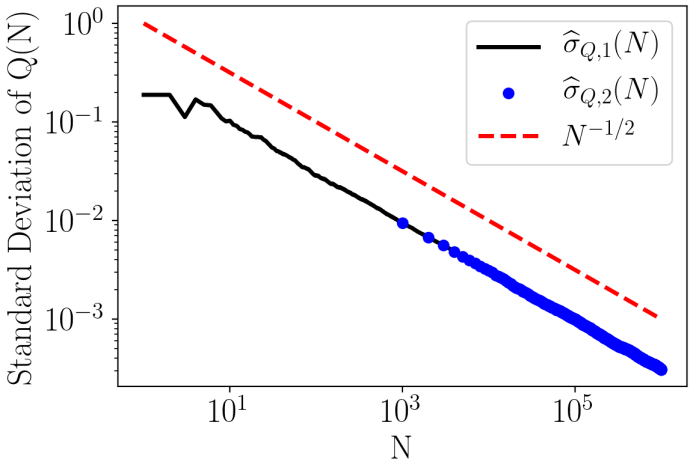

Figure 3.3: *Evolution of the standard deviation as a function of the number of realizations in a log-log scale in the two analyzed cases : black solid line is* $\widehat{\sigma}_{Q,1}(N)$ *of Eq. (3.8) in 1 MC trial of 1 million realizations; blue solid line is* $\widehat{\sigma}_{Q,2}(N)$ *of Eq. (3.11) with* $M = 1000$ *MC trials of* $P = 1000$ *realizations each; red dashed line is the line of slope* $-1/2$.

3.1.2 Quasi-Monte Carlo methods

The accuracy of a MC calculation is proportional to the variance σ^2_{int} and inversely proportional to the number of samples as $N^{-1/2}$. A possibility to accelerate the Monte Carlo convergence rate as a function of N consists in the use of alternative samplings such as low-discrepancy sequences. The resulting quadrature method is called Quasi-Monte Carlo (QMC).

Low-discrepancy sequences

This type of sequences aims at a more uniform filling of the sampled state space. This is illustrated in Fig. 3.4 where a MC sequence from a pseudo-random number generator is compared to a low-discrepancy Sobol sequence in two dimensions. The clustering seen with classical random sampling leaves

regions with few samples, thus making the MC convergence slower compared to the QMC method where points are more uniformly distributed.

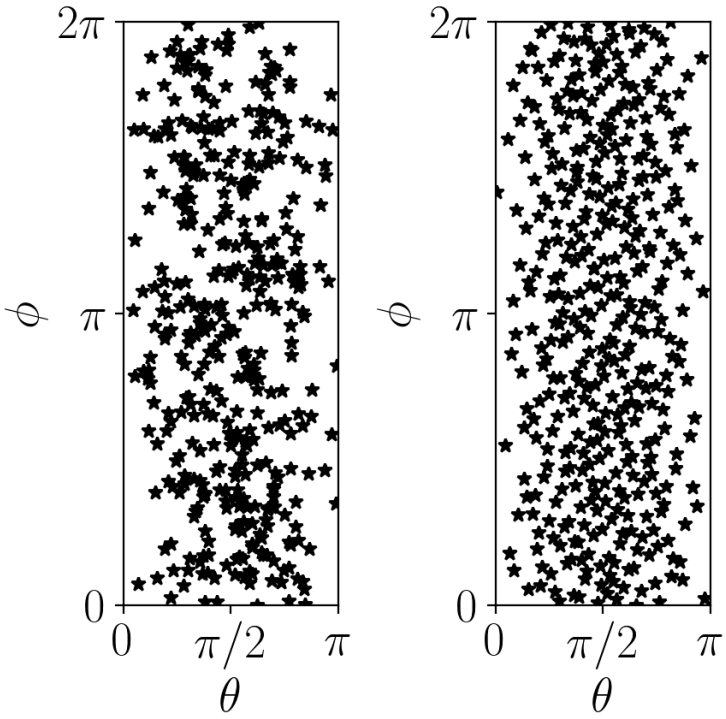

Figure 3.4: *Comparison of the sampling of polar (θ) and azimuthal angle (ϕ) generated accordingly to the probability function defined in Eqs. (3.4 - 3.5) using a a classic pseudo-random sequence (left) and a Sobol sequence (right) .*

As the Monte Carlo method, QMC methods are a numerical method to compute high-dimensional integrals. They rely on the *Koksma-Hlawka inequality* (Hlawka 1961) which states that for any sequence $\{u_n\}$ and any bounded function f defined in $[0,1]^d$, the integration error ϵ is bounded as:

$$\epsilon[f] = |Q(N) - I(f)| \leq V[f] D_n^*(\mathbf{u_1}, ..., \mathbf{u_n}) \tag{3.12}$$

where D_n^* is the discrepancy of the set of points $\mathbf{u}_i$ $1 \leq i \leq n$ and $V[f]$ is the variation of f in the sense of Hardy-Krause. The discrepancy D_n^* measures how much the sequence deviates from uniform filling. Building low-discrepancy sequences can allow then for more accurate cubature methods than relying on random samples of independent points. In QMC methods, random sequences used in MC are replaced by a deterministic sequence whose points are not independent anymore. The Central Limit Theorem doest not apply then to deterministic Quasi Monte Carlo simulations.
Details about the construction of low-discrepancy sequences are given in Lemieux (2009). Several algorithms have been proposed for the generation of such se-

quences, and the Halton (Halton 1960), Sobol (Sobol' 1976) and Faure (Faure 1982) sequences are the most usually considered. Morokoff and Caflisch (1995) demonstrated that the Halton sequence generally outperforms the others when the integral dimensionality is lower than six. For high-dimensional integrals, Sobol sequences exhibit better convergence properties than the Faure or Halton sequences (Galanti and Jung 1997). Since the integration dimension can be very high in the radiative heat transfer involving diffuse wall reflexions, the Sobol sequence has been retained in this study. The implemented construction algorithm follows the algorithm described in Joe and Kuo (2008).
The concept of discrepancy only provides bounds for the integration error and is in fact of little help in practice: D_n^* and $V(f)$ are not always known, and the upper bound actually significantly overestimates the actual error (Boyle et al. (2001), Joy et al. (1996)). Besides, low-discrepancy sequences not being based on independent and identically distributed (i.i.d) points, the CLT does not apply and no general theorem on asymptotic convergence rate properties is then available. While being far more accurate than MC methods, relying on a finite-size sequence for QMC integration does not provide any inherent error estimate. A practical method to obtain error estimates for QMC is based on the randomization of the low-discrepancy sequences and the resulting methods are called Randomized Quasi-Monte Carlo (RQMC) (L'Ecuyer and Lemieux 2005).

Randomized Quasi-Monte Carlo methods

The core idea behind RQMC is to randomize the existing low-discrepancy sequences. This can be done by building M low-discrepancy sequences of P points, where each sequence is a randomized version of the original low-discrepancy sequence and is independent from the others.
In this way, it is possible to create a random sample of M i.i.d. quasi-random estimators $Q_i^{\mathrm{QMC}}(P)$ of P points. The RQMC result is built as the average as in Eq. (3.9),

$$Q^{\mathrm{RQMC}}(N) = \frac{1}{M}\sum_{i=1}^{M} Q_i^{\mathrm{QMC}}(P) \tag{3.13}$$

and its variance is estimated as in (3.11) as

$$\sigma\left[Q^{\mathrm{RQMC}}(N)\right]^2 \approx \frac{1}{M(M-1)}\sum_{i=1}^{M}\left[Q_i^{\mathrm{QMC}}(P) - Q^{\mathrm{RQMC}}(N)\right]^2. \tag{3.14}$$

Contrary to MC methods where two error estimates, $\widehat{\sigma}_{Q,1}(N)$ and $\widehat{\sigma}_{Q,2}(N)$, can be used, only an equivalent to $\widehat{\sigma}_{Q,2}(N)$ can be built for Quasi Monte Carlo methods.
Many techniques exist to randomize low-discrepancy sequences, and they have to respect two conditions: the first one is that each point in the randomized

point set follows a law of uniform probability on the unity hypercube $[0,1]^d$ for the estimator to be not biased, and the second is that the low discrepancy of the new sequence is preserved after the randomization. The second condition guarantees that the fast convergence of the randomized QMC sequence is not penalized.
Shifting, *Full Scrambling* and *Linear Scrambling* are such randomization techniques. Randomizations based on a shift (the simplest one is proposed in (Cranley and Patterson 1976)) do not sufficiently scramble the point set and, for a certain type of functions, they risk to perform worse than MC integration (Lemieux 2009). This drawback is not present in the full scrambling approach (Owen et al. 1997). However, such a technique is expensive in terms of memory requirement. For this reason a technique of Linear Scrambling, and more precisely the *I-binomial scrambling* (Tezuka and Faure 2003), has been retained in this study, since it preserves the convergence results of the Full Scrambling insuring a good compromise between memory requirement and computational cost.

Application of Quasi-Monte Carlo integration

The characteristics of Quasi-Monte Carlo integration are here illustrated for the computation of the integral in Eq. (3.2) before considering its application to radiative heat transfer in the next sections.
The integral in Eq. (3.2) is first solved with a non-randomized QMC method. In Fig. 3.5, the evolution of $Q(N)$ (left) and of the absolute error $\varepsilon(N) = |Q(N) - I(f)|$ (right) is shown as a function of the number of realizations for QMC and compared to results obtained with MC estimation. In both plots of Fig. 3.5, it is pointed out that QMC converges faster than MC: in QMC calculation the expected value is attained for a number of realizations smaller than the one needed by MC, and the absolute error in QMC is smaller than MC for almost every value of N (especially for large values of N). However, low-discrepancy sequences are not based on i.i.d. sample of points, it is then not possible to get error estimates when applying QMC methods. In order to take advantage of both easy error estimation as done in MC and fast convergence of QMC, Randomized QMC methods are applied to the solution of the integral of Eq. (3.2), where random samples of quasi-random estimators are created.

MC and Randomized QMC methods are now compared consistently by considering a thousand independent integral estimates, *i.e.* $M = 1\,000$, based on MC and QMC quadrature for sequences of size P. The average of the M samples yield the respective MC and Randomized QMC estimates based on a total of $N = MP$ evaluations. In Fig. 3.6, the evolution of the quadrature estimate Q(N) is plotted as a function of P for a fixed M. Similarly to standard QMC, the randomized QMC method reaches the exact value with a smaller number of realizations than MC integration. Note that the numerical estimate are already

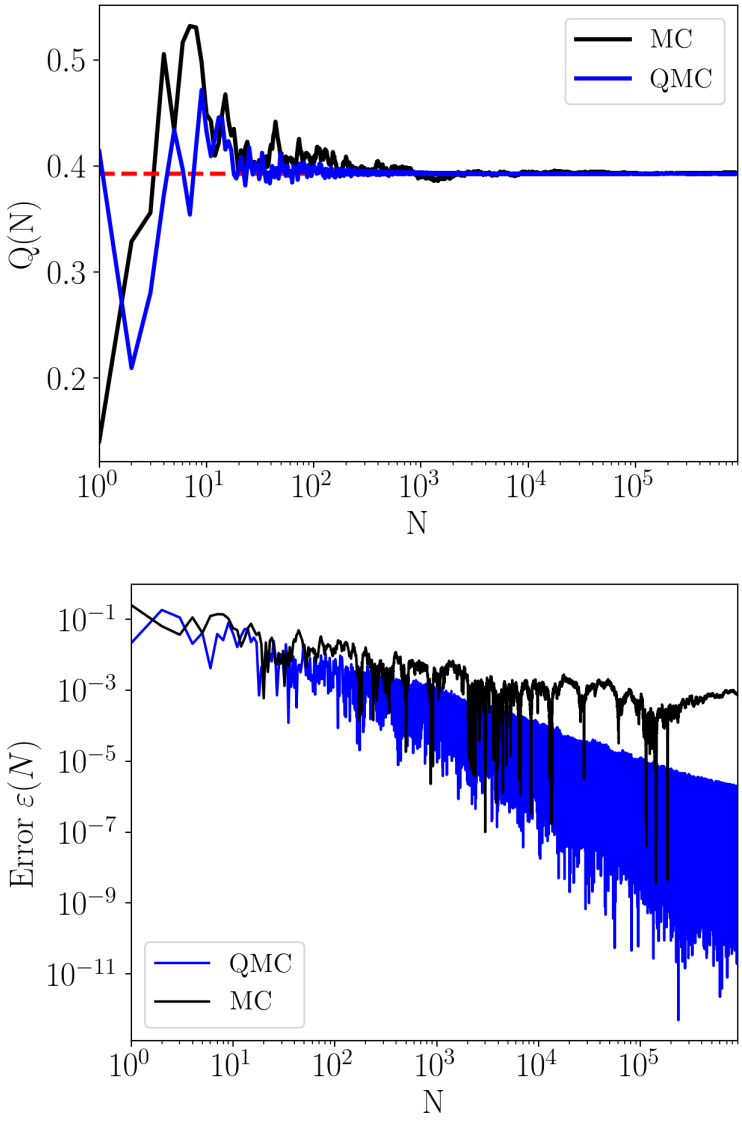

Figure 3.5: *Evolution of $Q(N)$ (top) and error $\varepsilon(N)$(bottom) as a function of the number of realizations in a log-log plot. Black solid line: 1 MC trial of 1 million realizations; blue solid line: 1 QMC trial of 1 million realizations; red dashed line: expected value.*

quite accurate for small values of P because of the retained high value of M chosen to momentary get rid of uncertainties due to the selected value.

In addition to fast convergence attributed to standard QMC, the randomized Quasi-Monte Carlo method benefits from en error estimate. Contrary to classical Monte Carlo integration which provides two error estimates through

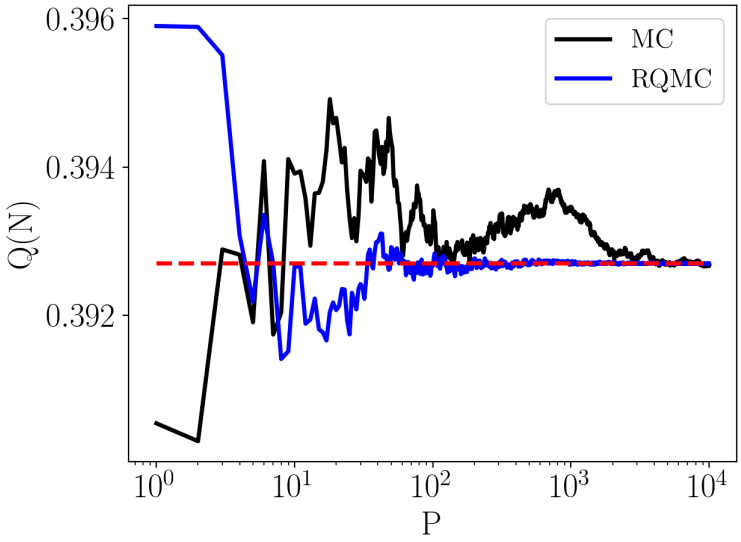

Figure 3.6: *Evolution of $Q(N)$ as a function of the number of realizations in each trial, P, where $N = MP$ and $M = 1\,000$. Black solid line: Monte Carlo results. Blue solid line: Quasi-Monte Carlo results. Dashed red line: exact integration result.*

Eq. (3.8) or (3.11) , RQMC relies on Eq. (3.14) which is only equivalent to Eq. (3.8). The error estimate $\sigma[Q(N)]$ for RQMC method is compared to the corresponding Monte Carlo result in Fig. 3.7 where P is varied while M is still fixed to 1 000. As expected from theory, the MC convergence rate (dashed yellow line) scales as $N^{-1/2} \propto P^{-1/2}$. For the investigated case, the upper bound of the RQMC error (dashed red line) appears to scale as P^{-1}. The error estimate confirms the significantly enhanced convergence rate of the RQMC method. A standard deviation of 10^{-4} is obatined for $P \approx 300$ whereas it is not yet achieved with standard MC with $P = 10^4$. This estimate of the RQMC error allows for controlling the number of realizations needed to reach a desired accuracy. Once again, the estimated error is already small for a small P value because of the chosen value M.
Looking at the lower plot of Fig. 3.7, it is possible to observe the presence of several sub-peaks in $\sigma\left[Q^{\mathrm{RQMC}}(N)\right]$ (blue solide line). These peaks correspond to those realizations where $P = \{2^2,\ 2^3,\ \ldots\ ,\ 2^{13}\}$ and are characterized by a higher accuracy. This is a property of the Sobol sequence which performs better for powers of two. Thus, one can define two laws for the convergence rate that bound the error estimate: an upper bound which was already introduced and a lower bound that correspond to the point $P = 2^i$. Both are drawn in Fig. 3.7. For the studied example, the highest convergence rate obtained for powers of 2 scales as $P^{-1.27}$. For Quasi-Monte Carlo simulations with a fixed number of realizations, it is then optimal to choose it as a power of 2.

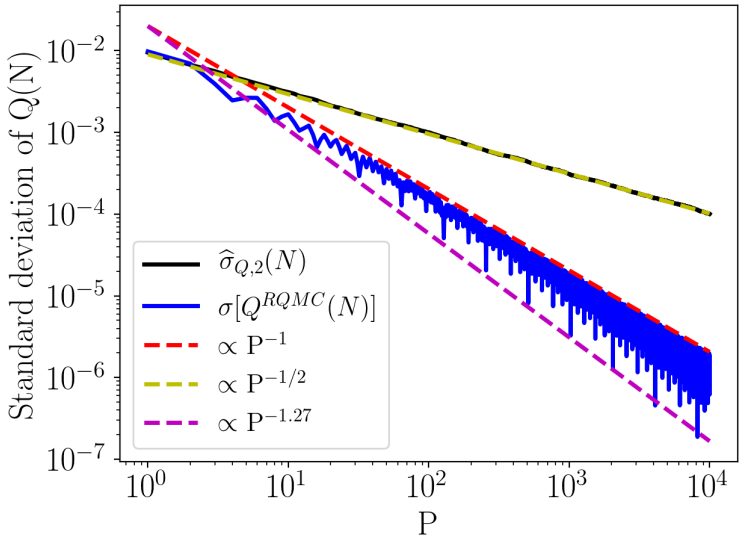

Figure 3.7: *Evolution of error estimate computed from standard deviation formula in Eqs. (3.11) and (3.14) for MC and RQMC, respectively. Results are reported as a function of the number of realizations in each trial, P, for a fixed number $M = 1\,000$ of integration trials. Black solid line: Monte Carlo results. Blue solid line: Quasi-Monte Carlo results. Red dashed line: upper bound RQMC convergence rate. Magenta dashed line: convergence rate of RQMC for $P = \{2^2,\ 2^3,\ \ldots,\ 2^{13}\}$.*

The dependency of RQMC results on the number M of random QMC estimate is now considered with a fixed size of the sequences set to $P = 1\,000$. Figure 3.8 presents the error estimate $\sigma[Q(N)]$ as a function of the number of trials, M, for both MC and RQMC. As expected from the CLT which states that $\sigma[Q(N)]^2 \approx \sigma[Q(P)]^2/M$, both MC and RQMC errors scale as $M^{-1/2}$. The shift between both curves is due to the higher accuracy of RQMC compared to MC for a given sequence size P.

The computational cost of each method depends on the total number of realizations N, *i.e.* the product of both M and P. Previous results have shown that MC and RQMC convergence rates scale as $M^{-1/2}P^{-\beta}$ where $\beta = \frac{1}{2}$ in the MC method, while it is appreciably larger in RQMC and unknown *a priori* for a given case. In standard MC simulation, the convergence rate depends then eventually as $N^{-1/2}$ and is not sensitive to the M-P distribution. The number of MC trials M used to compute the error estimate must nonetheless be large enough for Eq. (3.11) to be reliable. A minimum value of M often admitted in the literature is 10 (Lemieux 2009). In RQMC, the trade-off between M and P for a given N is not at all trivial. Error estimates as a function of the total number of samples N are shown in Fig. 3.9 for both MC and RQMC computations with different M-P repartitions. On the one hand, all MC results

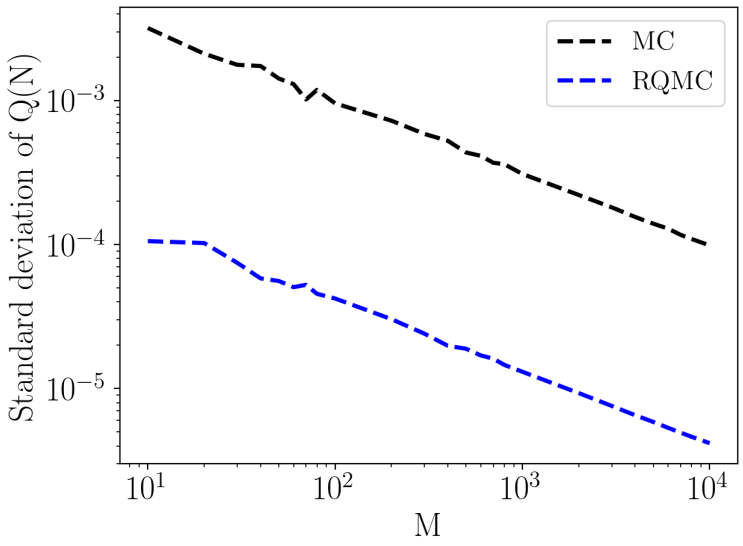

Figure 3.8: *Evolution of error estimate as a function of the number of trials, M for MC (black) and QMC (blue). Each trial contains $P = 1000$ points.*

are similar and tend to the same asymptotic convergence rate as previously explained. On the other hand, it can be clearly seen that each M-P combination yields a different convergence rate for RQMC. For a same computational cost (identical N), the combination with small values of M achieves significant higher accuracy. This is due to the $M^{-1/2}P^{-\beta}$ convergence law with $\beta > 1/2$: it is more interesting to increase the size of the low-discrepancy sequence, P, for a same N in order to benefit from the QMC enhancement. The choice of M is then critical in RQMC method.

However, M cannot be too small, otherwise the error estimate in Eq. (3.14) can not be trusted. A compromise must then be found. A sensitivity analysis has been performed to study the evolution of $\sigma[Q(P)]$ as a function of the trials number M, keeping fixed the number of realizations to $P = 10\,000$ per trial. The results for the retained example are presented in Fig. 3.10. As the number of trials M increases, the standard deviation $\sigma[Q(P)]$ converges towards a value around 4×10^{-5}. A good compromise to keep M sufficiently small and $\sigma[Q(P)]$ close to each converged value is found for a number of trials equal to 20, which is around classical values also retained in standard MC as reported previously. This value of M is retained for the numerical setup of the following simulations.

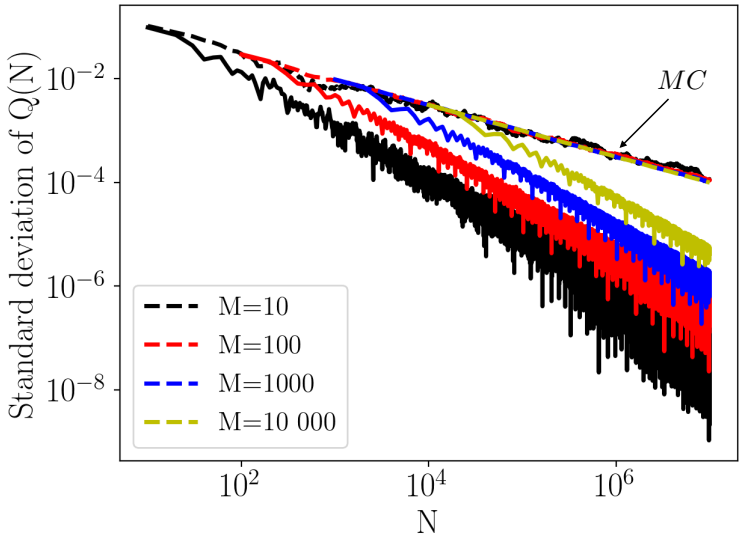

Figure 3.9: *Evolution of error estimate as a function of the total number of realizations, $N = MP$, for several combinations of M and P identified by colors. Dashed lines: MC results pointed out by black arrow. Solid lines: RQMC results.*

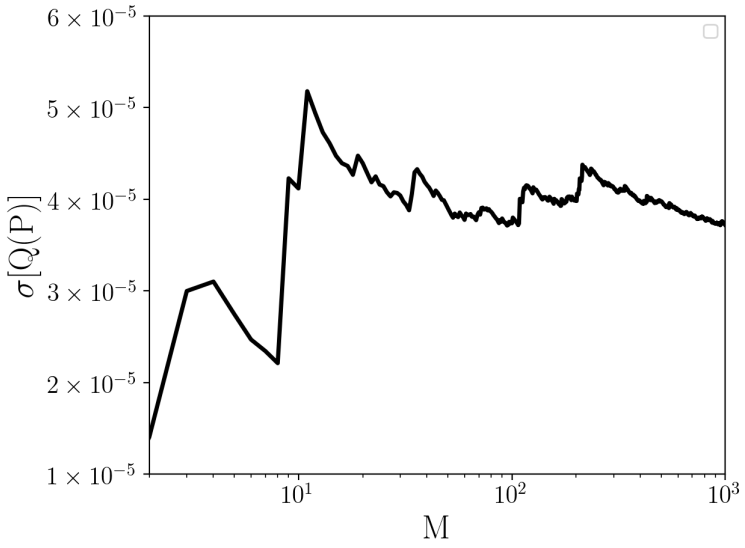

Figure 3.10: *Evolution of* $\sigma[Q(P)] = \left[\frac{1}{M-1}\sum_{i=1}^{M}\left(Q_i^{QMC}(P) - Q^{RQMC}(N)\right)^2\right]^{1/2}$ *as a function of the number of trials M and for $P = 10\,000$.*

3.2 Monte Carlo numerical solver of radiative heat transfer

The in-house code Rainier (Zhang et al. (2012), Zhang et al. (2013), Koren et al. (2018), Palluotto et al. (2017)) is described in the present section. It solves the radiative transfer equation (RTE) with a Monte Carlo approach while relying on standard Monte Carlo or Randomized Quasi-Monte Carlo integration. Details of the solver, its adaptation to QMC integration and the retained description of radiative properties are given in the following.

3.2.1 Ray tracing in the Monte Carlo solver and adaptation to QMC

In the Rainier solver, the local radiative power is computed at each vertex of the computational domain (those where the solution is desired). Then, the departing position of a photon bundle is fixed and it is not determined by a random variable. Thus, a ray tracing starting at a given point is initially characterized by a direction determined the unit vector denoted as Δ, or equivalently by two angles θ and ϕ, and a frequency ν generated according to a given probability density function depending on the resolution method.
A ray is tracked along its optical path with possible absorption by the participating medium or walls, wall reflexions and exiting of the computational domain. To keep the simulation affordable, the ray tracing is interrupted when the equivalent transmission from the departing point is below a pre-defined threshold τ_{min}. In other words, a ray is stopped when its remaining energy has been lowered by a factor corresponding to τ_{min}. Here, τ_{min} is set equal to 0.01 in all the investigated cases.
During its optical path, a ray hitting a wall may be reflected. For black walls or specular reflexion, no additional random number than the previous three for frequency and departing direction is necessary. The corresponding three-dimensional space is then sampled with either a pseudo-random generator (the one used in the present work is L'Ecuyer's Multiple Recursive Generator MRG32k3a (L'ecuyer 1999)) or a three-dimensional Sobol sequence for QMC integration. However, cases with diffuse reflexions as later considered in confined configurations require a specific attention. In standard MC, the reflected direction then needs to be randomly generated and the integration dimension d of the problem increases as $d = 3 + 2r$ where r is the number of reflections performed. The number of reflexions that one ray can undergo is then unknown, making d undetermined as well. While this is transparent for standard MC where the pseudo-random generator provided i.i.d samples, this is critical for QMC integration that requires to *a priori* know the dimension of the integration problem to build the low-discrepancy sequence. In the present integration of such sequences, the maximum number of reflexions r_{max} is determined from the worst case scenario and is used to build a d-dimensional

sequence with $d = 3 + 2r_{max}$.
The worst case is considered as a transparent medium with wall diffuse reflectivities equal to $1-\epsilon_{min}$, where ϵ_{min} is the the lowest wall emissivity considered in the problem setup. After r reflexions, the energy of the ray is scaled down by the factor $(1 - \epsilon_{min})^r$. Given the criterion τ_{min} introduced earlier to stop the ray, the maximum number of reflexions follows

$$(1 - \epsilon_{min})^{r_{max}} < \tau_{min} \tag{3.15}$$

Thus,

$$r_{max} > \frac{\ln(\tau_{min})}{\ln(1 - \epsilon_{min})} \tag{3.16}$$

and the dimension d becomes:

$$d = 3 + \frac{2\ln(\tau_{min})}{\ln(1 - \epsilon_{min})}. \tag{3.17}$$

The formula obviously falls apart for purely reflective surfaces ($\epsilon_{min} = 0$), which is unrealistic in practical applications of radiative heat transfer.
Finally, the number of rays issued from a given point of interest is controlled by the prescribed accuracy. The standard Monte Carlo accuracy is estimated by assembling rays in several batches ($M = 20$) and using the estimate in Eq. (3.11) for the quantity of interest (radiative power of flux). This makes the implementation of the Randomized-Quasi Monte Carlo error estimate given by Eq. (3.14) straightforward. For both methods, the control is carried out on the relative and the absolute value of the standard deviation of the results estimate. Hence, the relative error of the radiative power is defined as the ratio of the local standard deviation to the local radiative power. However, this relative error is not appropriate in regions with negligible radiative contribution. A second control is then considered on the absolute value of the standard deviation which is checked to be lower than a prescribed maximum, typically set equal to a given percentage of the maximum radiative power. When error control is enabled, the prescribed tolerances for the absolute and relative errors allow for a local adaptation of the number of rays et each point.

3.2.2 Emission-based Reciprocity Method

Two backward Monte Carlo methods are implemented in the solver: the Emission Based Reciprocity method (ERM) (Tessé et al. 2002) and the Optimized-ERM (OERM) (Zhang et al. 2012). The main interest in such methods is the possibility to dynamically and independently control the local convergence of the computed radiative fields. Photon bundles are traced from volume or surface points of the computational domain where the radiative power or wall flux is predicted. The independent treatment of points of interest allows for a

high degree of scalability. A scalability test has been performed on a cluster equipped with Intel E5-2690 processors on a configuration characterized by a computational domain of 8 millions cells. The number of cpu cores is varied from 120 up to 1920. Results, displayed in Fig. 3.11, show that a very good scalability is obtained. Besides, ERM and OERM are reciprocal MC methods that exactly enforce the Reciprocity Principle (Case 1957), that is only statistically fulfilled by other Monte Carlo methods.

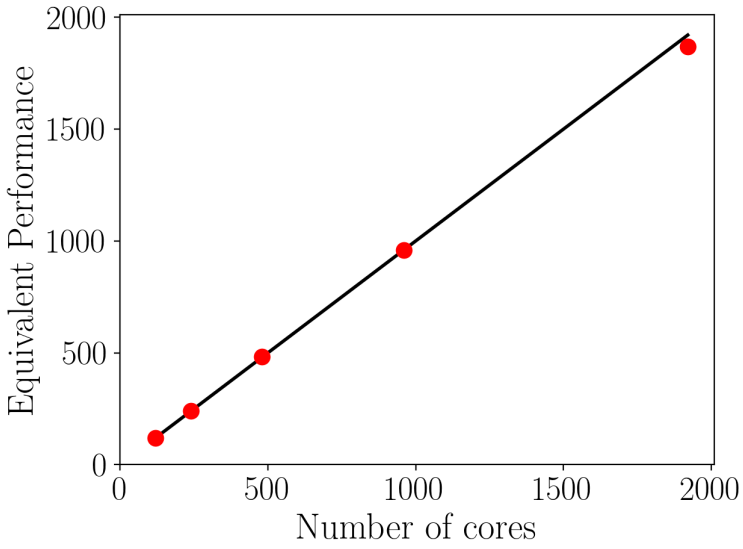

Figure 3.11: *Scalability of the Rainier solver with number of cores. Red circles correspond to the performed tests, dashed line corresponds to the ideal performance.*

In a reciprocal formulation the radiative power per unit volume of the node i of the discretization domain is calculated as the sum of the exchanged powers P_{ij}^{exch} between the node i and all the other cells j crossed or encountered by the optical paths generated by i.

$$P_i = \sum_{j=1}^{N} P_{ij}^{exch} \tag{3.18}$$

where N is the number of volume cells and faces in which the domain is discretized.
P_{ij}^{exch} is the difference between the radiative power emitted by j, transmitted by the medium and absorbed by i, and the radiative power emitted by i, transmitted by the medium and absorbed by j:

$$P_{ij}^{exch} = \int_0^{\infty} \kappa_\nu(T_i)[I_\nu^0(T_j) - I_\nu^0(T_i)] \int_{4\pi} A_{ij\nu} d\Omega_i d\nu \tag{3.19}$$

where κ_ν is the spectral absorption coefficient, I^0_ν the equilibrium spectral intensity, Ω_i is the solid angle issued from i, ν the photon frequency and $A_{ij\nu}$ accounts for all the paths between emission from i and absorption in j after transmission and possible walls reflections along the paths. Its expression is detailed in Tessé et al. (2002).
Introducing the volumetric power $P^e_i(T_i)$:

$$P^e_i(T_i) = 4\pi \int_0^\infty \kappa_\nu(T_i) I^0_\nu(T_i) d\nu \tag{3.20}$$

Equation (3.19) can be written as:

$$P^{exch}_{ij} = P^e_i(T_i) \int_0^\infty \left[\frac{I^0_\nu(T_j)}{I^0_\nu(T_i)} - 1 \right] \int_{4\pi} A_{ij\nu} f_i(\Delta, \nu) d\Omega_i d\nu \tag{3.21}$$

where $f_i(\Delta, \nu)$ is the joint PDF with Δ the direction.
$f_i(\Delta, \nu)$ can be separated in two independent parts:

$$f_i(\Delta, \nu) d\Omega_i d\nu = f_{\Delta_i}(\Delta) d\Omega_i f_{\nu_i}(\nu) d\nu \tag{3.22}$$

with:

$$f_{\Delta_i}(\Delta) = \frac{1}{4\pi}; \quad f_{\nu_i}(\nu) = \frac{\kappa_\nu(T_i) I^0_\nu(T_i)}{\int_0^\infty \kappa_\nu(T_i) I^0_\nu(T_i)} \tag{3.23}$$

$f_{\nu_i}(\nu)$ is the frequency distribution function and it is equal to the emission distribution function at the temperature T_i of the emitting node. Then, in the ERM formalism, the frequency ν_n associated with a realization n is obtained by a uniform random number R_n between 0 and 1, and ν_n is determined from the equation:

$$R_n = \int_0^{\nu_n} f_{\nu_i}(\nu) d\nu = \frac{\int_0^{\nu_n} \kappa_\nu(T_i) I^0_\nu(T_i) d\nu}{\int_0^\infty \kappa_\nu(T_i) I^0_\nu(T_i) d\nu} \tag{3.24}$$

In the OERM method, the frequency distribution function f_{ν_i} is based on the emission distribution at the maximum temperature encountered in the system, T_{max}; as a consequence, ν_n in the OERM formalism is determined from:

$$R_n = \frac{\int_0^{\nu_n} \kappa_\nu(T_{max}) I^0_\nu(T_{max}) d\nu}{\int_0^\infty \kappa_\nu(T_{max}) I^0_\nu(T_{max}) d\nu} \tag{3.25}$$

The direction Δ is determined in spherical coordinates by the polar angle θ and the azimuthal angle ϕ, which are determined according to Eqs. (3.4 - 3.5).
Statistical estimation of the radiative power P_i at the node i, indicated as $\hat{P}_i$, can be obtained by summing all the contributions of the N_i optical shots traced from i. And its final expression, as it is computed in the presented simulations, is:

$$\hat{P}_i = \frac{P^e_i}{N_i} \sum_{n=1}^{N_i} \sum_{m=1}^{M_n} \left[\frac{I^0_{\nu_n}(T_m)}{I^0_{\nu_n}(T_i)} - 1 \right] \tau_{\nu_n} \alpha_{n,m,\nu_n} \tag{3.26}$$

where $m = 1$ is the cell i, while $m = M_n$ represents the last cell crossed by the n^{th} optical path originating from i. Then, α_{n,m,ν_n} is the spectral absorptivity of the n^{th} optical path in the m^{th} cell crossing, while τ_{ν_n} is the spectral transmissivity from i to the cell m accounting for eventual wall reflections.
From the Eq. (3.26) it is possible to see that the radiative power exchanged between two cells identical temperatures is rigorously null, leading to more accurate results compared to conventional formalisms.

3.2.3 Gas radiative properties

Concerning the gas radiative properties, a good compromise between accuracy and computational cost is found with a narrow-band approach: the $correlated-k$ or ck model by Goody and Yung (1995) based on updated parameters due to Rivière and Soufiani (2012), which have been obtained for the range of temperature and pressure of interest, by using the CDSD-4000 database for the absorption spectra of CO_2 (Tashkun and Perevalov 2011) and HITEMP 2010 for the ones of H_2O (Rothman et al. 2010). The whole considered spectrum ranges from 150 to 9200 cm^{-1}. 44 spectral bands are considered for H_2O, whose width varies from 50 to 400 cm^{-1}. CO_2 spectrum overlaps the H_2O one and CO_2 absorbs in only 17 of the 44 bands. This leads to a total of 1022 quadrature points: 7^2 quadrature points for each of the 17 bands where both species absorb plus 7 quadrature points for the remaining 27 bands where only H_2O participates.

3.2.4 Validation of the RQMC implementation

In order to validate the RQMC implemented in the solver Rainier, a 1D slab geometry, for which a semi-analytical solution of the radiative transfer equation can be obtained from exponential integral functions (Modest 2013), is retained and two test cases are performed. The radiative power per unit volume is computed within a slab normal to X and bounded by two gray and opaque infinite planes. The slab thickness is $L = 0.1$ m and the walls are characterized by a diffuse emissivity of 0.6 and a wall temperature $T_w = 500$K. In the first test, denoted as $Case\ a$, a gray gas (constant κ_ν) with an optical thickness equal to 1 is considered. The second test, called $Case\ b$, represents more realistic conditions: a medium with an homogeneous composition (CO_2 and H_2O molar fractions are, respectively, 0.116 and 0.155) is considered. Spectral radiative properties of the gaseous mixture are taken into account through the aforementioned c-k model. For both investigated cases, the gas is at atmospheric pressure and has a parabolic temperature profile $T(X) = aX^2 + b$, where X is the normal to the walls, b is the maximum temperature, equal to 2500 K, and $a = \frac{T_w - b}{(L/2)^2}$.
For each investigated case, MC and RQMC simulations are performed. Profiles of radiative power across the normal to the slab, X are presented in Fig. 3.12, for $Case\ a$ and in Fig. 3.13 for $Case\ b$. Black solid lines represent the semi-

analytical reference solution in both cases. Figures 3.12 and 3.13 show that,

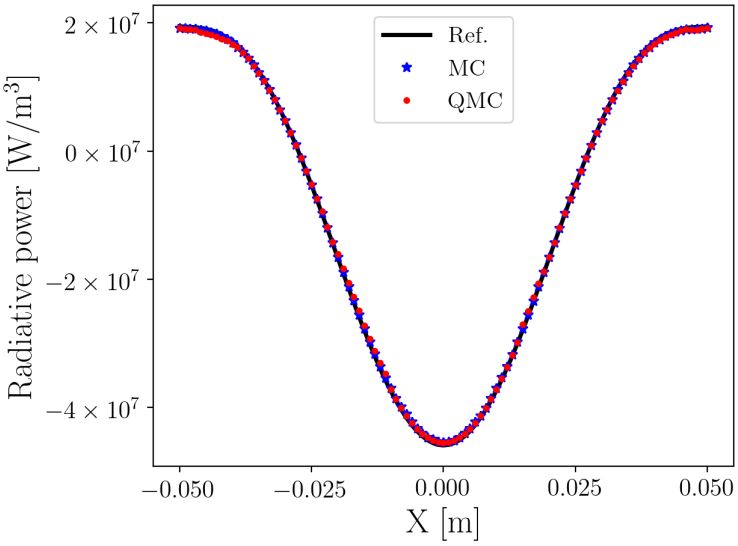

Figure 3.12: *Profile of radiative power in Case a across the slab coordinate X computed by MC (blue) and RQMC (red), compared to the reference solution (black solid line).*

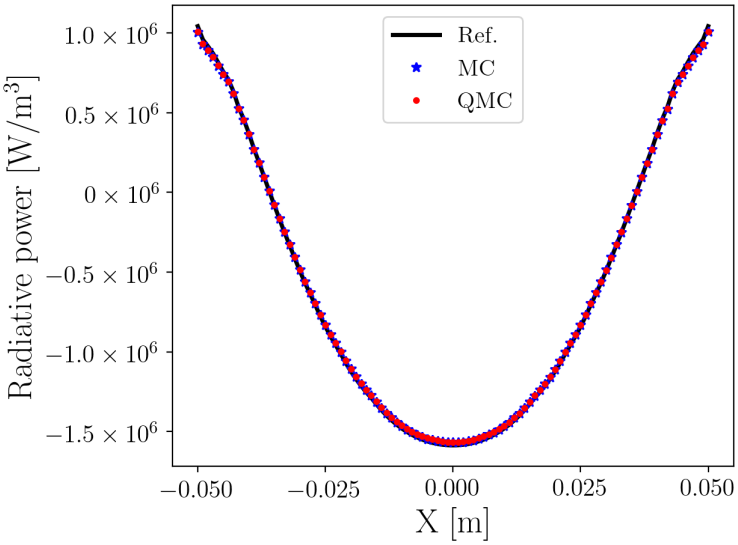

Figure 3.13: *Profile of radiative power in Case b across the slab coordinate X computed by MC (blue) and RQMC (red), compared to the reference solution (black solid line).*

for both investigated cases, the MC and RQMC results overlap on the reference

profile. This validates the implementation of RQMC in the Rainier solver. In the next section, more practical configurations are retained for the thorough comparison of MC and RQMC methods.

3.3 Investigated configurations

Three 3D configurations are investigated: a canonical flow configuration (turbulent channel flow at high pressure) and two combustion applications (a turbulent sooting jet flame and a combustion chamber featuring a premixed swirled flame). These three cases are characterized by different degrees of complexity and enable to study the impact of the radiative heat transfer in different practical situations: at high pressure, in reacting flows, in presence of soot or walls. This allows for comparing MC and RQMC methods behavior in several contexts. Besides, all temperature and composition fields are extracted from direct numerical simulations and large-eddy simulations. The numerical methods are then assessed in configurations relevant to coupled high-fidelity simulations.

3.3.1 Case 1: Turbulent channel flow

The first investigated application is a turbulent channel flow (case C3R1 from Zhang et al. (2013)) whose dimensions are: $L_x \times L_y \times L_z = 0.62$ m $\times 0.2$ m $\times 0.3$ m. The channel is filled by an homogeneous gas mixture of $CO_2 - H_2O - N_2$ with a corresponding molar fraction of $0.116 - 0.155 - 0.729$. Its pressure is 40 bars and two iso-thermal walls (at 2050 K on the top and 950 K on the bottom) with a total hemispherical emissivity of 0.8 confine the flow. Its structured computational grid is made by 4.2 millions nodes.
In Fig. 3.14, snapshots of 3D direct numerical simulations taken from Zhang et al. (2013) are shown: on the top the instantaneous temperature field and on the bottom the radiative power field are given. At the given high pressure, the optical thickness of the medium is large. The effect of a large optical thickness can be seen in the very thin layer close to the wall: the bottom one is dominated by the absorption, while the one close to the hot wall is dominated by emission. Consequently there is a negligible radiative interaction between the two walls, and the whole domain is characterized by absorbing (yellow pockets) and emitting (blue pockets) regions. The emitted thermal radiation is absorbed in the vicinity of the emitting point.

3.3.2 Case 2: Non-confined sooting jet flame

The second configuration is the turbulent jet diffusion flame experimentally studied at Sandia (Zhang et al. 2011). It is fed with pure ethylene at 300 K and is stabilized with the help of pilot flames fed by ethylene and air. Unlike the previous configuration, the participating medium is heterogeneous and contains

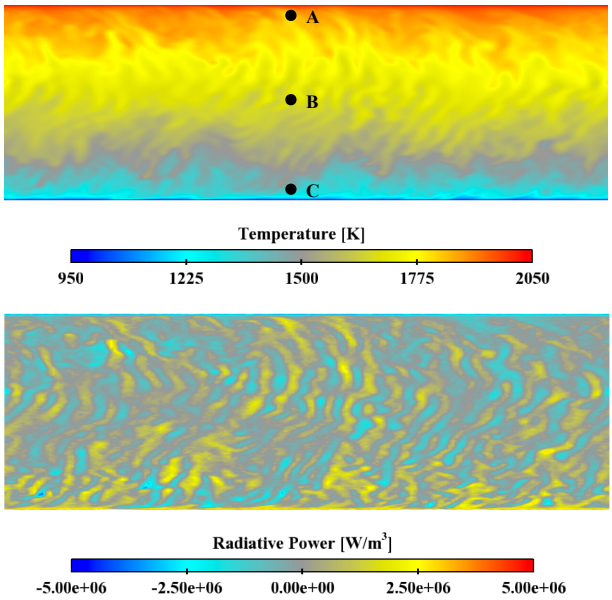

Figure 3.14: *Instantaneous fields of temperature (top) and radiative power (bottom) on a longitudinal section of the channel. Points A, B and C, whose results are analyzed in Sec. 3.4, are indicated by black circles on the top figure.*

soot particles. The presence of soot particles make the radiation heat transfer very important.

In Fig. 3.15, soot volume fraction and temperature fields extracted from 3D Large Eddy Simulations of Rodrigues et al. (2018) are shown along with the computed instantaneous radiative power field (left). Soot particles are present in richer regions of the flame and maximum instantaneous soot volume fraction is nearly 10 ppm. Radiative power issued from soot particles is located also in richer regions dominated by emission. Similarly, the radiative power is also negative in hot near stoichiometry burnt gases. On the other hand, lean regions where temperature is lower than 1000 K are dominated by the absorption from CO_2 and H_2O.

When soot radiation is included in the calculation, their absorption spectra need to be taken into account; then 93 spectral bands are introduced between 150 and 29 000 cm^{-1}, of which 44 overlap with the gas bands. The soot absorption coefficient is modeled through the Rayleigh's theory (Modest 2013): $\kappa_\nu^{soot} = C_0 f_\text{v} \nu$ with $C_0 = \frac{36\pi nk}{(n^2-k^2+2)^2+4n^2k^2}$ where n and k are the real and imaginary part of the complex index of refraction of soot particles, taken as equal to $m = n - ik = 1.57 - 0.56i$ (Smyth and Shaddix 1996), ν is the wavenumber (m^{-1}) and f_v is the soot volume fraction.

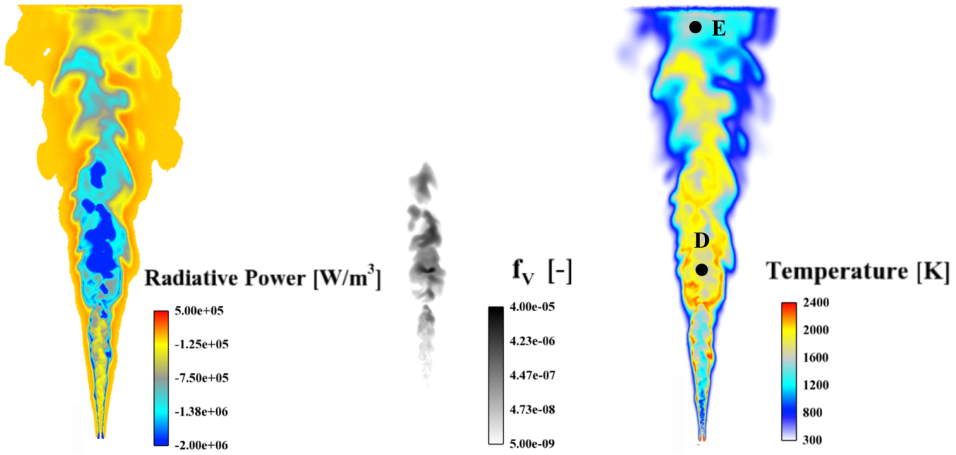

Figure 3.15: *Instantaneous fields of radiative power (left), soot volume fraction (center) and temperature (right) on a longitudinal section of the jet flame. Color scales are linear for radiative power and temperature and logarithmic for soot volume fraction. Points D and E, whose results are analyzed in Sec. 3.4, are indicated by black circles on the right figure.*

3.3.3 Case 3: Combustion chamber

The third investigated application is a laboratory scale combustor (30 cm long with a square section of 81 cm^2) studied experimentally (Guiberti et al. 2015; Guiberti et al. 2015) and numerically (Mercier et al. 2016; Koren et al. 2018). The chamber is operated at atmospheric pressure and a turbulent premixed flame of CH_4, H_2 and *Air* is stabilized. The flame is characterized by a thermal power of 4 kW and is confined by cold quartz windows. Such configuration is typical of industrial furnaces. Figure 3.16 shows the temperature field extracted from Large Eddy Simulations (Koren et al. 2017) on a longitudinal section of the chamber along with the presently computed radiative power field. The 3D computational grid is made of 1.26 millions points.
As in the previous configuration, heterogeneities of temperature and of participating species are present. The complexities seen in the previous cases (heterogeneities and participating walls) are simultaneously taken into account in this configuration and they represent typical situations encountered in a real enclosed application. The temperature field (Fig. 3.16 top) shows that burnt gases issued from the flame are hotter than the ones close to the walls. Because of the presence of recirculation zones between the flame and the walls, hot gases are recirculated toward the chamber bottom while they are cooled down by wall convective heat transfer. The radiative power field indicates that cold gases close to the walls are dominated by absorption (red regions/positive radiative power), while the higher temperature regions mostly emit radiation (negative values of radiative power). In the present radiative heat transfer

computations, the walls are considered as opaque with a total hemispherical emissivity of 0.75.

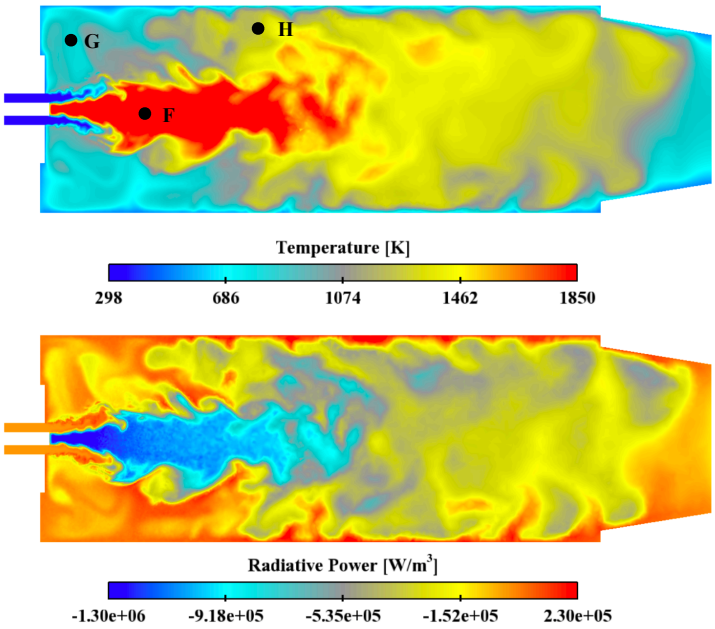

Figure 3.16: *Instantaneous fields of temperature (top) and radiative power (bottom) on a longitudinal section of the burner. Points F, G and H, whose results are analyzed in Sec. 3.4, are indicated by black circles on the top figure.*

3.3.4 Numerical set-up for MC and QMC simulations

For each application, radiative heat transfer simulations are performed using both MC and RQMC methods. For each method two different tests are carried out. The first test, Test 1, consists in imposing an identical number of rays at all the computed points, while no convergence criterion is imposed. Such an analysis allows to evaluate the level of convergence, i.e. the error achieved at every node of the computational domain where the solution is desired. On the contrary, in the second test, Test 2, two convergence criteria are imposed: relative and absolute error. In this case, the number of rays is not set a-priori but it spatially varies over the computational domain. Table 3.1 summarizes the setup used for the tests performed on each application.
For all the computations, inlet and outlet are considered as non-reflecting ($\epsilon = 1$) with a far-field temperature of 300 K (except for Case 1, where periodic conditions are considered). The retained method is the ERM method (Tessé et al. 2002) in its MC and QMC version.

	Test 1	Test 2	
Case	Number of Rays	Rel. Error	Abs. Error
1	5 000	1%	3% of P^R_{max}
2	5 000	1%	1% of P^R_{max}
3	5 000	3%	3% of P^R_{max}

Table 3.1: *Numerical set-up of the tests with a fixed number of realizations, Test 1, and at controlled convergence, Test 2, for the three applications.*

3.4 Results: three practical applications

For each configuration, results of radiative heat transfer simulations are shown. Tests with a fixed number of rays, also referred as realizations, are first carried out before considering tests with controlled convergence.

3.4.1 Tests with a fixed number of realizations

MC and RQMC methods are compared in simulations where the number of realizations is imposed (Test 1 in Tab. 3.1) in order to compare the local convergence attained in all the points of the computational grid. The error of the computations is determined as the standard deviation of the estimated radiative power following Eqs. 3.11 and 3.14. In Fig. 3.17, the absolute error scaled by the the maximum radiative power in the domain is shown for Case 1 for MC (top) and RQMC simulations (bottom). With the same number of realizations, the RQMC computation allows for converging all the points of the computational domain with a significantly smaller absolute error compared to the classical MC approach. For both methods, the resulting error field is not uniform. In particular, the error is larger close to the cold wall. This behavior is expected with the ERM approach whose drawback is a poorer convergence in cold regions with significant absorption. The same observation can be done for Cases 2 and 3 shown in Figs. 3.18 and Fig. 3.19 in terms of the local relative error, *i.e* the ratio between the standard deviation and the local value of the radiative power. It can be seen that RQMC simulations (on the bottom) are more accurate than MC ones (on the top) since, with RQMC, most of the points of the domain achieve a relative error lower than the one obtained when MC is used.

Additional tests are performed in order to check the convergence rate of MC and RQMC simulations as a function of the number of realizations N for the three investigated cases (M is still fixed to 20). For each configuration, the relative error is measured in several characteristic points of the domain, highlighted in Figs. 3.14, 3.15 and 3.16 and identified by letters. In Case 1, three points, A, B and C, are retained: they are located in proximity of the hot wall, at the half-height and close to the cold wall of the channel, respectively. In Case 2, two

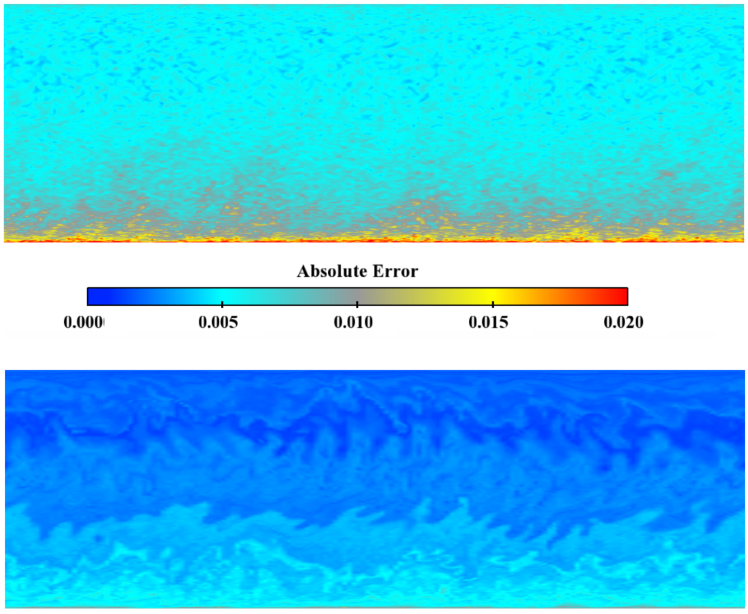

Figure 3.17: *Field of absolute error scaled by the the maximum radiative power in the domain. The computation is carrie out following Test 1 with MC (top) and RQMC (bottom) in the channel flow configuration (Case 1).*

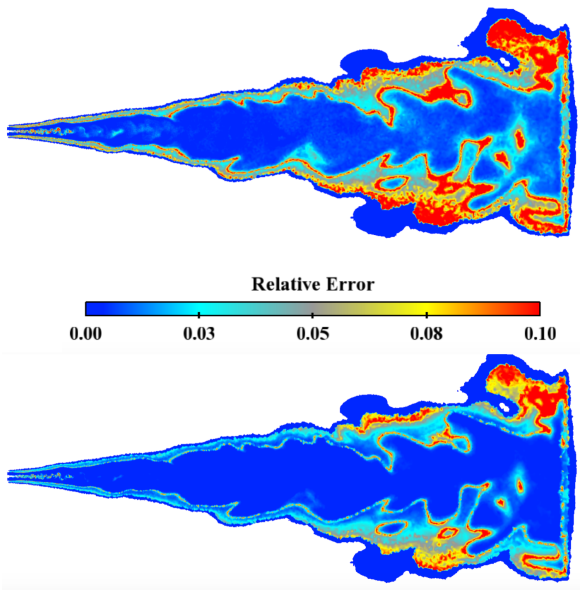

Figure 3.18: *Field of relative error achieved in Test 1 with MC (top) and RQMC (bottom) in a sooted jet flame application (Case 2).*

points, D and E, are chosen to represent, respectively, a hot and rich mixture characterized by a high soot concentration and downstream burnt gases at lower

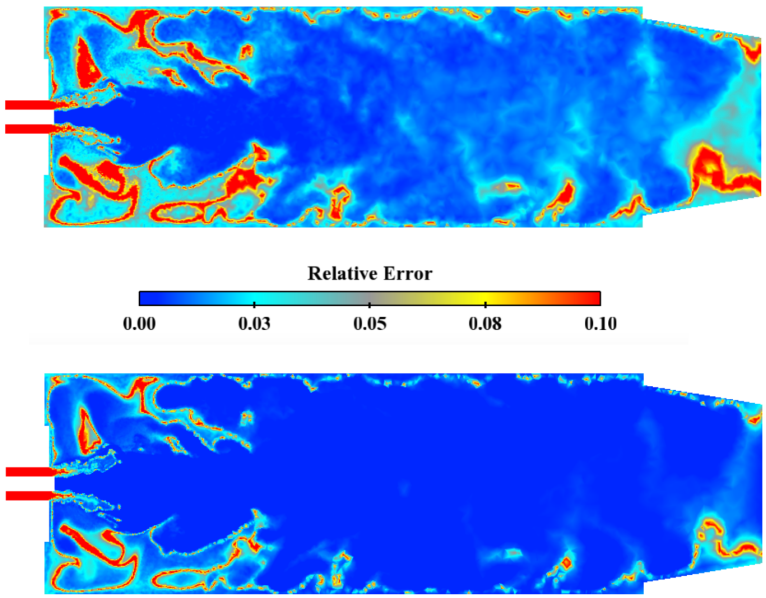

Figure 3.19: *Field of relative error achieved in Test 1 with MC (top) and RQMC (bottom) in a combustion chamber (Case 3).*

temperature where no soot is present. In Case 3, the probes, F, G and H, are located in the flame region, in the cold outer recirculation zone (ORZ) close to the chamber bottom and further downstream in the ORZ at an intermediate temperature, respectively.
Figures 3.20, 3.21 and 3.22 display the relative error obtained by MC (circles) and RQMC (diamonds) for each studied points in the different configurations. The convergence rates of MC (grey dashed lines) and RQMC (gray dotted line) are also highlighted on the figures. In the case of RQMC computations where no theoretical results provide the asymptotic convergence rate, the corresponding lines illustrate the convergence rate of the method by considering a slope computed by a linear fitting of the RQMC error on the different probes.
Figure 3.20 shows that the MC error (circles) is larger than the RQMC one (diamonds) for the high and low temperature probes (A and C) for every number of rays N considered. Instead, for the probe B at intermediate temperature, the MC error is lower than the RQMC one for $N = 1000$ before becoming larger for $N > 10^3$. Looking at the gray lines in Fig. 3.20 given for large values of N, RQMC simulations indeed always achieve faster convergence rates eventually than MC ones for each investigated point. In the three dotted lines representative of RQMC convergence rates which scale as N^b, the exponent b in fact varies according to the considered physical position inside the domain. The best fitted value for b is equal to -0.856 for the Point A, -1.017 for B and -0.902 for C. For the three considered points, the magnitude of the exponent b of RQMC convergence law is higher than $1/2$, corresponding to the classical

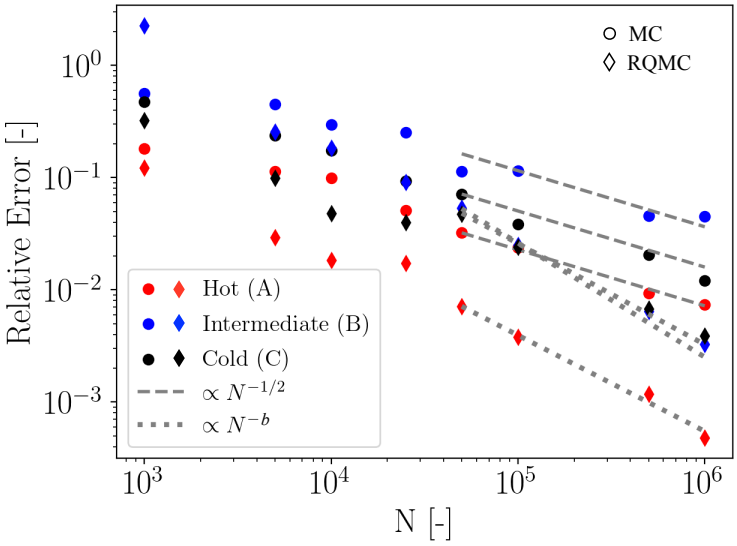

Figure 3.20: *Relative error as a function of the number of realizations N for three characteristic points of the channel flow configuration (Case 1): A (red), B (black) and C (blue). Circles: MC simulations. Diamonds: RQMC simulations. Grey lines: convergence rate of MC (dashed line) and RQMC (dotted line) results.*

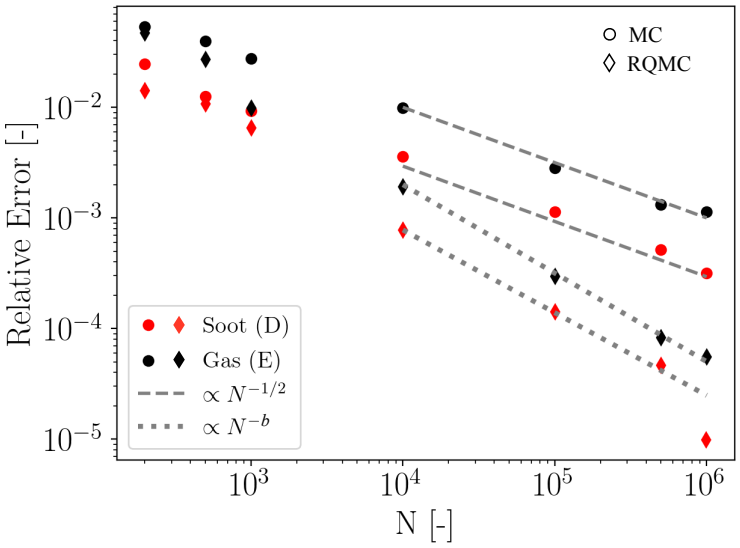

Figure 3.21: *Relative error as a function of the number of realizations N for two characteristic points of the sooting jet flame (Case 2): D (red) and E(black). Circles: MC simulations. Diamonds: RQMC simulations. Grey lines: convergence rate of MC (dashed line) and RQMC (dotted line) results.*

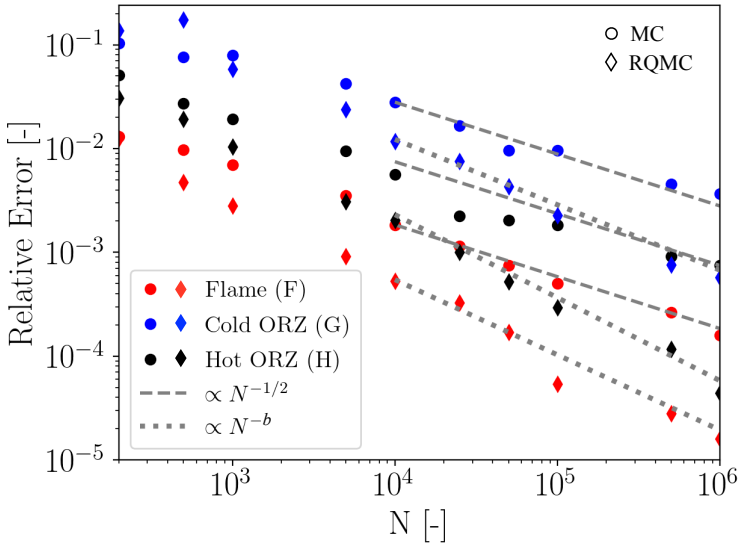

Figure 3.22: *Relative error as a function of the number of realizations N for three characteristic points of the considered combustion chamber (Case 3): F (red), G (blue) and H (black). Circles: MC simulations. Diamonds: RQMC simulations. Grey lines: convergence rate of MC (dashed line) and RQMC (dotted line) results.*

MC convergence.
The relative error achieved by MC and RQMC in the sooting jet flame, Case 2, as a function of the number of realizations N is displayed in Fig. 3.21. For both considered points, D and E, the RQMC error stays lower than MC one for every value of N. The exponent b of the RQMC convergence law is equal to -0.748 for Point D where, in addition to the gaseous contribution, soot radiation is significant, and $b = -0.804$ for the point E where soot particles are absent. Once again, the RQMC simulations converge faster than their corresponding MC computations. In Figs. 3.20 and 3.21, all MC simulations consistently reach an asymptotic convergence law proportional to $N^{-1/2}$. The proportionality factor is however different and all MC results appear as translated from each other in the logarithmic plots. As indicated by Eq. 3.8, this is the result of different intrinsic standard deviation (estimated as $\hat{\sigma}$) at the considered points. $\hat{\sigma}$ depends on the specific radiative exchanges for the given location and on the Monte-Carlo algorithm solving for radiative heat transfer. The ERM methods is used here, which is known to converge more poorly in colder regions as confirmed in Figs. 3.20 and 3.21. The figures reveal that, while RQMC simulations are more accurate than MC ones and present slightly different slopes, the RQMC convergence laws also exhibit translation shifts between the different points. Although the observed distance between RQMC results is different from the one seen with MC results, the same ranking of accuracy between the different probes is kept for both approaches. The RQMC results are then sensitive to

the intrinsic standard deviation of the integral to compute.
Figure 3.22 shows the error achieved in MC and RQMC simulations of the combustion chamber (Case 3), for the three considered points, F, G and H. Concerning the cold region of burnt gases represented by probe G, the RQMC error is higher than MC one for $N < 10^3$, showing again that RQMC does not always guarantee more accurate results with a reduced number of evaluations. Nonetheless, for higher values of N, the asymptotic stronger convergence law of RQMC at point G eventually yields the best results. For points F and H at high and intermediate temperature respectively, the RQMC method behaves better than MC for every N. The dotted lines, obtained by fitting the points from $N = 10^4$ to $N = 10^6$, show that RQMC convergence rate scales as $N^{-0.725}$ for Point F, as $N^{-0.632}$ for G and as $N^{-0.813}$ for H. Also in this configuration, the magnitude of the RQMC exponent b remains higher than $b = 1/2$ for MC methods for the three investigated regions of the combustion chamber.

3.4.2 Controlled convergence tests

In Figs. 3.20, 3.21 and 3.22, the smallest RQMC error is obtained in points characterized by the highest temperature, A, D and F. Instead, the largest error is found in the Point B at intermediate temperature for Case 1 and in the colder regions of the domain, Points E and G, for Cases 2 and 3. Considering a uniform number of rays for each point is then not ideal as some locations can be regarded as too accurate while the error at others points can remain unsatisfactory and suffer from the retained number of realizations N. In practice, a variable field $N(x, y, z)$ is preferred to spatially control the accuracy of the result and yield a more efficient computation of the radiative fields on the whole domain for a given computational cost. MC and RQMC results are then compared in such a situation described by Test 2 in Tab. 3.1.
Figure 3.23 shows the field of the number of rays that are tracked independently at each point to perform controlled-convergence simulation using a MC (top) or RQMC (bottom) method for the channel flow application (Case 1). In MC simulations (on the top), it is possible to notice the presence of a region characterized by a large number of realizations that corresponds to the colder region of the channel. This is consistent with the previous observation in Fig. 3.20: convergence is more difficult to achieve in the lower part of the channel compared to the hotter parts of the configuration. As expected from the enhanced convergence rate of the RQMC method, simulations performed with RQMC (bottom) needs fewer rays compared to MC in order to achieve the fixed accuracy criteria. This is seen in all regions including where the converge is harder at the bottom of the channel. The reduced number of tracked rays leads to a lower computational time for the simulation, which is determined in the next section.
The same test is performed for Case 2 where, unlike Case 1, the composition is heterogeneous and the effect the soot particles on the radiative heat transfer is

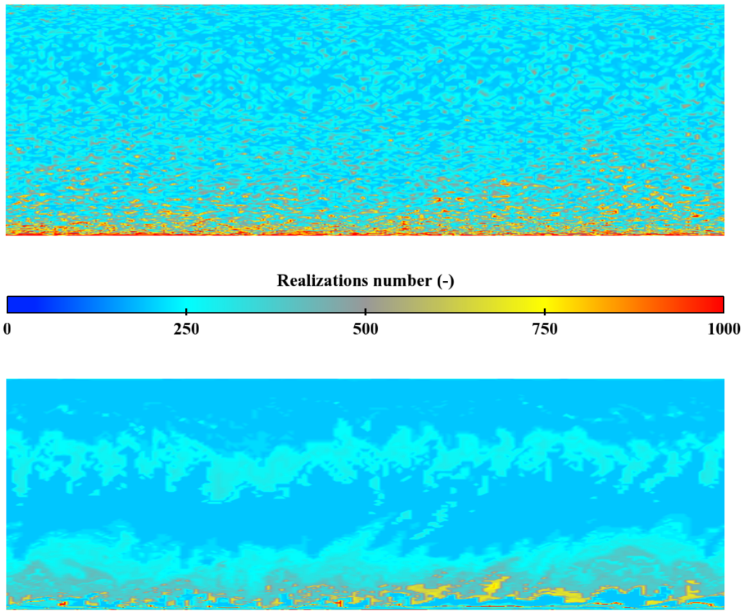

Figure 3.23: *Field of the required number of rays in controlled-convergence Test 2 with MC (top) and RQMC (bottom) for the channel flow configuration (Case 1).*

considered. MC and RQMC methods are compared in Fig. 3.24. In both cases, regions needing more realizations are the ones characterized by the presence of cooler pockets of burnt gases without soot. It clearly emerges that RQMC outperforms MC also in the second investigated configuration.
Case 3 represents a confined laboratory scale burner and accounts for heterogeneities of species and temperature fields but also for the presence of participating walls. Fig. 3.25 compares MC and RQMC methods: regions where a large number of rays is needed in order to achieve the convergence are the ones characterized by a strong gradient of temperature in the region between the burnt gases generated by the flame (dominated by emission) and these gases later trapped in the cold outer recirculation zone (dominated by absorption). The difficulty is associated to the small magnitude of the radiative power surrounded by positive and negative regions, making the fulfillment of the criterion on relative error hard. Nonetheless, the number of realizations is drastically reduced with RQMC in all regions.

3.4.3 CPU Efficiency of Monte Carlo and Randomized quasi-Monte Carlo methods

A more complete comparison can be done by evaluating the efficiency of both MC and RQMC methods. The MC efficiency is evaluated as a function of variance and computational time (Lemieux 2009). In the present analysis, the local efficiency η_i is computed from the variance associated to the point i,

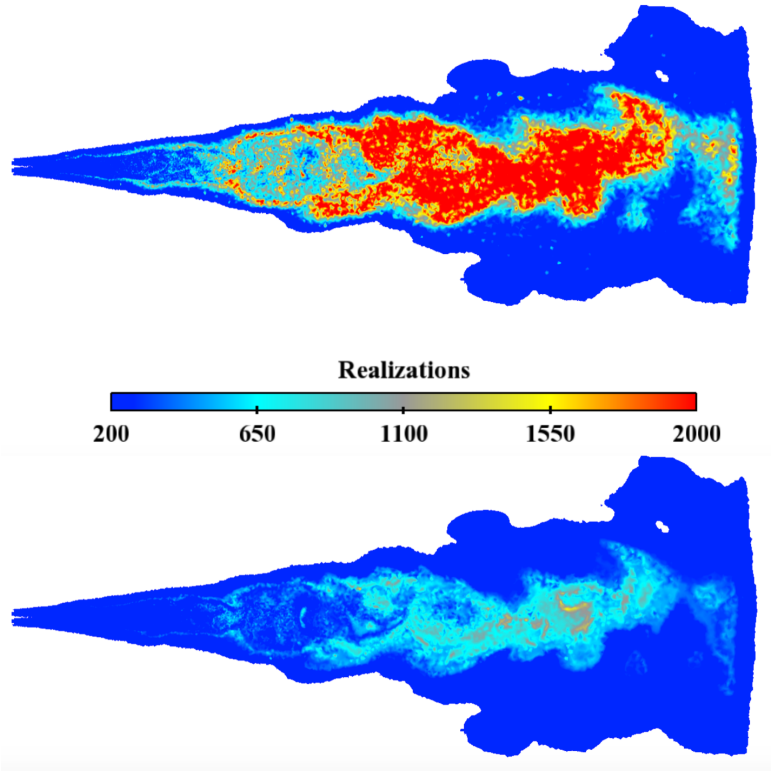

Figure 3.24: *Field of the required number of rays in controlled-convergence Test 2 with MC (top) and RQMC (bottom) in a sooted jet flame application (Case 2).*

$\sigma_i^2[Q(N)]$ computed from Eqs. (3.11) for MC and (3.14) for RQMC, and the local computational time, T_i^{CPU}. This last term is computed as the number of intersections that a ray traced from point i experiences along its optical path, $nb_{int,i}$, multiplied by the cost of one intersection, $T_{CPU}/nb_{int,tot}$:

$$\eta_i = \frac{1}{\sigma_i^2[Q(N)]\ T_i^{CPU}} \tag{3.27}$$

In Fig. 3.26, the ratio of the local efficiencies of RQMC and MC algorithms is shown on longitudinal planes of the three retained applications. For each configuration, almost the whole domain is characterized by an efficiency ratio larger than unity, meaning that the RQMC methods improve the computational efficiency by a factor that spatially varies in the domain and that may get values higher than 3.

In Case 1 (top), characterized by high pressure and homogeneous mixture, it can be observed that the improvement is significant close to the cold wall of the channel, where the convergence is harder to achieve, and on the region at intermediate temperature in the middle of the channel. In Cases 2 and 3, the improvement is obtained almost everywhere in the computational domain.

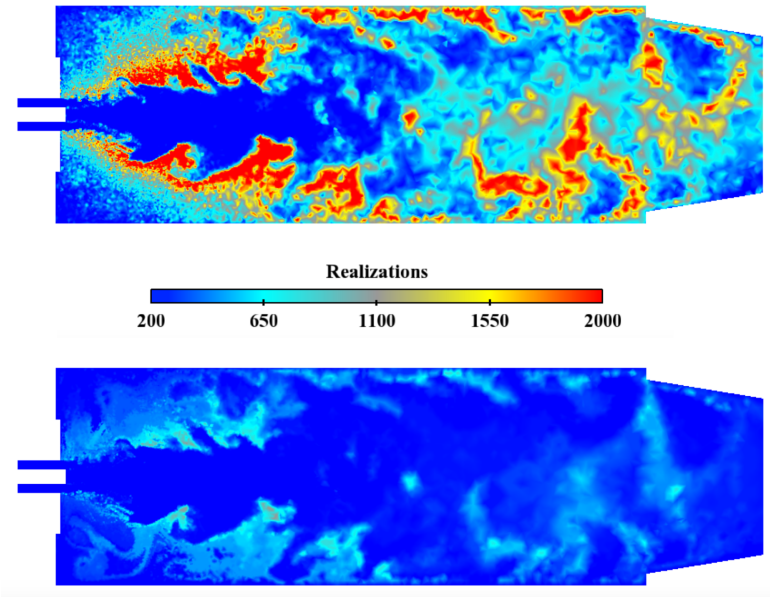

Figure 3.25: *Field of the required number of rays in controlled-convergence Test 2 with MC (top) and RQMC (bottom) for a combustion chamber (Case 3).*

Case	# mesh nodes	MC	RQMC
1	4 172 800	1 090Â s	467 s
2	964 163	653 s	363 s
3	1 241 299	3 080 s	1 238 s

Table 3.2: *Wall clock time in seconds needed for MC (3^{rd} column) and RQMC (4^{th} column) simulations (Test 2) for the retained configurations using 168 cores. The number of mesh nodes in each case is indicated in the second column*

It is straightforward to deduce that, for a fixed variance, the larger the efficiency is, the smaller the computational time will be. The computational time needed to perform each simulation in Test 2 is given in Tab. 3.2. In all the simulated cases, the use of RQMC allows to accelerate the computational time compared to MC simulations. The computation is sped up by a factor 2.3 for the channel flow application, 1.8 for the turbulent sooting jet flame and 2.5 for the combustion chamber.

3.4.4 RQMC combined with importance sampling

Previous results have shown that classical MC results can converge faster at different points depending on the corresponding intrinsic variance. Several strategies for variance reduction, such as importance sampling, are common to accelerate the convergence of Monte Carlo simulations. The RQMC results being sensitive to variance effects, it can also benefit from the same strategies

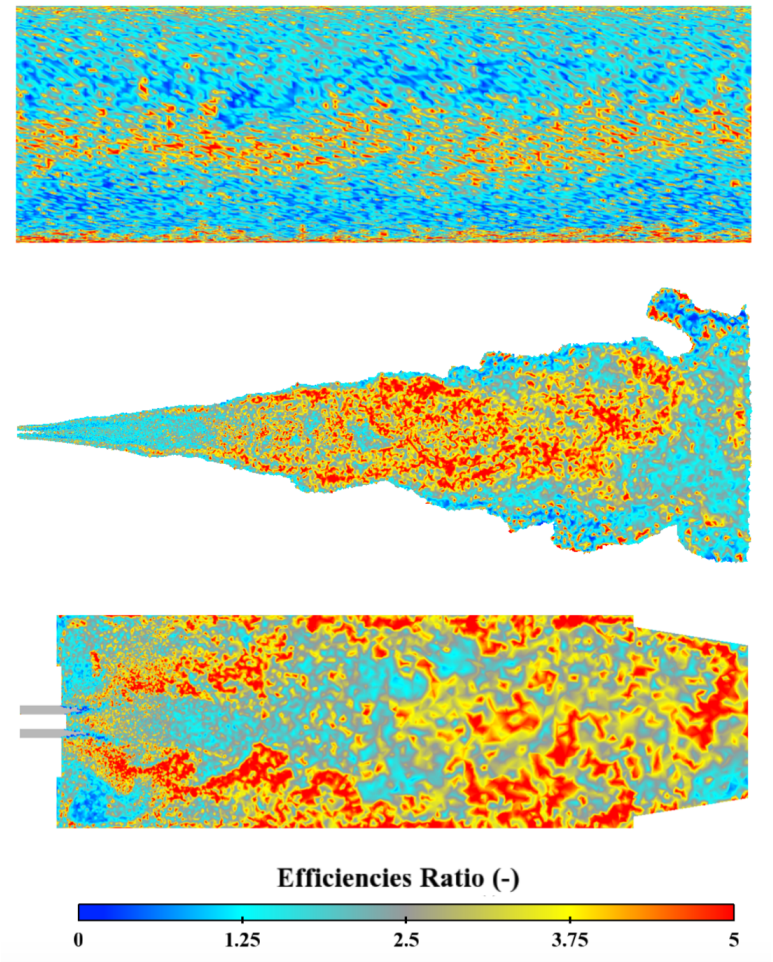

Figure 3.26: *2D map of the ratio between the efficiency of RQMC and the efficiency of MC methods for a channel flow application (top), a jet flame (middle) and a confined combustion chamber (bottom).*

derived for MC computations. In fact, the pseudo-random number generator or retained low-discrepancy sequence are set independently of any variance reduction technique. Quasi-Monte Carlo cubature and variance reduction can then be combined to achieve an even more efficient computation. This is here illustrated with the OERM method (Zhang et al. 2012) which is an importance sampling technique to improve the poor convergence of ERM in cold regions dominated by absorption.
The OERM method, shortly described in Sec. 3.2.2, consists in sampling the frequency according to the emission at the highest temperature of the computational domain. Both ERM and OERM are combined to MC and RQMC formalisms and the four corresponding combinations, MC-ERM, MC-OERM, RQMC-ERM and RQMC-OERM, are compared in the 1D test case studied in

Sec. 3.2.4, called *Case b*. The improvement of the convergence in cold regions is outlined by comparing the methods at a point close to the wall at the temperature $T = 550$ K. Figure 3.27 displays the relative error as a function of the number of realizations achieved by MC (circles) and RQMC (diamonds) when combined to ERM (blue) and OERM (red). Grey dashed lines highlight the convergence rate of MC: it can be seen that when MC is combined to OERM the line of slope $-1/2$ is shifted down because of the lower standard deviation obtained with OERM. Grey and black dotted lines instead represent the convergence rate of RQMC when combined with ERM and OERM, respectively. It is worth noticing the improvement accomplished by RQMC and OERM: the combination of RQMC and importance sampling technique shifts down the relative error obtained from RQMC-ERM, as also seen in MC results (dashed grey line), leading to the lowest error achievable among the four investigated combinations. The convergence rate of RQMC can then be indeed further accelerated when RQMC is combined to the OERM method.

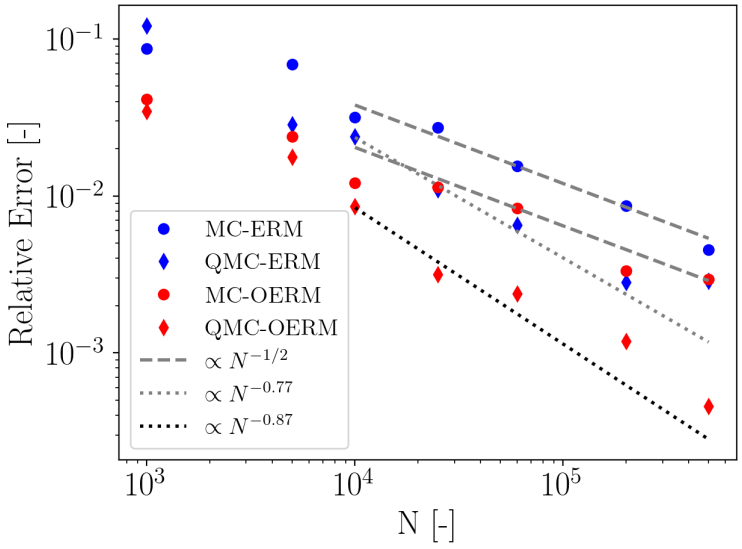

Figure 3.27: *Relative error as a function of the number of realizations N for a cold point close to the wall in the slab configuration achieved in MC (circles) and RQMC (diamonds) combined with ERM (blue) and OERM (red). Grey dashed line: convergence rate of MC. Grey dotted line: convergence rate of RQMC-ERM. Black dotted line: convergence rate of RQMC-OERM.*

3.5 Conclusion

Nowadays, coupled simulations involving combustion and radiative heat transfer are more and more used and targeted. Thanks to the increase in computing power and advances in numerical algorithms and solver scalability, the use of

accurate Monte Carlo methods in 3D unsteady simulations, such as Direct Numerical Simulations and Large Eddy Simulations, has become affordable. However, such coupled and multi-physics simulations remain very costly, and additional efforts are necessary to make MC methods more efficient. In this study, a technique to improve MC methods is investigated: Quasi-Monte Carlo method, where pseudo-random sequences of MC are replace by quasi-random sequences also known the low-discrepancy sequences. Sobol sequences are retained in this study. Their advantage lies in a higher convergence rate compared to MC methods, on the other hand their deterministic feature does not make possible to get an error estimation. Thus, a randomization of QMC (RQMC) is needed and among the existing randomization techniques, the one retained in this study is the *I-binomial scrambling*. The features of MC and RQMC methods are first shown on a 2-dimensional integration problem, highlighting the higher convergence rate of RQMC when compared to MC. The implementation of the RQMC method is then combined to the ERM formalism in the radiative heat transfer solver. After being validated on 1D test cases, it is applied successively to real applications of radiative heat transfer problems. Three configurations are retained, very different from each others: an academic test case of a channel flow at 40 bar, a non-confined turbulent sooting jet flame and a semi-industrial combustion chamber operating at atmospheric pressure. Simulations results show a significative improvement from RQMC compared to MC method in terms of computational efficiency, evenyually leading to a reduction of the computational time of a radiative heat transfer simulation of all the investigated cases by a factor that varies from 1.8 to 2.5, depending on the configuration. Convergence enhancement is due the stronger decay of the error with the number of realizations which overcomes the classical MC convergence law. Finally, RQMC is combined to a technique of importance sampling: it is shown that the efficiency of RQMC method can be further improved when RQMC is combined to a variance reduction technique, such as the OERM method considered here for illustration.

Chapter 4

Large Eddy Simulation of the OxyTec flame A: a CH4-Air premixed swirling flame

This chapter presents the large eddy simulation of the semi-industrial burner Oxytec, fed by a mixture of methane and air obtained thanks to a special axial-plus tangential swirler preceding the combustion chamber. First, a summary of the experimental studies carried out on the target applications is given and the experimental rig is presented, together with the measurements carried out by the experimental team. Then, the numerical set up of Large Eddy Simulation (LES) is presented. Results of a cold flow simulation are shown and characteristics typical of a swirled flow are retrieved. Finally, the reactive case is simulated, where the combustion is modeled through the Thickened Flame model for LES (TFLES). Measured temperatures are imposed on the walls surrounding the chamber.

Since the Oxytec chamber is characterized by a large residence time, the establishment of the steady flow is carefully assessed through the definition of convergence criteria.

Validations with experimental data are performed on flame and flow topologies, as well as quantitative comparisons of velocity fields, temperature measurements and wall fluxes. A good agreement is globally found for both non-reacting and reacting flow. Small discrepancies in comparison are attributed to the neglect of radiative transfer which is tackled later in this study.

Contents

4.1 Introduction

Oxytec is a project supported by the ANR (ANR-CHIN-01-2012) dedicated to OXY-combustion and heat transfers for the new energy TEChnologies, with the cooperation of Air Liquide, CentraleSupélec and CNRS. The goal is to improve and disseminate the knowledge about one of the new combustion technologies, the oxy-combustion, in operating conditions close to those ones of the industrial applications.
In this context, an experimental device has been developed at the EM2C laboratory: the Oxytec chamber. The reason for which this chamber has been targeted is the possibility to investigate two interesting swirl-stabilized premixed flames, a methane-air flame and a CO_2-diluted oxy-methane flame, which are different in composition but which finally share a lot of common features, such as flame topology, adiabatic temperature and heat fluxes through the walls. The characteristics of the two configurations, like equivalence ratio, ϕ, adiabatic flame temperature T_{ad}, laminar flame speed S_L, molar fraction of diluent X_d, bulk velocity u_b, Reynolds number Re, Swirl number S_0 and thermal power P_{th}, are given in Tab. 4.1.

Flame	ϕ	T_{ad} [K]	S_L [m/s]	X_d	u_b [m/s]	Re	S_0	$P_{th}[kW]$
A	0.95	2195	0.36	0.79	14.3	18000	0.85	14.5
B	0.95	2192	0.21	0.68	9.7	20500	0.75	14.5

Table 4.1: *Characteristics of the investigated flames.*

The high CO_2 dilution of Flame B makes this configuration very interesting to study in the context of radiative heat transfer: the high CO_2 concentration in burnt gases is expected to enhance the radiative power. However, a recent analysis of experimental results carried out by Degenève et al. (2019a) shows that Flame A and B surprisingly also share the approximatively same total wall heat flux distribution. Coupled simulations of both flames should eventually explain this phenomenon. The configuration retained in this chapter is the methane air flame (Flame A) characterized by an equivalence ratio $\phi = 0.95$, a Swirl number $S_0 = 0.85$, a Reynolds at the injection $Re = 18\ 000$ and a cup angle $\alpha = 10°$.
The peculiarity of the Oxytec chamber is its large residence time, partially due to its big volume. This feature leads to long convergence time and consequently to a very high computational cost. This is the main reason for which only converged results of LES simulations of Flame A are presented.
The first numerical results of the Oxytec chamber are thus presented in this chapter: the LES formalism is applied to the simulation of the premixed methane-air flame in order to retrieve the experimental data on flame topology, flame front position, temperature and conductive fluxes.

The chapter is organized as follows: the first part is dedicated to the description of the experimental test rig and its operating conditions and to the illustration of the available measurements. The second part is dedicated to the numerical simulations of the Oxytec chamber, in non-reacting and reacting flow configurations. An air flow simulation is first performed in order to validate the sub-grid model and computational grid, followed by an analysis about the characteristics of the swirled flow. Then a simulation of the methane-air flame is performed without accounting for thermal radiation. An analysis is conducted to understand the characteristics of the reacting flow such as the flame topology and the effect of the wall heat losses, and a comparison with experimental data is shown in order to validate the study.

4.2 Presentation of the Oxytec chamber

4.2.1 Experimental test rig

The Oxytec chamber is shown in Fig. 4.1. The combustion chamber operates at atmospheric pressure and is a parallelepiped characterized by a cross section of *150 mm* × *150 mm* and *250 mm* height. The base of the chamber is made

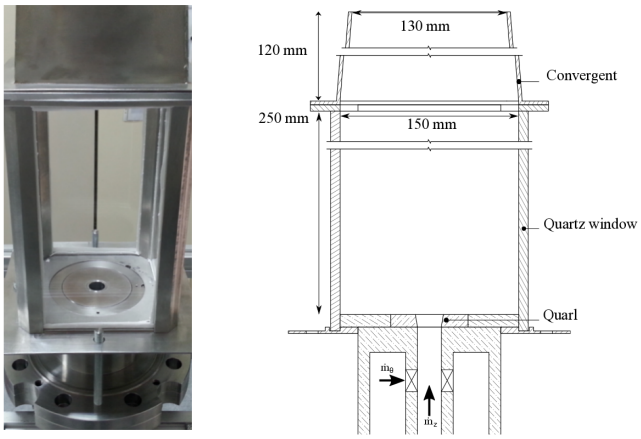

Figure 4.1: *Photograph (left) and scheme of an axial cut (right) of the experimental burner Oxytec.*

of stainless steel 316L and four windows in fused silica, 8 mm thick, surround the chamber allowing optical access to the flame region. At the corners, four stainless steel bars hold the quartz windows. A stainless steel convergent of 120-mm height is installed on the top of the chamber to fix the recirculation zones of the flow inside the combustion chamber and evacuate the burnt gases preventing air back-flow from the atmosphere. A 15-mm thick bar has been inserted between the quartz windows and the convergent. This modification has been included in the computational geometry presented later.

The stainless steel injector feeding the chamber comprises an axial-plus-tangential swirler (see Fig. 4.2): reactants are injected both axially and tangentially. The tangential flow rate is injected into a plenum and then arrives in two tangential slits linking the plenum with the axial injector. Another injection is realized, for gaseous fuel, at the slits through three small circular holes (2 mm diameter) distributed over the slit height. The axial flow rate enters a 350 mm long axial injector characterized by a 20 mm diameter. The reactants that are injected axially and tangentially are then premixed by the swirler before entering the combustion chamber. At the end of the axial injector a divergent of 10 mm height is added to facilitate the flame stabilization. Among the several values of the quarl angle α experimentally tested, a value of α =10° is retained in the studied configuration.

The axial-plus-tangential injector is a very interesting configuration since it allows to continuously vary the Swirl number, and consequently the swirl velocity imparted to the flow exiting the burner, playing on axial and tangential mass flow rates.

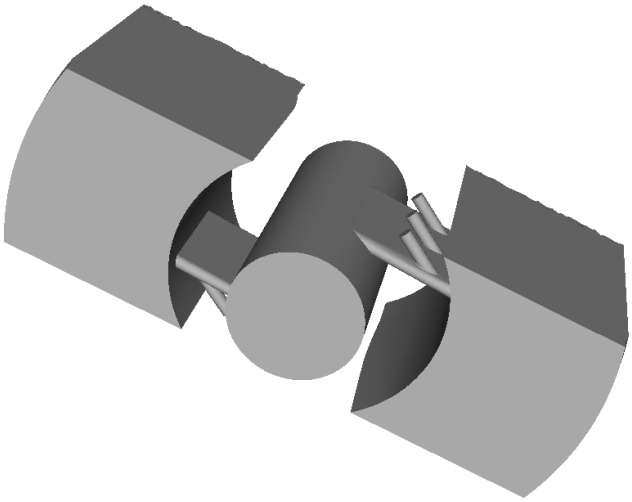

Figure 4.2: *Sketch of the axial-plus-tangential swirler of the Oxytec burner.*

4.2.2 Measurements and experimental investigations

First development and results on the experimental level have been carried out during the PhD thesis of Paul Jourdaine (Jourdaine 2017); experimental measurements such as Laser Induced Fluorescence on the hydroxyl radical (OH-PLIF), Particle Imaging Velocimetry (PIV), Laser Doppler Velocimetry (LDV) completed by chemiluminescence imaging and thermocouples have been performed and have allowed to elucidate the stabilization mechanisms of the investigated flames. The impact of several parameter, like the swirl number, the bulk injection velocity, the injector cup angle and the laminar flame velocity on the flame stabilization can be found in Jourdaine et al. (2018) and Jourdaine et al. (2017). These studies have shown the possibility to aerodynamically stabilize the flame thanks to a flow topology typical of swirled flows. In particular, it has been shown that swirl numbers S_0 ranging between 0.7 and 0.9, an injection Reynolds number $Re = 18\,000$ and an equivalence ratio $\phi = 0.95$ allow to aerodynamically stabilize the CH_4/Air flames in a V-shape close to the burner outlet.
The flame stabilisation strongly depends on the establishment of an internal recirculation zone (IRZ). It has been observed that stable IRZ are found from $S_0 > 0.8$, and results on axial velocity fields from Jourdaine et al. (2018) are shown in Fig. 4.3.

Another parameter having a strong impact on the flame stabilization is the injector cup angle α: the opening angle of the diffusor at the burner exit. The impact of such a parameter on the flame stabilization has been studied in Jourdaine et al. (2016) and it is shown in Fig. 4.4: for smaller cup angles,

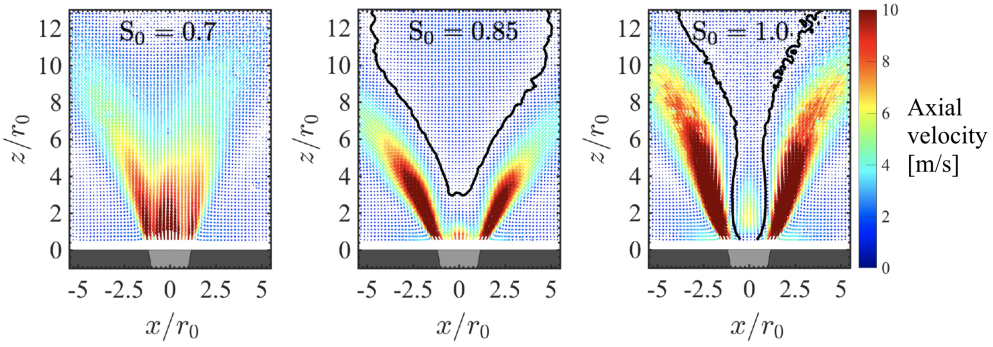

Figure 4.3: *Velocity field in reacting conditions measured in a longitudinal plane of the chamber, obtained for three different swirl numbers S_0 (0.7, 0.85 and 1.0) . Black lines delineate the position of the inner recirculation zone, where the axial velocity is zero. Source: Jourdaine et al. (2017)*

$\alpha <$ 10°, the IRZ is far from the injector but the flame is difficult to stabilize. For $\alpha >$ 30°, the flame takes a torus shape and leads to too high thermal stress on the dump plane of the combustion chamber.

Subsequent experimental studies on the Oxytec rig have been conducted by

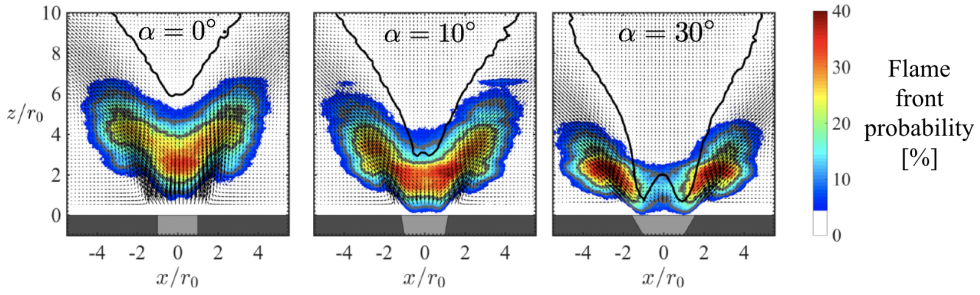

Figure 4.4: *Probability of presence of the flame front in an axial plan. Grey line delineates the position where the flame front is present 20% and 10% of the time, while black line the position of the inner recirculation zone. ϕ= 0.95, S_0 = 0.85, Re = 18 000.*

Degenève et al. (2019a): a Laser Induced Phosphorescence (LIP) has allowed to determine the temperature distribution on solid walls in both the investigated cases (CH_4/Air and CO_2-diluted flames). Moreover, temperatures measured on internal and external quartz have been used to derive the conductive flux through the quartz windows of the chamber.
All the experimental data gathered during the experimental campaigns have been used to validate the simulations performed in the present thesis work, which provides the first numerical studies of the Oxytec chamber.

The experimental results used to validate the simulations come from a set of

diagnostics, most of which are optical, that have allowed to experimentally investigate aerodynamic flow and flame characteristics. Such methods are briefly summarized here; however a more detailed description of the equipment used in the experimental campaign can be found in Jourdaine (2017).

- Flame position and heat release have been experimentally determined with mesures of chemiluminescence.
- Planar Laser Induced Fluorescence of OH radicals (OH-PLIF) measurements have been carried out to identify mean and instantaneous position of flame front and brunt gases on longitudinal sections of the combustion chamber.
- Mean and instantaneous gas velocities have been measured in both non-reacting and reacting flow through Particle Image Velocimetry (PIV).
- Burnt gases temperature are measured through thermocouples positioned inside the combustion chamber (precisely in the inner and outer recirculation zones and near the exhaust outlet) as well as within the metallic bars surrounding the burner.
- In addition, Laser Induced Phosphorescence (LIP) measurements have been used to determine the temperature distributions along the internal and external surfaces of quartz windows, dump plate and convergent. Fig. 4.5 displays the temperature distribution along axial and transverse directions on the walls where measurements are carried out.

The position of thermocouples as well as the cross and longitudinal planes of PIV and OH-PLIF measurements are shown in Fig. 4.6.

4.3 LES of non-reacting flow

In this chapter two cases are presented: the non-reacting and reacting simulations of the flame A. Common features of numerical set up and mesh used for the computations are summarized in the following.

4.3.1 Computational domain and mesh

The numerical domain is identical to the experimental one: it includes both the combustion chamber and the axial-plus-tangential swirler injector. The plenum for tangential inlet is entirely included in the computational geometry, as well as the axial injection, while the tangential injection in the slits (observable in Fig. 4.2) is done through 6 guides (3 per side) of a 2 mm diameter. Including the swirler in the computation avoids to impose velocity profiles at the swirler exit which are not known, since measurements are available at some millimeters after the burner exit.

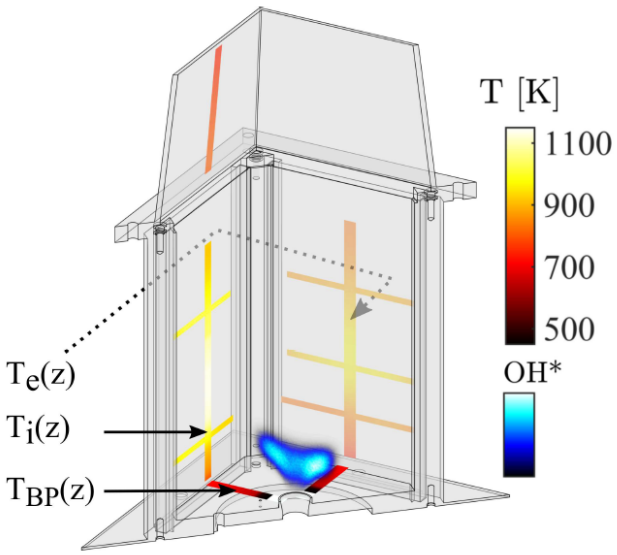

Figure 4.5: *Cut of the Oxytec chamber with the temperature profiles extracted from LIP measurements. $T_e(z)$ and $T_i(z)$ correspond respectively to external and internal temperatures of the quartz windows, while $T_{BP(z)}$ is the temperature of the dump plate: extracted from Degenève et al. (2019a).*

The computational mesh is an unstructured grid composed by 51.5 million tetrahedral cells and 9 million nodes. It is displayed in Fig. 4.7. Because of small injection diameters and thin slits width, a refinement (0.2 mm cell size) is required in some parts inside the injector.
The mesh refinement is also applied on the inlet of the chamber: the cell size is 0.5 mm in the flame region in order to capture the flame dynamics. The mesh linearly coarsen approaching to the walls, where cell size becomes 1 mm. The grid is progressively coarsened up towards the top of the chamber where the cell size is around 4 mm. A large atmosphere is added at the exhaust outlet.
The same computational domain is used for non-reacting and reacting simulations presented in the following sections.

Simulations of reacting and non-reacting flow are carried out with the AVBP (Schoenfeld 2008) code, jointly developed by Cerfacs and IFPEN, which solves the three-dimensional Navier-Stokes equations for reactive and compressible flows on structured and unstructured computational grids. The software is based on a two-step Taylor-Galerkin weighted residual central distribution scheme (TTGC) (Colin and Rudgyard 2000), third order in time and space. The subgrid scale turbulence is described with the Sigma model (Nicoud et al. 2011) in order to correctly access the subgrid stresses in such swirled flow.

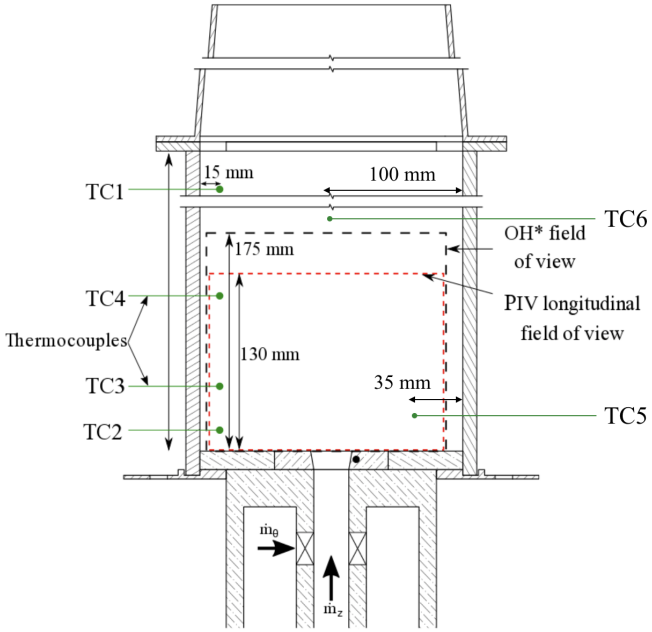

Figure 4.6: *Sketch of the combustion chamber indicating the position of thermocouples along with PIV and OH* fields of view.*

4.3.2 Numerical set up

In a first step, Large Eddy Simulations of the turbulent non-reacting flow of the configuration A are carried out. The numerical setup retained for this simulation and a comparison of numerical results with experimental data are presented in the following.

In the cold flow simulation, only air is injected in the burner at atmospheric pressure and 300 K, with a mass flowrate of 0.0055 kg/s and a bulk velocity in the injection tube of 14.3 m/s. The bulk Reynolds number Re_b based on the axial injector diameter ($D_0 = 20\ mm$) is 18 000. At the end of the injector a divergent 1 cm long is applied and the flow exists the swirler through a diameter of $D = 23\ mm$ with a swirl number $S_0 = 0.85$ defined as:

$$S_0 = \frac{1}{R_{ref}} \frac{\int_r u_x u_\theta r^2 dr}{\int_r u_x^2 r dr} \tag{4.1}$$

where R_{ref} is a characteristic radius chosen as the radius of the injector $r_0 = D_0/2 = 10\ mm$ without accounting for the divergent, while u_x and u_θ are respectively the axial and tangential component of velocity.

The boundary conditions are standard Navier-Stokes characteristic boundary conditions (NSCBC, Poinsot and Lelef (1992)) and are set according to the ex-

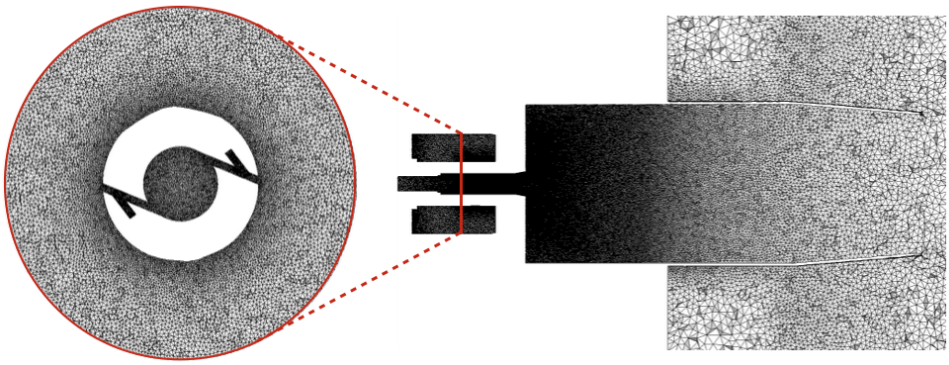

Figure 4.7: *Visualization of the numerical domain through a 2D cut of the numerical domain on a cross section of the injector (left) and on a longitudinal plane of the chamber (right).*

Boundary Condition	Physical variables	Relax coefficients
Air Inlet	$\dot{m} = 0.0055\ kg.s^{-1}$ $T = 300$ K $Y_{O_2} = 0.233$ $Y_{N_2} = 0.767$	50 000 s^{-1}
Atmo Inlet	$\dot{m} = 0.1\ kg.s^{-1}$ T = 300 K $Y_{O_2} = 0.233$ $Y_{N_2} = 0.767$	50 000 s^{-1}
Outlet	$P = 101325$ Pa	500 s^{-1}
Walls	Adiabatic wall law	-

Table 4.2: *NSCBC conditions imposed on the boundary in the cold flow simulation.*

perimental input data. Tab. 4.2 summarizes the boundary conditions imposed for the cold flow simulation.
The flow through time t_f, calculated as the ratio of the length of the combustion chamber (37 cm) to the bulk velocity (14.3 m/s), is 26 ms. In order to statistically converge the cold flow simulation a transient time of $10 \times t_f$ ms is simulated to establish the velocity fields; successively an additional averaging time of $8 \times t_f$ is run in order to compute the statistical mean fields. The computational cost for such a simulation is 247 000 CPUh on Intel E5-2690V3 cores.

4.3.3 Results

Large Eddy Simulations of the non-reacting flow are carried out in order to validate the numerical tools used in this thesis work; moreover they also represent an opportunity to analyse the characteristics of the investigated swirling flow.

Particle Image Velocimetry (PIV) data and LES results are compared and they are used to conduct the analysis.
The instantaneous (top) and mean (bottom) fields of the axial velocity for the simulation of the non-reacting flow are shown on a longitudinal plane passing through the burner axis in Fig. 4.8. Characteristics typical of a swirling flow are retrieved, like the presence of two kind of recirculation zones: the inner recirculation zone (IRZ) in proximity of the axis chamber, and the outer recirculation zone (ORZ), created by the gas recirculation and located in the bottom corners between the combustor lateral walls and the chamber bottom.
Moreover, the flow exhibits three regions with high axial velocities: the first one is located along the center axis of the chamber, while the other two, characterized by the highest velocities, are located along two side branches. The presence of the central peak of axial velocity is a typical characteristic of the axial-plus-tangential-swirl generator and is due to the axial flow rate contribution. This local maximum affects the position of the IRZ which appears downstream unlike the classical swirl generators, but also the intensity of the recirculation. The two lateral maxima, instead, are mainly due to the azimutal component of the flow.
It is possible noticing that the angle of the lateral branches is very close to the angle of the injector cup outlet α, meaning that the divergent added at the end of the injector determines the jet spreading of the flow inside the chamber.

The investigated flow is characterized by a swirl number equal to 0.85. This value is sufficiently high to generate a phenomenon that usually occurs in swirling flow and that remains controversial since no generally accepted explanation has emerged (Lucca-Negro and O'doherty 2001): the vortex breakdown. Among the theories proposed to explain the structure of the vortex breakdown, the flow-stagnation concept considers the vortex breakdown as a disturbance promoted by adverse pressure gradients (Sarpkaya 1974), i.e. a pressure increasing in the direction of flow, that in this configuration is impressed upon the vortex core by a deceleration of the outer flow due to the 10° divergent added to the axial injector. Further analysis about the impact of the pressure gradient, induced by the diverging cup, on the stabilization of the swirling flow taking place in the Oxytec chamber is carried out by Degenève et al. (2019b). Figure 4.9 (left) shows the mean pressure field extracted from LES, revealing a low pressure region along the central axis, originated from the balance between the radial pressure gradient and the centrifugal forces associated to the large swirl velocities occurring especially at the swirler exit:

$$\frac{\partial P}{\partial r} = \rho \frac{w^2}{r} \tag{4.2}$$

where w is the azimuthal velocity and r the radial position.

Plotting the pressure as a function of the radius for different heights along the chamber (see plot on the right side in Fig. 4.9), it is possible to see that there is an intense radial pressure gradient in proximity of the swirler exit that

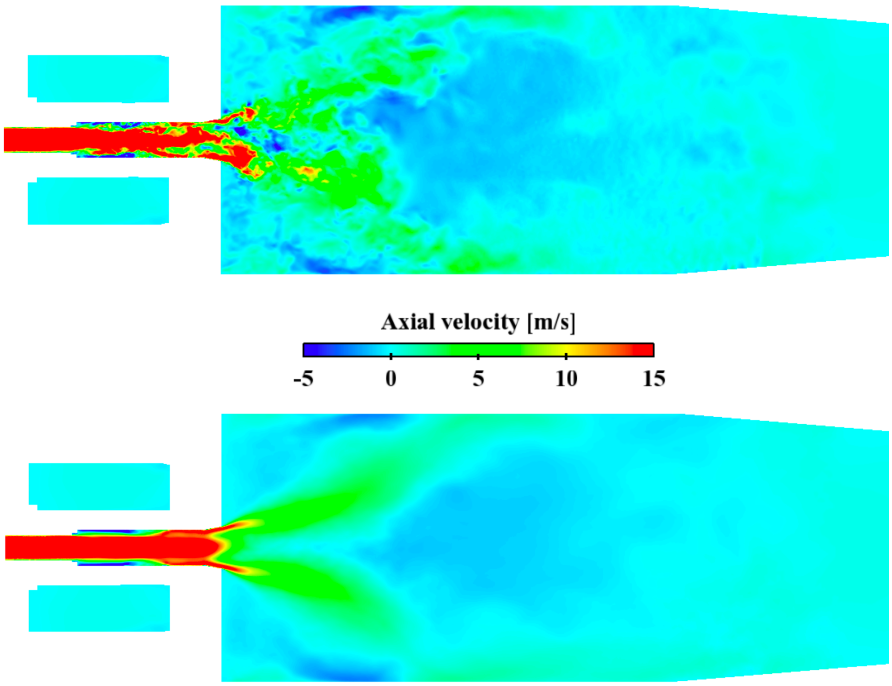

Figure 4.8: *Instantaneous (top) and average (bottom) fields of the axial velocity for the non-reacting flow simulation.*

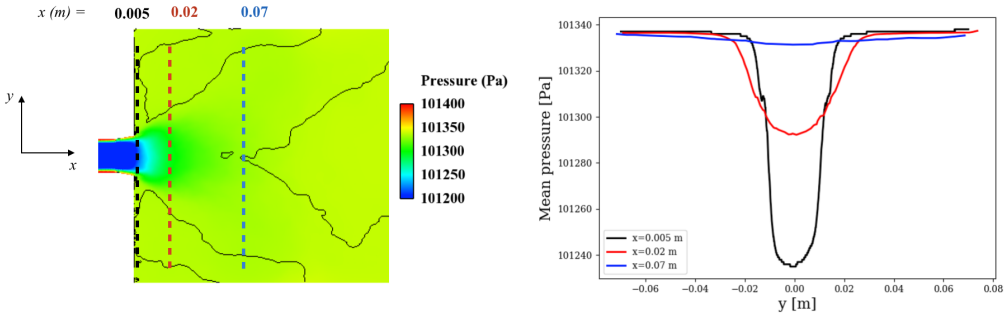

Figure 4.9: *2D field of mean pressure taken from LES with iso-contours of axial velocity equal to zero (black lines) (left) and plot of mean pressure along the y-axis for different heights along the chamber axis (right).*

vanishes downstream in the chamber.
Swirl is also responsible for axial pressure gradients (Lucca-Negro and O'doherty 2001). The azimuthal velocity is plotted against the y-axis for several heights along the burner in Fig. 4.10 (left). It can be seen that w decreases in the streamwise direction. On the right of Fig. 4.10, the mean pressure against the chamber axis is displayed, highlighting the presence of a positive pressure gra-

dient also in the axial direction.

Axial and radial pressure gradients occurring in the flow lead to the formation

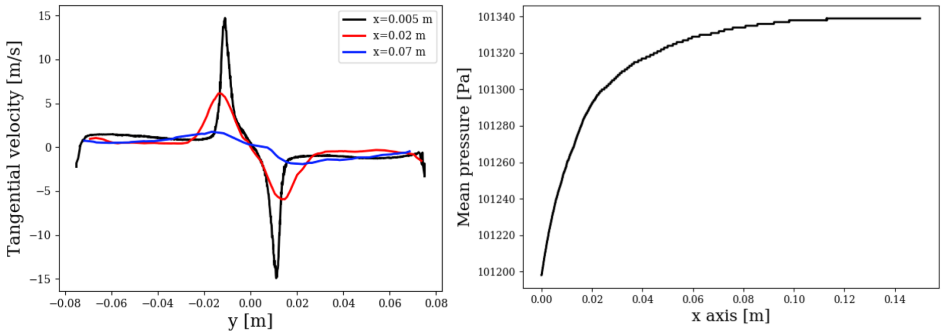

Figure 4.10: *Plots of mean tangential velocity along the y-axis for different heights along the chamber axis (left) and mean pressure along the chamber axis (right) .*

of an internal stagnation point on the vortex axis, followed by reversed flow, the inner recirculation zone (IRC), which is a typical characteristic of a swirled flow.

Another feature of swirling flows is the Precessing Vortex Core (PVC) that LES are able to predict as it is evidenced in Fig. 4.11 through an iso-surface of pressure at P = 101100 Pa.

A feature of confined flow characterized by high Swirl number, like the one

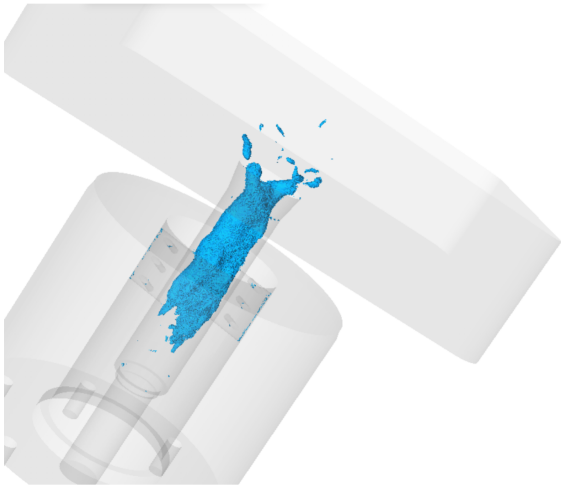

Figure 4.11: *Visualization of the precessing vortex core (PVC) in an instantaneous solution through an iso-surface of pressure at P = 101100 Pa.*

studied in this work, is the presence of an outer or corner recirculation zone (ORZ) due to the fact that the fluid impinging the lateral walls of the chamber recirculates back to the dump plate. Both inner and outer recirculation zones

can be appreciated through vector arrows of velocity vector on a longitudinal plane of the chamber displayed in Fig. 4.12.

The results of LES simulation are finally compared with the Particle Imag-

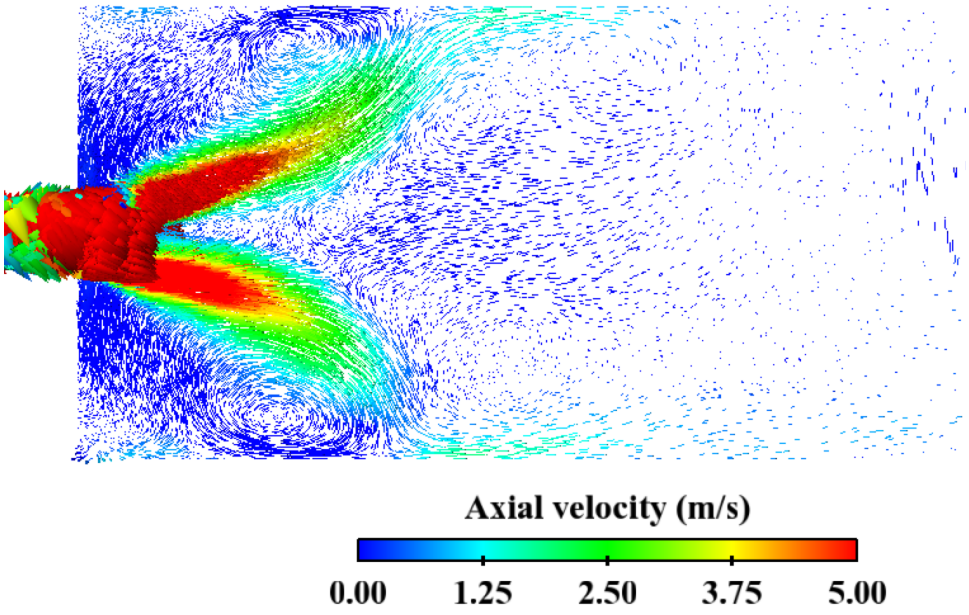

Figure 4.12: *Vector arrows of velocity vector colored by axial velocity.*

ing Velocimetry (PIV) measurements taken from Jourdaine et al. (2018). Figure 4.13 displays mean and RMS of axial, radial and tangential velocity profiles at a height of 10 mm from the injector exit.

Looking at the axial velocity profiles (on the top), one can clearly identify three velocity peaks which form a W-shape profile. A typical tangential velocity profile formed from a swirl generator (Sloan et al. 1986) can be seen in Fig. 4.13 (bottom). This is a combination of a forced and a free vortex distribution also known as Rankine vortex. The flow exhibits a substantial swirl at a given radius close to the burner axis.The region where the gas flows at high rotational speed is called forced vortex region. In this region, all fluid particles rotate at a constant angular velocity as a solid body, for this reason the forced vortex is also called solid body rotation. In this region the tangential velocity profile is proportional to the radius: it increases sharply as the radius increases.The fluid loses its swirl while flowing away from the axis and its tangential velocity becomes inversely proportional to the radius; this region is called free vortex region.

The mean radial velocity profile shows the presence of two peaks (one positive and one negative) as the tangential component but with more moderate values. The same comparisons are carried out at a height of 20 and 30 mm from the

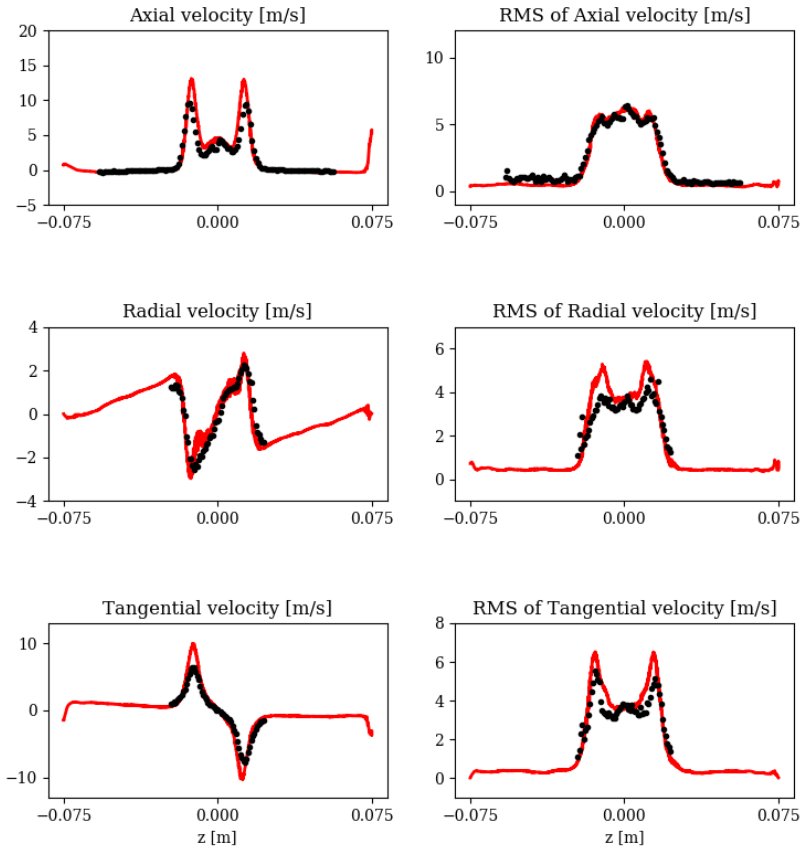

Figure 4.13: *Profiles of mean (left) and RMS (right) velocity at $x = 1$ cm from the injector outlet: axial (top), radial (middle) and tangential (bottom) component.* —*-: Numerical results;* • *: Experimental data.*

swirler exit and it is represented in Figs. 4.14 and. 4.15 respectively. From Figs.4.13, 4.14 and 4.15 it can be seen that the distance between the peaks increases moving along the burner axis, while their absolute value decrease.

Axial velocity profiles for different heights along the burner, 10, 30 and 50 mm, are displayed in Fig. 4.16. Both experimental data and LES results show a very similar trend: at the swirler exit, the distance between the lateral peaks of velocity is very small. Moving far from injector, the central local maximum decreases until becoming the absolute minimum, and this correspond to the position of the stagnation point and consequently to the installation of the IRZ. Moreover, moving along the burner axis, as expected, the lateral peaks

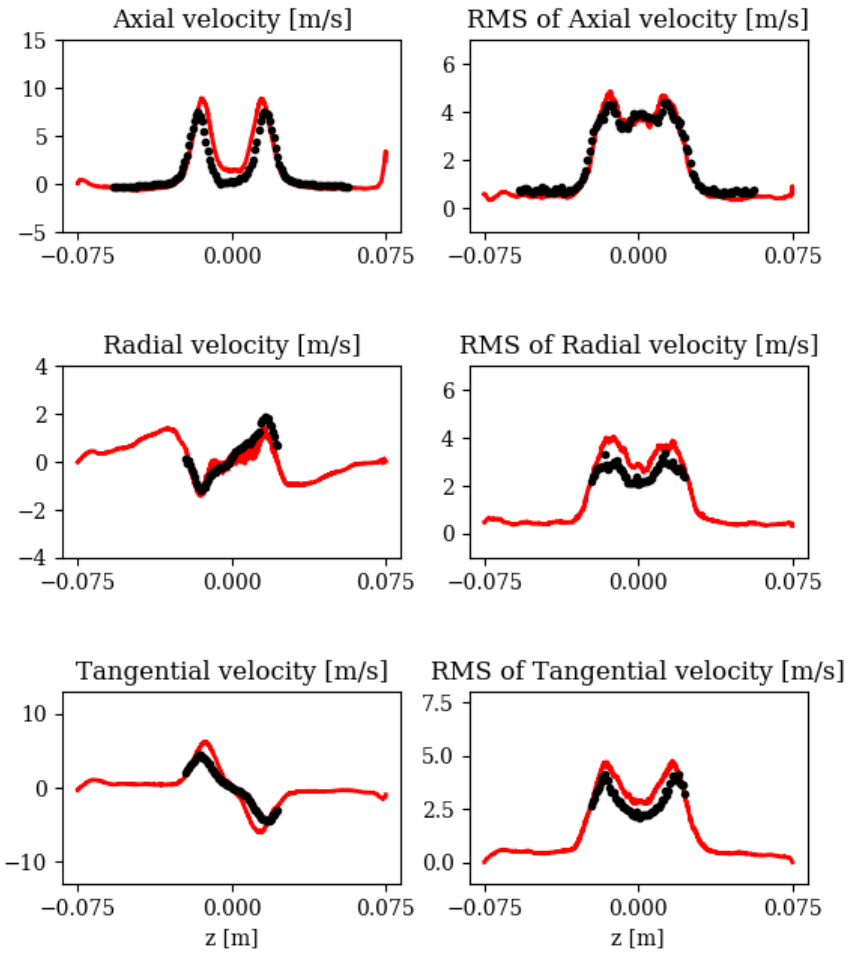

Figure 4.14: *Profiles of mean (left) and RMS (right) velocity at x = 2 cm from the injector outlet: axial (top), radial (middle) and tangential (bottom) component. –-: Numerical results; • : Experimental data.*

decrease and distance between them increase, meaning that the diameter of the IRZ increases.

If the trend of LES and experimental axial velocities along the chamber axis is very similar, a disagreement can be noticed: LES results reveal that the stagnation point is located at x = 5 cm, while in PIV measurements it appears at a height of x = 3 cm. Moreover, still from Fig. 4.16, it appears that the axial velocity predicted by LES is slightly overestimated and that the jet appears more closed compared to experiments. The reason of such a mismatch is not clear; however in order to account for the uncertainty of experimental data,

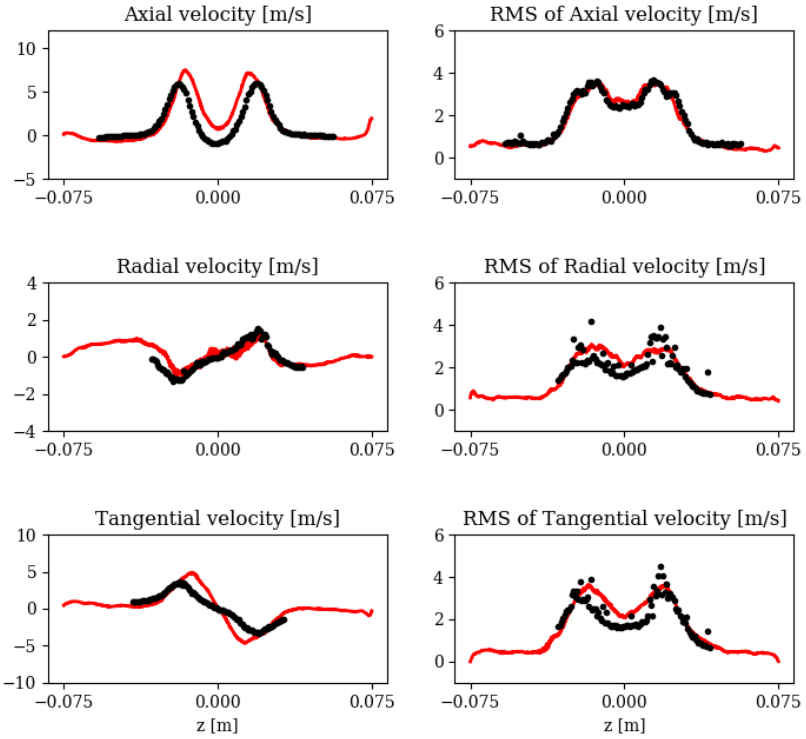

Figure 4.15: *Profiles of mean (left) and RMS (right) velocity at x = 3 cm from the injector outlet: axial (top), radial (middle) and tangential (bottom) component.* –-*: Numerical results;* • *: Experimental data.*

LES results have also been compared to Laser Doppler Velocimetry (LDV) data available at x = 5 mm and such a comparison is shown in Fig. 4.17. It emerges that LDV data and PIV data are in perfect agreement on the jet opening angle, however the measured values on the three velocity peaks are different: LDV maximum values of axial velocity are higher than PIV ones and it can be seen that the two lateral peaks given by LDV data are closer to LES results compared to the PIV. Recording the peak of velocities with a fine resolution remains experimentally challenging and this may contribute to explain the discrepancies between PIV and LDV measurements. However, LDV is known to be more spatially resolved than PIV up to 0.5 mm. LDV measurements are therefore chosen to be compared to numerical predictions when they are available. The limit of the PIV about peak velocities could be the reason of the discrepancy between the maximum values of axial velocity predicted by PIV and numerical predictions.

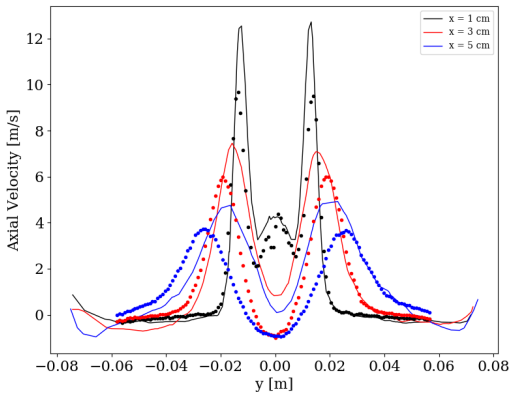

Figure 4.16: *Plot of mean axial velocity along the y-axis for different heights along the chamber axis for the non-reacting flow simulation. Solid lines are numerical results; dots are experimental data*

Globally, it can be concluded that the simulation is able to retrieve the main features of the swirling flow both at the chamber inlet and further down the flow. However, a discrepancy is found about the position of the stagnation point. The three velocity components profiles show a very good prediction of spreading angle of the swirling jet. Finally, the turbulence levels are very well predicted (see RMS profiles on the right side of Figs. 4.13 , 4.14 and 4.15).

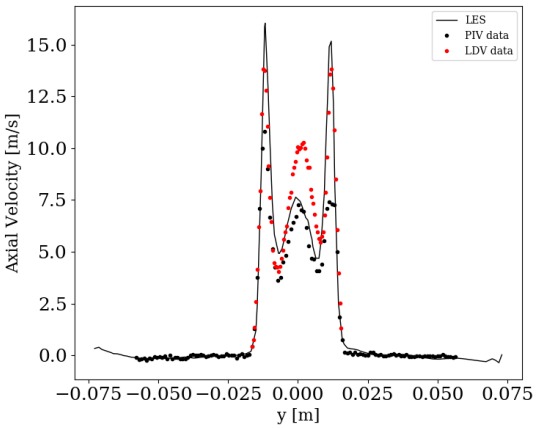

Figure 4.17: *Profiles of mean velocity at $x = 5$ mm from the injector outlet: —: Numerical results; • : PIV data; • : LDV data.*

The globally good agreement between numerical results and experimental data allows to validate the computational grid and the sub-grid model used in the cold flow simulations, and these are retained for the reacting flow simulation

presented in the next section.

4.4 Numerical set up of reactive LES and thermal transient

4.4.1 Numerical set-up

The combustion model used in LES of reacting flow to describe the flame structures in the unresolved smallest scales, the flame propagation and the flame-turbulence interaction is the Thickened Flame scheme (TFLES, Colin et al. (2000)).

The thickened flame model for LES

The need of combustion modeling comes from the observation that the reactive thickness of a flame front is of the order of magnitude of $10^{-5}-10^{-4}$ m, whereas the typical size of a LES grid cell can range between 0.1 and a few millimeters. For this reason, solving the flame front on the LES grid is not possible and a model is needed. Moreover, in presence of turbulent flows, some coupling mechanisms take place and turbulence and combustion interact with each other, and their interactions have to be taken into account in the combustion model. Among the existing modeling approaches, a premixed combustion model, the Thickened Flame model for LES, is used in this study. The concept of this model, which was first proposed by Butler and O'rourke (1977), is to thicken the flame front for it to be resolved on the LES computational mesh. A thickened flame can be obtained by applying a thickening factor F to some relevant quantities; however this operation must ensure that the laminar flame speed is not modified.
In a premixed flame the following expressions for the laminar flame speed S_L° and the laminar flame thickness δ_L° are verified:

$$S_L^\circ \propto \sqrt{D_{th}A} \qquad \delta_L^\circ \propto \frac{D_{th}}{S_L^\circ} = \sqrt{\frac{D_{th}}{A}} \tag{4.3}$$

where D_{th} is the thermal diffusivity and A the pre-exponential constant in the Arrhenius law for a single-step chemistry.
According to Eq. (4.3), keeping the correct laminar flame speed while increasing the flame thickness is possible if the diffusivity is multiplied by a factor F and the Arrhenius constant is divided by the same factor. The thickened flame, characterized by a thickness $\delta_L^1 = F\delta_L^\circ$ can then be solved on the LES grid.
The species mass fraction transport equation, Eq. (1.23), is then modified multiplying the species diffusion flux, $J_{k,i}$, by F and dividing the chemical source term by the same factor:

$$\frac{\partial \rho Y_k}{\partial t} + \frac{\partial}{\partial x_i}(\rho Y_k u_i) = -\frac{\partial}{\partial x_i}(F J_{k,i}) + \frac{\dot{\omega}_k}{F} \tag{4.4}$$

And the same modification is applied to the energy equation (Eq. (1.25)).

However, in turbulent combustion, two-way interactions are present between the flame and the turbulent structures. With the flame thickening, the flame wrinkling is lost: the flame surface and the reactants consumption rates become smaller.
In order to account for the subgrid scale wrinkling factor, Colin et al. (2000) introduced an efficiency function E in the conservation equations. The filtered equation for species mass fraction, Eq. (1.30), writes:

$$\frac{\partial \overline{\rho}\widetilde{Y_k}}{\partial t} + \frac{\partial}{\partial x_i}(\overline{\rho}\widetilde{Y_k}\widetilde{u_i}) = -\frac{\partial}{\partial x_i}(\overline{J_{k,i}}) + \frac{E\overline{\dot{\omega}_k}}{F} - \frac{\partial}{\partial x_i}(EFJ^t_{k,i}) \tag{4.5}$$

where the efficiency function E corresponds to the ratio between the subgrid scale wrinkling of the non-thickened flame and that of the thickened flame:

$$E = \frac{\Xi(\delta_L^\circ)}{\Xi(\delta_L^1)} \tag{4.6}$$

In the present work the efficiency function derived by Charlette et al. (2002) is used where the model constant β is taken equal to 0.5.
Since the thickening process changes the gas transport properties, the dynamic thickening proposed by Legier et al. (2000) is applied so that the combustion model impacts only the flame region with the help of a flame sensor.
In order to achieve a compromise between chemistry details and computational cost, the 2S-CM2 global two step reaction mechanism for methane air flames (Bibrzycki and Poinsot 2010a)) is used, which has been validated for fresh mixture at temperature $T = 300$ K, pressure $p = 0.1$ MPa and equivalence ratios between 0.6 and 1.0.
Reactions and Arrhenius parameters of the 2S-CM2 mechanism are reported in Tab. 4.3. A, β and E_a refer, respectively, to pre-exponential factor, temperature exponent and activation energy of the Arrhenius law.

Reaction	A	β	E_a	*Reaction orders*
$CH_4 + 1.5O_2 \Rightarrow CO + 2H_2O$	2×10^{15}	0	35000	$[CH_4]^{0.9}\ [O_2]^{1.1}$
$CO + 0.5O_2 \Leftrightarrow CO_2$	2×10^{9}	0	12000	$[CO]\ [O_2]^{0.5}\ [CO_2]$

Table 4.3: *Reactions and Arrhenius parameters for 2S-CM2 mechanisms. The activation energy is in cal/mole and the pre-exponential constant in cgs units.*

Boundary conditions for the reacting flow

The boundary conditions are standard Navier-Stokes characteristic boundary conditions (NSCBC, Poinsot and Lelef (1992)) and are set according to the experimental input data. Tab. 4.4 summarizes the boundary conditions imposed for the reacting flow simulation.

Boundary Condition	Physical variables	Relax coefficients
Perfectly premixed axial injection	$\dot{m} = 0.0028\ kg.s^{-1}$ $T = 300$ K $Y_{CH_4} = 0.05248$ $Y_{O_2} = 0.22078$ $Y_{N_2} = 0.72674$	50 000 s^{-1}
Perfectly premixed tangential injection	$\dot{m} = 0.0003\ kg.s^{-1}$ $T = 300$ K $Y_{CH_4} = 0.05248$ $Y_{O_2} = 0.22078$ $Y_{N_2} = 0.72674$	50 000 s^{-1}
Perfectly premixed plenum injection	$\dot{m} = 0.0024\ kg.s^{-1}$ $T = 300$ K $Y_{CH_4} = 0.05248$ $Y_{O_2} = 0.22078$ $Y_{N_2} = 0.72674$	50 000 s^{-1}
Atmo Inlet	$\dot{m} = 0.1\ kg.s^{-1}$ T = 300 K $Y_{O_2} = 0.233$ $Y_{N_2} = 0.767$	50 000 s^{-1}
Outlet	$P = 101325$ Pa	500 s^{-1}
Walls	Isothermal wall law	-

Table 4.4: *NSCBC conditions imposed on the boundary in the reacting flow simulation.*

The temperature field imposed on the chamber walls (bottom chamber, quartz and convergent) are extrapolated from profiles of Laser Induced Phosphorescence (LIP) measurements shown in Fig. 4.5.
The extrapolation is performed with the *interpolate* function from Python. A linear 2D interpolation (*interp2D* from Python) is performed on the quartz windows measured temperatures, while a 1D interpolation is done for those ones concerning chamber bottom and convergent. The obtained interpolation functions are then used to extrapolate the measured temperature on the whole boundaries of the computational domain. The resulting wall temperature field, that is imposed in LES simulations, is shown in Fig. 4.18.

In order to describe the solution of the shear-stress at the wall, the approach used in this study is the wall function, in which the boundary layer profiles are analytical functions obtained in classical boundary layer theory.
Useful dimensionless variables defined in the boundary layer are the dimensionless distance from the wall, y^+, and velocity u^+:

$$y^+ = \frac{y u_\tau}{\nu} \tag{4.7}$$

$$u^+ = \frac{u}{u_\tau} \tag{4.8}$$

where y is the distance from the wall, ν the kinematic viscosity, u the mean

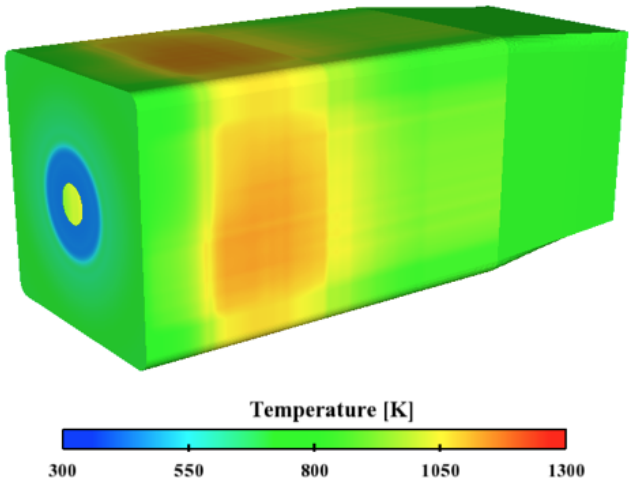

Figure 4.18: *Temperature distribution extrapolated on the chamber walls from LIP measurements provided by Degenève et al. (2019a).*

velocity tangential to the wall and u_τ the friction velocity, defined as:

$$u_\tau = \sqrt{\frac{\tau_w}{\rho}} \tag{4.9}$$

function of the wall shear stress τ_w and the gaseous density ρ.
Figure 4.19 shows the mean field of y^+ on the chamber walls. The observed y^+ values show that the mesh would be suitable for Wall-Resolved LES (WRLES). The wall laws are kept anyways as boundary conditions and are expected to have a negligible impact.

4.4.2 Ignition procedure

The ignition inside the combustion chamber is simulated through the insertion of a sphere of burnt gases in the cold flow previously converged with adiabatic walls. The flame kernel is placed 60 mm away from the axis chamber to keep the same distance of the experimental ignition electrode from the axis, seen in Fig. 4.20. At the instant of ignition, the chamber is filled by a reactive mixture of CH_4 and Air at 300 K, and the boundary conditions are switched to iso-thermal walls.

Convergence criteria

A previously mentioned characteristic time is the flow through time, t_f, which is computed from the characteristic length of the combustor and the bulk velocity

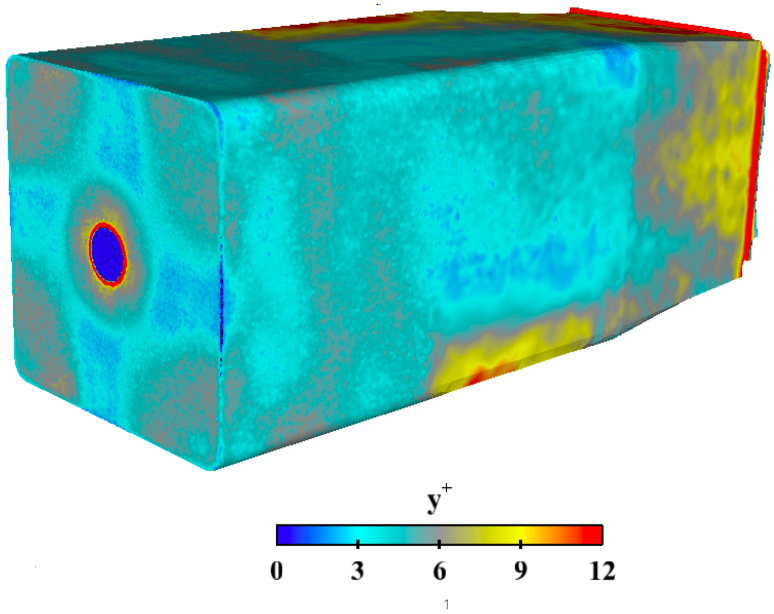

Figure 4.19: *Visualization of the mean y^+ field on the internal chamber wall.*

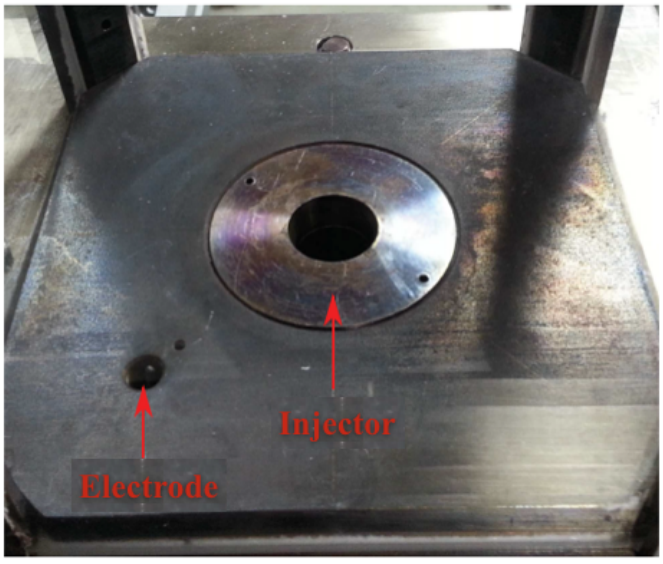

Figure 4.20: *View from the top of the chamber of injector and ignition electrode.*

at the injection. In the investigated configuration, t_f is equal to 26 ms. However, it supposes that burnt gases flow inside the chamber at a velocity equal to the injection bulk velocity. In practice, gas velocity inside a combustion

chamber is not homogeneous. In the investigated configuration, burnt gases are accelerated because of the expansion due to the flame but, downstream the flame, due to the wall confinement, they are recirculated back towards the back plate. The big recirculation zones, encountered in the investigated configuration, make t_f inappropriate, since it leads to an under-estimation of the time spent by burnt gases in the combustor. As a consequence, the residence time τ, obtained by dividing the chamber volume by the volumetric flow rate of burnt gases, is considered to be more relevant and representative of the flow configuration encountered in the Oxytec chamber.
The Oxytec chamber is characterized by a big volume and consequently by a large residence time τ. The residence time, τ, is equal to 220 ms if the temperature of burnt gases is equal to the adiabatic flame temperature. Because of the wall heat losses, the volume-averaged temperature of burnt gases is smaller than T_{ad}, consequently its volumetric flow rate, which is inversely proportional to density, decreases. This leads to a space residence time τ of around 380 ms. In order to converge the LES of the reactive case of the flame A while accounting for heat losses, 1.3 seconds of physical time have been simulated, corresponding to around 3.5 times the characteristic residence time.
In order to evaluate the convergence of the flow fields in non adiabatic LES, several variables have been monitored in the course of the simulation, such as the surface integrated heat fluxes and volume averaged gas temperature.
Concerning the former, Fig. 4.21 shows the evolution of the surface integrated wall heat flux for the boundaries where temperature is imposed: chamber bottom, quartz windows and exhaust convergent. Fluxes are considered as negative if transferred from the fluid to the wall.

From Fig. 4.21, the temporal variation of integrated wall fluxes can be analyzed: during the first 800 ms of simulation they are characterized by a temporal transient regime, while, after 1 second of simulated physical time, they start to stabilize.
For this reason, a transient of 1 second, corresponding to around three times the space time, is simulated before accumulating statistics. The solutions are then averaged over a physical time approximately equal to the characteristic residence time of the combustion chamber: 350 ms.
Another verification has been done on the volume averaged temperature. This variable has been estimated in two cases: in one case the retained volume is limited to a parallelepiped ending at the height of the quartz windows, in the other case the whole chamber is retained. Figure 4.22 shows the evolution of the averaged temperature in both the analyzed cases.
At $t = 0$, the spherical kernel is placed in the chamber filled by cold reacting mixture and then it is convected by the flow until the flame is stabilized at the burner outlet. In the first instants after the initiation of ignition, the average temperature inside the chamber increases until the whole chamber is filled of burnt gases, and this corresponds to $t = 290\ ms$. Thus, this time value is retained as the initial instant to trace the evolution of T_m.

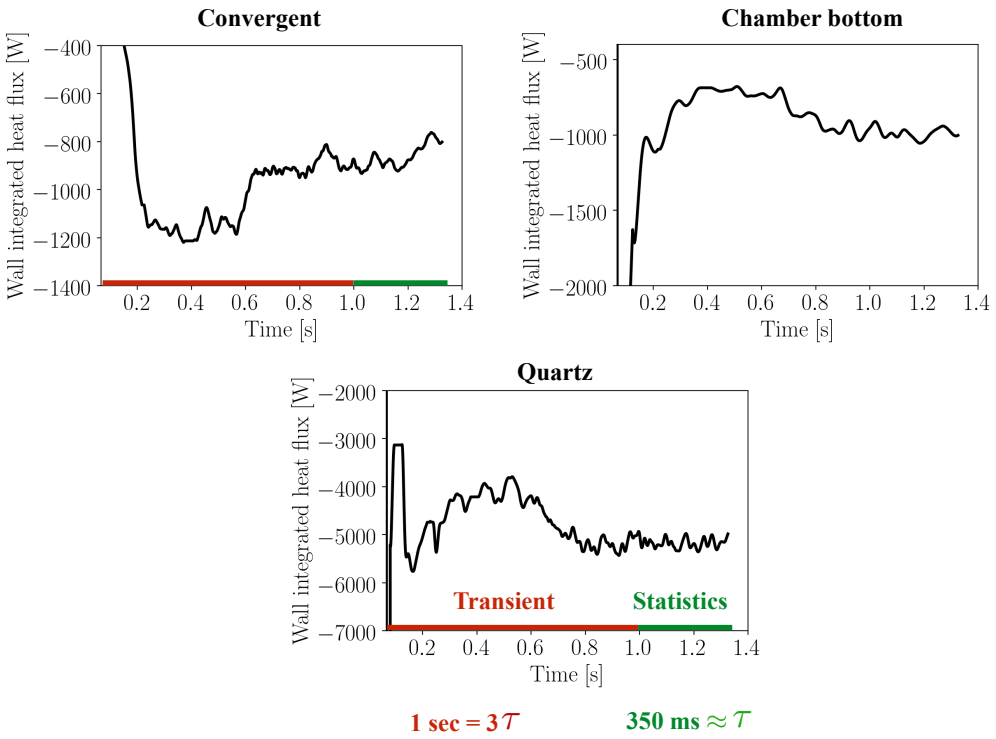

Figure 4.21: *Evolution of the instantaneous wall integrated heat fluxes along the whole simulated physical time for convergent, dump plate and quartz windows.*

From this instant on, the average temperature of the burnt gases decreases because of the effect of the wall heat losses, until reaching the estimated steady state.
In Fig. 4.22, dots represent the mean temperature for each run of the simulation, then each dot corresponds to the temperature averaged on 40 ms of simulation. A fitting is realized on a, b and c in the exponential function $ae^{-b*t} + c$ where t is the physical time and c is the steady state temperature. On the left side of Fig. 4.22, it can be seen that the steady state is reached inside the region of the combustion chamber delimited by quartz windows. When the retained volume to compute the temperature includes the convergent, values of mean temperature are smaller because cooler burnt gases inside the convergent are included. Moreover, the steady state is not attained, meaning that this part of the chamber is characterized by a slower convergence. Nonetheless, the 90 % of convergence is attained.
From Fig. 4.22 (right), it can be seen that 100% of convergence is attained after simulating 3 seconds of physical time. Such a computation would have required a wall clock time of 63 days running the simulation on the super-computer OCCIGEN on 100 nodes of 24 cores each, and it would have been computationally

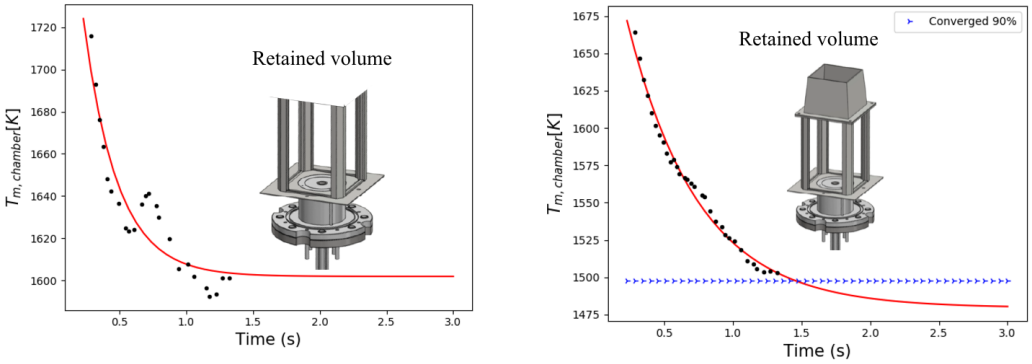

Figure 4.22: *Transient evolution of the volume-averaged temperature inside the chamber excluding the convergent (left) and including it (right). The dots correspond to numerical data, and they are approximated by an exponential curve in red full line. The blue horizontal line mark the 90% of the estimated final value.*

unaffordable.
While obtaining 90 % of the estimated final value of T_m (represented in triangles in Fig. 4.22) allows to end up the calculation after a physical time of 1.3 s, corresponding to $3.5 \times \tau$, and a wall clock time of 28 days running on 2400 cores.
The corresponding amount of CPUh consumed for such a simulation is 1 598 621 on Intel E5-2690V3 cores.

Analysis of the transient before reaching the thermal equilibrium

Previously, the effect of wall heat losses on the gaseous temperature inside the combustion chamber has been shown. The evolution of wall heat losses can also be appreciated by comparing a sequence of images representing the mean temperature field on a longitudinal plane of the chamber. The images are shown in Fig. 4.25: each image corresponds to a solution averaged on 40 ms and the retained solutions are taken from several instants of the simulation.

Taking a look at the first 700-800 ms of the simulation (top of Fig. 4.25), it is possible to notice the presence of very hot burnt gases inside the IRZ and cooled burnt gases on the bottom of the chamber. These are the green regions on the bottom corners of the plane in Fig. 4.25, corresponding to the burnt gases cooled down by the contact with the quartz. This outer recirculation zones (ORZ) drive the cooled burnt gases towards the bottom of the chamber until joining the foot of the flame. The heat losses at the bottom of the chamber affect the flame topology because they prevent the attachement of the flame front: the side branches of the flame are quenched and in the region between chamber bottom and flame front the fresh mixture is mixed to burnt gases but no reaction takes place. The absence of reaction in the lateral branches can

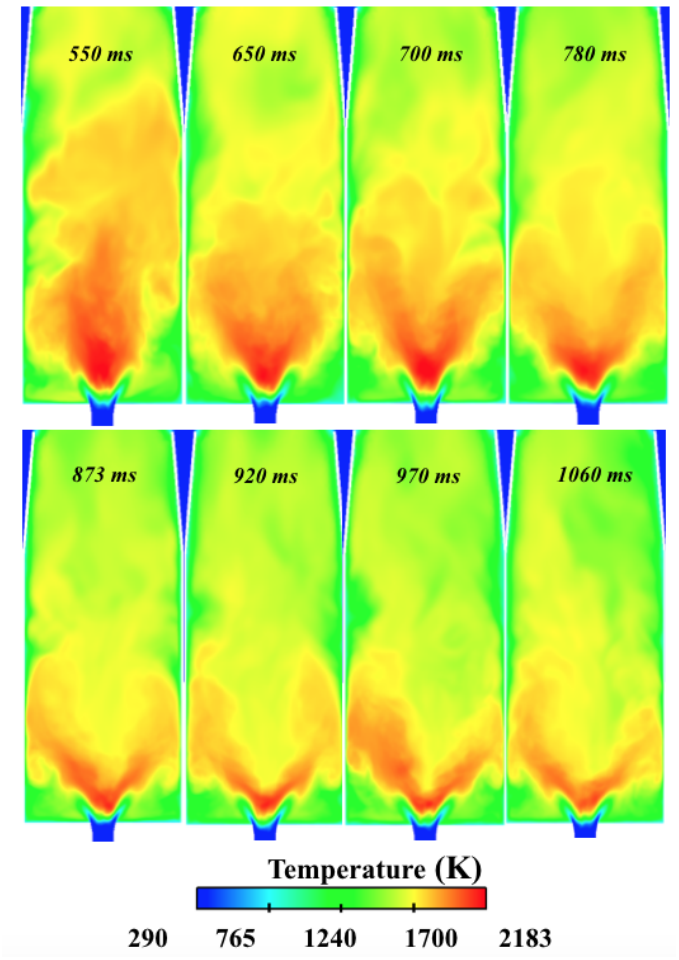

Figure 4.23: *Temperature fields on a longitudinal plane of the chamber averaged on 30 ms and taken from different instants of the simulation of the Flame A with imposed wall temperature.*

be seen in Fig. 4.24 where the mean heat release field is shown. The interface between fresh mixture and burnt gases is highlighted by the iso-line tracking the normalized progress variable equal to 0.9.

However, burnt gases at high temperature still appear in the inner recirculation zone in proximity of the axis chamber. Starting from 800 ms, this region gets colder because of the recirculation of the burnt gases which have exchanged heat transfer with the cold windows of the chamber and recirculate in the inner recirculation zone.
It is clear that temperature and velocity fields are related through density, thus it could be interesting to look at the evolution of the axial velocity field in the course of the simulation, represented in Fig. 4.25. After 300 ms (first image

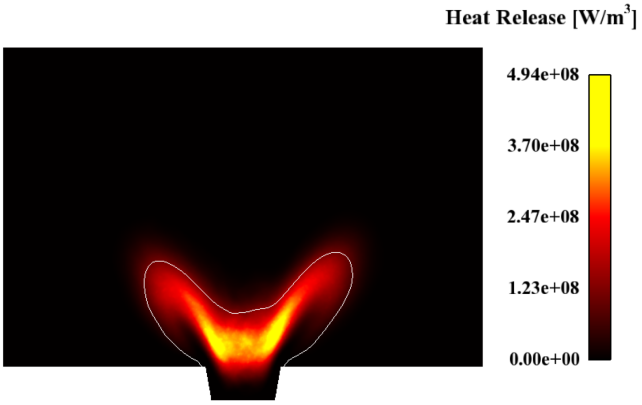

Figure 4.24: *Mean heat release field on the longitudinal plane passing for the chamber axis. White line is the iso-surface of normalized progress variable equal to 0.9.*

on the left) the jet appears long and asymmetric; moreover, no IRZ appears. The burnt gases exchanging with the walls cool down and recirculate towards the bottom chamber: outer recirculation of cooled gases can be noticed in the blue pockets close to the lateral walls and at the corners on the bottom of the longitudinal plane. As the outer recirculation zones are formed, the jet spreads and the inner recirculation zone (blue region around the axis chamber) appears: the hot gases exchanging with the walls are cooled and are recirculated towards the central region of the burner. From 650 ms on, the swirled jet spreads and the IRZ widens.

The IRZ in the retained combustion chamber is very important since it allows to drive hot burnt gases towards the burner exit and to create a region at low velocity where the flame can easily stabilize far from the solid parties of the burner. Particularly, the IRZ causes the formation of a stagnation point of the flow, which is the point on the axis chamber, close to the burner, characterized by zero axial velocity, which appears in spite of the high velocities of the flow coming out from the injector.

In the course of the simulation, the position of the stagnation point of the flow lowers along the the burner axis until stabilizing around $x = 2.3$ cm. The position of the stagnation point is fundamental for the swirled-stabilized flame since the flame stabilizes above the burner exit, upstream the inner recirculation zone. In Fig. 4.26, on the top, the inner recirculation zone is represented through an iso-surface of axial velocity equal to zero colored by tangential velocity to represent the swirling. On the bottom of Fig. 4.26, an iso-surface of progress variable equal to 0.9, colored by heat release, represents the flame position. The flame looks like attached to the bottom chamber but this is due to the fact that, at the flame foot, burnt gases are mixed to the fresh gases; consequently a gradient of progress variable is present but no reaction takes place as it can be seen later, when the heat release field is shown.

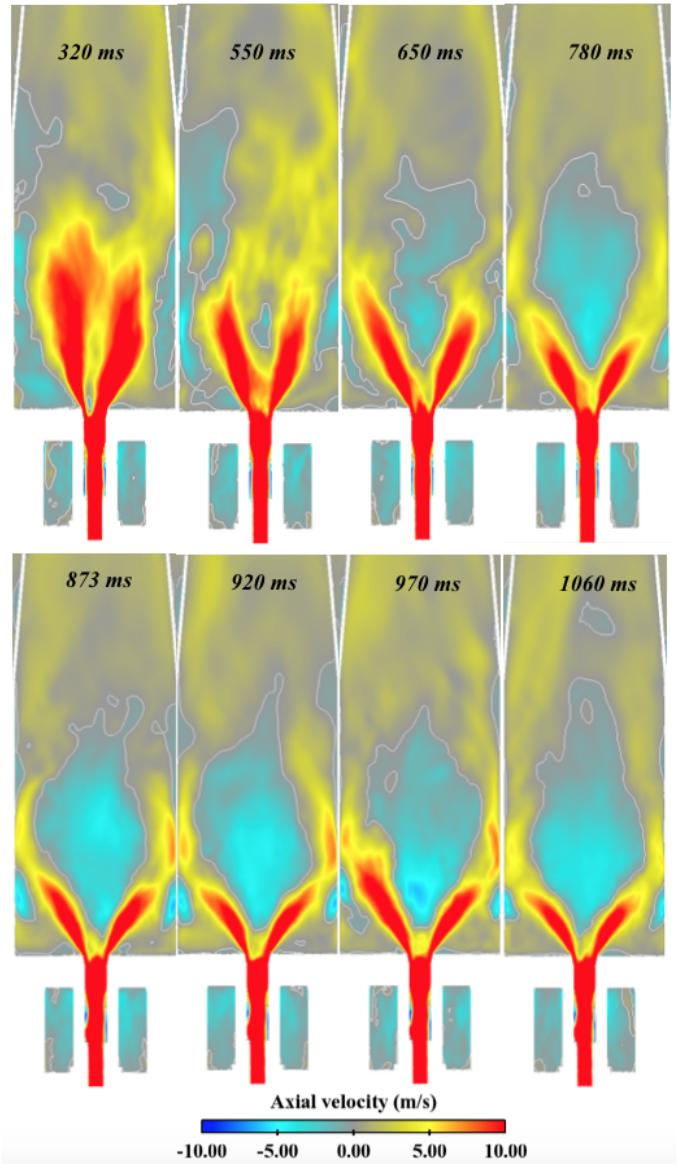

Figure 4.25: *Axial velocity fields on a longitudinal plane of the chamber averaged on 30 ms and taken from different instants of the simulation of the Flame A with imposed wall temperature. White lines are the iso-contour of axial velocity equal to zero.*

4.5 Reactive flow simulation results

4.5.1 Velocity profiles

In this section, numerical results of LES with imposed wall temperature are compared to experimental velocity fields of the reacting flow.
Large Eddy Simulation carried out in this study show that the flow topology

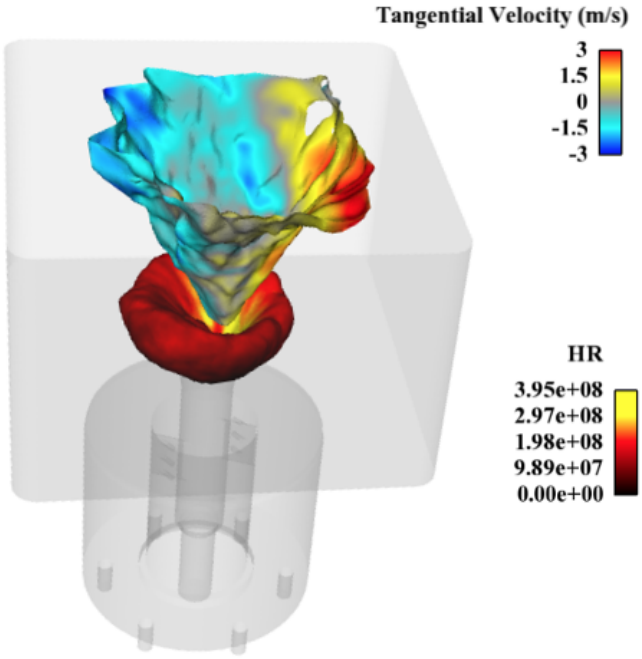

Figure 4.26: *Iso-surfaces of axial velocity equal to 0 delineating the inner recirculation zone, colored by the tangential velocity, and iso-surface of progress variable equal to 0.9 colored by the heat release.*

with and without combustion is similar. Figure 4.27 shows the axial velocity field on a longitudinal plane of the chamber from reacting (left) and non-reacting (right) flow simulations. Some common features can be found, such as the presence of inner and outer recirculation zones and the two high velocities lateral branches.
However, several differences can be observed. When the flame is present the spread of the jet is clearly larger than the one present in the cold case; moreover axial velocity peaks are higher compared to the air flow case since the gases are accelerated when they pass through the flame front. Concerning the IRZ, the reverse flow velocity is higher in flame conditions, then the strength of the recirculation zone is greater in presence of a flame. These differences have been highlighted also by experimental measurements presented in Jourdaine (2017).

In LES simulations, it appears that the local maximum of axial velocity on the axis chamber, present in cold flow simulation, disappears in presence of the flame. However, PIV measurements show the presence of this peak also in reacting conditions, as it can be seen in Fig. 4.28, where the mean axial velocity field from LES is compared to experimental data on a longitudinal plane of the chamber.

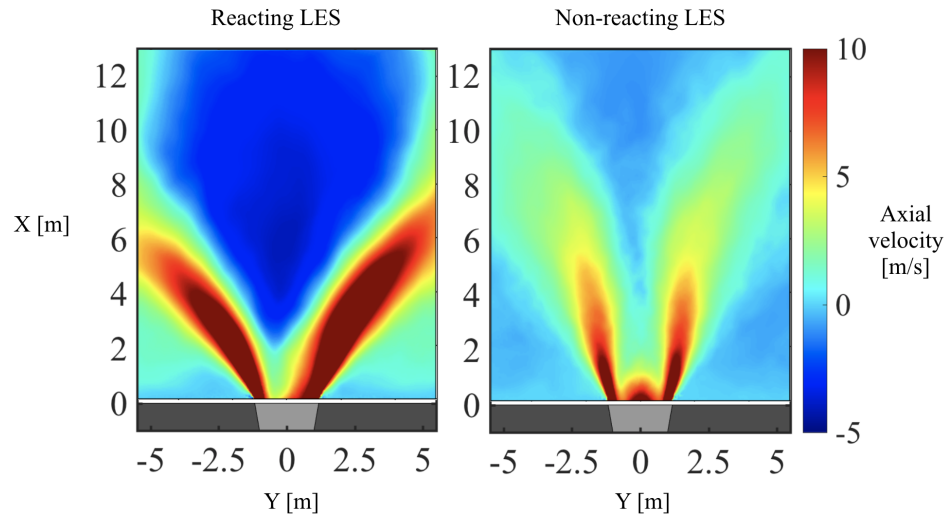

Figure 4.27: *2D fields of mean axial velocity in reacting conditions (left) and non reacting conditions (right) taken from LES.*

The absence of central peak of axial velocity in reacting conditions may be

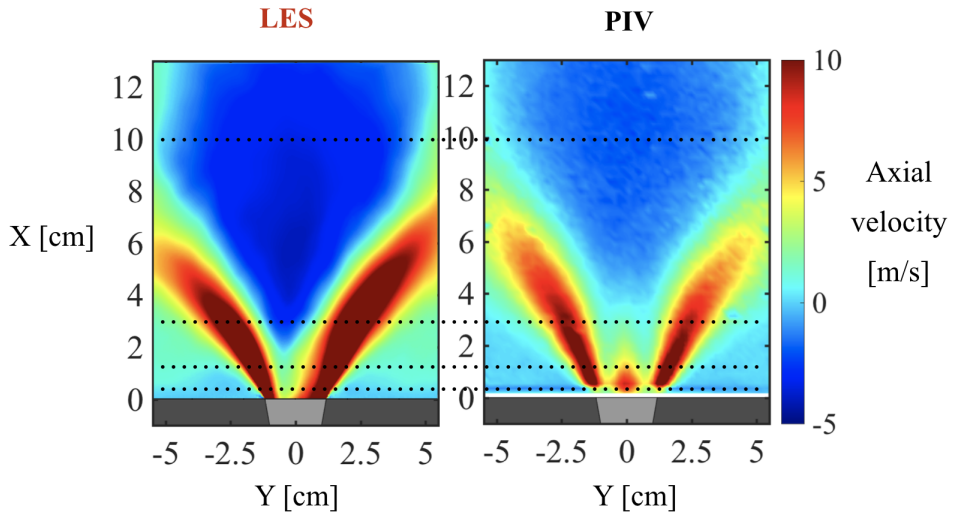

Figure 4.28: *2D fields of mean axial velocity on a longitudinal plane of the chamberin LES (left) and experimental PIV (right). Dotted lines trace the transverses used for comparison of 1D velocity profiles.*

linked to an over-estimation of the reversed flow in LES, and then to the fact that the predicted stagnation point is located upstream compared to the experiments. A possible explication can be the neglecting of radiative heat transfer, which would affect the temperature distribution of burnt gases inside the cham-

ber, altering then the density field.
Inner and outer recirculation zones in reacting flow simulations can be visualized in Fig. 4.29, where vector arrows of the velocity vectors colored by axial velocity are shown, together with the mean axial velocity field on a cross section of the chamber (cut at $x = 5$ mm). On the top, vector arrows are shown on a longitudinal plane of the chamber according to the vertical axis, whose cut is shown through a white line on the cross section of the chamber; on the bottom velocity vectors are shown on a longitudinal plane according to the diagonal of the chamber section, whose cut is shown through the white dashed line on the right. It can be seen that an intense recirculation of burnt gases towards the bottom of the chamber takes place at the corner of the chamber (negative axial velocity in blue regions). The recirculated gases then join the main flow on the horizontal and vertical axis of the chamber, in the yellow cross-shaped region, where the axial velocity assumes positive values.

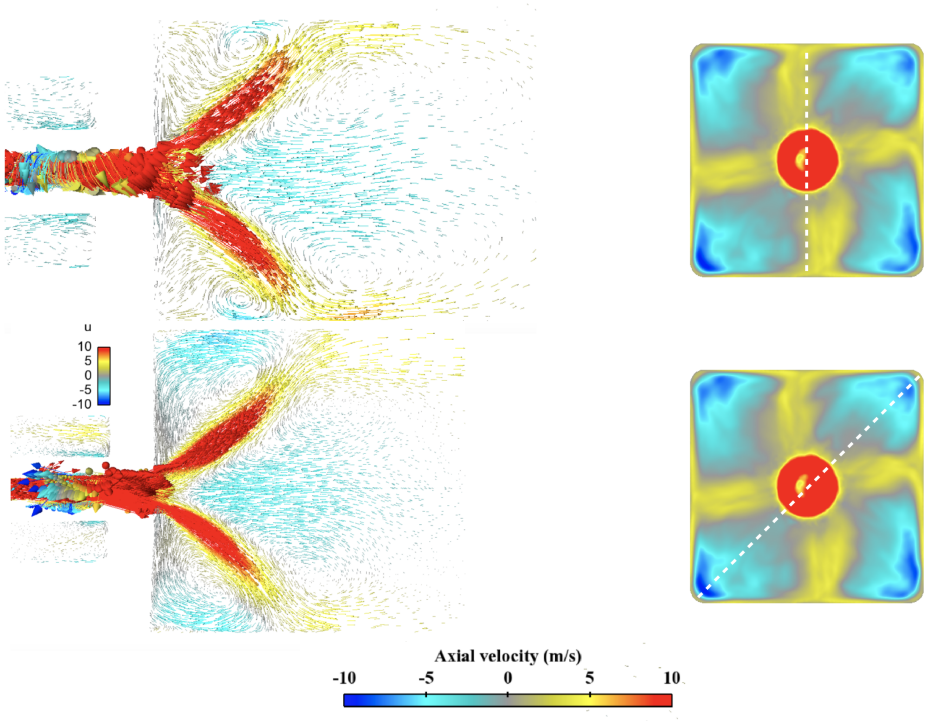

Figure 4.29: *Vector arrows of the velocity vector colored by axial velocity on a longitudinal plane of the chamber (left) and mean axial velocity field on a cross section of the chamber at $x = 5$ mm (right). White dashed line represents the line cut used to create the longitudinal planes.*

LES velocity profiles are now compared to PIV ones. In Fig. 4.30 the profiles of mean axial velocity (on the left) and rms of axial velocity (on the right) are compared on four different heights along the burner axis: $x = 5$ mm, $x = 15$ mm, $x = 30$ mm and $x = 100$ mm. Experimental data are represented in

black dots while numerical results by red solid lines.

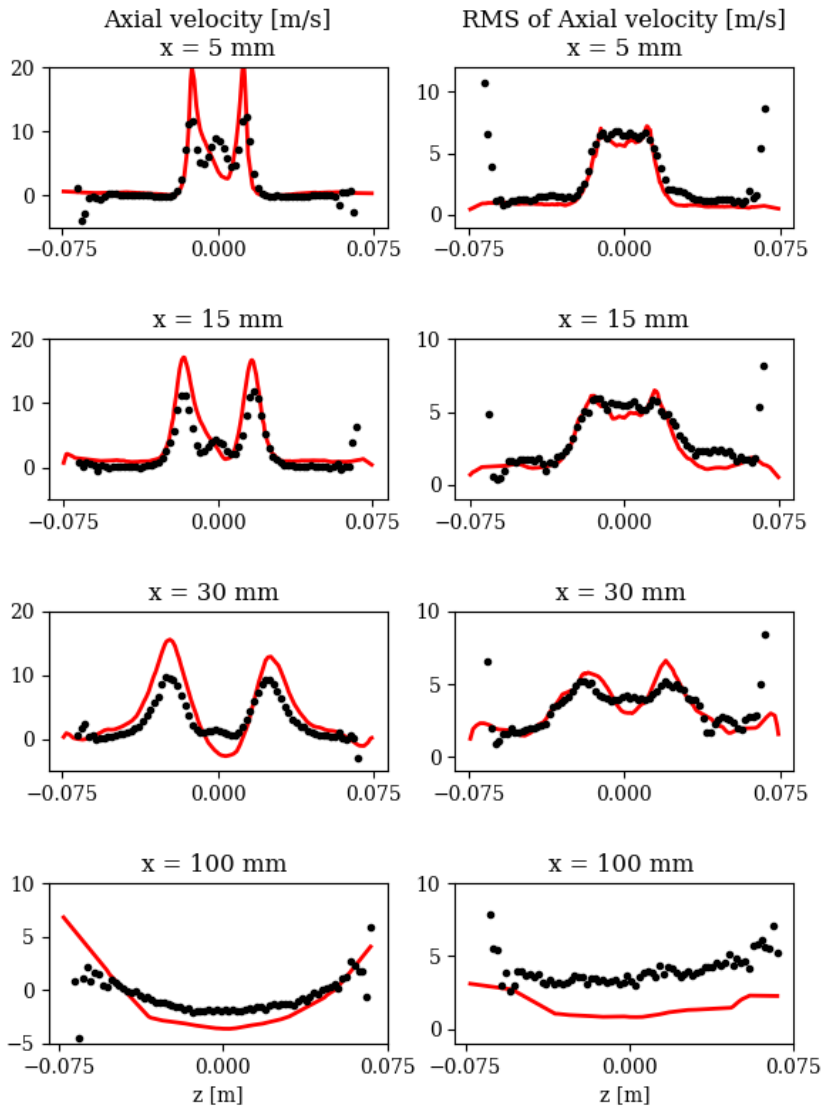

Figure 4.30: *Profiles of axial velocity (left) and RMS of axial velocity (right) on several cuts along the chamber axis. –-: Numerical results; • : Experimental data.*

Looking at the mean axial velocities (left), it can be seen that at 5 and 15 mm from the swirler exit, the central peak of velocity is absent in LES, as anticipated, however the jet width is very well predicted. At a distance of 30 mm

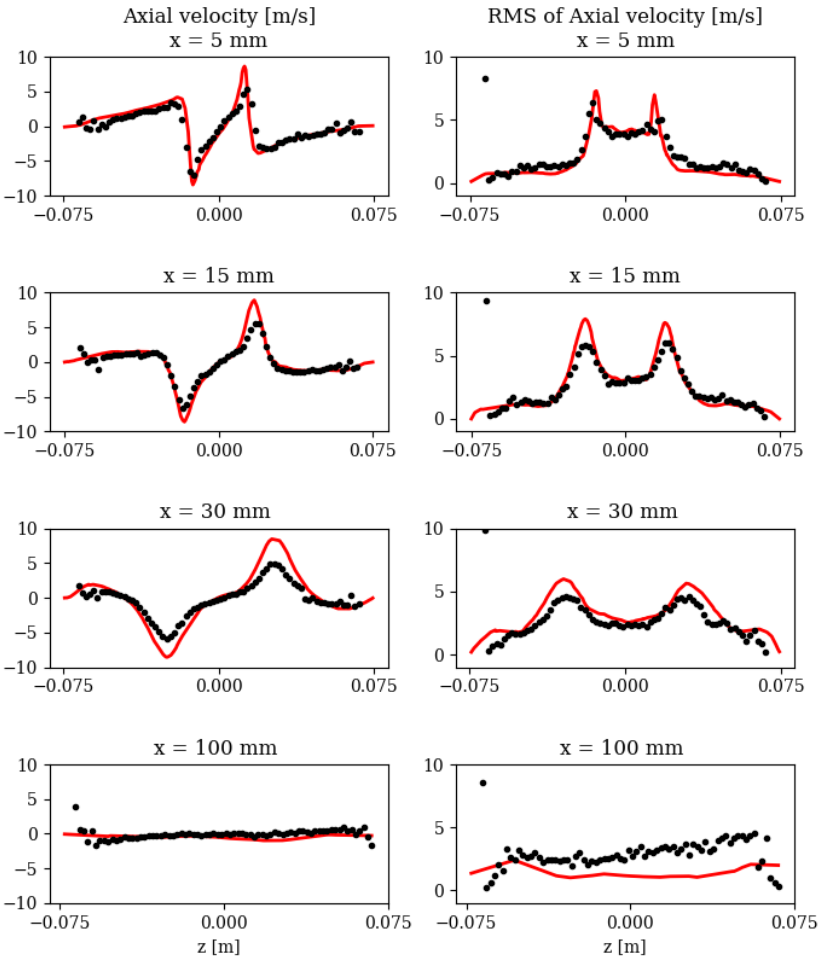

Figure 4.31: *Profiles of radial velocity (left) and RMS of radial velocity (right) on several cuts along the chamber axis. –-: Numerical results; • : Experimental data.*

from the burner exit, it is possible to notice the presence of a reversed flow around the central axis ($y = 0$) in LES, while in experiments the stagnation point is found at a higher height. Downstream, a good agreement is found between numerical results and experimental data. If one looks at the RMS of axial velocity (the right side of Fig. 4.30), the experimental profiles are quite satisfactorily retrieved. A second comparison is done on the radial velocity and it is shown in Fig. 4.31. A very good agreement between numerical results and experiments can be found for both radial velocity and rms profiles. The validation cannot be performed for the azimuthal velocity since no experimental

data are provided.

In conclusion, a good global agreement is obtained for the velocity fields and the recirculating zones, although a discrepancy is observed in the position of the stagnation point and on the axial velocity peaks. The first phenomenon can be due to the neglecting of radiative heat transfer in the reactive case simulation, while the second one might be due to the inability of PIV to record high velocities peaks, as seen in cold flow simuations.

4.5.2 Flame topology

OH* chemiluminescence measurements allow to visualize the position and the shape of the flame. The light emission of a flame represents an indirect measure for its heat release distribution. For this reason the integral emissions of chemiluminescent species like OH* are often compared to the line-of-sigth integrated heat release of flames.
This comparison is done for the investigated flame and it is shown in Fig. 4.32. The OH* signal recorded in experiments (on the right side) is compared to the results obtained from two simulations: the image on the left of Fig. 4.32 is the results of reacting LES with adiabatic walls, while the one in the middle is taken from LES with imposed wall temperature.
In experiments, OH* emissions are recorded with a camera with an exposure time quite long. The resulting images therefore show the flame integrated along the line of sight. For this reason, OH* chemiluminescence images are compared to the mean heat release issued from LES simulations integrated along the line of sight.
Looking at the experimental images, it can be noticed that the flame is aerodynamically stabilized close to the injector rim, taking a well defined V−shape with a flame leading edge lying in proximity of the burner outlet.
On the contrary, in simulations with adiabatic walls (left side of Fig. 4.32), the flame stabilizes with significant reaction in inner and outer shear layers and is attached to the dump plate of the chamber taking an M−shape. The flame also appears much more compact than the experimental one: the flame height, marked by white dashed line in Fig. 4.32, (approximatively 3 cm), is half the size of the experimental one.
When heat losses are taken into account, quenching effects appear in the outer shear layers, and the flame stabilizes predominantly in the inner shear layer, with a V-shape very similar to the experimental one. In LES with isothermal walls, indeed, the flame foot is well retrieved if compared to the OH* images. When compared to the adiabatic case, the flame appears much less compact and this is also indicated by the higher value of the maximum heat release in adiabatic simulations. However, even accounting for heat losses, the flame is still more compact than the experimental one, consequently the height is not well predicted (4.6 cm vs 6 cm).

This comparison demonstrates that the neglect of wall heat losses is not realistic and may lead to a totally wrong flame shape. On the contrary LES with isothermal walls are able to predict the lift-off of the flame: the extinction of the lateral branches due to wall heat losses can be seen in the comparison with adiabatic walls case. Even if the flame foot is very similar between experiments and non adiabatic LES, the experimental flame height is not retrieved in LES. A study carried out by Lauer and Sattelmayer (2010) shows that OH* or CH* chemiluminescence are not reliable measures for the spatially resolved heat release rate in turbulent flames. The reason is found in the turbulence which causes reduction of chemiluminescence intensity near the burner exit, consequently the flame length obtained from chemiluminescence images is longer than the actual flame length indicated by the heat release rate. In their investigated flame, the flame length observed in chemiluminescence images is overestimated by a factor of two compared to the one indicated by the heat release rate (Lauer 2011).
The high turbulent intensity of the flame investigated in this thesis work can then explain the reason of such a mismatch between numerical heat release and experimental images of OH* chemiluminescence.
Finally, one cannot exclude possible modelling errors in the turbulent combustion modelling and their possible impact on the presented results. Besides, during the writing of the present manuscript, a recent preliminary study has highlighted a possible hysteresis effect on the flame stabilization depending on the flame history.

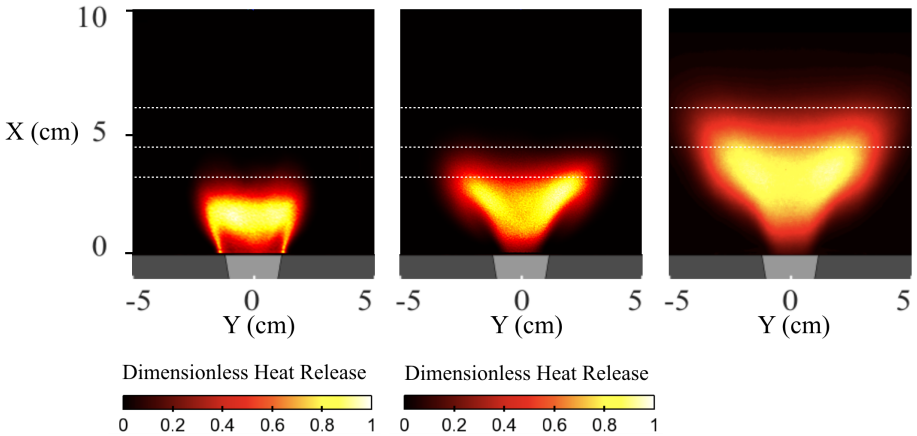

Figure 4.32: *Mean heat release integrated along the line of sight issued from adiabatic walls case (left) and isothermal walls case (center). OH* intensity distribution from experiments (right).*

OH-PLIF diagnostics are also available: Fig. 4.33 compares some OH-PLIF snapshots from Jourdaine (2017) to 2D cut of the instantaneous heat release

issued from LES with isothermal walls. The OH-PLIF represents the OH concentration and consequently it is a useful tool to trace the flame front. As this species is not available in LES because of the reduced mechanism, OH species are here compared to the instantaneous heat release from LES.
From both experiments and simulations, it can be deduced that the flame is highly fluctuating and that the flame front close to the chamber axis oscillates moving upstream towards the divergent tube and downstream towards the chamber.

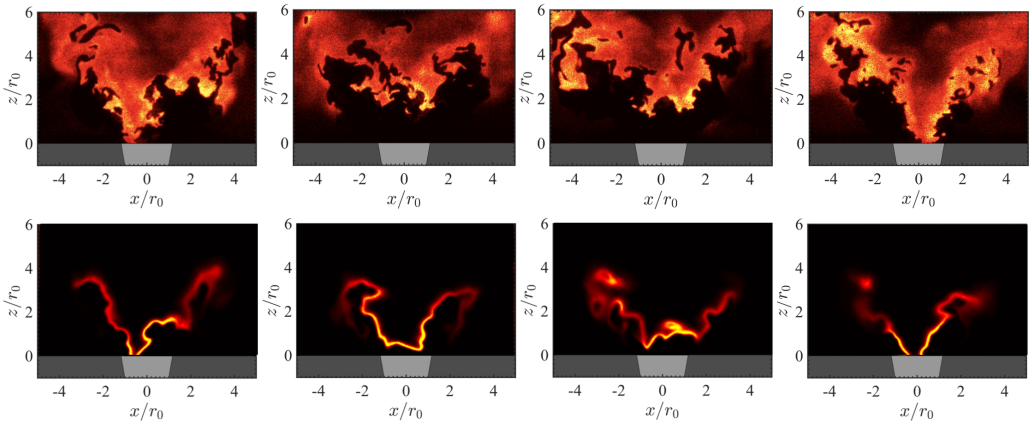

Figure 4.33: *OH-PLIF snapshots on the top, 2D cut of heat release field from instantaneous LES snapshots on the bottom.*

For a 3D visualization of the flame inside the chamber, Fig. 4.34 shows the iso-surface of heat release $= 3 \times 10^8\ W\ m^{-3}$ taken from an instantaneous solution. Its shape confirms the observations already done about the V-shape. Instantaneous fields allow to appreciate the flame resolved wrinkling which cannot be seen in averaged fields.

4.6 Heat transfer results

4.6.1 Energy balance

The energy balance around a control volume delimitating the combustion chamber (i.e.: excluding the atmosphere) is investigated. For the non-adiabatic case, a sensible enthalpy budget is used and the macroscopic balance equation of sensible enthalpy leads to:

$$\int_{out} \rho h_s \mathbf{u} \cdot d\mathbf{S} - \int_{in} \rho h_s \mathbf{u} \cdot d\mathbf{S} + \int_{walls} \phi^{\mathbf{cond}} \cdot d\mathbf{S} - \dot{\Omega} = 0 \tag{4.10}$$

where the first two terms account for the outlet and inlet convective fluxes, the third term represents the integrated wall conductive flux while the last term is

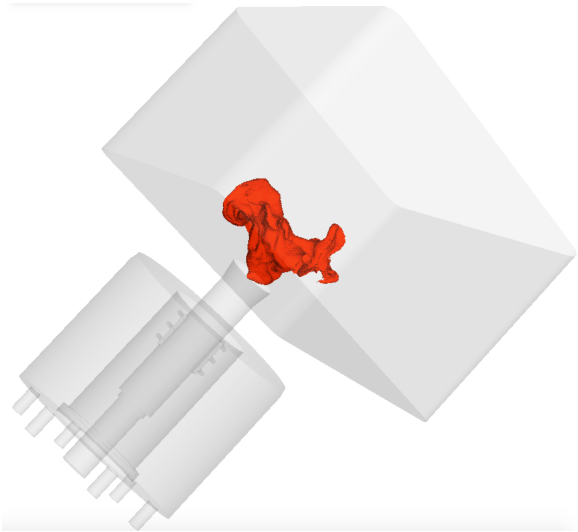

Figure 4.34: *Iso-surface of the heat release rate* $hr = 3 \times 10^8\ Wm^-3$ *from an instantaneous solution.*

the integrated heat release.
Rigorously, the radiative source term should appear in the Eq. (6.8), but in this chapter radiation is neglected. For this reason, in this simulation, the total wall heat flux is only due to the convective flux from gaseous flow inducing a wall conductive flux predicted by the wall law in LES.

After 1.3 seconds of simulated physical time, the enthalpy balance is closed with an error lower than 1 % of $\dot{\Omega}$ and an analysis of the predicted wall heat losses may be carried out. The total mean wall flux $\overline{\Phi}_w$ can be obtained by a time average of the total flux interesting lateral walls, bottom chamber and convergent. The temporal average of heat fluxes is carried out from the converged solution over 350 ms (from 0.97 to 1.32 s of physical time) and is computed as:

$$\overline{\Phi}_w = \int_{walls} \overline{\phi}^{\mathbf{cond}} \cdot \mathbf{n_w} dS = 7.01\ kW \tag{4.11}$$

Where $\mathbf{n_w}$ represents the normal to the walls. The total wall fluxes are distributed among bottom chamber (985 W), lateral walls (5161 W) and convergent (862 W).
The integrated heat release (last term in the enthalpy balance equation Eq. (6.8)) accounts for 14.5 kW; then around 50 % of the thermal energy produced inside the chamber is lost through heat losses at the walls, while the remaining half represents the fluid thermal energy mainly due to the hot burnt gases exiting the system.
This means that heat losses have a very important impact in the retained combustor and they have to be taken into account in order to retrieve the correct

behavior of the flame.

4.6.2 Temperature comparison

Punctual measurements of temperature are available thanks to four thermocouples installed inside the combustion chamber measuring the gas temperature in different positions, shown in Fig. 4.6. They are all installed in one of the chamber corners, 15 mm far from the metallic bars. Table 4.5 summarizes the gas temperature predicted by LES, the experimental measured one and the error between numerical results and experiments.

Thermocouple	**Exp. T [K]**	**LES T [K]**	**Error [%]**
TC2 (X = 1.5 cm)	1294	1569	21
TC3 (X = 4 cm)	1669	1665	0.19
TC4 (X = 11 cm)	1393	1678	20
TC1 (X = 20 cm)	1150	1620	41

Table 4.5: *Temperature measured in experiments, predicted by LES and relative error for each thermocouple installed in the combustion chamber.*

Large errors are highlighted for $TC2$, the thermocouple located in the outer recirculation zone, at $x = 1.5\ cm$ from the dump plate. Numerical temperature is 20 % higher than the measured one. The same order of magnitude is retrieved in the relative error between measured and experimental temperature for $TC4$, located at $x = 10\ cm$, corresponding to the region where hot gases impinge the wall.
Smaller errors appear for $TC1$ and $TC3$, located respectively at $x = 20\ cm$ and $x = 4\ cm$ away from the dump plate. Precisely, numerical temperature perfectly agrees with experimental one in $TC3$. This thermocouple is positioned very close to $TC2$ probe (located at at $x = 1.5$ cm), indeed numerical temperatures are very close in these positions, while experimental temperatures differ by 360 K from $TC2$ to $TC3$.
$TC1$ is located near the combustor outlet, at $x = 20\ cm$, in this region burnt gas temperature appears over-estimated by 15 % compared to the measured one.
To conclude, mean temperature is higher than experimental one for almost every thermocouples. However some discrepancies appear between the experimental temperatures measured in probes located close to each other.
Numerical temperature values correspond to those ones of a simulation where thermal radiation is neglected; lower temperatures are expected when radiative fluxes are included.

4.6.3 Conductive flux validation

In Fig. 4.35, the mean convective wall heat flux obtained from LES is shown, as well as the field of mean radial velocity (left) and temperature (right) on a longitudinal plane of the chamber. The maximum of heat losses is located in the region where $x = [5; 10]$ cm. This area corresponds to the high temperature region of the quartz (see Fig. 4.18) where high temperature burnt gases are convected by the swirled flow and impinge the walls, as it can be seen in mean temperature and radial velocity fields of Fig. 4.35 (left and right).

The numerical wall heat flux can be validated through comparison with the

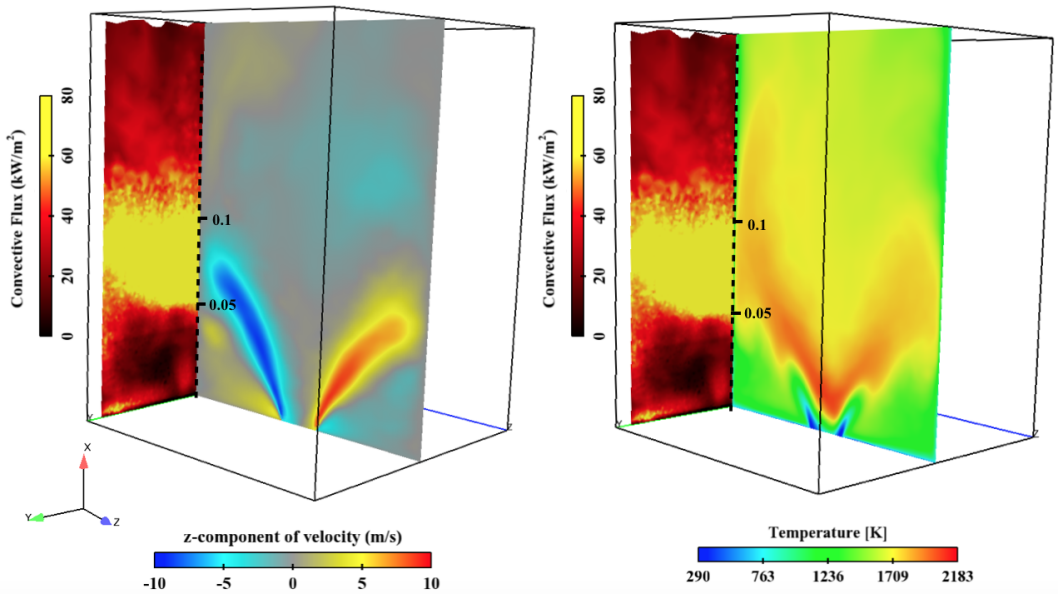

Figure 4.35: *Numerical field of mean normal energy flux on the chamber internal wall (right and left) represented together with the numerical field of mean radial velocity (on the left) and mean temperature (on the right) on a longitudinal plane passing through the axis chamber.*

experimental conductive flux profile from Degenève et al. (2019a). Starting from measurements of internal T_i and external T_e temperature of quartz windows, the experimental conductive heat flux on the axis x of the quartz, ϕ^{cond}, is derived from Fourier's law:

$$\phi^{cond}(x) = \frac{1}{s} \int_{T_i}^{T_e} k(T) dT \tag{4.12}$$

where s is the quartz thickness and k is the thermal conductivity of the quartz which is function of temperature.

The thermal conductivity is approximated with the data from the manufacturer (Heraeus), and it is obtained from the following polynomial relation (Combis

et al. 2012) as a function of temperature:

$$\frac{k(T)}{k_0} = \beta_0 + \beta_1 \left(\frac{T}{T_0}\right) + \beta_2 \left(\frac{T}{T_0}\right)^2 + \beta_3 \left(\frac{T}{T_0}\right)^3 \tag{4.13}$$

$T_0 = 293$ K, k_0 is the thermal conductivity at T_0 equal to 1.38 W.m.K^{-1}, while the coefficients are β_0= 1.02, β_1= -0.179, β_2= 0.186 and β_3= 0.0216.
The experimental ϕ^{cond} is compared to the convective flux issued from numerical LES averaged on 350 ms in Fig. 4.36. The experimental profile shown in Degenève et al. (2019a) is slightly different from the one presented here because of a mistake in the reported values in the original publication. The newly computed experimental profile in Fig. 4.36 is the one to consider.

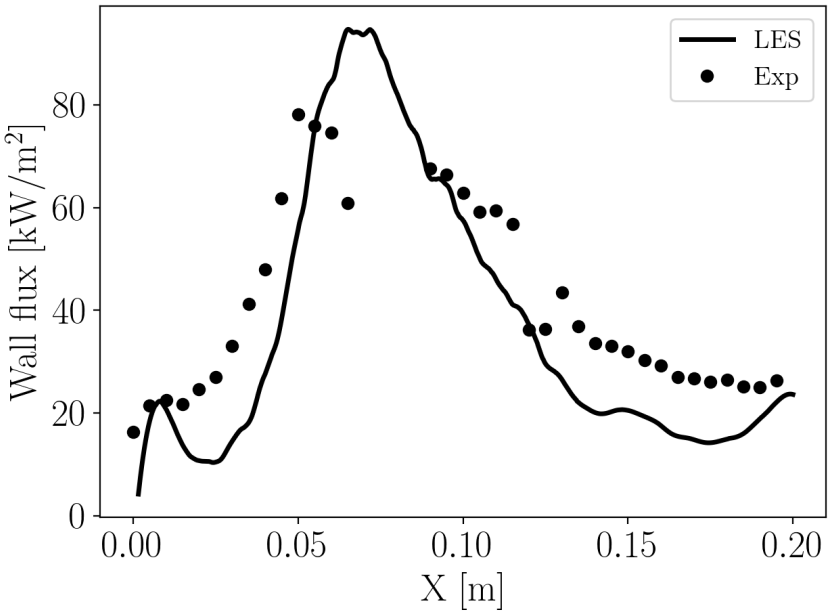

Figure 4.36: *Mean conductive heat flux along the quartz window height. Dots are the experimental data.*

The two profiles exhibit a similar trend: they increase in the lower part of the quartz window, corresponding to the ORZ, they attain a maximum and then decrease in the higher part of the quartz window. In both profiles, the maximum heat transfer takes place in the region where the hot gases brush the quartz, meaning that the jet spreading close to the walls is correctly predicted. The global trend is well retrieved, however some slight discrepancies can be observed : the numerical wall flux results to be underestimated in the cold regions of the quartz, where $x < 0.06$ m and $x > 0.1$ m. Another mismatch also appears in the region where the jet impacts the wall where the convective flux predicted by LES results overestimated compared to experiments.

In Degenève et al. (2019a) a physical interpretation is given to the conductive flux distribution. It is shown that the region where the flux is maximum is dominated by convective transfers promoted by the flow pattern induced by the swirling flow. On the contrary, in the ORZ ($x < 0.06$ m) radiative heat transfer is dominant due to the low velocities found in this region.
The comparison between numerical and experimental flux seems to confirm the analysis of Degenève et al. (2019a). On the one hand, the over-prediction of the maximum wall heat flux found in numerical results could be due to the overestimation of the gas temperature inside the chamber. And the cause could be the neglect of the radiative heat transfer. On the other hand, the under-estimation of conductive flux, obtained in LES, in the cold regions of the quartz ($x < 0.06$ m and $x > 0.1$ m), where convective transfers are less important, could be compensated, again, by accounting for radiative transfer. Indeed, CO_2 and H_2O are present with a mass concentration respectively of 14 % and 13 % and they are two highly participating media that can contribute to a redistribution of temperature field inside the combustion chamber, affecting consequently the wall heat transfer.

4.7 Conclusions

The present chapter reports large eddy simulations of the application target of this thesis work, the Oxytec chamber. It is a semi-industrial burner equipped with an axial-plus-tangential swirler where methane and air are premixed before entering the combustion chamber. The chamber is also equipped with quartz walls that allow full optical access to the combustion region to visualize the flame.
First, the Oxytec chamber has been presented, together with the available experimental measurements and a short summary on the experimental works carried out by the experimental team of the EM2C laboratory. Then first numerical results of the Oxytec chamber have been presented.
In a first step, LES of non reacting flow are carried out in order to validate the computational grid and the sub-grid model through comparison with experimental data. An analysis of the numerical results has allowed to better characterize the flow topology of this axial-plus-tangential burner: the W-shape of the axial velocity field, internal and external recirculation zones are retrieved. Comparison between experiments and numerical results show a fair global good agreement and the set up used for cold flow simulation has been retained also for reacting flow LES.
In a second step, the reacting flow of the premixed methane air flame is simulated by imposing the measured temperature on chamber walls. The definition of a criterion to evaluate the convergence of the simulation of the Oxytec chamber has been necessary, since the burner is characterized by a large residence

time, yielding a long thermal transient. Several integrated quantities are compared, such as the evolution of the wall fluxes and the mean temperature inside the combustion chamber. A physical time of 1.3 seconds is retained to get over the transient and reach the permanent regime.
LES results of the reacting flow are compared with available measurements such as PIV, OH^* and OH-PLIF images. Flow characteristics and flame topology are investigated and compared to experiments, showing a good agreement. Then, heat transfer results are presented in terms of enthalpy balance, gas temperature and conductive fluxes. A fair agreement is found on thermal fields, however discrepancies appear which may be attributed to the neglect of radiative heat transfer in such simulation. For this reason, radiative heat transfer is taken into account through accurate methods in the coupled combustion-radiation simulations presented in the next chapters.

Chapter 5

Modelling and accuracy in numerical set-up of coupled LES-Monte Carlo simulations

The objective of this chapter is to introduce the coupling between the LES fluid solver, AVBP, and the Monte Carlo radiation solver, Rainier. Given the computational cost of a coupled LES-MC simulation, an analysis is carried out in terms of accuracy and computational cost. Two important parameters are retained in such an analysis: the size of the computational grid used for radiation simulations and the coupling frequency between fluid and radiation solver. Their impact on the computational cost of a coupled simulation is derived and several scenarios are defined.

Successively, the numerical set-up of coupled simulation is described, focusing on the the radiation solver Rainier. A Randomized Quasi-Monte Carlo method is used, combined with the ERM version. Since the ERM allows to control the local convergence, convergence criteria are defined and the values imposed in the simulations are justified.

The boundary conditions imposed in Rainier are also specified with a special attention to the modeling of the transparent quartz viewing windows of the Oxytec chamber.

Contents

5.1 Introduction

In a coupled simulation, two or more solvers exchange information at a given coupling frequency. The kind of information depends on the phenomena that are coupled during a simulation. For instance, when combustion is coupled to radiation, as it is done in this thesis, the radiation solver needs input fields of gaseous temperature, pressure and species concentration in order to solve the RTE, as well as wall temperature which are imposed in the boundary conditions. The fields needed by the radiation code are sent by the fluid solver at each coupling time step. The output of the radiation solver is the radiative power field P^R, that, at each coupling time step, is sent to the fluid solver that put the radiative source term in the energy equation. A scheme about solver communication is given in Fig. 5.1, where the name of the solvers and the exchanged variables are specified.

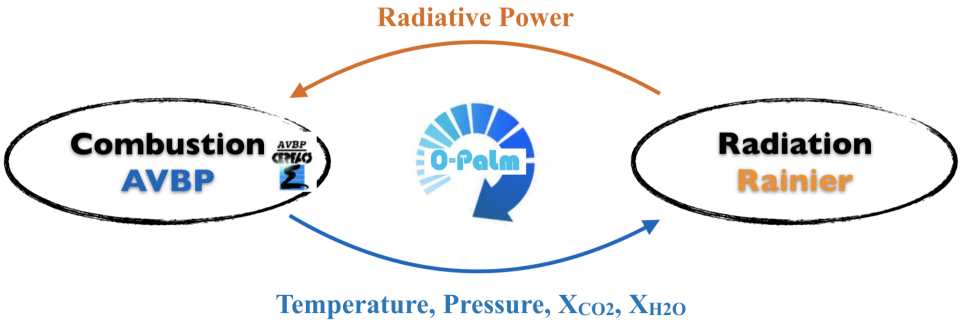

Figure 5.1: *Scheme of coupling between flow solver (AVBP) and radiation solver (Rainier) indicating the variable fields exchanged by the solvers.*

The advantage of a coupled simulation is the possibility to use dedicated codes for each simulated phenomenon. Indeed, each code has its own system of equations, and fluid and radiation solvers solve their own equations independently from each other, until the coupling is performed.

One of the questions that arise when a coupled simulation is performed concerns the coupling frequency, i.e. how often fluid and radiation solvers exchange data. Such frequency has an impact on both the accuracy of the results and the computational cost of a coupled simulation.
Another parameter which affects accuracy and CPU cost is the number of nodes in the computational grid used by the radiation solver.
When LES is coupled to accurate MC methods, the cost of a simulation can be even 10 times larger than the cost of a combustion simulation. For this reason a compromise between accuracy and CPU cost need to be found in order to make a coupled LES-MC simulation affordable for practical 3D configurations. The use of QMC methods instead of classic MC ones allows to decrease the computational cost by a factor 2 or 3, depending on the configuration. Thus, coupling frequency and mesh size are retained as the main parameters impacting the CPU cost of a simulation and an analysis of their influence on the CPU cost is given in the following section.

5.2 CPU cost-accuracy analysis for the set-up of coupled simulations

5.2.1 Choice of mesh size for radiative simulation

Given the high computational demand of a coupled simulation, a mesh convergence is performed where three computational grids are compared, here named: Mesh 1, Mesh 2 and Mesh 3.
The Mesh 1 is the same computational grid of LES simulations presented in chapter 4. Whereas Mesh 2 and 3 are characterized by grid cells sizes that are 1.5 and 2 times larger, respectively, than Mesh 1. The three computational grids are shown in Fig. 5.2.
The characteristics of the three analyzed meshes are summarized in Tab. 5.1

Mesh	Millions cells	Millions nodes	Min. cell size [mm]
1	50	9	0.5
2	22.4	4	0.75
3	15.2	2.7	1.0

Table 5.1: *Computational grids used in mesh convergence tests.*

Mesh 2 and 3 are also characterized by a coarser grid in those parts of the

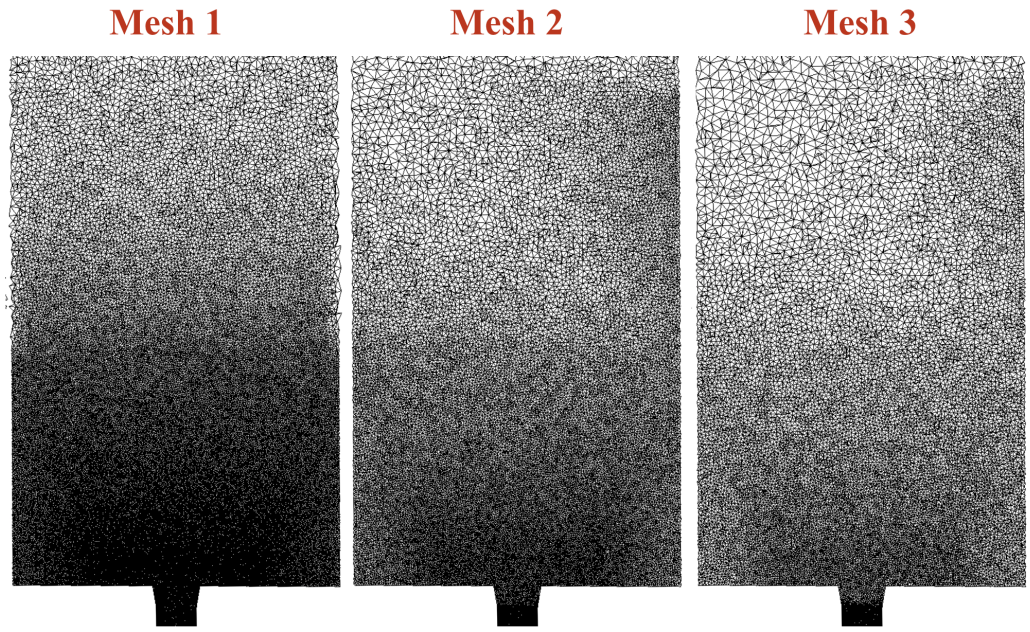

Figure 5.2: *Visualization of the three computational grids compared in the mesh convergence tests: Mesh1, Mesh2 and Mesh3.*

domain where the radiative power is not solved; this is the reason for which there is no perfect proportionality among the number of cells and nodes of the three retained grids.
These three grids are compared in terms of surface integrated radiative fluxes. Radiative heat transfer simulations, for the three investigated cases, are performed with the following convergence criteria:

- Relative error : 2 %;
- Absolute error for Radiative Power : 1 % of maximum radiative power;
- Absolute error for Radiative Flux : 1 % of maximum radiative flux.

The solution obtained with the Mesh 1 is considered as the reference one, then the solutions obtained with Mesh 2 and 3 are compared to the reference solution. The error obtained with the coarser meshes is evaluated as:

$$\epsilon_{\phi,i} = \frac{\phi_i^{rad} - \phi_1^{rad}}{\phi_1^{rad}}$$

where ϕ_i^{rad} is the surface integrated radiative flux obtained with the Mesh i and ϕ_1^{rad} is the surface integrated radiative flux obtained with the Mesh 1. Such an error, together with the ratio of CPU cost needed for the Mesh 1 to the CPU cost for the Mesh i, is summarized in Tab. 5.2.

Mesh	ϵ_ϕ [%]	CPUh ratio [-]
1	-	-
2	1.7	3
3	3.2	5.6

Table 5.2: *Error on radiative flux ϵ_ϕ and decreasing of CPUh compared to Mesh 1 for the investigated computational grids.*

The size of the computational grid used by the radiation solver is not the only parameter considered in the analysis about CPU cost and accuracy. Another parameter is retained in this study, the coupling frequency, and it is evaluated in the next section.

5.2.2 Choice of coupling frequency

The coupling procedure between the two codes is based on a parallel coupling: once the necessary information is exchanged between solvers, they carry out their separate computations concurrently on a separate set of cpu cores. An important parameter to be considered in a coupled simulation is the coupling frequency., i.e. the number of interactions between the LES solver and the MC solver. The two codes exchange data every coupling time step, Δt_{cpl}. Ideally, the codes should exchange data each iteration, as shown in the scheme presented in Fig. 5.3 (top): for each iteration of the LES solver, Rainier performs one simulation and the output is returned to AVBP, and so on. In practice such a simulation is very expensive and it becomes unaffordable for real 3D configurations.

In order to make a coupled simulation more affordable, the number of iterations performed by the LES solver before interacting with the radiation solver, N, is retained as parameter (see Fig. 5.3 (bottom)) , and it represents a compromise between the cost of a simulation and the accuracy of the results.

In literature a precise metric to choose the frequency coupling does not exist. In this context, the metric used by Rodrigues et al. (2018) is retained in order to estimate the error associated to the coupling frequency: a simulation characterized by an intense codes communication, in which the two codes interact every iteration of the LES solver, is performed. This strategy aims to find a threshold on the number of iterations of the fluid solver to keep the accuracy acceptable. At the first iteration, indicated with the subscript 0, AVBP computes the flow fields, for example the temperature, and pass them to Rainier, which in turns computes the radiative power field associated to its input data. Temperature and radiative power fields at the reference iteration are defined as T_0 and P_0^R respectively. Then, the calculation goes on for N iterations of the fluid solver and the corresponding temperature and radiative power fields are T_N and P_N^R.

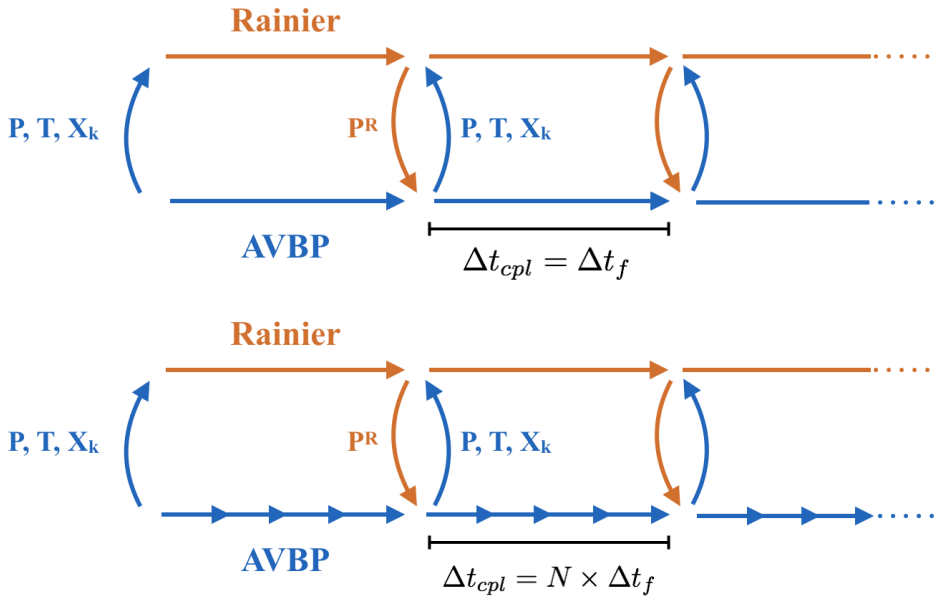

Figure 5.3: *Scheme of coupling between the fluid solver, AVBP, and the radiation solver, Rainier, exchanging data at every iteration of the fluid solver (top) and every N iterations of the fluid solver (bottom).*

The error is evaluated in terms of L2 error norms, $\alpha_T(N)$ and $\alpha_{PR}(N)$, of temperature and radiative power:

$$\alpha_T(N) = \sqrt{\int_V |T_N - T_0|^2 \, dV} \Big/ \sqrt{\int_V |T_0|^2 \, dV} \tag{5.1}$$

$$\alpha_{PR}(N) = \sqrt{\int_V \left|P_N^R - P_0^R\right|^2 dV} \Big/ \sqrt{\int_V \left|P_0^R\right|^2 dV} \tag{5.2}$$

$$\tag{5.3}$$

The norms are integrated over the volume of the whole combustion chamber. The evolution of $\alpha_T(N)$ and $\alpha_{PR}(N)$ as a function of the number of fluid iterations, N, is shown in Fig. 5.4. It can be observed that if the codes are coupled every 440 iterations of the fluid solver the error $\alpha_{PR}(N)$ is lower than 2%. Fig. 5.4 can then be used to determine the number of iterations N that the LES solver performs before exchanging information with the radiation solver, in order to have $\alpha_T(N)$ and $\alpha_{PR}(N)$ lower than a given threshold. These informations, together with the results of the mesh convergence are both taken into account to estimate the computational cost of a simulation, and the corresponding analysis is presented in the next section.

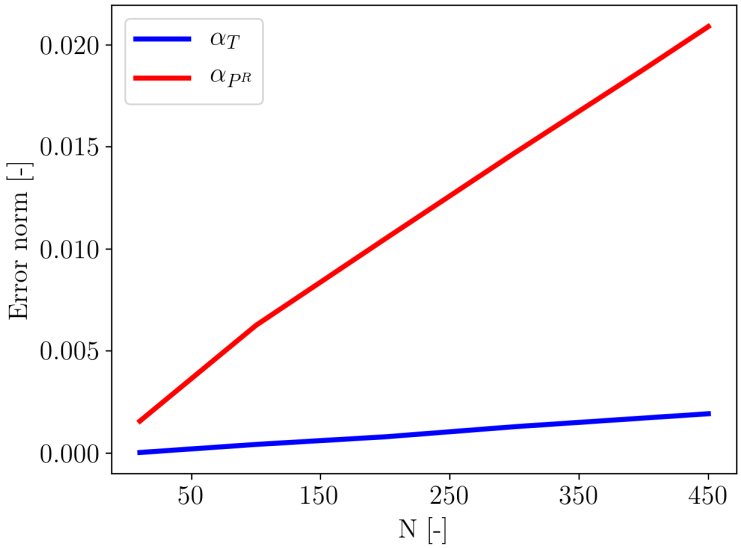

Figure 5.4: *Evolution of L2 error norms of temperature (α_T) and radiative power (α_{PR}) as a function of the fluid solver iteration N.*

5.2.3 CPU-cost accuracy trade off

The influence of the two investigated parameters, mesh size and frequency coupling, on the computational cost of a coupled simulation is now analyzed. In Fig. 5.5, all these informations are summarized: the one axis represents the size of the computational grids used for radiative heat transfer simulations; another axis displays the number of iterations performed by the fluid solver during a coupling time step and in round brackets the corresponding error associated to the coupling frequency (α_{PR}); the vertical axis represents the millions of CPU hours needed by a coupled simulation of 200 ms of physical time. The green blocks corresponding to the highest coupling frequency are scaled by a factor 50.
Looking at the Fig. 5.5, several scenarios can be defined.

Scenario 1: Optimistic AVBP and Rainier are coupled at each time step of the fluid solvers (green bars). If a refined mesh is used for MC simulations, simulating 200 ms of physical time in a coupling framework would cost around 4.4×10^8 CPU hours. Assuming to run on 2400 cores architecture, such amount of computational time corresponds to 20 years of wall clock time. The Scenario 1 corresponds to the highest accuracy attainable in such a coupled simulation, however the computational cost associated to this configuration makes such a computation unaffordable.

Scenario 2: Pessimistic The coarser grid is retained for Rainier simulations

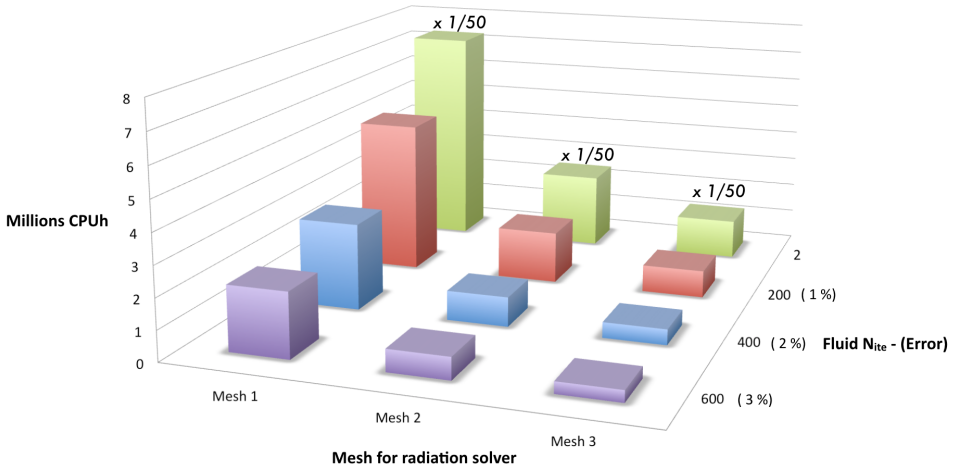

Figure 5.5: *3D bar graph displaying the millions of CPUh needed to simulate 200 ms of physical time (vertical axis), the computational grid used by the radiation solver (x axis) and the number of iteration performed by the fluid solver and the respective coupling error in brackets (y axis). Green bars are resized by a factor 50.*

(Mesh 3 with 2.7 millions nodes), while AVBP and Rainier are coupled every 600 iterations of fluid solver (corresponding to a coupling error of 3 %). In such a configuration, 200 ms of coupled simulation would take one week of parallel computing on 2400 cores to end up, with a computational cost of around 400 000 CPUh. Such scenario, which is 1000 times less expensive than the Scenario 1, would represent the most practical choice but also the lowest attainable accuracy.

Scenario 3: Intermediate #1 One possible intermediate scenario can be defined considering an intermediate mesh size for radiation, the Mesh 2, and an intermediate error associated to the coupling frequency (2 %). It corresponds to the blue bar in the middle, characterized by a computational demand of 1 million CPUh, or equivalently 20 days running the simulation at 2400 cores. However, when a computation is run on HPC, one should also consider the waiting time due to the fact that the necessary cores are not always available. Moreover, the analysis on the convergence time of the Oxytec chamber presented in the precedent chapter, has shown that 200 ms are not enough to converge a simulation. If at least 500 ms have to be simulated in order to consider a solution converged, and if 100 ms more are then considered to get the statistics, the real cost of a simulation would be 3 times more expensive. As a consequence, 600 ms of simulated physical time would take 60 days without considering cores unavailability, which means three or more months of calculation before getting a converged solution. For this reason an other intermediate scenario is defined.

Scenario 4: Intermediate #2 The same computational grid retained for the Scenario 3 is chosen, Mesh 2, but a coupling error a little higher (3 % instead of 2 %). It corresponds to the purple bar in the middle of the diagram. The resources necessary to simulate 200 ms of physical time lowers to 700 000 CPUh. Then to converge the calculation, around one month is necessary, running at 2400 cores.

Given the availability of computer resources and considering the time needed to end up a computation, the configuration chosen for the coupled simulations that will be presented in the next chapter, is the one of the Scenario 4. Then, to satisfy the 3% of frequency coupling error, AVBP and Rainier are coupled every $N = 600$ iterations of the fluid solver, AVBP. The AVBP time step is limited by the acoustic time scale and it is equal to $\Delta t^{AVBP} = 9 \times 10^{-8} s$. Consequently AVBP and Rainier are coupled every $\Delta t_{cpl} = 600 \times \Delta t^{AVBP} = 5.4 \times 10^{-5} s$, where Δt_{cpl} stands for the coupling period.
With the configuration of the Scenario 4, a coupled simulation becomes 3.3 times more expensive than a combustion simulation in AVBP when QMC are used. Instead, if a classical MC method is applied, a coupled simulation would be more than 6 times more expensive than a combustion simulation.

The coupled simulation presented in the next section has been run on a cluster equipped with Intel E5-2690 processors. In order to minimize the time that a code would spend in waiting for the other code to finish its defined iterations number, a balance of the cores is needed. The cores repartition adopted for the coupled simulations of this study is shown in Tab. 5.3.

Codes	AVBP	Rainier
Number of processors	750	1770

Table 5.3: *CPUs repartition between AVBP and Rainier codes in coupled simulations.*

The balance is obtained attributing 1770 cores to Rainier code while 750 cores are dedicated to AVBP. Dedicating a larger number of cores to Rainier does not allow to obtain a good scalability for the considered mesh. For this reason, 1770 cores have been retained for radiative heat transfer simulations. Moreover requiring more than 2500 cores, would have increased the waiting time for a job to be started. Since in Rainier every node is charged by the whole mesh and solution, nodes characterized by 128 Gb of memory have been used.

5.3 Numerical set-up

The set-up of the fluid solver AVBP is the same as the one presented in Chapter 4. For this reason the attention is here paid to the numerical set-up of the

radiative heat transfer solver.
Concerning the radiation part of the coupling, the Rainier code is used. It solves the radiative transfer equation with Monte Carlo methods. For coupled simulations, the Randomized Quasi Monte-Carlo method (Lemieux 2009) illustrated in Chapter 3 is used, based on Sobol low-discrepancy sequences from Joe and Kuo (2008). This method allows to increase the efficiency of the classical Monte Carlo method (Palluotto et al. 2017) and to make the computation more affordable. The Randomized QMC is combined with the ERM method (Tessé et al. 2002) to compute the radiative power field and the radiative flux.
Only the radiative properties of CO_2 and H_2O are considered since the contribution of other participating species is at least one order of magnitude lower than those ones of CO_2 and H_2O in this kind of flame (Rivière and Soufiani 2012). Spectral radiative properties of gases are accounted for through a narrow-band approach, the c-k model (Goody et al. 1989) based on updated parameters of Rivière and Soufiani (2012).

5.3.1 Coupling framework

The coupling between the fluid solver AVBP and the radiation solver Rainier is achieved through the use of the OpenPALM coupler (Duchaine et al. 2015) codeveloped by CERFACS and ONERA. The OpenPALM software allows the concurrent execution of in-house or commercial codes with the help of three main libraries: PALM, CWIPI and PrePALM.

The PALM (Projet d'Assimilation par Logiciel Multimethodes) library manages the parallel communications for data exchanging and the launching of the coupled applications which are split into elementary components. PALM behaves like an interface between the codes since each coupled code sends its own data to the palm application which in turns redistributes the information (Buis et al. 2006).

The CWIPI (Coupling With Interpolation Parallel Interface) library is an interpolations tool. It is in charge of the mesh based coupling between the codes with MPI communications (Refloch et al. 2011). Indeed, the mesh used by the different codes can be non conforming, then an interpolation is needed. In CWIPI, coupling can be made through 1D, 2D or 3D exchange zones with all types of geometrical elements with an unstructured description. The communication graph created by CWIPI between distributed geometric interfaces is optimized for High Performance Computing (HPC) applications in order to minimize the global cost of the parallel communications.

OpenPALM applications are implemented via a graphical user interface (GUI): PrePALM. It allows for an easy creation of the coupling between the different codes: links and communications between the different codes are created

through this interface.

5.3.2 Convergence criteria for Rainier in coupled simulations

One of the main interests of the ERM method, retained in this study, is the possibility to control the local convergence. Therefore, local convergence criteria are imposed.
For radiative heat transfer simulations a relative error of 3% is fixed; an other threshold has to be imposed to avoid huge number of realizations when radiative power is close to zero. Thus, an absolute error is also imposed to consider a point converged when the absolute value of the statistical error (RMS) is lower than a given value. This value represents the percentage of the maximum absolute value of the radiative power (or equivalently of the radiative flux when the computation concerns the walls of the chamber).

First, an analysis has been performed in order to find an optimal value of the flux absolute error and the impact of this parameter on the flux estimation is quantified. Then, the same analysis has been performed for the choice of the absolute error of the radiative power. This is done to find a good compromise between accuracy of results and CPU cost of the calculation.
An instantaneous snapshot of a 3D LES performed in non-adiabatic conditions (as the ones presented in Chapter 4) is retained for radiative heat transfer simulations.
Four values of absolute errors are investigated: 0.8 % (2000 W/m^2), 1.2% (2000 W/m^2), 1.6% (4000 W/m^2) and 2% (5000 W/m^2). For each case the maximum error on flux estimation is evaluated as the ratio between the surface integral of the radiative flux on the chamber walls and a reference value which is obtained from a computation performed with strict convergence criteria (relative error lower than 2% and absolute error lower than 1%).
In Tab 5.4, for each investigated case, the maximum error on flux estimation, the CPU time needed by the simulation and the number of realizations needed to converge the simulation are illustrated. All the tests have been performed with 960 cores.

Absolute Error (%)	Error on Flux Estimation (%)	CPU time (s)	Realizations
0.8	-	22000	7 000 000
1.2	2.7	1365	1 000 000
1.6	2.9	115	800 000
2	7.6	59	8 000

Table 5.4: *Effect of the choice of the flux absolute error fixed in radiative simulations in terms of accuracy and CPU cost.*

In order to keep the error below the 3% on the flux estimation, an absolute error of 1.6% for flux computation is retained in the setup of the coupled radiative simulations and in the tests presented in the following.

The same analysis is performed to choose the absolute error for the computation of the radiative power inside the combustion chamber. In this test, both domain and walls are resolved in the Rainier computation. Five values of absolute errors are investigated: 0.8 % (16000 W/m^3), 1.6% (32000 W/m^3), 2.5% (48000 W/m^3), 4% (78000 W/m^3) and 5% (97000 W/m^3). Their impact on the volume integral of the radiative power is quantified with the same approach of the previous test.
Table 5.5 summarizes, for each investigated case, the maximum error on the radiative power estimation and the CPU time needed by the simulation. Once again, all the tests have been performed with 960 cores.

Absolute Error (%)	Error on Rad. power Estimation (%)	CPU time (s)
0.8	-	1000
1.6	0.17	660
2.5	0.4	550
4	0.5	539
5	0.53	538

Table 5.5: *Effect of the choice of the absolute error fixed in radiative simulations in terms of accuracy and CPU cost.*

It can be seen that the CPU time decreases for higher absolute errors because a larger number of points are considered converged and consequently excluded from the computation. The decreasing of CPU time is not significant above 2.5% of absolute error; for this reason this value is retained in the setup of the performed simulations.

5.3.3 Boundary conditions

For the fluid solver AVBP, the boundary conditions are the same as the ones indicated in Chapter 5: measured wall temperature are imposed. Only the boundary conditions for the MC solver are illustrated in the following.

The numerical domain used for the radiative heat transfer simulations differs a little from the real domain, since the metallic bars present at the corners of the chamber are not included. As a consequence, all the lateral walls of the chamber are considered as made in quartz.
The following boundary conditions are considered for the radiative heat transfer solver:

- Inlet and outlet are considered as a black body at a far-field temperature equal to 300 K.

- The bottom chamber and the convergent tube are composed of stainless steel 316L. They are considered opaque and the value chosen for their global emissivity is taken from Hunnewell et al. (2017). In this study the total hemispherical emissivity is measured, i.e. averaged with respect to all wavelengths and directions. It is shown that the emissivity of the stainless steel strongly depends on surface conditions, and that it can vary from 0.3 in "as received from the manufacturier" conditions, to 0.6 in "oxidized in air" conditions. But it also depends on temperature. Given the range of measured temperatures of wall chamber (400-700 K) and convergent (700-900 K) a value of 0.28 has been retained for the bottom chamber and 0.32 for the convergent.
  Regarding the temperature, measured temperature profiles from Degenève et al. (2019a) are imposed.
- For the fused silica VI 942 quartz windows, the measured temperature is imposed. From a radiative point of view they are considered as semi-transparent. Detailed radiative properties for these boundary conditions are considered, accordingly to the methodology applied by Rodrigues et al. (2018). The imposed radiative properties are detailed in the next section.

Quartz radiative properties

For the following, it is helpful to introduce the complex index of refraction:

$$m_\lambda = n_\lambda - ik_\lambda \tag{5.4}$$

where the real part, n, is the refractive index and the imaginary part, k, represents the absorptive index. The absorption coefficient or attenuation factor is expressed as:

$$\kappa_\lambda = 4\pi k_\lambda / \lambda \tag{5.5}$$

The transmittance τ_λ is expressed as:

$$\tau_\lambda = exp(-\kappa_\lambda s) = exp(-4\pi k_\lambda s/\lambda) \tag{5.6}$$

where s is the slab thickness. In Fig. 5.6 the transmissivity curve as a function of the wavelength λ provided by the manufacturier (Verre Industrie) is shown. Knowing τ_λ from the Fig. 5.6, it is possible to determine the absorption coefficient κ_λ, and then the absorptive index k_λ.
From Fresnel's relations for an interface between a solid with refractive index $n_{2,\lambda}$ and absorptive index $k_{2,\lambda}$ and an absorbing medium characterized by $n_{1,\lambda}$,

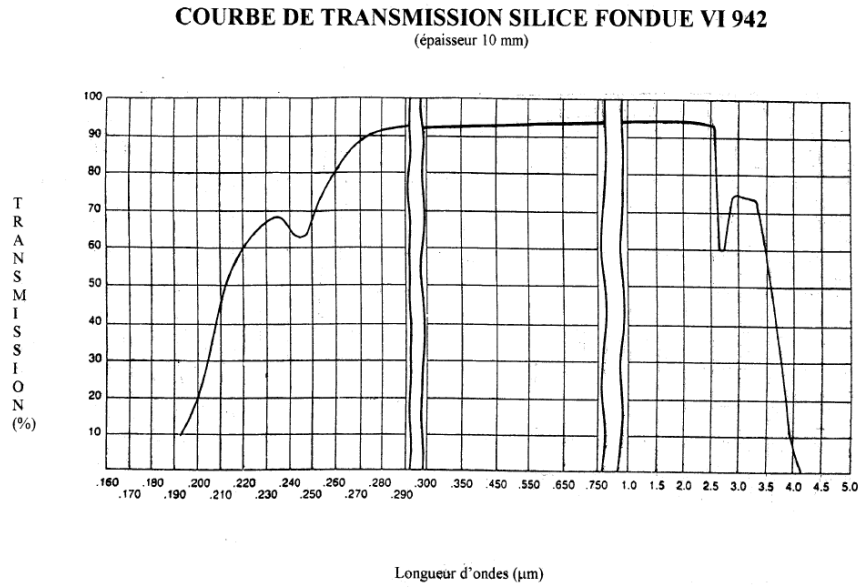

Figure 5.6: *Transmissivity of a 10 mm window of fused silica VI 942 between 0.16 µm and 5.0 µm. Data provided by Verre Industrie.*

and for normal incidence, it is possible to calculate the reflectivity ρ_λ of the material as:

$$\rho_\lambda = \frac{(n_{1,\lambda} - n_{2,\lambda})^2 + k_{2,\lambda}^2}{(n_{1,\lambda} + n_{2,\lambda})^2 + k_{2,\lambda}^2} \tag{5.7}$$

Considering an interface with air ($n_1 = 1$) and a value of $n_2 = 1.4585$ provided by the manufacturer, ρ_λ is then computed:

$$\rho_\lambda = \frac{(1 - n_{2,\lambda})^2 + k_{2,\lambda}^2}{(1 + n_{2,\lambda})^2 + k_{2,\lambda}^2} \tag{5.8}$$

Consequently the spectral emissivity is given by:

$$\epsilon_\lambda = \alpha_\lambda = 1 - \tau_\lambda - \rho_\lambda \tag{5.9}$$

From Modest (2013) it is possible to define a slab absorptance, transmittance and reflectance to take into account multiple reflections inside the quartz:

$$A_\lambda^{slab} = \frac{(1 - \rho_\lambda)(1 - \tau_\lambda)}{1 - \rho_\lambda \tau_\lambda} \tag{5.10}$$

$$T_\lambda^{slab} = \frac{(1 - \rho_\lambda)^2 \tau_\lambda}{1 - \rho_\lambda^2 \tau_\lambda^2} \tag{5.11}$$

$$R_\lambda^{slab} = \rho_\lambda \left[1 + \frac{(1 - \rho_\lambda)^2 \tau_\lambda^2}{1 - \rho_\lambda^2 \tau_\lambda^2} \right] \tag{5.12}$$

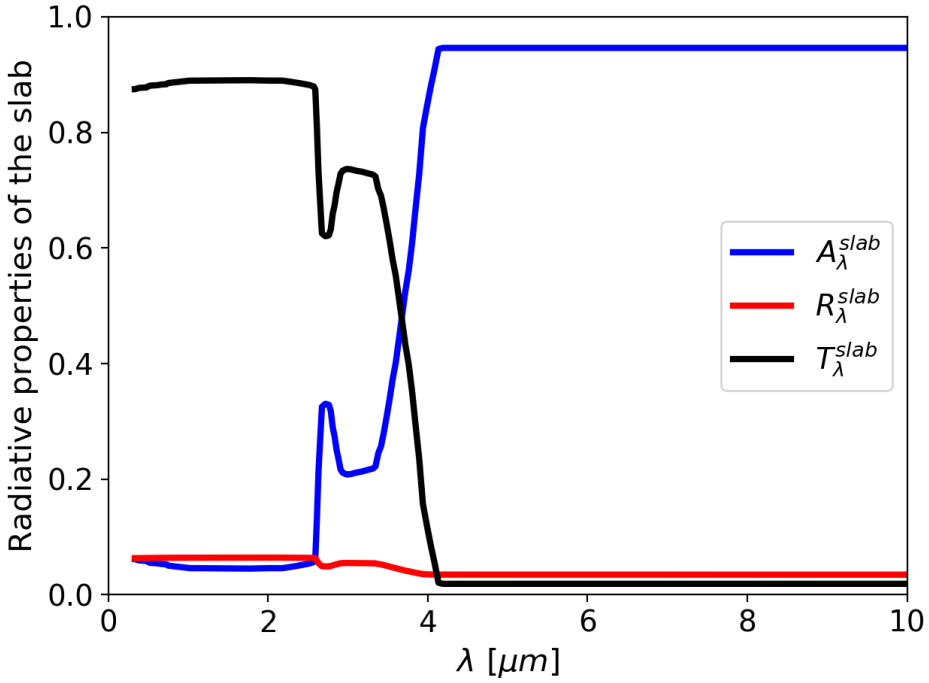

Figure 5.7: *Computed slab absorptance (A_λ^{slab}), transmittance (T_λ^{slab}) and reflectance (R_λ^{slab}) as a function of the wavelength for a 8 mm thickened fused silica VI 942.*

These three quantities are shown in Fig. 5.7 as a function of the wavelength λ for a quartz slab of 8 mm thickness, corresponding to the Oxytec viewing windows. It is worth noticing that for small wavelengths the quartz is transparent characterized by a small reflectivity, while it is transparent and highly absorbing for higher values of λ.

Following the methodology of Rodrigues et al. (2018), the slab radiative properties are simplified in a band model where the bands can only be opaque or transparent. In order to obtain a band model, a criterion has to be found according to which the quartz, for each wavelength λ, is considered as transparent for slab transmittivity values above a threshold value, or opaque for T_λ^{slab} below the given threshold. In the opaque bands, in order to account for the directional dependency of absorptance and reflectance, hemispherical properties are considered and:

$$T_\lambda^{slab,mod} = 0 \tag{5.13}$$

$$A_\lambda^{slab,mod} = A_\lambda^{slab,hem} \tag{5.14}$$

$$R_\lambda^{slab,mod} = 1 - A_\lambda^{slab,hem} \tag{5.15}$$

where $A_\lambda^{slab,hem}$ is equal to the spectral hemispherical emittance $\epsilon_\lambda^{slab,hem}$. How-

ell et al. (2010) provides a formula, given in Eq. (3.20) of their book, to compute the hemispherical emittance as a function of the refractive and absorptive index, n_λ and k_λ.
In the transparent bands, replacing $\tau_\lambda = 1$ in Eq. (5.12), the following modeled radiative properties are considered:

$$T_\lambda^{slab,mod} = \frac{1-\rho_\lambda}{1+\rho_\lambda} \tag{5.16}$$

$$A_\lambda^{slab,mod} = 0 \tag{5.17}$$

$$R_\lambda^{slab,mod} = 1 - T_\lambda^{slab,mod} \tag{5.18}$$

The criterion used to determine the threshold value of the spectral band model consist in finding a switch-value of slab transmittance T_{slab}^{switch} that minimizes the error, ϵ_T, between the evolution of the total transmittance with the temperature and the one obtained with the detailed slab trasmittance T_λ^{slab}:

$$\epsilon_T = \left| \frac{\int_0^\infty T_\lambda^{slab} I_\lambda^0(T) d\lambda}{\int_0^\infty I_\lambda^0(T) d\lambda} - \frac{\int_0^\infty T_\lambda^{slab,mod} I_\lambda^0(T) d\lambda}{\int_0^\infty I_\lambda^0(T) d\lambda} \right| \tag{5.19}$$

For the considered 8 mm quartz slab, the found threshold value is $T_{slab}^{switch} = 0.64$, yielding an average error on the temperature range of interest of 1.97%. The corresponding obtained spectral band model, *i.e.* the modeled radiative properties, is plotted in Fig. 5.8 as a function of the wavelength λ for the 8-mm quartz slab.

5.4 Conclusion

Before showing the results of the coupled simulations of the methane air flame in the Oxytec chamber, attention has been dedicated in this chapter to the description of the numerical set-up of the codes involved in the simulation and the coupling framework.

Before running coupled simulation two questions have arisen: the first one concerns the size of the computational grid used in MC simulations, while the second one is about the coupling frequency. A mesh convergence is performed and three computational grids are compared, a fine one (Mesh 1), an intermediate one (Mesh 2) and a coarse one (Mesh 3). The error associated to the coupling frequency has also been estimated thanks to a metric that computes the L2 error norm of temperature and radiative power as a function of the number of iterations of the fluid solver. Finally the impact of both these parameters, i.e. mesh and coupling frequency, on the computational cost of a simulation has been evaluated and several scenarios have been defined. Among the 4 scenarios, the trade-off between accuracy and CPU cost have been found with an intermediate size mesh for radiation, and coupling fluid and radiation

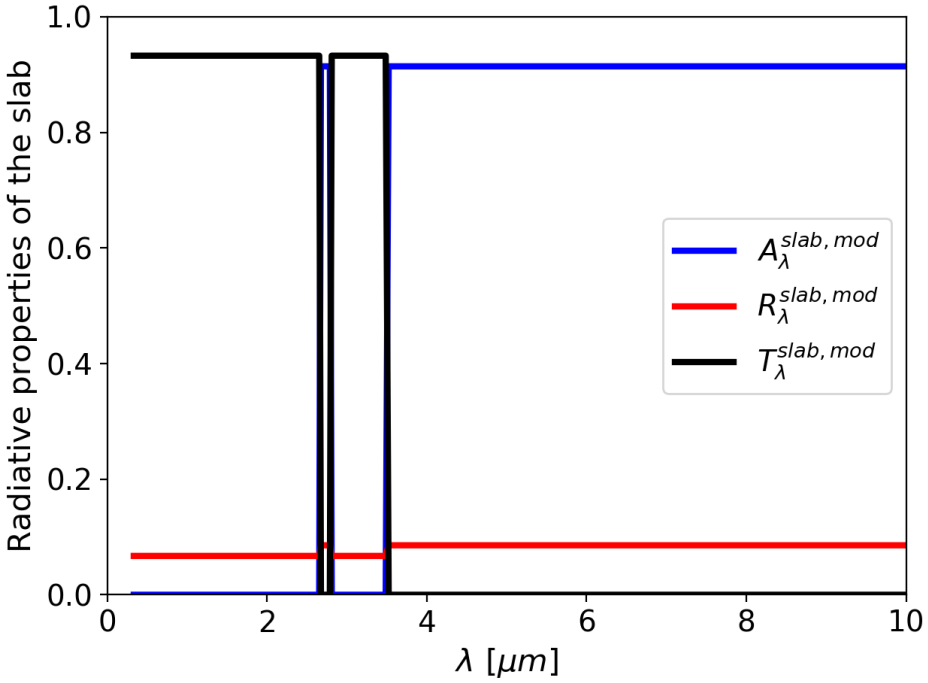

Figure 5.8: *Modeled slab absorptance (A_λ^{slab}), transmittance (T_λ^{slab}) and reflectance (R_λ^{slab}) as a function of the wavelength for a 8 mm thickened fused silica VI 942.*

solver every 54 μs of physical time.
In the description of the coupling framework, most of the attention has been paid to the MC solver Rainier. Randomized QMC is used with its ERM version because of its advantage to control the local convergence. Then, convergence criteria have to be imposed and their choice is justified on a non-coupled radiative heat transfer simulation. The boundary conditions imposed in Rainier also have been detailed with a special attention to the description of the modeling of the spectral radiative properties of the quartz windows surrounding the Oxytec chamber.

Chapter 6

Impact of radiative heat transfer in the coupled simulation of OxyTec flame A

In this chapter, large-eddy simulations of the premixed methane-air flame studied in Chapter 4 are coupled with radiative heat transfer through accurate Monte Carlo methods. The radiative transfer equation is solved using a Quasi Monte-Carlo method with a ck model describing gas radiative properties, as presented in Chapter 3. Spectral radiative properties of the viewing windows confining the flame are taken into account and their impact on the wall radiative flux is quantified, compared to a case with opaque windows. An a-priori estimation of wall radiative flux is also made. The objective of this chapter is to study the impact of radiative heat transfer on the swirled premixed flame of methane and air in the Oxytec chamber. The comparison with the LES results of Chapter 4 allows to highlight the radiation effects on velocity and temperature fields, wall fluxes distribution and flame shape. Numerical results are compared to experimental measurements (PIV, OH chemiluminescence and thermocouples). A spectral analysis about transmissivity of burnt gases present in the different regions of the combustor is also carried out in order to elucidate the interactions between gases inside the chamber and between gas and quartz windows.*

Contents

6.1 Introduction

The prediction of wall fluxes is an important aspect in the choice of materials and design of combustion chambers. For a correct quantification of wall thermal loads, radiative fluxes have to be taken into account, since the heat transfer from flame to the walls is driven, apart from convection, also by radiation of burnt gases inside the chamber.
Moreover, wall fluxes depend on the temperature distribution inside the chamber, and the flow temperature field is, in turn, strongly modified by radiation from hot gases. Accounting for both convective and radiative contributions to wall fluxes requires the simultaneous solution of the radiative transfer equation (RTE) and the governing equations for reactive flows. Indeed, RTE needs variables from flow fields to be solved, and flow field, in turns, needs the radiative source term in the energy equation.
In the coupling between combustion and thermal radiation, attention has to be paid to radiative heat transfer modeling, since a small error in the prediction of the radiative source term may lead to very large error in the energy equation. On the other side, the approach used for fluid simulations is also

important, because local radiative intensity shows a highly non-linear response to temperature and species concentrations. Therefore, accurate calculation of radiative heat transfer requires detailed information in both space and time, regarding temperature and species composition fields. Such information are available only from DNS or LES.
These considerations have been taken into account in the choice of the approaches. For computing thermal radiation, Monte Carlo methods are used, since they allow to control the accuracy of thermal radiation computations. Instead, for turbulent combustion simulation, LES represents a good compromise between the prohibitive cost of DNS and the modeling demand of RANS simulations.
Detailed gas radiative properties of gases are considered, based on a narrow band c-k model. These models, which are more accurate than global models, offer the further advantage to easily account for spectral properties of walls. In this study, spectral properties of the quartz windows confining the flame are considered. More details about the numerical setup of such coupled simulations have been presented in Chapter 5. The configuration retained for the coupled simulation presented in this chapter is the Oxytec chamber described in Chapter 4: a premixed swirled flame fed with methane and air, called Flame A.
The results of coupled LES-MC simulations are presented in the following sections. In the first section, attention is focused on the treatment of quartz windows. A preliminary study is carried out on the importance of considering semi-transparent properties of quartz windows, instead of global properties. Moreover, an a-priori estimation of the wall radiative fluxes is done, by considering an instantaneous LES solution of Flame A. In the second section, the convergence criterion discussed in Chapter 4 is checked. Once the thermal transient terminated, averages are computed. Mean flow fields and flame topology are described, and velocity and heat release fields are compared to experimental data. The comparison with non-coupled simulations of Chapter 4 allows for highlighting the impact of radiative heat transfer on flow and flame topology. The third section is mainly dedicated to heat transfer results: balances of enthalpy and radiative heat transfer are used to quantify the impact of heat losses in the investigated configuration. Temperature and numerical wall heat flux are compared to experimental data. Finally, an analysis of spectral variables is carried out in order to characterize the radiative interactions taking place in the Oxytec chamber.
In the fourth section, the last milliseconds of the pursued coupled simulation are shown.

6.2 Impact of semi-transparent properties of the quartz windows

6.2.1 Planck mean quantities

Starting from the modeled slab properties presented in Chapter 5, the corresponding mean Planck quantities (Transmittance, Absorptance, Reflectance) can be obtained through:

$$T^{slab,mod} = \int_{\lambda=0}^{+\infty} T_\lambda^{slab,mod} I_\lambda^0(T) d\lambda / \int_{\lambda=0}^{+\infty} I_\lambda^0(T) d\lambda \tag{6.1}$$

$$A^{slab,mod} = \int_{\lambda=0}^{+\infty} A_\lambda^{slab,mod} I_\lambda^0(T) d\lambda / \int_{\lambda=0}^{+\infty} I_\lambda^0(T) d\lambda \tag{6.2}$$

$$R^{slab,mod} = \int_{\lambda=0}^{+\infty} R_\lambda^{slab,mod} I_\lambda^0(T) d\lambda / \int_{\lambda=0}^{+\infty} I_\lambda^0(T) d\lambda \tag{6.3}$$

The evolution of these global properties with temperature is shown in Fig. 6.1, for the range of interest, 300 K - 2500 K. It can be observed that when radiation comes from a source at low temperature quartz mostly absorbs, whereas, at high temperature, it is transparent.

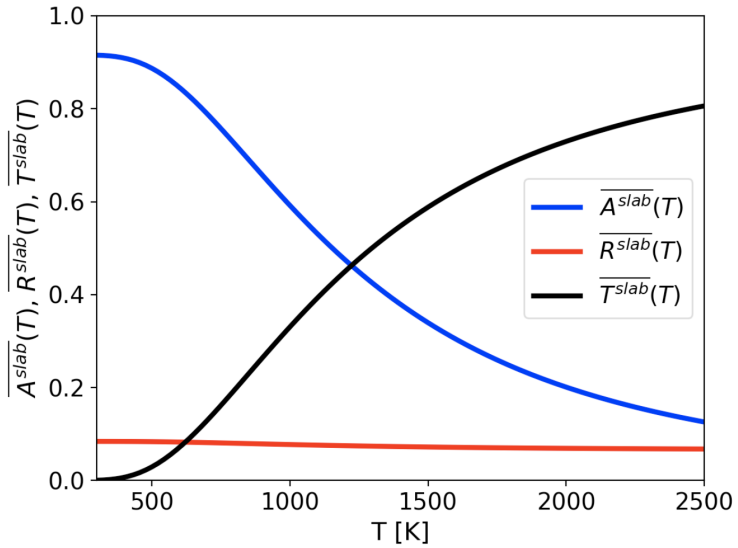

Figure 6.1: *Planck mean modeled slab absorptance* $\overline{A^{slab}(T)}$*, transmittance* $\overline{R^{slab}(T)}$ *and reflectance* $\overline{R^{slab}(T)}$ *as a function of temperature for a 8-mm thickened fused silica VI 942.*

In order to compute the mean Planck emissivity of the quartz surface as a function of the wall imposed temperature, the mean Planck emissivity given

from Eq. (6.2), which in an intrinsic property of the quartz window, is fitted with a a seven order polynomial (through the function *polyfit* in Python) as a function of the local window temperature. The resulting field of wall Planck emissivity is shown in Fig. 6.2: the semi-transparent quartz properties highlight a strong variation with the imposed temperature. As already seen in Fig. 6.1, large values of total emissivity are observed in the colder region of the quartz (lower and upper parts of the quartz) with values varying from 0.4 to 0.8.

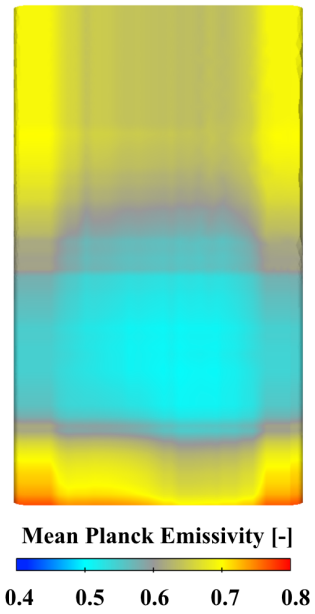

Figure 6.2: *Mean Planck emissivity as a function of the imposed temperature on the quartz surface.*

6.2.2 Opaque and semi-transparent properties of quartz windows

In order to quantify the impact of the semi-transparent properties of quartz on the wall radiative fluxes, two simulations have been performed. Wall radiative fluxes have been calculated in two different conditions, starting from an instantaneous LES solution: in one simulation, spectral properties of quartz are retained (the ones of Fig. 5.8), while in the other case quartz are considered opaque with the following spectral properties:

$$T_\lambda^{slab,mod} = 0 \tag{6.4}$$

$$A_\lambda^{slab,mod} = 1 - R_\lambda^{slab,mod} \tag{6.5}$$

$$\tag{6.6}$$

In Rainier code, the active part of the radiative flux, meaning the part of radiative flux that is absorbed and emitted, but not transmitted by the quartz windows, is computed as the flux exchanged between a face i and a volume cell j:

$$\phi_{rad} = \sum_j \Phi_{ij}^{exch} = \int_0^{+\infty} A_\nu^{slab,mod}[I_\nu^0(T_j) - I_\nu^0(T_i)] \int_{S_i} \int_{4\pi} A_{ij\nu} cos(\theta_i) d\Omega_i dS_i d\nu \tag{6.7}$$

where $A_{ij\nu}$ accounts for all the paths between emission from any point of the cell or face i and absorption in any point of the cell j, after transmission and possible wall reflections, while θ_i is the angle of the path with the surface normal S_i.
ϕ_{rad} is displayed in Fig. 6.3 for both investigated cases. Concerning the quartz, in the opaque case (on the top), radiative fluxes are more intense, compared to the semi-transparent case (on the bottom). Indeed, absorbing (red) and emitting (blue) regions appear wider in the opaque case, and characterized by higher absolute value of wall flux.
It can be seen that the type of the quartz radiative properties also affects the radiative flux on the opaque walls of the chamber (such as convergent and back plate) through the wall-wall exchange and gas-gas exchange. In the case with opaque quartz, the chamber bottom and convergent, but also participating gases, exchange radiative heat transfer with an opaque wall characterized by a higher emissivity compared to the case where quartz are treated as semi-transparent.
Fluxes of Fig. 6.3 are plotted along the axis of one of the 4 quartz windows in Fig. 6.4. The active part of the radiative flux, ϕ_{rad}, in the opaque case (blue line) corresponds to the total radiative flux , whereas in the semi-transparent case (red line) it corresponds only to a part of the total radiative flux, since a part of it is transmitted through the quartz window. For this reason the absolute value of ϕ_{rad} on the opaque quartz is higher than the one obtained in semi-transparent conditions. High radiative flux characterizes the cold regions of the quartz ($X < 0.04$ and $X > 0.15$) in both cases. Its value is larger in the opaque case compared to the semi-transparent one. In the high temperature region, the radiative flux through the quartz windows becomes positive in the semi-transparent cases, while it is around -10 kW/m^3 in the opaque case.
Finally, the radiative flux integrated over the walls is equal to 2.4 kW when quartz are considered semi-transparent, while a value of 3.1 kW characterizes the case with opaque walls.

6.2.3 An a-priori estimation of the radiative flux

It could be interesting to compare the total (convective + radiative) flux for the two investigated cases, opaque and semi-transparent.

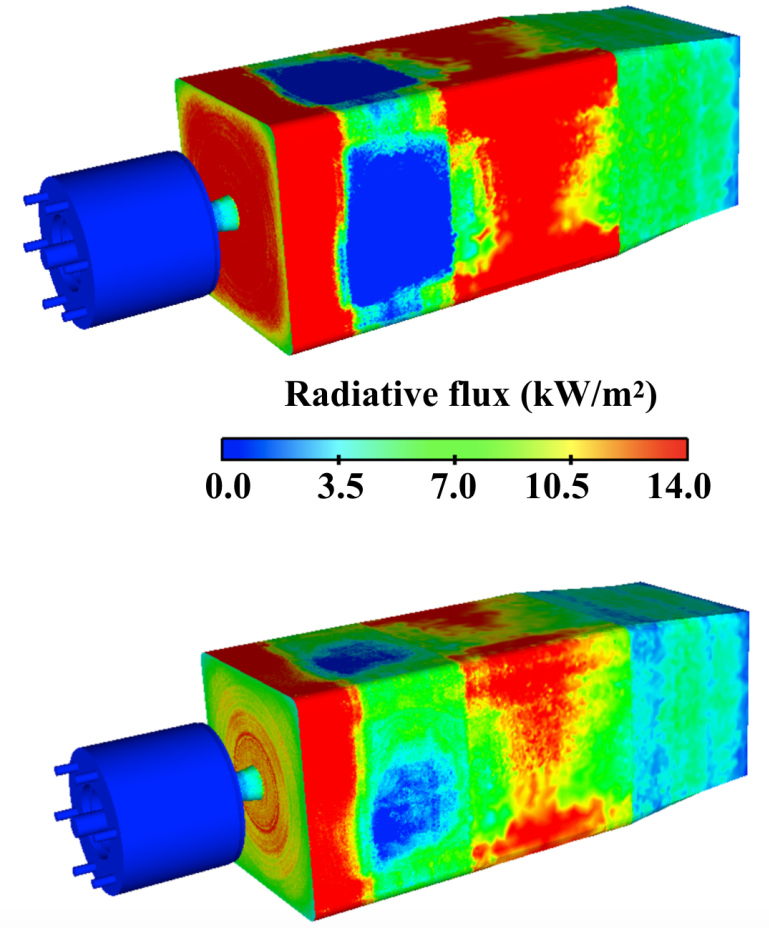

Figure 6.3: *Instantaneous radiative heat flux field on the chamber walls obtained from radiative heat transfer simulations imposing opaque quartz (on the top) and semi-transparent quartz (on the bottom).*

Such estimation is just preliminary, since results are obtained by instantaneous fields taken from LES of Chapter 4, where radiation is not accounted. As a consequence, in this analysis, a big approximation is done: convective flux are supposed to be the same than the ones retrieved in simulations without accounting for radiation. But, in reality, radiation also impacts the convective flux distribution.

To approximatively quantify the effect of quartz properties on the total wall flux, the instantaneous radiative flux issued from radiative heat transfer simulations is added to the mean convective flux issued from non coupled LES simulations of Chapter 4.
In Fig. 6.5 the experimental conductive flux represented by blue dots is com-

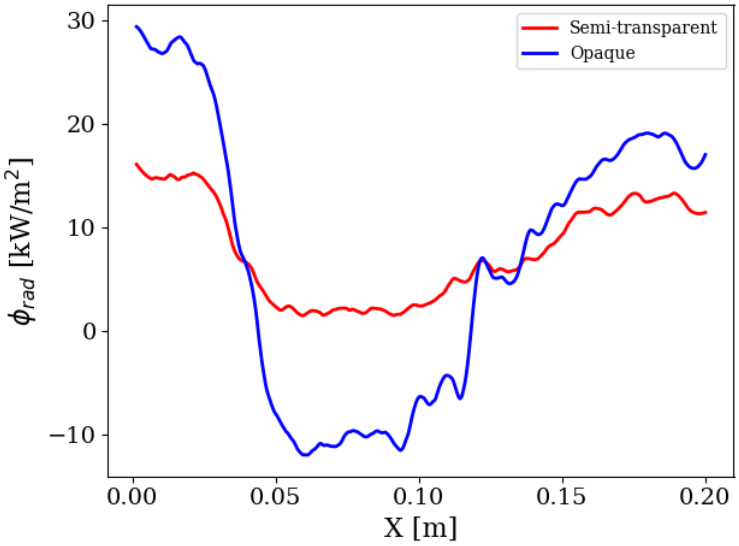

Figure 6.4: *Instantaneous radiative heat flux along the axis of a quartz window in opaque conditions (blue line) and semi-transparent conditions (red line).*

pared to the mean total flux issued from three different cases: a case without radiation (black line) where the total flux is equal to the convective flux, and two cases including radiation and considering the quartz windows as opaque (blue line) or semi-transparent (red line), where the total flux is the sum of convective and radiative components.

It can be observed that when no radiation is accounted for (black line), the maximum wall heat flux is over-estimated, while an under prediction of the total flux is observed in the colder regions of the quartz where x is comprised in [0; 0.05] m and [0.10; 0.20] m, as seen in Chapter 4.

When radiation is considered, the total flux changes depending to the treatment of the quartz windows. In the case with opaque quartz (blue line) the maximum radiative flux is smaller than the case without radiation, and it gets closer to the one obtained in experimental data. The high emission due to the high value of absorptance ($A^{slab,mod}$= 0.93 in the opaque case), together with the high temperature characterizing this region, gives a high negative (thus emitting) radiative flux as seen in Fig. 6.4. In the cold regions, dominated by absorption, and, consequently, by a positive radiative flux, the total flux ($\phi_{conv} + \phi_{rad}$) is higher compared to the non coupled case and to experimental data as well.

On the other hand, when semi-transparent windows are considered (red line), the maximum value of the total flux does not vary compared to the non coupled case (black line) because, as it is shown in Fig. 6.4, ϕ_{rad} is close to zero when X is comprised in [5 cm; 10 cm]. Indeed, this region is actually characterized by high values of transmittivity. This means that most of the radiative flux is

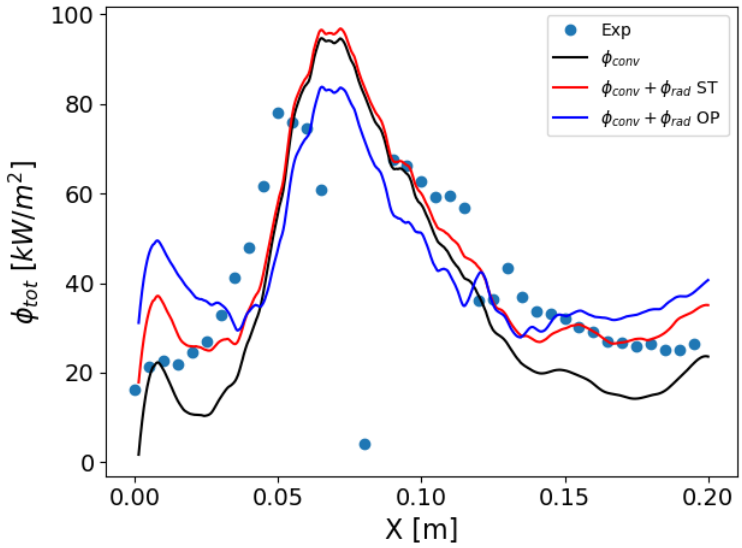

Figure 6.5: *Wall heat flux along the axis of a quartz window in a case without radiation (black line), in a case with radiation and opaque quartz (blue line) and in a case with radiation and semi-transparent quartz (red line). Blue dots are the experimental data of conductive flux.*

transmitted through high temperature quartz region, while the active part of the radiative flux, ϕ_{rad}, is very small (3 kW/m^2).
Concerning the upper and lower parts of the quartz axis, it can be seen that the absorbed radiative flux is significant and helps to compensate the discrepancy appeared between experimental data and convective flux of non coupled simulations, where no radiation is considered.

6.3 Simulation results

6.3.1 Instantaneous fields

Figure 6.6 displays instantaneous fields of axial velocity (on the left) and heat release rate (on the right) in order to visualize both flow and flame topology in the investigated configuration. As already seen in non-coupled simulation, the instantaneous axial velocity field shows the three high velocity regions at the exit burner, a big Inner Recirculation Zone (IRZ) around the chamber axis and two small Outer Recirculation Zones (ORZ) close to the corners of the chamber. The flame (Figure 6.6 right) has a V-shape, it is stabilized upstream the IRZ and, at the retained instant of simulation, it slightly enters the burner, in the location where it is anchored to a small recirculation bubble near the injector.

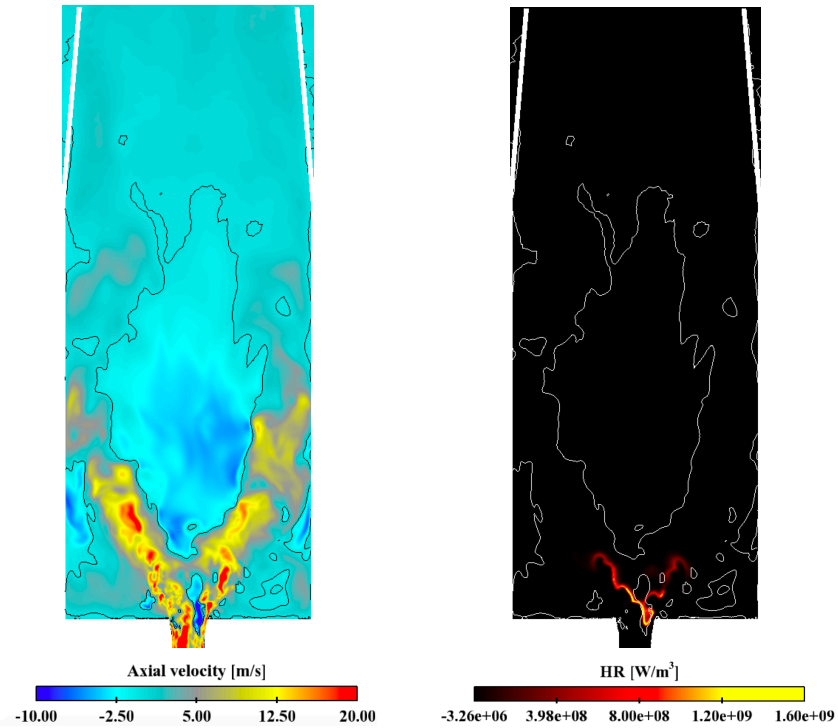

Figure 6.6: *Instantaneous field of axial velocity (left) and heat release rate (right) on a longitudinal plane of the chamber. Black and white lines are iso-contour of axial velocity equal to zero.*

In Fig. 6.7, instantaneous fields of temperature, CO_2 molar fraction and radiative power are shown. The radiative power is strongly linked to temperature field and to the presence of participating gases. High temperature regions are characterized by negative radiative power; since P^R is given by the difference between absorbed and emitted radiative power, such regions are characterized by a high emitted radiative power. On the contrary, in colder regions, such as the pockets located in the outer recirculation zones or the ones downstream close to the walls, the radiative power is positive, as these regions are dominated by re-absorption.

A simplifying approximation in radiative transfer is to consider the gas as optically thin, meaning that the radiative power absorbed by the gas is neglected. In order to visualize the error that such approach may lead, Fig. 6.8 shows the instantaneous field of radiative power in the investigated case (left), where absorption is considered, and in the optically thin case (right). If the absorbed radiative power is neglected, the radiative power becomes equal to the opposite of emitted power: $P^R = -P^e$.

Integrating the radiative power in these two cases, one obtains that the radiative source term in the energy equation is equal to 2.8 kW in the real case,

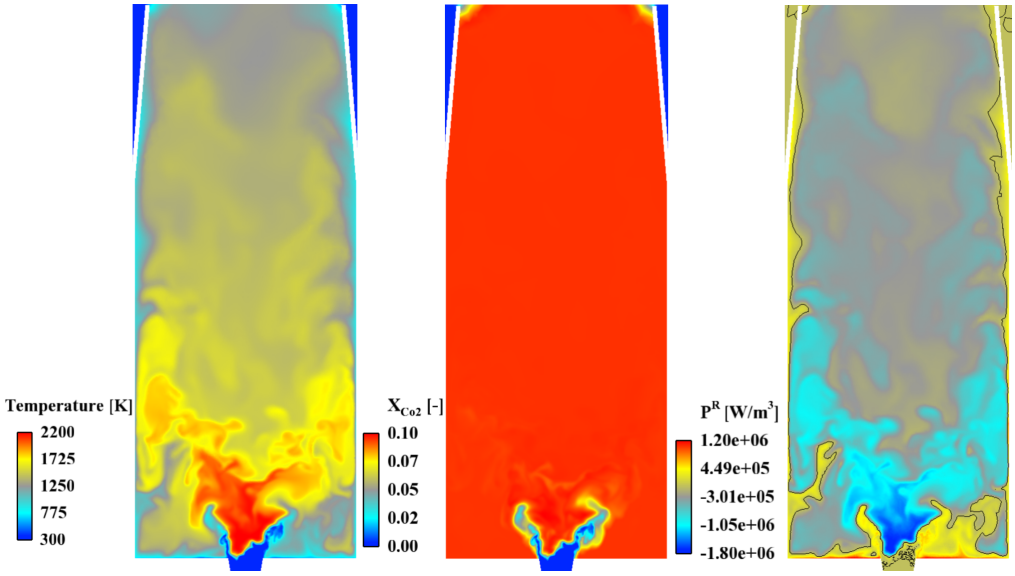

Figure 6.7: *From left to right: instantaneous field of temperature, CO_2 molar fraction and radiative power on a longitudinal plane of the chamber. Black lines are iso-contour of P^R=0.*

while it increases to 10.4 kW in the case where the absorption is neglected.
From this analysis, it comes out that, in the realistic approach, more than 70% of the emitted radiative power (7.6 kW) is reabsorbed by the gas. This demonstrates that the optically thin approach would strongly overestimate the radiative heat losses.
Moreover, the significant value of the radiative source term emerged by such analysis justifies the need to solve the Radiative Transfer Equation in the investigated configuration.

6.3.2 Convergence of coupled LES

The multi-physics simulation presented in this chapter starts from a converged solution of LES presented in Chapter 4.
In order to check the convergence status of such a simulation, the convergence criterion defined in Chapter 4 is used.
The evolution of the volume-averaged temperature inside the volume, during the first 350 ms of coupled simulation, is shown in Fig. 6.25.
At t = 1.08 s, the LES code and radiation solver are coupled to each other. From this moment on, it is possible to see the presence of a thermal transient in the evolution of the averaged temperature inside the chamber.
Because of the introduction of the radiation source term in the energy balance equation, the temperature field inside the combustion is inevitably impacted.
The thermal transient, taking the first 250 ms of physical time, is characterized

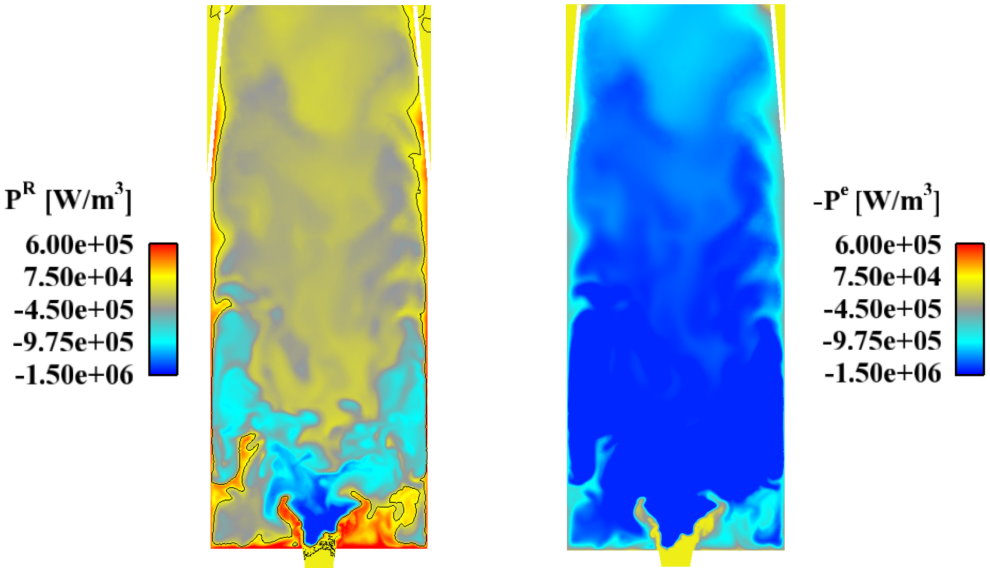

Figure 6.8: *Instantaneous field of radiative power considering the re-absorption on the left and in optically thin case on the right.*

by a strong decreasing of temperature inside the combustor: it lowers from 1450 K to 1385 K. Successively, at $t \approx 1.3$ s the temperature evolution is characterized by small oscillations around the steady state value.
Therefore the last 100 ms, going from 1.29 s to 1.41 s, are retained to average the results and compute the statistics.

6.3.3 Mean fields

In this section, results of coupled simulation are compared to the LES results of Chapter 4 in order to quantify and analyze the impact of radiative heat transfer in the investigated flame on velocity field and flame topology.

Velocity fields

Figure 6.10 shows the mean axial velocity field in the two investigated cases: without radiation (on the left) and with radiation (on the right) compared to experimental PIV (in the middle).

Looking at Fig. 6.10, qualitative comments can be made. By comparing coupled (right) and non coupled (left) simulations, one can observe that when radiation is included, the jet appears more closed and the jet spreading angle looks like more similar to the one retrieved in experimental measurements (middle).
Another observation concerns the central peak of velocity. In non-coupled simulations, the local maximum located on the axis disappears. A possible reason

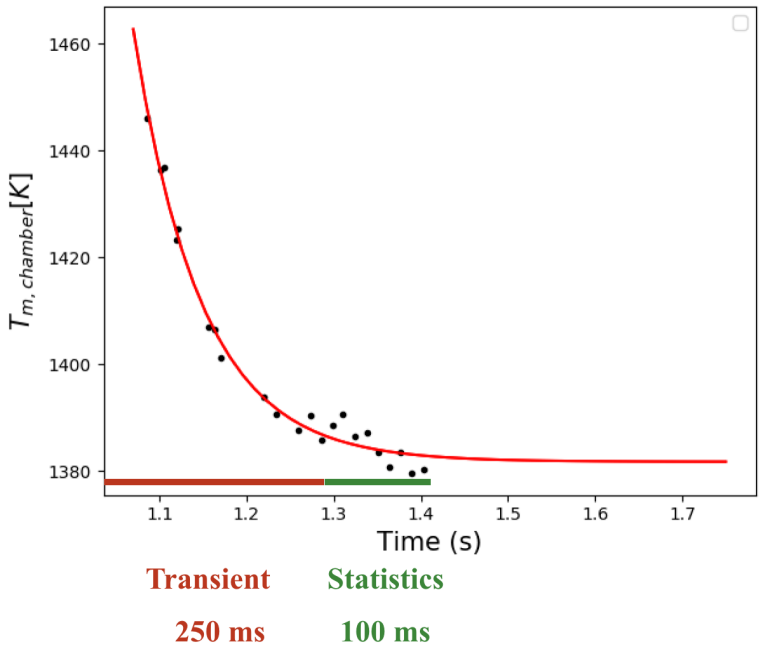

Figure 6.9: *Transient evolution of the volume-averaged temperature inside the chamber. Dots correspond to numerical data, and they are approximated by an exponential curve in red full line.*

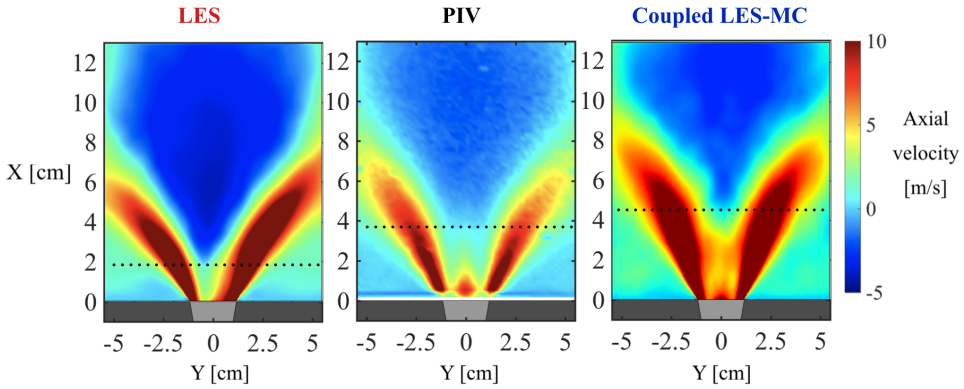

Figure 6.10: *Mean velocity fields on a longitudinal plane of the chamber taken from non-coupled LES (left), experimental PIV (centre) and coupled LES-MC simulations (right). Black pointed line highlights the position of the stagnation point.*

can be found in the high negative velocities in the IRZ predicted by only LES, which stabilizes the stagnation point close to the burner. The height of the stagnation point on the axis chamber is highlighted by the black dotted line. On the contrary, in coupled simulations, this local peak is retrieved, however a high velocity region is found in proximity of the central axis up to 4 cm from

the burner exit.
The position of the stagnation point is in better agreement with experimental data in coupled simulations compared to the non coupled case. However, the axial velocity in the lateral branches is over-estimated in both coupled and non coupled simulations, compared to experiments.
All these differences qualitatively noticed in Fig. 6.10 are quantified in the velocity profiles along the Y axis of the chamber, for different heights along the burner.
Figure 6.11 displays profiles of the mean (left) and rms (right) axial velocity for four different heights: x = 5 mm , x = 15 mm, x = 30 mm and x = 100 mm. On these plots, the experimental results (in black dots) are compared to numerical predictions obtained from coupled simulations (blue line) and non coupled ones (red line).
Close to the burner exit, at x = 5 mm and x = 15 mm, axial velocity profiles are very similar with and without radiation: lateral maxima are closely the same for both simulations, however the central maximum of velocity which is not predicted by LES without radiation, appears when radiation is accounted.
Downstream the flame, at x= 30 mm the profiles become different: the value of the lateral maxima is still closely the same for both the simulations, however the position of the maxima changes since the opening angle of the jet is altered. More precisely, in presence of radiation, the jet is more closed and more similar to experiments.
Another difference concerns the axial velocity in proximity of the axis: it is over-predicted by coupled simulations, meaning that the recirculation zone is stabilized downstream, while it is under-predicted in LES because the IRZ appears upstream.
Finally, at x = 100 mm, in the core of the IRZ, good predictions are found in both coupled and non-coupled simulations.
As concerning the RMS of axial velocity a good agreement is found at all the investigated cases, except for x = 100 mm where numerical RMS are slightly under-estimated.

Radial velocity profiles are also available from experiments. Figure 6.12 displays the mean radial velocity field (on the left) and profiles of radial velocity (on the right). The legend is the same as before.
By comparing coupled and non coupled simulations, it can be observed that the position of the maximum and minimum value of radial velocity is approximatively the same in both the cases (slightly closer to the axis in coupled simulation), however mean axial velocity profiles are in better agreement with experimental data when radiation is considered.

In conclusion, the comparison of axial velocity fields with experiments reconfirms the difficulties already faced in non reacting and reacting flow LES of Chapter 4, about the prediction of the IRZ which is usually challenging in swirling flows, but also about the jet opening angle and the maximum values

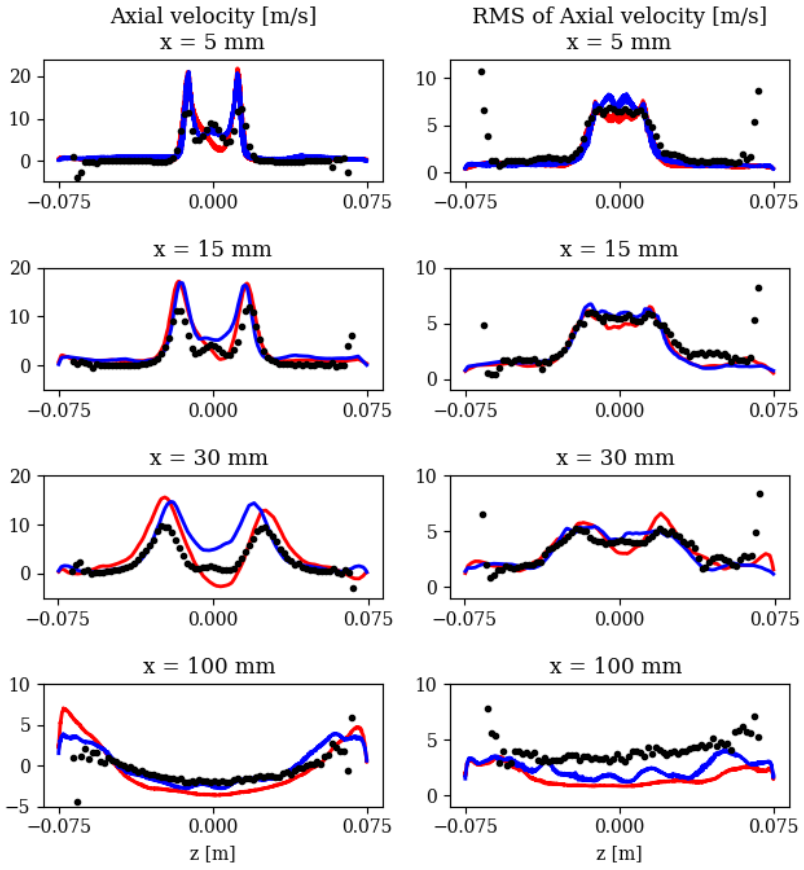

Figure 6.11: *Profiles of axial velocity (left) and RMS of axial velocity (right) on several cuts along the chamber axis.* ——*: Non coupled LES;* ——*: Coupled LES-MC simulations;* • *: Experimental data.*

of axial velocity profiles. On the contrary, the comparison on radial velocities shows results very close to experimental data, in both coupled and non coupled simulations.

When radiation is accounted for, a great variation in velocity fields is observed. Due to temperature variations, which alters the density field, the burnt gases velocity is impacted by radiation. This may let think that the stabilisation of the IRZ is highly sensitive to the temperature field, and that slight discrepancies on burnt gases temperature could affect the position of the stagnation point

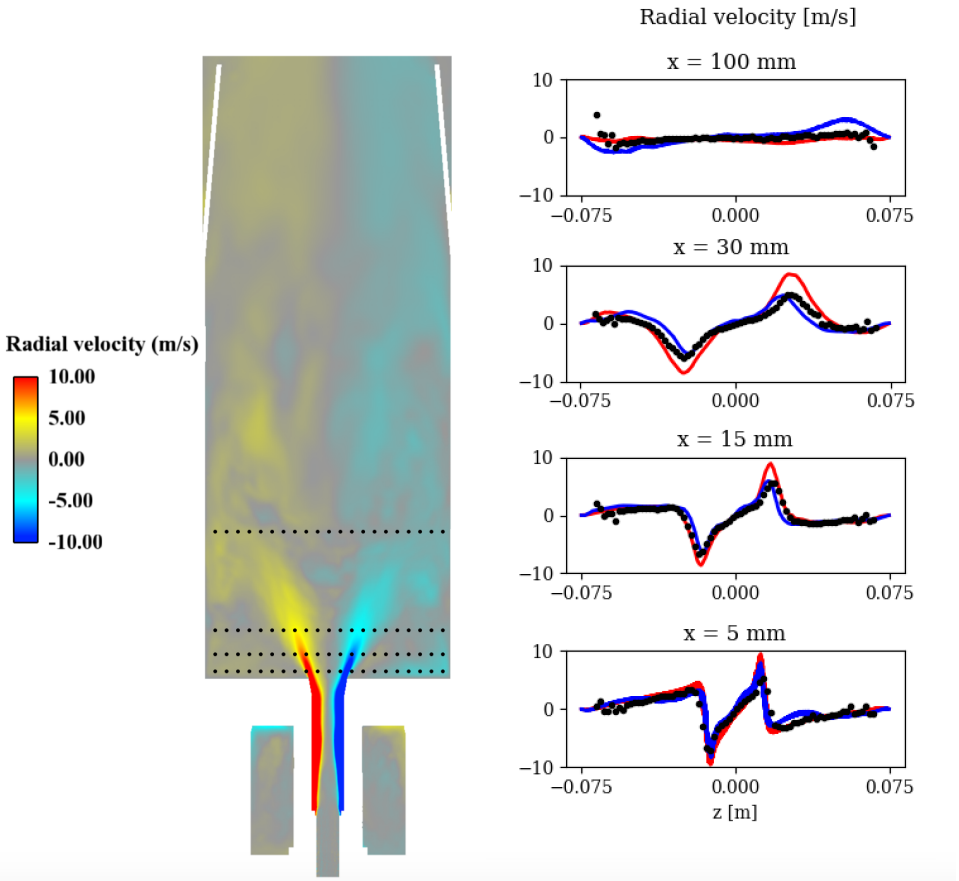

Figure 6.12: *Profiles of radial velocity on several cuts along the chamber axis.* —: *Non coupled LES;* —: *Coupled LES-MC simulations;* • *: Experimental data.*

Flame topology

The impact of radiative heat transfer can be seen also on the flame shape. Figure 6.13 compares the mean heat release field obtained in non coupled simulations (left), coupled simulation (centre) and experimental averaged Abel transform (right). The inner and outer recirculation zones are highlighted by white solid lines. In the experimental image, only IRZ appears; indeed, ORZ cannot be appreciated since the field of view of the camera for PIV measurements is zoomed and centered on the flame region, then it does not reach the lateral walls.

For the numerical fields of Fig. 6.13, the same range of heat release rate is used, however the maximum value of heat release rate is higher in non coupled simulation compared to coupled one; their values are, respectively: 4.4 $\times 10^8$ W/m^3 and 3.8 $\times 10^8$ W/m^3. The slightly higher value of HR in LES simulation indicates that the flame is more compact than the one retrieved when radiation

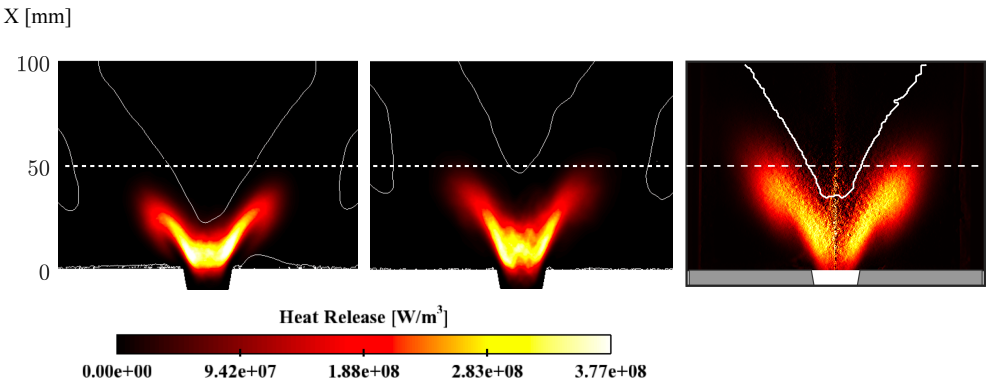

Figure 6.13: *2D cut of mean heat release field in non coupled LES (left), in couples LES-MC (center) and averaged Abel transform from experiments (right). White solid lines are iso-contour of axial velocity equal to zero.*

is accounted for.
Moreover, in presence of radiation, the gases recirculating towards the bottom chamber (ORZ) are colder and characterized by higher axial velocity than non coupled case ; consequently they contribute to extinguish the lateral branches of the flame more than they do when radiation is neglected. Indeed, by comparing the two numerical fields of *HR*, it can be noticed that the flames lateral branches are shorter in coupled simulation. The simplifying scheme displayed in Fig. 6.14 helps to localize the lateral branches of the flame, represented with yellow solid lines and their extinction (yellow dashed lines) operated from the cold burnt gases in ORZ.
In the three images in Fig. 6.13, the flame is slightly inside the divergent cup of the injector. The striking difference is that the flame appears longer when radiation is accounted for. Indeed, flame height is much closer to the one obtained in experiments. As observed in experiments, the investigated flame is swirled-stabilized. As a consequence, if the velocity field, and thus the position of the IRZ, changes, as it happens when radiation is accounted for, this has surely an impact on the flame shape and position. Variations in velocity fields may be attributed to the impact of thermal radiation on burnt gases temperature. Temperature variations and comparison with experimental data are presented in the next section.

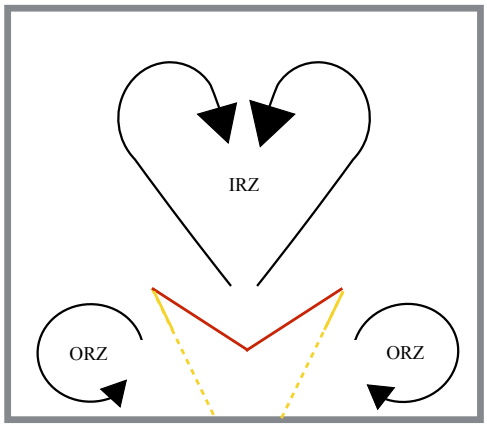

Figure 6.14: *Scheme of flame and recirculation zones in the Oxytec chamber.*

6.3.4 Temperature fields

When radiative heat transfer is taken into account, temperature distribution inside the combustion chamber varies. Figure 6.15 shows the mean fields of temperature extracted from coupled (top) and non coupled simulations (bottom), meaning with and without the account for radiative source term. They are averaged, respectively, on 100 and 300 ms.

The first striking difference is that the high temperature region looks more compact when radiation is accounted for, probably because of the temperature homogenization due to radiation. The second one is that in coupled case, colder burnt gases are recirculated in internal and external recirculation zone.
The volume averaged temperature $T_{m,chamber}$ inside the combustor is globally lower when radiation is included, because of the radiative exchanges between the gases (gas-gas interaction) and between gas and walls (gas-wall interaction). In non-coupled case, $T_{m,chamber}$ is approximately equal to 1480 K, while in presence of radiative heat transfer $T_{m,chamber}$ decreases to 1380 K, 100 K lower than the first case, meaning that the contribution of radiative heat transfer is significant.
A first comparison with experimental data can be done on the base of thermocouples measurements in one of the 4 corners of the combustion chamber at 4 heights above the burner: 1.5 cm, 4 cm, 11 cm and 20 cm. The experimental local temperature is compared to the mean temperature taken from non coupled LES simulations and LES-MC simulations in Tab. 6.1.
Temperature measurements of the gas phase with thermocouple is experimentally challenging. Radiative heat losses between the sidewalls and the thermocouple bead can lead to underpredicting the gas temperature. This error may be as high as 200-300 K. The experimental data taken by A. Degenève are characterized by a much smaller uncertainty (order of magnitude $\approx$ 30 K) (

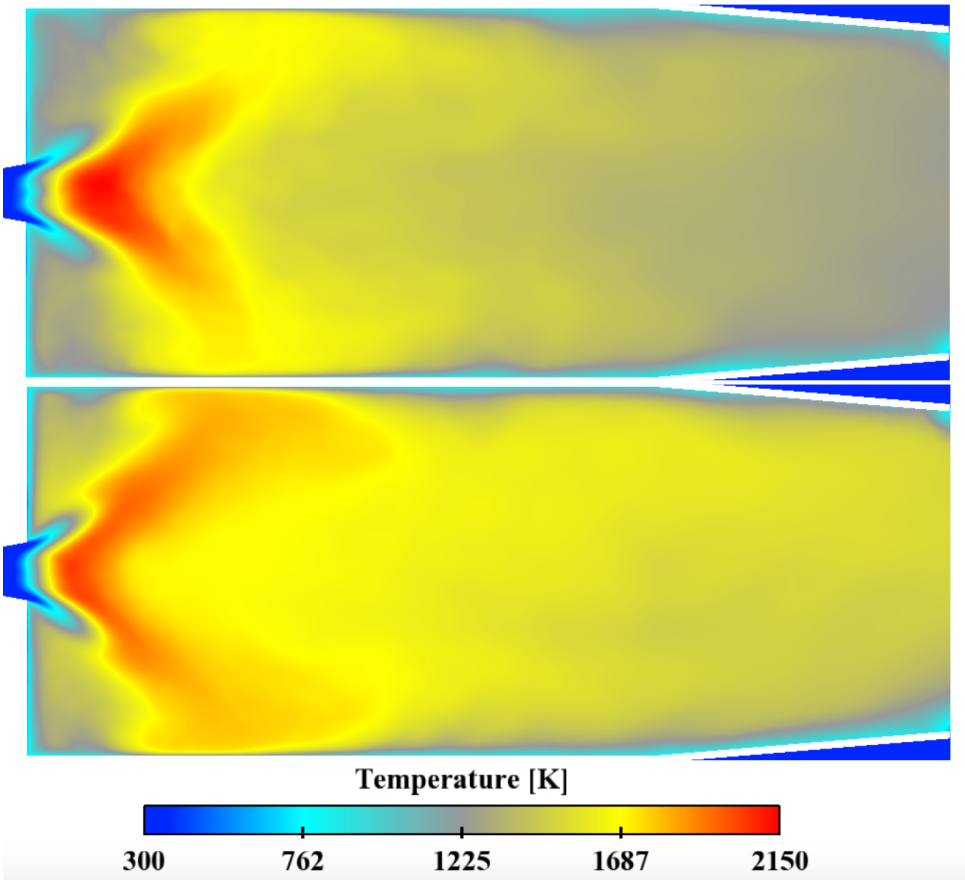

Figure 6.15: *Mean temperature fields on a longitudinal plane of the chamber taken from coupled (top) and non-coupled (bottom) simulations of the Flame A.*

A. Degenève private communication). Indeed, the retained experimental temperatures are corrected in order to take into account the radiative exchange between thermocouples and their surrounding. However, a small uncertainty about experimental values of temperature could be due to the position of the thermocouples, with an error of around 0.2 cm. The comparison between numerical and measured temperature is done on the 4 corners of the chamber; then minimum and maximum value of temperature and the corresponding relative errors are presented in Tab. 6.1.

It can be seen that experimental measurements reveal a gas temperature lower than the numerical one, for both non coupled and coupled simulations. The exception is the probe located at $x = 4$ cm where higher temperature is found in experiments.

The first thermocouple located at 1.5 cm is representative of burnt gases temperature in the ORZ. The mean temperature field on the chamber plane crossing the axis chamber at $x = 1.5$ cm (the x-coordinate of the first thermocouple) is

X [cm]	Exp. [K]	LES [K] (Err [%])	LES-MC [K] (Err [%])
1.5	1294	1569-1638 (21-26.5)	1476-1511 (14-16.7)
4	1669	1665-1719 (0.2-3)	1584-1554 (5-8)
11	1392	1678-1762 (20-26.5)	1584-1620 (13.7-16.3)
20	1150	1327-1620 (15-41)	1402-1437 (22-25)

Table 6.1: *Table summarizing, for each position of the thermocouple, the experimental temperature and the numerical mean temperature predicted by LES and coupled LES-MC simulations. In brackets the relative errors compared to experiments is specified. Both minimum and maximum values of temperatures and errors are given.*

shown in Fig. 6.16: on the left the field obtained with non coupled simulation, on the right the one associated to coupled simulations. The position of the thermocouple is also highlighted by a black dot, while black line is the iso-contour of the experimental temperature (T=1294 K). Temperature field distribution inside the combustor cannot be validated by experimental data since no measured temperature profiles inside the combustion chamber are available. From numerical simulations, it emerges that temperature field is not homogeneous, but strongly related to the 4 outer recirculation zones.

Table 6.1 shows that, in both numerical simulations, burnt gases recirculating

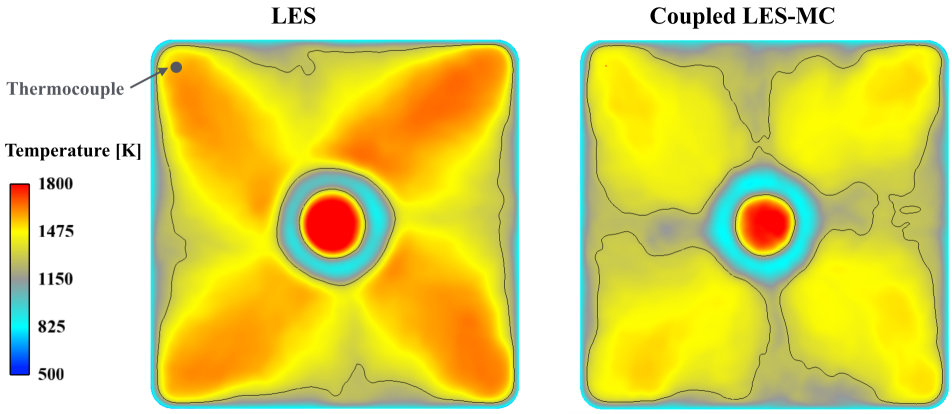

Figure 6.16: *Mean temperature field on a cross plane of the chamber passing at x = 1.5 cm taken from non-coupled LES (left) and coupled LES-MC simulations (right). Black line is the iso-line of experimental temperature (T = 1294 K). The position of the thermocouple is also highlighted.*

in this region (x = 1.5 cm) are hotter than experimental ones. However, values predicted by coupled simulations are closer to the ones obtained from thermocouples.

Better predictions about gas temperature are obtained in coupled simulation also for the probes located at 11 and 20 cm along the burner. It can be seen in Fig. 6.15 how in coupled simulation temperature downstream in the burner is

lower when radiative heat transfer is accounted for.
The second probe, installed at $x = 4$ cm, provides the highest value of experimental temperature measurements. Since the thermocouples are installed 15 mm far from the metallic bars located in the chamber corners, some relations with experimental wall flux can be found: since the maximum value for experimental wall conductive flux (presented later in this chapter) is located at $x = 5$ cm, the thermocouple at 4 cm is then representative of the high temperature gases issued from the flame that impinge the walls. In this case, non coupled LES results appear to better reproduce the high temperature gases.
From Tab. 6.1, it can be concluded that numerical simulations over-predict the temperature of the gas located in the colder regions of the burner, i.e. in the ORZ and downstream the flame. However, the high temperature of gas impinging the walls is better predicted by LES of Chapter 4, while it is underestimated when radiation is included. In spite of the large errors found in temperature predictions compared to experiments, wall heat fluxes, which are further discussed in the next sections, are in fact well predicted. A more attentive analysis leads to think that the deviation of numerics from experiments is likely due to the high sensitivity of numerical temperature with the thermocouple position. Indeed, as seen in Fig. 6.16, a high temperature gradient is observed in proximity of the walls, where the thermocouple are installed. As a consequence, the experimental uncertainty in the thermocouples position, may explain the discrepancy found between numerics and experiments.

6.4 Heat transfer results

6.4.1 Wall fluxes

The variation observed in velocity and temperature fields, when radiation is accounted for, is also found in the wall fluxes distribution.
Before investigating the impact of radiation on wall heat fluxes through quartz windows, some concepts about wall fluxes have to be reminded:

- Wall fluxes issued from AVBP, ϕ^{conv}, are the normal quartz convective fluxes from gases that induce a conductive flux predicted by the wall law.

- Radiative flux from Rainier, ϕ^{rad}, is the radiative flux normal to the quartz windows, and it accounts for the part of the total radiative flux that is absorbed and emitted by quartz, but non transmitted.

In Fig. 6.17, the experimental mean conductive flux through the quartz windows, ϕ^{exp}, is compared to the convective flux, ϕ^{conv} in non coupled simulation, and to $\phi^{tot} = \phi^{conv} + \phi^{rad}$ in coupled one.
The total flux in coupled simulation (blue solid line) is different from the one obtained in non coupled simulation (red dashed line). If the global trend stays

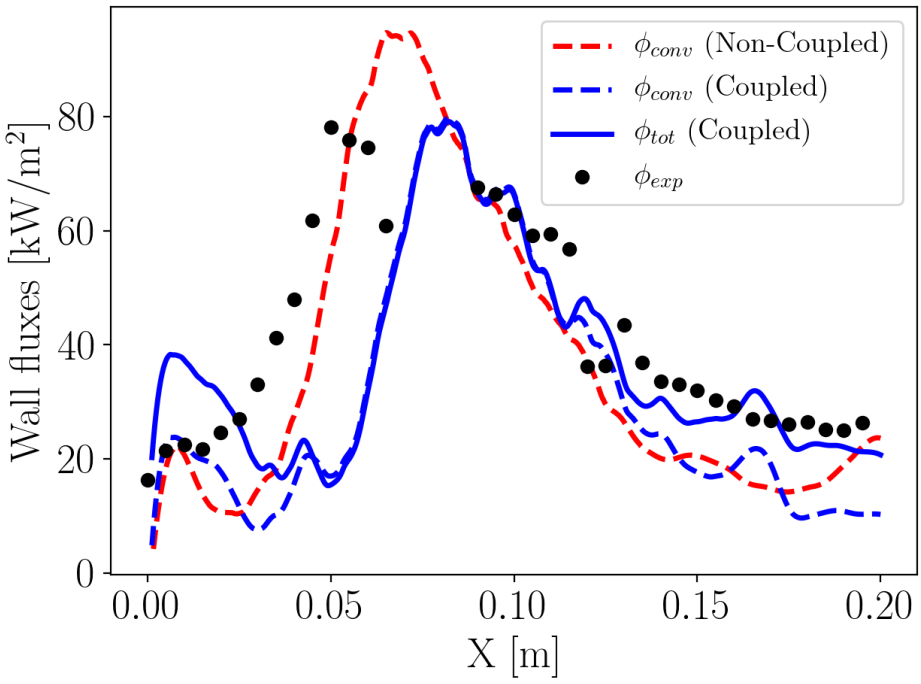

Figure 6.17: *Okat y = 0 mm) mean wall fluxes fluxes at the inner face of a quartz window. ——: ϕ^{tot} is the conductive heat flux issued from coupled simulation (convective+radiative), - - -: ϕ^{conv} is the conductive heat flux issued from non coupled simulation (just convective). - - -:ϕ^{conv}, the convective contribution to ϕ^{tot} is also plotted. • : Experimental conductive flux.*

the same (i.e. a relatively high flux close to the bottom chamber, that increases in flame region to then lower downstream) the maximum flux and its position are not the same.

Concerning the maximum value of wall fluxes, it can be noticed that it is overestimated in non coupled simulation (95 kW/m^2), while it is perfectly predicted by coupled simulation (80 kW/m^2). This is coherent with the better agreement found in the gas temperature in presence of radiation: since the hot gases temperature is lower than the one observed in non coupled LES, also the maximum wall flux decreases.

The position of the maximum flux, in coupled simulation, is translated 1 cm downstream compared to non coupled simulations. This is due to the variation observed in the jet opening angle: in coupled simulation the jet appears more closed than the one observed in non coupled one, consequently hot gases impinge the walls downstream. This variation can be better appreciated in Fig. 6.18, where the mean velocity field is shown together with the mean convective wall heat flux obtained in non coupled (left) and coupled (right) simulations.

When radiation is considered, convective flux does not stay the same as non coupled simulation.

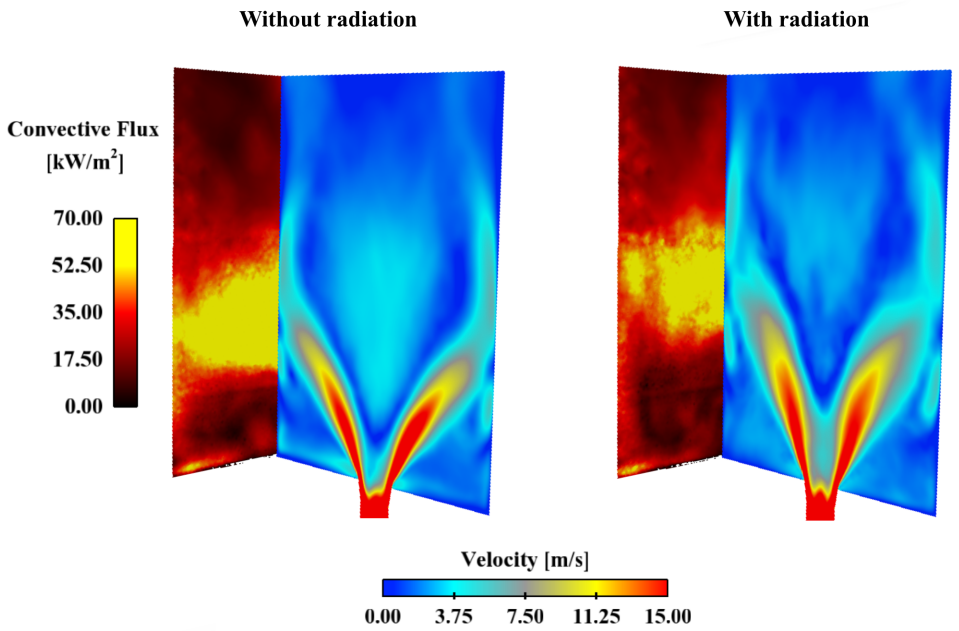

Figure 6.18: *Numerical field of mean normal energy flux on the chamber internal wall represented together with the numerical field of mean velocity on a longitudinal plane passing through the axis chamber in non coupled (left) and coupled simulation (right).*

In Fig. 6.17, the biggest difference between the convective flux issued from coupled and non coupled simulation is the region comprised in $X = [0.04\,m;\ 0.07\,m]$: the position where wall flux increases is closer to experiments in non coupled simulation, while convective flux in presence of radiation under-estimate wall fluxes in this region.
In the regions downstream and upstream, numerical convective fluxes are low and very close to each others, in coupled and non coupled simulations. However, the radiative flux in this regions seems to have a great impact: the radiative flux, corresponding to the difference between ϕ^{tot} and ϕ^{conv}, has the same order of magnitude of convective flux in the regions close to the chamber bottom and downstream the flame. Indeed, in Fig. 6.19, where radiative flux on quartz windows is displayed, it is shown that these regions are mainly dominated by absorption, yielding a positive contribution from radiation..
Close to the chamber bottom, meaning X comprised in $[0\ m;\ 0.02\ m]$, the total flux is over-estimated compared to experiments in presence of radiation, whereas a very good agreement is found in the region downstream, leading to a much better prediction of wall fluxes compared to the one obtained in non-

coupled simulations.

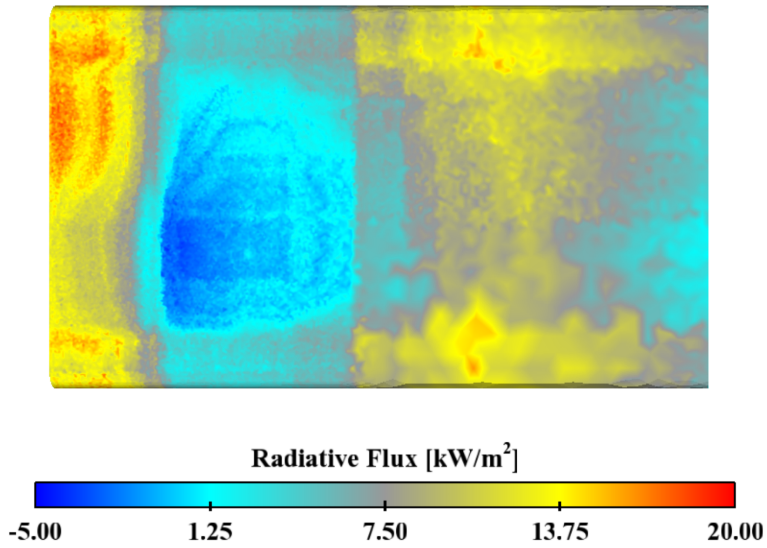

Figure 6.19: *Mean radiative flux on the quartz windows of the chamber issued from coupled simulation.*

Still in Fig. 6.19, it can be seen that the emission-dominated part of the quartz windows is characterized by a very small absolute value of radiative flux, compared to ϕ^{tot}. This explains why total flux, ϕ^{tot} and its convective contribution, ϕ^{conv}, in the central region of the quartz (Fig. 6.17) are closely the same.
In Fig. 6.20, the active radiative flux, ϕ_{rad}, through the quartz windows, which has been estimated a-priori in Section 6.2.3, from an instantaneous LES solution, is compared to the final ϕ_{rad} obtained from coupled simulation. It can be noticed that the trend of ϕ_{rad} is very well predicted, even with an a-priori approach, because the imposed wall temperature is the same in both cases. However a high relative error (200%) is found in the prediction of the minimum radiative flux: 2 kW/m^2 are found in the a-priori estimation, against a value of -2 kW/m^2 predicted by coupled LES. Given the high convective contribution of the wall conductive flux of the investigated configuration (ϕ_{tot}^{max}= 80 kW/m^2), the wrong a-priori estimation on the minimum radiative flux would lead to minor errors on the total wall flux at the studied locations. However, in a case where the total wall flux is characterized by a significant radiative contribution compared to the convective one, an a-priori estimation on wall radiative flux could lead to huge errors on the total wall flux prediction.

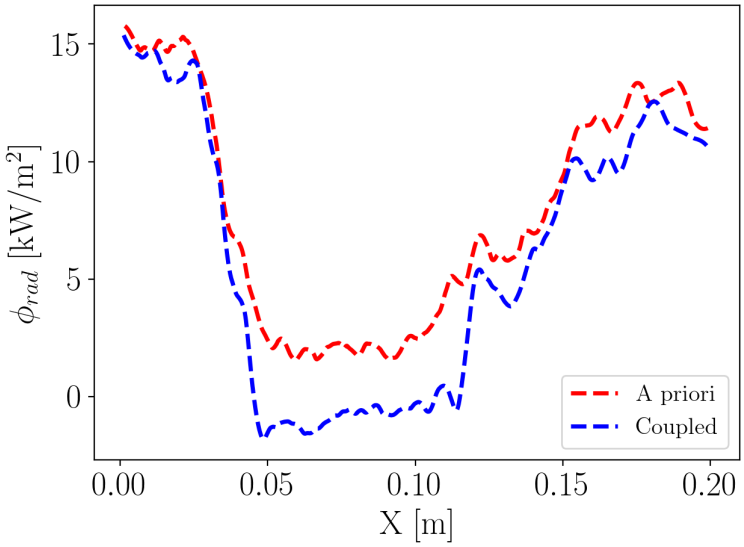

Figure 6.20: *Wall radiative flux profiles along the quartz window centerline a-priori estimated in Section 6.2.3 (red dashed line) and issued from coupled simulation (blue dashed line).*

6.4.2 Combustor energy balance

As done for the non coupled case, a sensible enthalpy balance on a control volume delimitating the combustion chamber is performed also for the presented coupled simulations; it considers only the inlets and the outlet of the combustion chamber, excluding the hemispherical domain representing the atmosphere.

The macroscopic balance equation of sensible enthalpy leads to:

$$\int_{out} \rho h_s \mathbf{u} \cdot d\mathbf{S} - \int_{in} \rho h_s \mathbf{u} \cdot d\mathbf{S} + \int_{walls} \phi^{cond} dS + \int_V -P^R dV = \dot{\Omega} \quad (6.8)$$

The first two terms represent, respectively, the outlet and inlet convective fluxes, the third term the conductive flux integrated on the chamber walls, the fourth term is the source term due to radiation while the last term is the integrated heat release.
All the terms of the energy balance, expressed in kW, are presented in Tab 6.2 for both the investigated cases: with and without radiation.

When radiation is accounted for, a radiative source term, equal to 2.82 kW is introduced in the balance equation. The fact that this term is positive means that thermal radiation introduces heat losses.
Since both chemical source term and inlet convective flux are the same in both coupled and non coupled simulations, the sum of the remaining 2 terms (outlet convective and wall conductive fluxes) decreases. By detailing these two

Case	Convective flux (Out-In)	Conductive flux	Radiative source term	Chemical source term
LES	7.49	7.01	0	14.5
LES-MC	5.91	5.77	2.82	14.5

Table 6.2: *Contributions of the terms present in the global enthalpy balance for the two investigated cases: with and without accounting for radiation. All the terms are expressed in kW.*

contributions it emerges that both of them decrease: the outlet convective flux is 1.6 kW lower in the coupled case and the wall conductive fluxes are 2 kW smaller than the non coupled case. This is due to the decreasing of burnt gas temperature when radiative heat transfer is considered.
Conductive flux, which accounts for the 48 % of flame thermal power P^{th} in non coupled case, lowers to the 40 % of P^{th} when radiation is considered. The sum of conductive and radiative fluxes accounts for 8.6 kW, corresponding to around 60 % of P^{th} .
In coupled simulations, burnt gases loose enthalpy through radiation and heat losses near the combustor walls. In this specific configuration, the radiative flux is equal to the half of the wall-integrated conductive flux, meaning that for a correct estimation of the heat losses to the walls, the radiative energy transfer needs to be described.
In order to detail the radiative source term and quantify the main radiative contributors, a balance of radiative transfer is performed in the next section.

6.4.3 Radiative transfer balance: quantification of the transmitted flux

A radiative transfer balance can be written for the control volume represented in Fig. 6.21. The balance accounts for the radiative power P^R integrated over the control volume, which represents a source term, and it is equal to the sum of the radiative fluxes through all the surfaces of the chamber.
Then the balance of radiative transfer writes:

$$\int_V P^R dV = \int_{In+Out} \phi_{rad}\, dS + \int_{Opaque\ walls} \phi_{rad} dS + \int_{Quartz} \phi_{rad} dS \quad (6.9)$$

The Right Hand Side (RHS) of the Eq. 6.9 is made of 3 contributions:

- the radiative flux absorbed and emitted at the inlet and outlet far-fields;
- the radiative flux absorbed and emitted by the opaque components of the chamber (chamber bottom and convergent);
- the radiative flux absorbed, emitted and transmitted by the quartz windows.

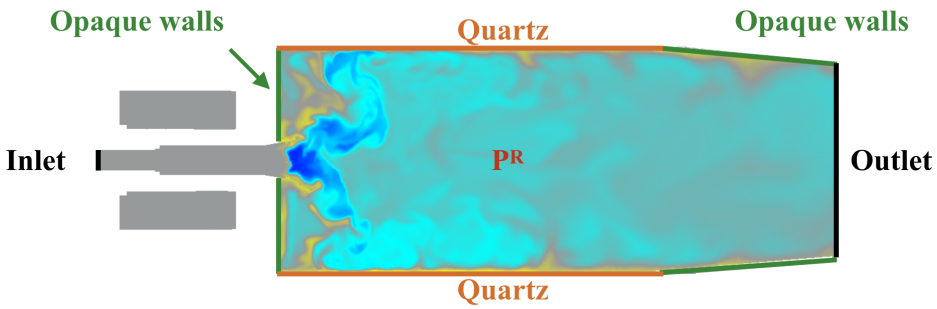

Figure 6.21: *Control volume retained for the radiative transfer balance*

It should be noticed that the radiative flux solved by Rainier accounts only for the active part, i.e. the absorbed and emitted flux.

All the contributions of Eq. 6.9 are summarized in Tab. 6.3

Radiative source term	In+Out	Opaque walls	Quartz (active part)
2.82	0.44	0.36	1.07

Table 6.3: *Contributions of all the terms of the radiative transfer balance, excluding the transmitted flux. All the terms are expressed in kW.*

The radiative power integrated over the entire volume, $\int_V P^R dV$, is equal to 2.82 kW, representing the 21% out of the thermal power of the flame (14.5 kW). Considering only the active part of the radiative flux, the difference between the radiative source term and all the other terms on the RHS gives access to the amount of radiative flux passing through the quartz windows in the transparent bands.
The active part of the quartz radiative flux, solved by Rainier, accounts for 1.07 kW, which is the 38% of S^R. Consequently the transmitted flux is equal to 0.95 kW: approximatively 35 % of S^R leaves the combustion chamber without being absorbed by quartz windows.
Finally, two main conclusions can be drawn: the first one is that radiation plays a significant role in the investigated configuration, since the 20% of the flame thermal power is loss through radiative heat flux.
The second conclusion concerns the spectral properties of the quartz windows; it has been shown that more than 30% of radiative flux leaves the combustion chambers through the transparent bands of the viewing windows, making then necessary accounting for spectral properties when quartz windows are present.

6.4.4 Radiative power field

The mean radiative power field shown in Fig. 6.22 is, as expected, strongly related to the mean temperature field. It shows that the flame region is characterized by high emission, as seen in the instantaneous fields shown in the latter section.

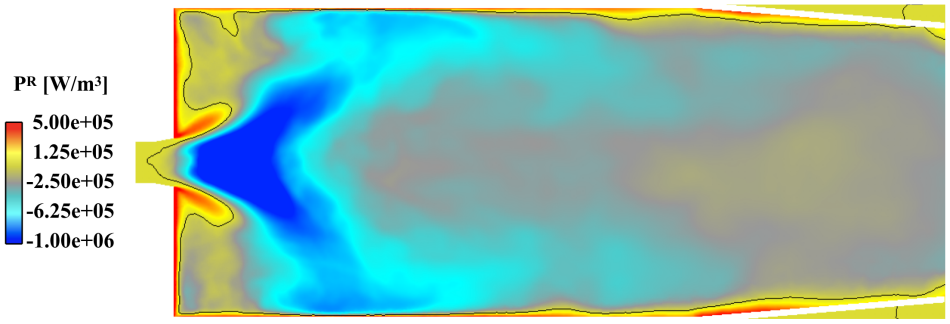

Figure 6.22: *Mean radiative power field on a longitudinal plane of the chamber taken from coupled LES-MC simulations of the investigated flame.*

In order to analyze what happens from the point of view of radiative heat transfer, two kinds of interactions are here analyzed: gas-gas interactions and gas-wall (mainly quartz windows) interactions.

Gas-gas interactions

Three points are chosen to be representative of the investigated combustion chamber and they are localized in the IRZ, ORZ and flame region.
The burnt gases composition is nearly the same in these three regions, however their temperature is very different from each other. The point representative of the flame region is characterized by burnt gases at high temperature, $T \approx$ 2200 K. Gases recirculating in IRZ and ORZ are colder, because of the heat losses. Precisely, gases in IRZ are characterized by a mean temperature of 1500 K, while those ones in ORZ are at $T \approx 1100$ K.
It can be interesting to evaluate the optical thickness of these regions for a better understanding of the role played by radiative heat transfer in the investigated configuration. To do it, the transmissivity for each spectral band, $\overline{\tau}^{\Delta\nu}$, is analyzed. It is defined as:

$$\overline{\tau}^{\Delta\nu} = \sum_{i}^{M} \omega_i exp(-\kappa_i \ell) \tag{6.10}$$

where M is the number of the quadrature points (M=7 if only H_2O is present, while M=49 in the bands where CO_2 and H_2O overlap); ω is the quadrature weight, κ is the reordered absorption coefficient evaluated at the quadrature

point and ℓ is a characteristic length, chosen equal to 7.5 cm, which is the halfwidth of the chamber.
The wavenumbers participating to the heat radiative transfer span between 100 cm^{-1} and 19 000 cm^{-1}. The spectral transmissivity defined in Eq. 6.10 is plotted against the wavenumber in Fig. 6.23 (top) for each characteristic point. It is also highlighted, through the black dashed line, the threshold above which the medium is considered as optically thin, corresponding to $\tau_\nu \approx exp(-0.1)$.

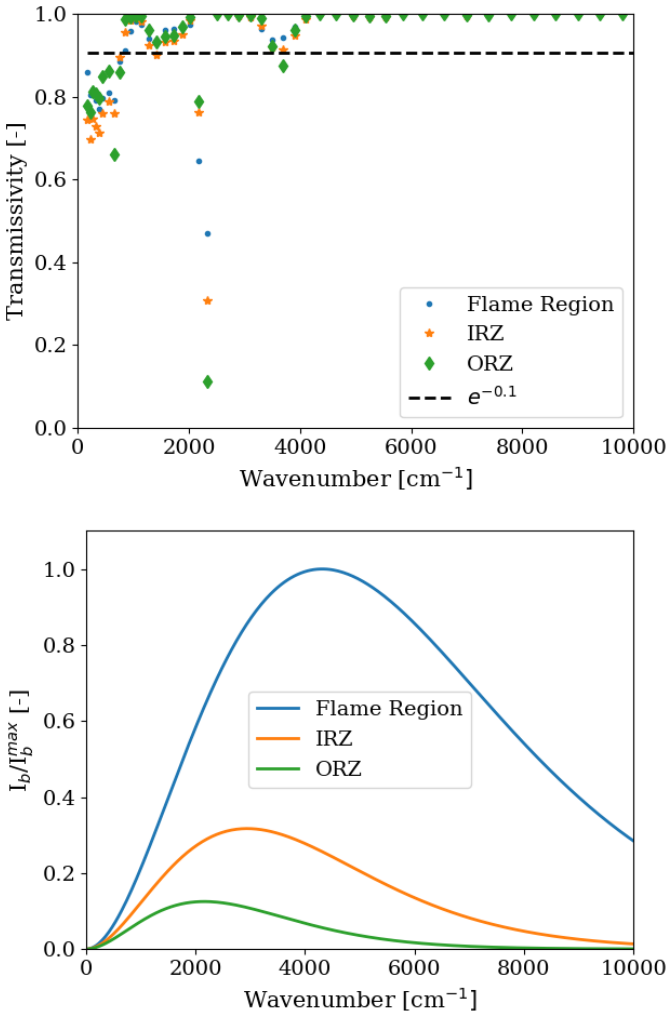

Figure 6.23: *Spectral transmissivities (top) and dimensionless spectral Planck function (bottom) in three characteristic regions of the burner: flame region (blue), inner recirculation zone (orange) and outer recirculation zone (green). The horizontal dashed line denotes the limit of the optically thin medium.*

All the three considered points show a transmissivity lower than $exp(-0.1)$ in two spectral ranges: the first one corresponds to wavenumbers comprised in

[170 cm^{-1}, 750 cm^{-1}], while the second one in [2100 cm^{-1}, 2400 cm^{-1}]. On the bottom of Fig. 6.23, it is shown the dimensionless spectral radiative intensity of a black body for the investigated temperatures, defined as:

$$\frac{I_b}{I_b^{max}} = \frac{I_b(\nu, T)}{max[I_b(\nu, T = 2200)]} \tag{6.11}$$

Looking at spectral transmissivity and dimensionless spectral radiative intensity, two messages can be deducted and both come from the observation that the minimum of transmissivity is found around 2300 cm^{-1}. One conclusion is that, since the emissivity is complementary to the transmissivity, and since the maximum of the dimensionless Planck function of a point representative of ORZ is also located around 2300 cm^{-1}, ORZ are characterized by very high emission in this spectral band. The second consequence concerns the optical thickness of gases in ORZ: since $\overline{\tau}_\nu$ is very small, the burnt gases in the ORZ are characterized by the highest optical thickness in the considered spectral band, therefore, most of the radiative power emitted inside the ORZ is also re-absorbed by cold gases in proximity of the ORZ.

Gas-quartz interactions

It is also interesting to look at the interactions between the gas inside the chamber and the confining walls. The attention here is focused on the semi-transparent viewing windows surrounding the flame.
The knowledge of their spectral properties allows to understand the interaction with the gas inside the burner. Figure 6.24 shows the modeled spectral properties of the quartz (top) and the emission term, $\overline{\kappa}_\nu I_\nu^\circ$, divided by its maximum (bottom) as a function of the wavenumber.
The red shaded area includes the wavenumbers where the quartz absorb radiative power, while black shaded area comprise the ones where quartz windows are transparent. From the comparison of the two plots of Fig. 6.24, it emerges that most of the radiation emitted in flame region, IRZ and ORZ is absorbed by the quartz. This phenomenon happens for wavenumbers lower than 2840 cm^{-1}.
For wavenumbers larger than 3740 cm^{-1} and included in the range [2830 cm^{-1}, 3580 cm^{-1}], corresponding to the black shaded area in Fig. 6.24 (bottom), the quartz is mostly transparent. In these spectral bands, a significative amount of radiative power is emitted in the flame region, meaning that the radiative power passing through the quartz and transmitted to the exterior is mainly due to a part of the radiative power emitted by the flame. Moreover, Fig. 6.23 shows that in the spectral bands where the quartz is transparent, the gas is optically thin for all the investigated cases when considering the halfwidth of the chamber as characteristic length, meaning that the radiative power emitted inside the chamber is not absorbed before reaching the wall.
It can be interesting to verify from these spectra the amount of thermal radia-

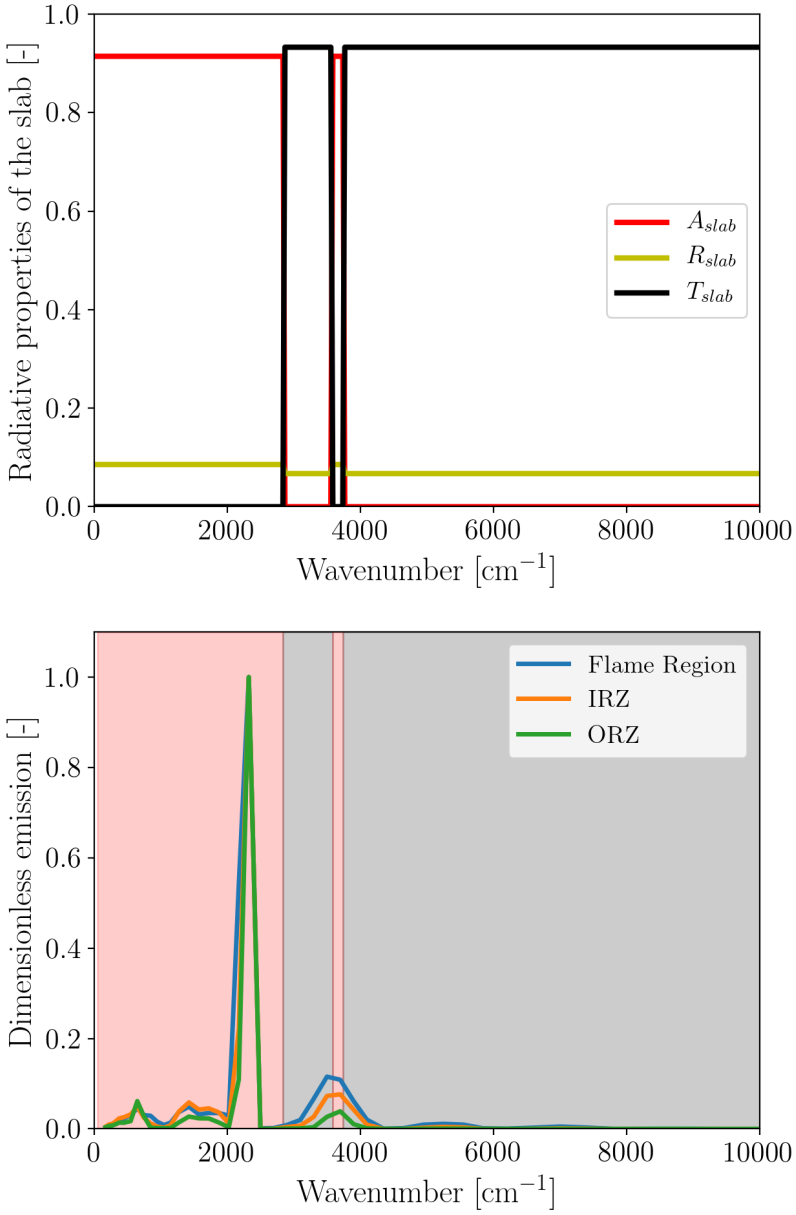

Figure 6.24: *Modeled spectral properties of the slab (top) and dimensionless spectral emission (bottom) as a function of the wavenumber. Red and black shaded areas represent, respectively, absorbing and transparent bands of the quartz windows.*

tion emitted in flame region which is transmitted through quartz. This is done by evaluating the fraction F as the ratio between the radiative power emitted by gas in flame region (T_{ad} = 2200 K) in the transparent band of quartz windows and the radiative power emitted by the same gas in the whole spectrum:

$$F = \frac{\int_0^{+\infty} \epsilon_{\nu,g} I_{\nu,b}(T_{ad}) T_{slab} d\nu}{\int_0^{+\infty} \epsilon_{\nu,g} I_{\nu,b}(T_{ad}) d\nu} \tag{6.12}$$

$\epsilon_{\nu,g}$ represents the emissivity of burnt gases computed as the complementary of the transmissivity defined in Eq. (6.10), $I_{\nu,b}$ is the spectral Planck function at $T = T_{ad}$ and T_{slab} is the transmittance of quartz windows, described in the previous chapter. From Eq. (6.12), it comes out that $F = 0.2$, meaning that around 20% of radiative power emitted by gas in the flame region is emitted in the transparent spectral bands of the confining viewing windows and transmitted to the exterior. The obtained value is coherent with the percentage of radiative flux transmitted by quartz windows, whose value is 35% and comes from a balance interesting the whole 3D combustor in Eq. (6.9).

6.5 Continuation of the simulation

The analysis carried out in the previous sections concerns the steady state which is attained after 300 ms of simulation. After that, two-hundred milliseconds more have been run (from 1.4 s to 1.6 s). The evolution of the volume-averaged temperature, displayed in Fig. 6.25, confirms that the thermal transient is ended up: starting from $t = 1.3$ s, the average temperature oscillates around the steady state value.

However, during the next 150 ms of simulation, great variations are observed in the flow topology. Figure 6.26 shows the evolution of the axial velocity field in the course of the last milliseconds of simulation. At $t = 1.46$ s, the opening angle of the jet and the position of the IRZ are very similar to the ones retrieved in the averaged fields shown in the previous sections. However, for $t > 1.5$ s, great variations are observed: the jet becomes more and more closed and long, and the IRZ is pushed far from the exit burner.

Another metric which is considered to check the evolution of the simulation is the introduction of some probes inside the computational domain. Several probes have been located along the chamber axis, in order to trace the evolution of the IRZ.

Figure 6.27 shows the temporal evolution of velocity and temperature in a probe placed on the chamber axis at $x = 8$ cm, inside the IRZ. It can be seen that during the first 350 ms of simulation, no variations are observed. However, at $t = 1.5$ s, a sudden increase in both axial velocity and temperature can be observed in the IRZ: the axial velocity which is negative in the first 350 ms assumes, starting from 1.5 s, high positive values.

It has been experimentally observed that swirl-stabilized flames stabilize close to the stagnation point. Considering the evolution of the axial velocity, one could expect that the flame is also lifted off with the IRZ. However, this is not the case, as it can be seen in Fig. 6.28 where mean (left) and instantaneous

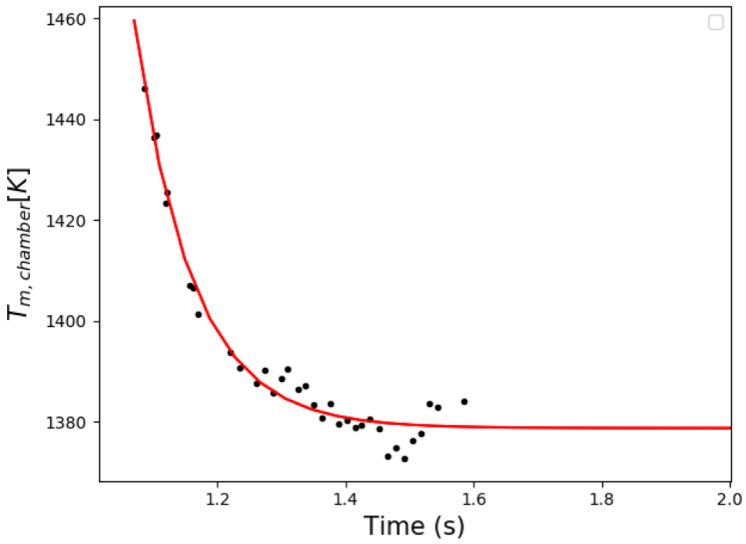

Figure 6.25: *Transient evolution of the volume-averaged temperature inside the chamber. Dots correspond to numerical data, and they are approximated by an exponential curve in red full line.*

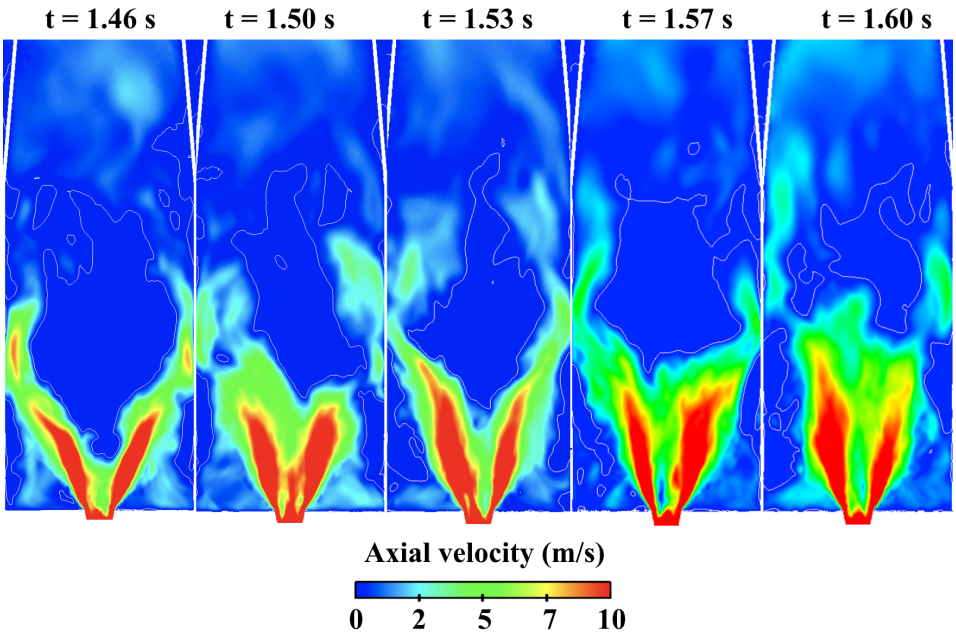

Figure 6.26: *Axial velocity fields on a longitudinal plane of the chamber averaged on 13 ms and taken from different instants of the coupled simulation. White lines are the iso-contour of axial velocity equal to zero.*

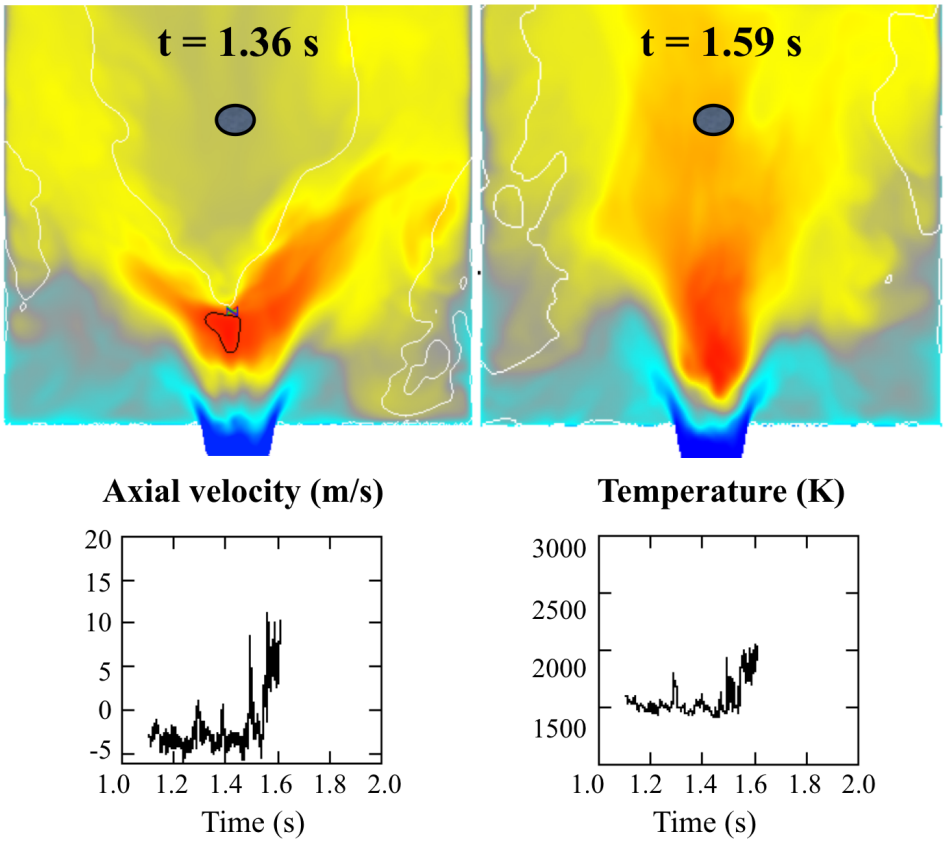

Figure 6.27: *On the top: 2-D longitudinal cuts of temperature field averaged on 13 ms taken in two different instants of the simulation: t = 1.36 s (on the left) and t =1.59 s (on the right).*
On the bottom: temporal evolution of the axial velocity and temperature in the point marked by a black circle during the cours of the coupled simulation.

(right) axial velocity fields are displayed. In the average solution one can observe that the flame topology is not impacted: the flame remains stabilized in proximity of the injector and its shape does not vary. The instantaneous solution clearly shows that the flame is anchored to the low and/or negative axial velocities pockets close to the burner exit.
The variation observed in the flow topology starting from t =1.5 s may be due to several reasons. One reason could be the possibility that some confined swirling flows exhibit bifurcating behaviors (Vanierschot and Van den Bulck 2007). Moreover, a recent study shows the probability to incur bifurcations in LES of swirling confined flows and the large sensitivity of LES results to grid size and sub-grid scale models in such configurations (Falese et al. 2014). Another possible reason is the presence of numerical oscillations of pressure inside the combustor that appear in the last period of the computation only. These strong oscillations are observed close to the back plate of the combustor and

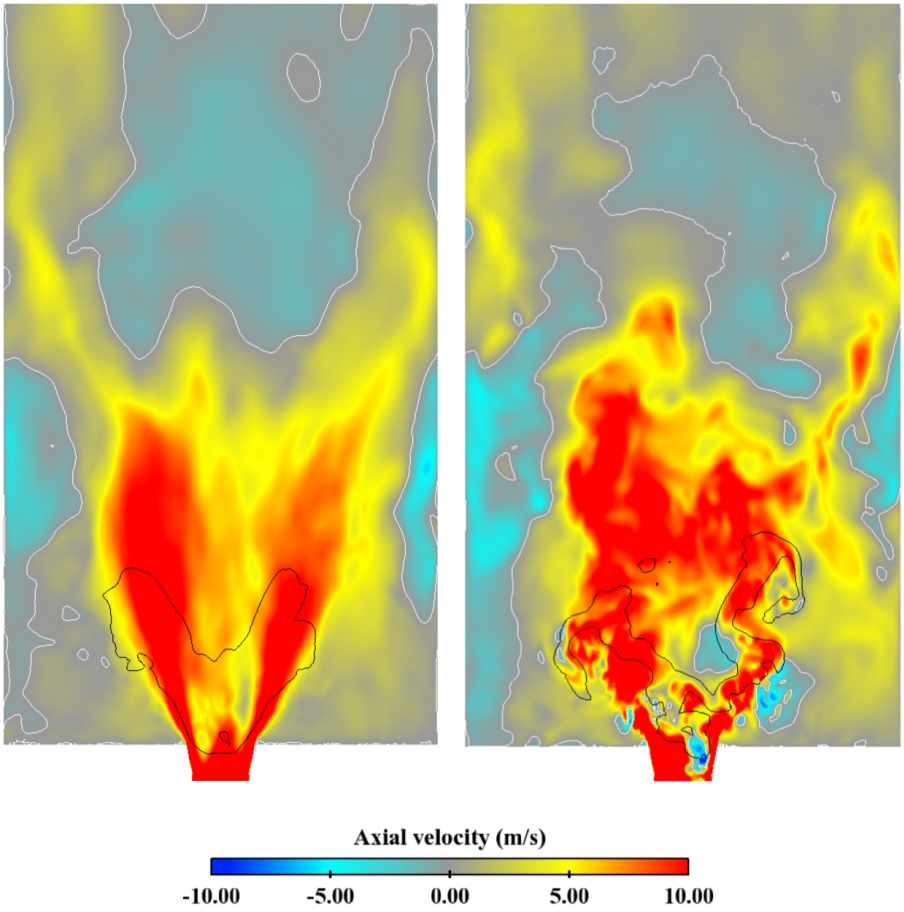

Figure 6.28: *2-D longitudinal cuts of average (left) and instantaneous (right) axial velocity fields in the coupled simulation. White lines are the iso-contour of axial velocity equal to zero and black iso-lines of the heat release rate* $HR = 3 \times 10^7\ W\ m^{-3}$ *are added.*

are attributed to numerical issues. They are characterized by an amplitude of 2 kPa and their frequency is around 6 kHz; such a frequency does not correspond to any physical phenomenon observed in the experiments. Numerical issues are probably due to an undesired behavior of the chosen numerical setup with wall functions in AVBP.

6.6 Conclusions

A multi-physics simulation where radiation and LES solvers are coupled to each other is performed. It combines LES modeling of turbulent combustion and accurate Monte Carlo methods to solve the radiative transfer equation.

Semi-transparent viewing quartz are also accounted for, through a band model retrieved from the spectral transmissivity of the quartz.
The objective of this chapter is to quantify the impact of radiation in the investigated configuration. The comparison between non-coupled and coupled simulations helps to isolate the effect of radiative heat transfer.
In the first part, the importance of accounting for semi-transparent properties of quartz windows is highlighted by a comparison with a case where quartz are considered as opaque: in the opaque case, radiative wall fluxes are overestimated compared to the semi-transparent case. The analysis is carried out by solving the RTE starting from a non-coupled LES simulation; this allows to make an a-priori estimation of the wall heat flux in Oxytec chamber.
In the second part of the present chapter, flow and flame topology are described based on instantaneous solutions. Then, mean fields are presented and compared to non-coupled LES of Chapter 4 and to experimental data. From comparison, it emerges that thermal radiation has an impact on both velocity fields and flame shape. Indeed, in results obtained from coupled simulations, the position of the IRZ gets closer to the one observed in experiments, and also the flame shape becomes very close to experiments when radiative heat transfer is considered. These results let think that the stabilisation of the IRZ is highly sensitive to the temperature field, and that slight discrepancies on burnt gases temperature could affect the position of the stagnation point. A comparison with 4 thermocouples installed in the chamber corners highlights the needing to include radiative heat transfer in order to predict gas temperatures more accurately.
The third part of the chapter is dedicated to the heat transfer results. Despite of the relatively large errors retrieved between numerical and experimental temperature (order of 20%), numerical wall fluxes present a good agreement with the experimental wall flux distribution: the maximum flux is perfectly predicted, but some slight discrepancies arise, especially towards the chamber bottom. The reason of discrepancy with measured temperature could be, then, the proximity of thermocouples to the chamber walls where high temperature gradient are found.
Successively, a sensible enthalpy balance is applied to the whole combustor, from which it emerges that 60% of flame thermal power leaves the combustor through heat losses, and that radiative fluxes through the walls and chamber outlet account for 20 % of the flame thermal power, demonstrating the importance of including radiation in combustion simulations.
A radiative heat transfer balance allows to identify and quantify all the terms that participate to radiative heat transfer. It is found that the main contributors are the quartz windows: they are responsible of around 70 % of the radiative source term. Precisely, the 34 % of the radiative power emitted and absorbed inside the volume of the combustor is transmitted to the exterior, while the 38 % is absorbed by the quartz windows. Accounting for spectral properties of quartz windows is, then, significant in the investigated configura-

tion.
A spectral analysis about transmissivity of burnt gases present in the different regions of the combustor allows to elucidate the interactions between gas inside the chamber and between gas and quartz windows. It is found that gas in ORZ are the ones characterized by the highest optically thickness and they are responsible of re-absorption of emission from hot gases issued by flame but especially from cold gases inside the ORZ. Concerning the gas-wall interactions, it emerges that the radiation transmitted by viewing windows is mainly due to hot gases issued from the flame.
However, last calculations show that the analyzed steady state is followed by a second transient, which is not a thermal one, where the flow topology completely changes, despite flame position and shape remain unchanged. Such variations are attributed to numerical pressure oscillations arising in the computations during this second transient or to the bifurcating behavior that some highly swirling flow can show.

Computational cost of coupled and non coupled simulations

Finally, the computational cost of the large eddy simulations presented in Chapter 4 and coupled LES-MC simulations presented in this chapter is given.
Both simulations have been run on the super-computer OCCIGEN, equipped with Intel E5-2690V3 processors. Table 6.4 summarizes the simulated physical time, the total computational time expressed in CPU hours, the number of cores dedicated to each solver and the real wall clock time, expressed in days of simulation, needed to end-up each simulation of the Oxytec chamber.

Case	Physical time (s)	CPUh	Cores AVBP	Cores Rainier	Days
Non Coupled	1.32	1 598 621	2400	-	28
Coupled	0.54	2 260 720	750	1770	37.4

Table 6.4: *Simulated physical time, number of CPU hours, number of cores used per each solver and number of days needed for coupled and non coupled simulations.*

It can be concluded that, with the numerical configuration presented and justified in Chapter 5, the coupled LES-MC simulation results 3.4 times more expensive than the LES simulation. The real wall clock time given in Tab. 6.4 does not account for the time that a job has to wait before starting, due to the fact that the needed cores are not available at every moments. Consequently, the real time took to end-up a simulation is around 2.4 times higher than the wall clock time: 3 months were needed to simulate 540 ms of the Oxytec chamber with a coupled approach.

Chapter 7

Towards coupled simulations of CO2-diluted oxyflames

In this chapter is presented preliminary study on the CO_2-diluted oxymethane flame (Flame B), which has been experimentally investigated during the Oxytec experimental campaign.
After a summary about the main experimental results, attention is given to the effects of CO_2-dilution in a combustion process, especially from the point of view of radiation absorption operated from fresh gases. A state-of-the-art on flames operating with CO_2 dilution is given, and impacts of radiation re-absorption are discussed in the context of 1D flame archetypes of A and B configurations. The study is carried out through the coupling of a numerical code that solves 1D equations for reacting flows and the radiation solver, Rainier. Results show a big impact of CO_2 re-absorption on the laminar flame speed but also a high dependence from the domain size used in the simulation.
In the final part of the chapter, first 3D LES of the Flame B are presented; their numerical-set up is discussed and first non-converged but encouraging results are shown.
Finally, a preliminary study on radiative heat transfer taking place in Flame B is carried out, and a comparison with the Flame A is done; this analysis allows to quantify the effect of high CO_2 concentration of burnt gases on radiative heat transfer. LES simulations of Flame B, started in this thesis work, are pursued in the PhD thesis of A. Degenève where a coupling of les with radiative heat transfer will be performed.

Contents

7.1 Introduction

As already introduced in Chapter 1, in the context of the Oxytec project, significant attention is given to the oxy-combustion operated with CO_2-dilution. The stabilisation of technically premixed swirled-stabilized CO_2-diluted oxy-methane flames has been investigated during the experimental campaign carried out at the EM2C laboratory from the experimental team of Prof. Thierry Schuller and Dr. Clément Mirat (Jourdaine et al. (2017), Degenève et al. (2019a)).
Jourdaine et al. (2017) demonstrated that it is possible to switch the Oxytec chamber from combustion in air to oxy-combustion experimentally stabilizing two flames, a methane air and an oxy-methane flame, sharing the same thermal power, equivalence ratio and flame adiabatic temperature.
The operating conditions of the flame B are detailed in the Chapter 4 in Tab. 4.1. The only different parameters between the two flames are the bulk velocity and the Swirl number.
OH^* chemiluminescence images (Jourdaine et al. 2017) show that Flames A and B are characterized by a very similar flame topology, as it can be seen in Fig. 7.1.
Moreover, thermocouples installed in the solid corners of the burner and inside the chamber show that gas and solid temperature of the two investigated flames are very close to each other.
Also, LIP measurements from Degenève et al. (2019a) show that replacing the nitrogen of the air by the carbon dioxide does not significantly alter the temperature and heat flux distribution over the solid walls of the chamber.

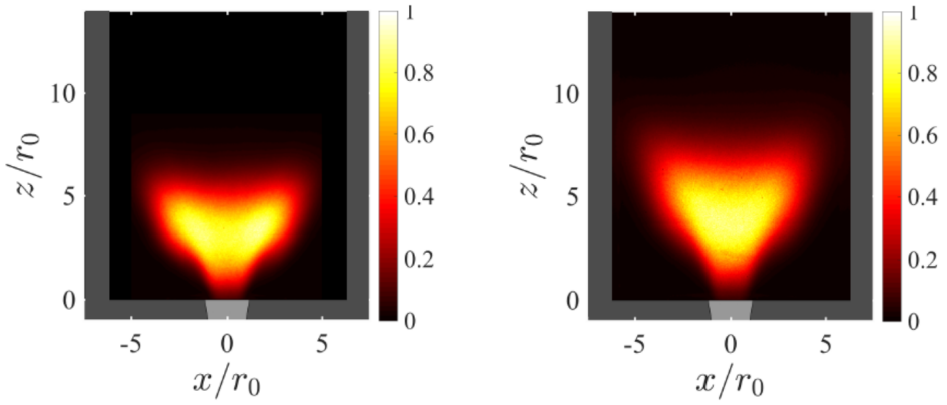

Figure 7.1: *OH^* chemiluminescence images of Flame A (left) and B (right).*

This observation is striking, since the CO2-diluted oxy-flame is characterized by a very high concentration of CO_2 in burnt gases, and this species intensively participates to the radiative transfer through gas-gas interactions and gas-wall interactions.
A possible explication is given by the physical analysis carried out in Degenève et al. (2019a) through a low order model, which justify the similarity observed in wall thermal loads by a counterbalancing between flow pattern and radiative effects when comparing an air-methane flame to a CO2-diluted oxy-methane flame.

In the following sections, some first numerical studies about the CO_2-diluted flames are shown.
In the first section, thermal and chemical effects due to the presence of CO_2 in the fresh mixture is discussed.
In the second section, the effect of CO_2 dilution is studied in one dimension geometries. Special attention is placed on the radiation re-absorption effects which are investigated on the Flame B studied in the Oxytec experimental campaign. This study is obtained by coupling two codes: one solving the 1D equations for the reacting flows, and the other one which solves the radiative heat transfer equation. The impact of radiation reabsorption from fresh carbon dioxide on the laminar flame speed is analyzed.
In the third section, a first step towards the investigation of the phenomena involved in the 3D configuration of the Flame B is illustrated: 3D Large Eddy Simulations accounting for heat losses through walls by imposing measured temperatures are implemented. Details about the numerical set-up and state of the computations are given, and first (non-converged) results are presented. Such a study represents a starting point for coupled LES simulations which could provide a better understanding about the role of radiation in the investigated CO_2-diluted flame, but also to elucidate the mechanisms responsible of

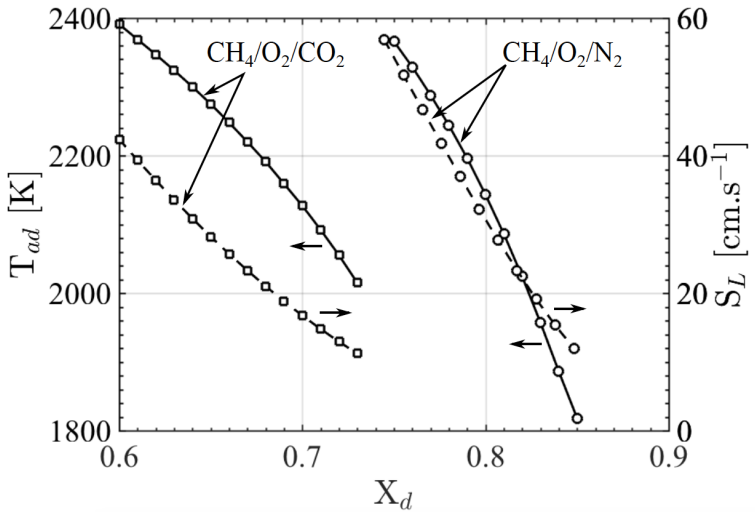

Figure 7.2: *Temperature and laminar flame speed against the molar fraction of diluent X_d for Flame A and B computed with the GRI 3.0 mechanism. Extracted from Jourdaine (2017).*

the similarity in wall temperature and heat fluxes distribution that has been experimentally observed.

7.2 CO2 dilution in oxy-methane flames: Thermal and chemical effects

In CO_2-diluted oxy-methane flames nitrogen from air is totally or partially replaced by carbon dioxide. The presence of CO_2 among the reactants has several effects on the combustion process: thermal, chemical and radiative. In this section, thermal and chemical effects are first discussed by comparing Flames A and B of the Oxytec configuration.
It is known that increasing the CO2 dilution of the combustible mixture decreases the laminar burning velocity and the adiabatic flame temperature.
The two flames investigated in this thesis work, Flame A (methane-air) and flame B (CO_2-O_2-CH_4) have been compared in terms of adiabatic temperature and laminar flame speed as a function of the molar fraction of the diluent (N_2 for the flame A and CO_2 for the flame B) in Jourdaine (2017). Figure 7.2 clearly shows that both T_{ad} and S_L decrease with the increasing of the diluent. Moreover it can be seen that to ensure that Flame B has the same adiabatic flame temperature, $T_{ad} = 2195$ K, of Flame A, a molar fraction of CO_2 equal to $X_{CO_2} = 0.68$ is needed.

Temperature profile obtained in 1D simulations of A and B Flames through GRI 3.0 mechanism (Smith et al. 2011) is shown in Fig. 7.3: even if the two flames

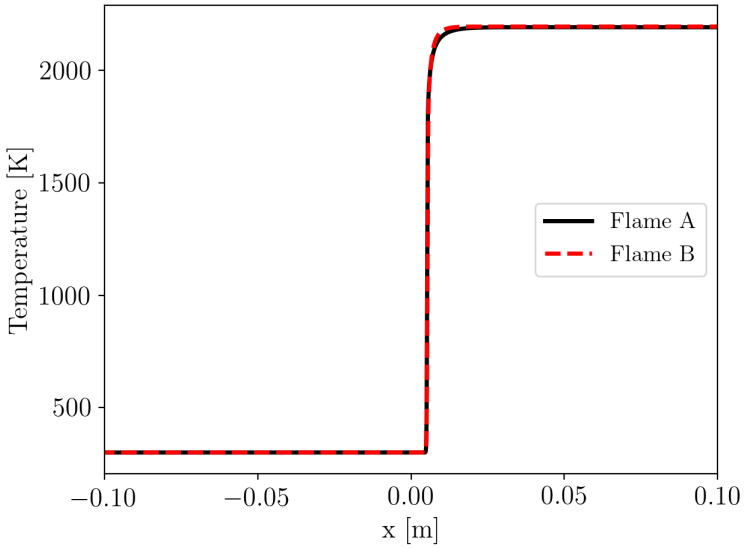

Figure 7.3: *Temperature profile for Flame A (black solid line) and B (red dashed line) computed with the GRI 3.0 mechanism.*

are different in composition and laminar flame speed, they are characterized by a very similar temperature profile.
Chemical and thermal effects due to the presence of carbon dioxide among the fresh reactants has been widely investigated in literature (Glarborg and Bentzen (2007), Halter et al. (2009), Cong and Dagaut (2008), Mazas et al. (2010), De Persis et al. (2013), Xie et al. (2013), Liu et al. (2003), Chan et al. (2015)). These studies highlight that the impact of CO_2 on laminar burning velocity and adiabatic flame temperature is mainly due to:

- transport and thermal properties of the mixture
- chemical effect of CO_2 in reaction mechanisms

In order to separate thermal and chemical effects of CO_2 dilution, a common strategy consists in replacing the CO_2 of the unburnt mixture with a fictitious species characterized by identical thermal and transport properties as CO_2 but which does not take part to the chemical reactions, as it was done in the work of Liu et al. (2003) and Halter et al. (2009).
When CO_2 is present instead of N_2, mass/thermal diffusivities and specific heat capacity of the mixture change. Specifically, the heat capacity c_p of carbon dioxide is higher than the one of nitrogen (41.0 $J\ mole^{-1}\ K^{-1}$ vs 34.2 $J\ mole^{-1}\ K^{-1}$). The effect is that to lower flame temperature and laminar flame speed compared to conventional combustion in air, for the same mole fraction of diluents in the oxidizer.
As concerning the chemical effect of CO_2 dilution, several studies (Glarborg

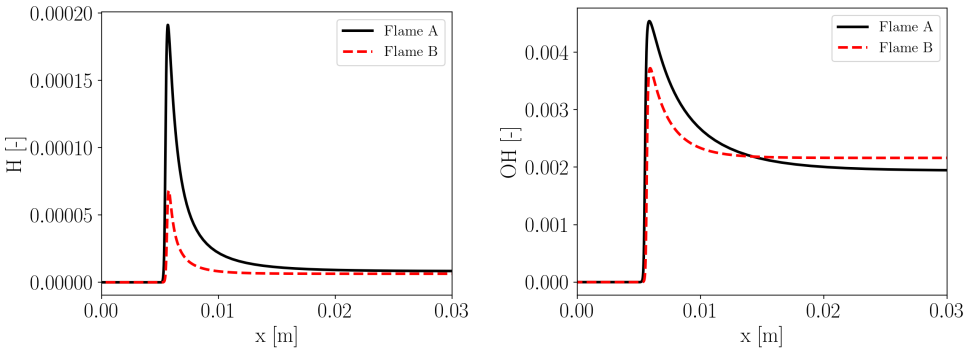

Figure 7.4: *Profiles of H (left) and OH (right) radicals for Flame A (black solid line) and B (red dashed line) computed with the GRI 3.0 mechanism.*

and Bentzen (2007), Cong and Dagaut (2008), Xie et al. (2013)) indicate that the most important chemical contribution of carbon dioxide in hydrocarbon combustion is related to the following reaction:

$$CO_2 + H \leftrightarrow CO + OH$$

Thus, the CO_2 competes for H radicals with the most important chain branching reaction in combustion process:

$$H + O_2 \leftrightarrow O + OH$$

As a consequence, the concentration of important radicals is reduced limiting the fuel burning rate.

One dimensional flames representative of A and B configuration are simulated using GRI 3.0 mechanism (Smith et al. 2011). The lower concentration of some important radicals, such as H and OH, in the flame B compared to the A, can be observed in Fig. 7.4.

Apart from thermal and chemical effects, presence of carbon dioxide in reactant mixture is also responsible of radiative effects enhanced by the absorption of CO2 in the fresh gases. Such effect is illustrated in the next section.

7.3 Radiation effects of CO2 dilution in oxy-methane flames

7.3.1 State of the art

While thermal and chemical impact of carbon dioxide in CO_2-diluted flames has been widely studied in the past, a few studies exist in literature about the radiative contribution of this participating species when present also in the fresh mixture.

Ju et al. (1998) studied 1D planar premixed methane flames in O_2/CO_2 atmosphere by accounting for non-gray radiation of participating gases. Radiative transfer equation is solved by Discrete Ordinate Method, while spectral radiative properties of gases are included with a statistical narrow band model (SNB).
The study shows that the presence of a strongly absorber, such as fresh CO_2, leads to higher burning velocities widening the extinction limits of the investigated flames. Results are compared to an adiabatic 1D flame, where radiation is neglected, and a case where radiation is accounted through the optically thin assumption. It is shown that the lowest burning velocities are found when the gas is considered as optically thin, while the highest ones are found when spectral radiation is solved. However, this work presented only a numerical study, since no experimental data on laminar flame speed in planar flames exhibiting optically thick conditions were available, in order to validate numerical results.
A very similar work is performed by Ruan et al. (2001) together with the author of the previous work adding the comparison with some experimental data obtained from particle laden flame. However, the large heat capacity of particles was not able to confirm the radiation effect.
A more recent work conducted by Chen et al. (2007) investigates the effects of spectral radiation absorption on the flame speed of CO_2 diluted outwardly propagating CH_4-O_2-He flames. DOM is used to solve the radiative transfer equation together with a statistical narrow band model more detailed than the one used in Ju et al. (1998), the SNB based correlated-k method, and adapted for spherical flames.
Both experimental and numerical investigations are performed in this work. Results show that the optically thin approach highly under-predict the laminar flame velocity while SNB narrow-band gray model over-predicts it. Results obtained with the SNB-CK model adapted to spherical flames, can well reproduce experimental data.
Experimental and numerical investigations of laminar flame speed S_L of spherically expanding flames of methane and air in presence of various diluents, among which CO_2, are also performed in Qiao et al. (2010) by comparison with experimental data. The inadequacy of the optically thin assumption with a grey gas model is shown for CO_2-diluted flames; results obtained with the optically thick model, even they over-estimate S_L, are in better agreement with experiments compared to the optically thin model.

The objective of the present study is to investigate the impact of radiation on the laminar flame speed of a 1D steady flame of $CH_4 - O_2 - CO_2$. The flame retained in this study is the flame B of the Oxytec application, characterized by a high CO_2 concentration.
The EM2C radiation solver, Rainier, is coupled to AGATH, a library to compute thermodynamics, transport and kinetics properties which also solves 0D and 1D sets of equations found in reactive flows. Spectral radiative proper-

ties are considered for participating species, CO_2 and H_2O, through the $c-k$ model.
Spectral absorption bands of hot burnt gases and fresh absorber are analyzed to investigate the radiative heat losses. Simulations also highlight a big influence of the domain extention on the laminar flame speed.

7.3.2 Numerical methods

As already mentioned AGATH and Rainier solvers are coupled to each other in order to include the radiative source term in the energy conservation equation. The energy and chemical species conservation equations for steady planar premixed-gas flames are solved in AGATH solver. AGATH communicates with the radiation solver that is in charge to solve the Radiative Transfer Equation after receiving temperature, species concentration and pressure profiles from AGATH. Once Rainier has solved the RTE, it sends the radiative power P^R to AGATH solver that includes it in the energy conservation equation.
In 1D geometries it is possible to obtain a semi-analytical solution of the RTE, consequently the radiation solver uses analytical methods to obtain the radiative source term (Modest (2013), Taine et al. (2014)).
Thus, the only approximation used in this study to solve the RTE is the c-k distribution model (Goody et al. 1989) presented in Chapter 1, in order to account for the spectral radiative properties of gases. For methane oxidation, the GRI-MECH 3.0 (Smith et al. 2011) is used.
Upstream boundary conditions for AGATH solver are: ambient temperature (300 K) and composition, while downstream boundary conditions are zero-gradient.
As concerning the radiation solver, inlet and outlet boundary conditions are considered as two infinite parallel blackbody walls. Ambient temperature and burnt gases temperature are assumed, respectively, at upstream and downstream boundary conditions.

The configuration retained to assess the radiation effect on the laminar flame speed is a freely propagating steady premixed flame of $CH_4-O_2-CO_2$, with the concentrations of the Flame B investigated in the Oxytec campaign. Radiation impact is investigated by comparing the Flame B to the Flame A, *i.e.* the methane-air flame presented in Chapter 4.
The characteristics of the investigated flames are summarized in Tab. 7.1.

7.3.3 Results

First, results on the CO_2-diluted oxy-methane flame are presented in two investigated cases, *i.e.* with and without accounting for radiative heat losses.
Figure 7.5 (top) shows the temperature profiles for the two cases.
It can be observed that when radiation is accounted, variations in temperature

Flames	Φ	T_{ad} [K]	S_L [m/s]	Y_{CH4}	Y_{O2}	Y_{N2}	Y_{CO2}
A	0.95	2192	0.36	0.0525	0.2208	0.7267	-
B	0.95	2192	0.21	0.0572	0.2404	-	0.7024

Table 7.1: *Characteristics of the investigated Flames A and B: equivalence ratio, adiabatic flame temperature, laminar flame speed without radiation and reactants mass fractions. The GRI 3.0 mechanism (Smith et al. 2011) is used.*

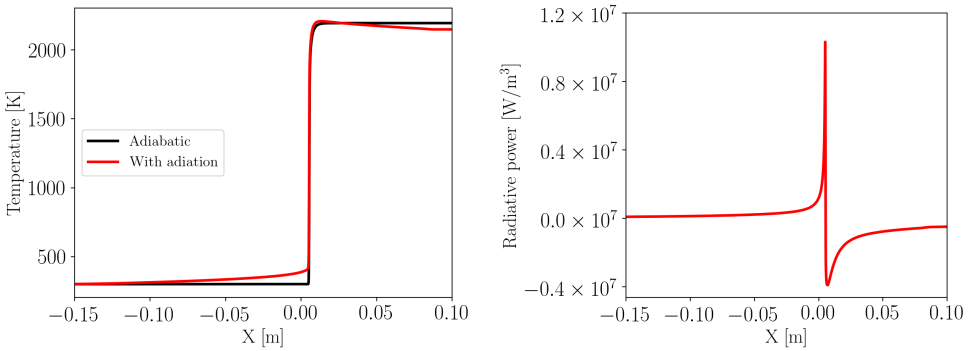

Figure 7.5: *Temperature profile with and without radiation (left) and radiative power profile (right) for Flame B.*

profile appear. Compared to the adiabatic case, three main differences can be found:

- temperature increases in the pre-heating zone;
- the peak temperature is slightly higher than the adiabatic value T_{ad};
- burnt gases temperature decreases.

These observations can be explained looking at the radiative power displayed in Fig. 7.5 (bottom): radiation absorption and emission phenomena are involved in both unburnt and burnt gases. Precisely: in the fresh mixture, only one species participates to the radiative heat transfer, CO_2 (since CH_4 radiation is neglected). The net radiative power in the fresh mixture is mainly absorbed, as indicated by positive values of radiative power. Thus, fresh CO_2 present in the unburnt mixture absorbs the radiation emitted by hot products. This radiation absorption operated from fresh CO_2 is responsible of a radiative pre-heating of the unburnt mixture. As a consequence the peak temperature is higher than one observed in adiabatic conditions.
Downstream the flame, radiative power is negative, meaning that hot burnt gases mainly emit radiation and their temperature is decreased.
Figure 7.6 compares temperature and radiative power profiles in a methane-air flame (Flame A) and in a CO_2-diluted flame (Flame B).
Contrarily to Flame B, radiative power is obviously null upstream the flame

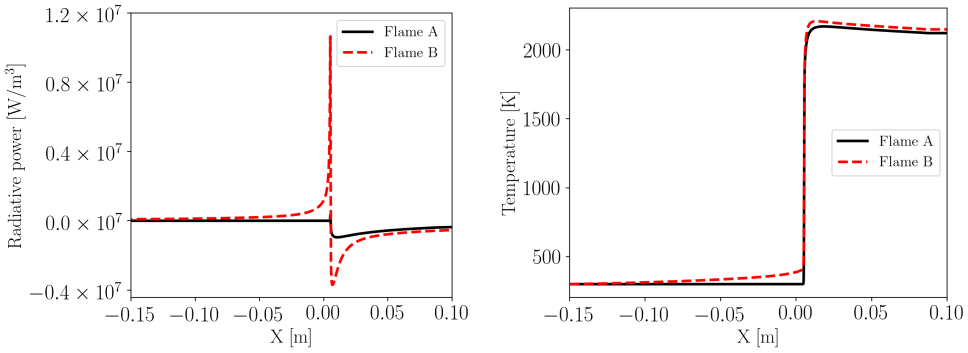

Figure 7.6: *Radiative power (left) and temperature profile (right) in flames A and B.*

in Configuration A, while it is different than zero on the flame front and downstream the flame because of the presence of participating species in burnt gases. Because of the lower CO_2 concentration in burnt gases and the absence of CO_2 in the fresh mixture, the radiative power of Flame A is several orders of magnitude lower than one obtained in the Flame B. On the contrary, when fresh CO_2 is present, the radiative power, emitted and absorbed, becomes very high.

In order to understand what happens from the point of view of radiative heat transfer, the absorption coefficient averaged over each band is plotted against the wavenumber for both fresh carbon dioxide and hot burnt gases in Fig. 7.7. It can be noticed that the absorption bands of the fresh mixture, where the

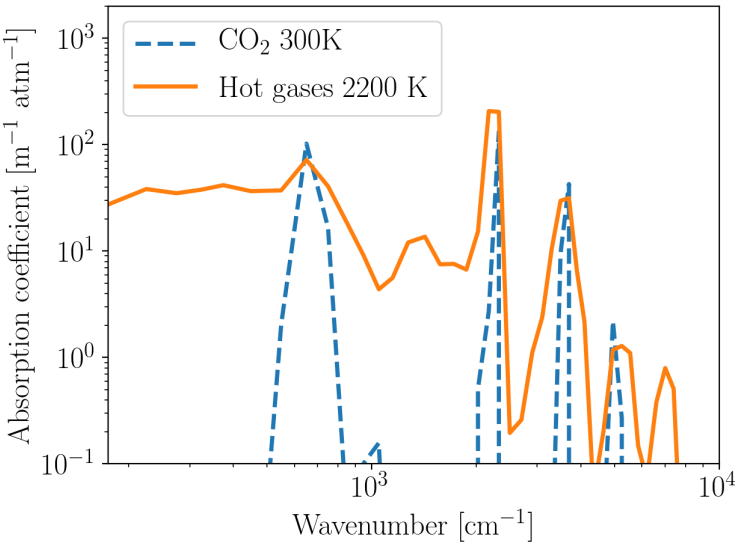

Figure 7.7: *Absorption coefficients for pure CO_2 at 300 K (blue dashed line) and hot burnt gases (H_2O and CO_2) at 2200 K (orange solid line).*

only participating species is CO_2, are narrower than the ones of the hot gases because: a) H_2O is not present in fresh gases and b) CO_2 bands at high temperature are broader than ones at 300 K.
For this reason, most of the radiation emitted downstream by burnt gases cannot be absorbed upstream. Such mechanism is then responsible for the heat losses.
These observations justify the importance of accounting for spectral radiative properties of participating gases in order to catch the mechanisms responsible of the radiative heat losses present in CO_2-diluted flames. Indeed, the use of an optically thin model would neglect the radiation absorption from fresh gases, and, consequently, no variation in the temperature profile could be observed in the pre-heating region. Moreover, neglecting the absorption in the burnt gases, would overestimate the heat losses, leading to an underestimation of burnt gases temperature in the post-flame region, as it is found in Ju et al. (1998).
The impact of radiation absorption observed on temperature profiles has an effect also on the laminar flame speed of CO_2-diluted flames, as it has been seen in literature, and this effect is discussed in the next section.

Impact of radiation on laminar flame speed

Figure 7.8 shows the predicted laminar flame speed for the two investigated flames, i.e. with and without CO_2 dilution, in two different conditions, i.e. with and without accounting for radiation, as a function of the equivalence ratio.
In Flame A, since reabsorption does not affect the flame front, S_L is not impacted. In presence of radiation, burnt gases are cooled downstream without perturbing the flame reactive layer.
It may be interesting to look at the effects of radiation on the fuel reaction rate $\dot{\omega}_{CH_4}$, which, in turns, depends on temperature. Temperature and methane reaction rate profiles, for the two investigated flames, with and without CO_2 dilution and with and without accounting for radiation, are plotted in Fig. 7.9. For the Flame A (Fig. 7.9 left), no variations of temperature (on the top) are observed with and without radiation in the pre-heating zone and flame front. The only variations are found in the post-flame region where burnt gas temperature decreases, due to radiation heat losses. As a consequence, methane source term (on the bottom) is not modified by adding radiation heat losses.
On the contrary, when carbon dioxide is present in the fresh mixture (Fig. 7.9 right), as already observed, temperature variations can be found in pre-heating zone, front flame and post-flame zone (on the top). Consequently, fuel reaction rate (on the bottom) is also impacted: because of the increasing of temperature in the flame front due to radiation, the maximum of $\dot{\omega}_{CH4}$ increases. Indeed, from Fig. 7.8, it can be seen that, for the CO_2-diluted flame, laminar flame speed increases when radiation is considered.

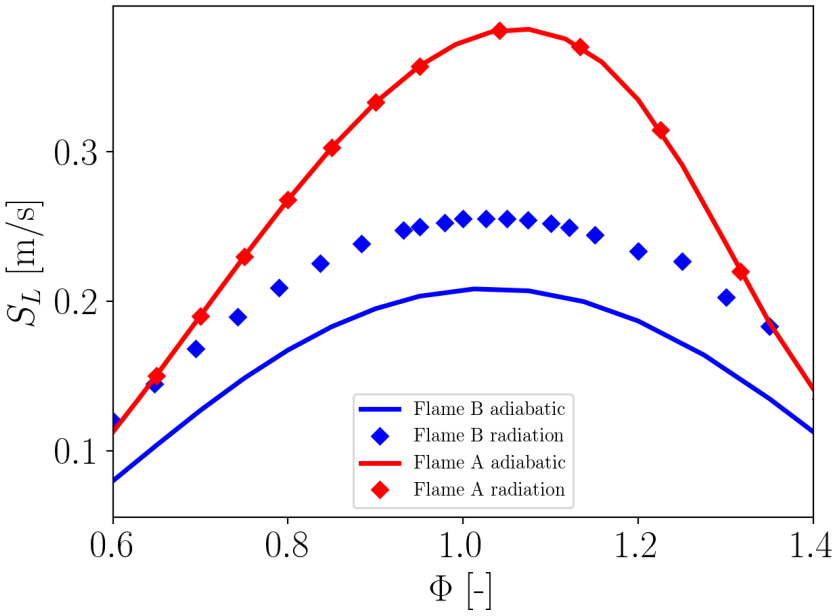

Figure 7.8: *Predicted laminar flame as a function of equivalence ratio for flames A (red) and B (blue) in adiabatic conditions (solid line) and with radiative heat losses (dots).*

The reason for which S_L increases in presence of radiation can be found in the definition of the flame speed.
The laminar flame speed measures the velocity at which the flame front moves in respect to the fresh gases in 1D geometry and it can be defined as (Poinsot and Veynante 2005):

$$S_L = -\frac{1}{\rho^1(Y_F^1 - Y_F^2)} \int_{-\infty}^{+\infty} \dot{\omega}_F dx \tag{7.1}$$

where ρ^1 is the fresh gases density, Y_F^1 and Y_F^2 are the fuel mass fractions in fresh and burnt gases, respectively, and $\dot{\omega}_F$ is the reaction rate of fuel which is integrated along the normal to the flame front x.
Finally, the temperature increase in the flame front due to radiation absorption leads to an increase in the fuel reaction rate. Consequently, the laminar flame increases as well.
Results presented in this section consider a computational domain of 25 cm, whose boundaries are located at x_0 = -15 cm and x_1 = 10 cm. However, in computations performed on wider domains, it has been observed that laminar flame speed strongly depends on the position of the upstream and downstream boundaries. This phenomenon is discussed in the following.

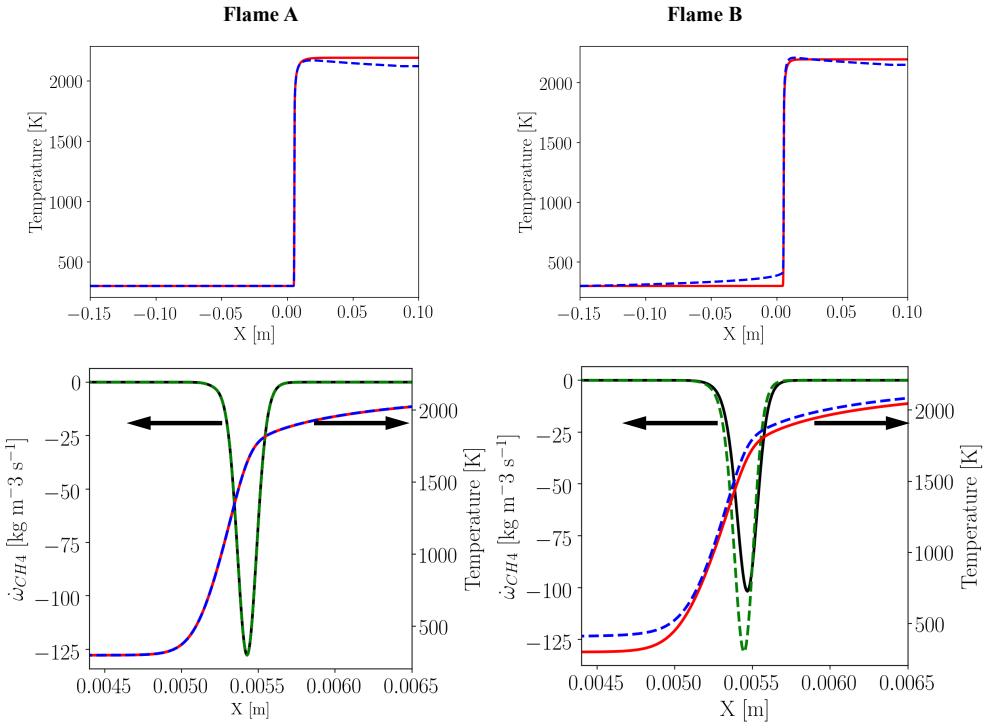

Figure 7.9: *Temperature (top) and methane source term-temperature (bottom) profiles for flames A (left) and B (right). Solid line: radiation is accounted; dashed line: adiabatic case.*

Effect of domain extention on laminar flame speed

The value of laminar flame speed predicted in computations accounting for radiative heat losses depends on the extension of the retained domain, as also observed by Ju et al. (1998).
In the present study, in order to understand the origins of such an impact, two cases are investigated:

- in the first one, the upstream boundary location, x_0, is fixed at -15 cm, and the downstream one is varied;
- in the second case the downstream boundary location, x_1, is fixed at 10 cm (coherently with the order of magnitude of the investigated combustion chamber), and x_0 is the varied parameter.

Concerning the first case, Fig. 7.10 illustrates the decreasing of laminar flame speed (top) and burnt gases temperature (bottom) with the position of the downstream boundary, x_1. The laminar flame speed of the CO_2-diluted oxymethane flame lowers with the increasing of the downstream domain until reaching a constant value, equal to 0.25 m/s for x_1 higher than 3 meters. However

the laminar flame speed remains higher than the one obtained in adiabatic conditions, represented by the blue dashed line.

The fact that S_L reaches a constant value for $x_1 > 3\ m$, means that fresh

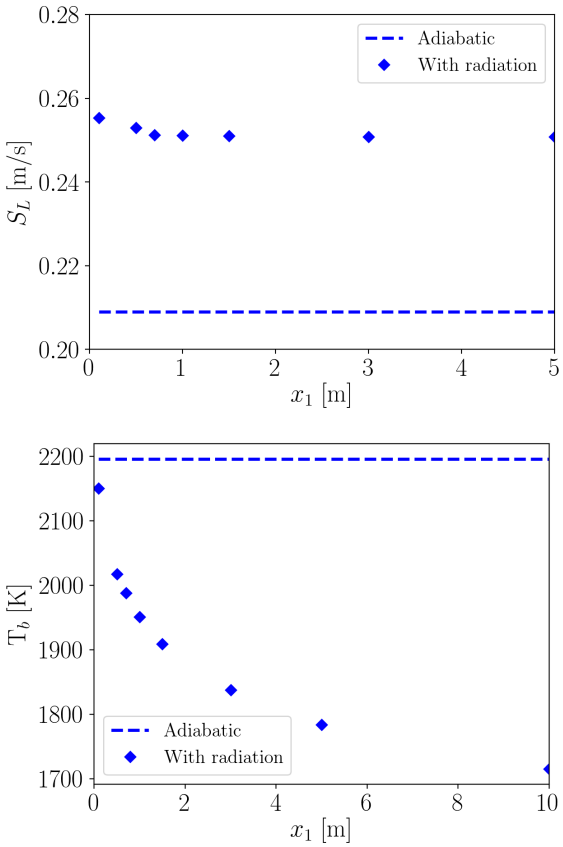

Figure 7.10: *Laminar flame speed (top) and burnt gas temperature (bottom) as a function of the downstream boundary position in adiabatic conditions (dashed line) and with radiative heat losses (blue diamonds) for the Flame B.*

CO_2 reabsorption is not affected by hot gases emitting at a distance larger than $x_1 = 3\ m$. This observation can be demonstrated by looking at Fig. 7.11. On the top, the dimensionless equilibrium spectral intensity at 300 K, corresponding to the temperature of CO_2 in the fresh mixture, shows that the maximum emission of fresh carbon dioxide takes place around 700 cm^{-1}; moreover, the emission bands of fresh CO_2, highlighted with red rectangles, show that only one band is responsible of re-absorption, and it is comprised in [400, 1200] cm^{-1}.

On the bottom, the spectral transmissivities of hot gases at $x_1 = 0.1$ and 3 m are shown. The characteristic length is chosen to be equal to x_1. Focusing on the main absorption band of CO_2, it can be seen that the transmissivity of fresh CO_2 decreases with x_1. In other words, absorption from fresh CO_2 increases

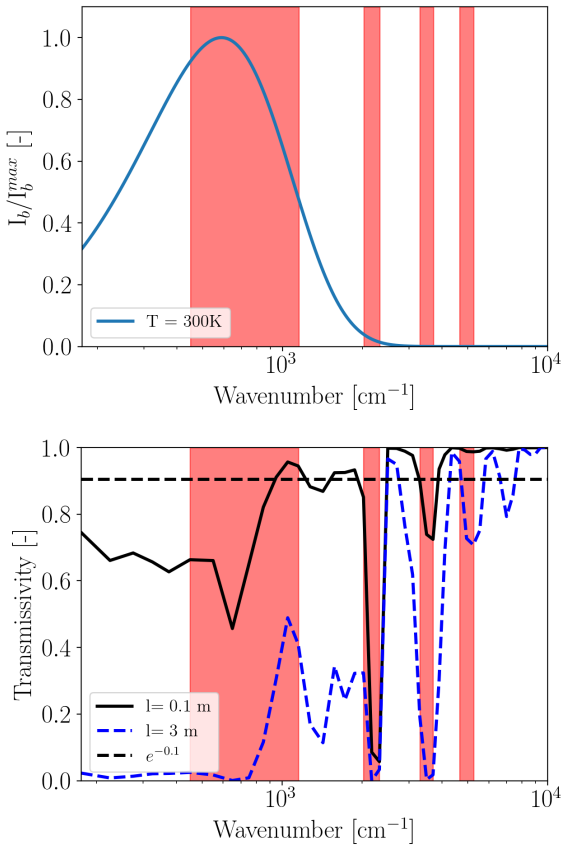

Figure 7.11: *On the top: dimensionless spectral intensity of a black body at 300 K. On the bottom: spectral transmissivity of a column of hot gases issued from Flame B with a characteristic length, l, of 0.1 m and 3 m accounting for the corresponding burnt gases temperature (2195 K and 1837 K, respectively). The horizontal dashed line denotes the limit of the optically thin medium. Red areas highlight absorption bands of fresh CO_2. Both plots are in semi-logarithmic scale.*

with x_1 because the higher x_1, the thicker becomes the column of burnt gases. As a consequence, further increase of x_1 do not lead to further decrease of temperature in the radiative pre-heating zone. This can be observed in Fig. 7.12, where temperature profile in the pre-heating zone is shown for $x_1 = 0.1$ m, 3 m and 5 m. The fact that the temperature in the preheating zone does not vary for x_1 larger than 3 m implies that the laminar flame speed reaches a plateau in correspondance of high values of x_1, as seen in Fig. 7.10.

Contrarily to S_L, the burnt gases temperature at the downstream boundary (Fig. 7.10 bottom) continues to fall, even for high values of x_1 ($x_1 >> 10\ m$). This can be explained by the observation that the radiation received by hot gases coming from the left side of the domain is constant. However, due to the

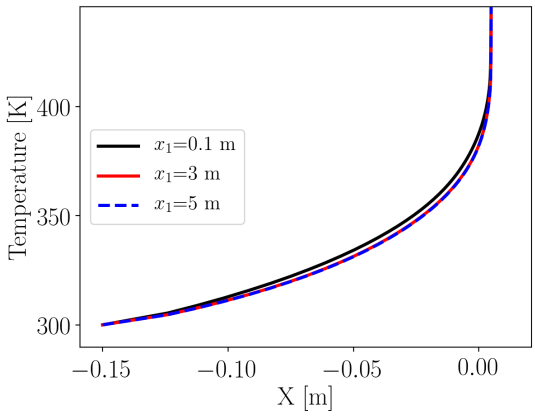

Figure 7.12: *Temperature profile in the radiative pre-heating zone of Flame B for three values of the downstream boundary condition x_1: 0.1 m, 3 m and 5 m.*

presence of emission bands of hot gases characterized by a high transmissivity (Fig. 7.11 bottom), there will be a part of radiation that still leaves the domain. In Fig. 7.10 (bottom) it can be seen that T_b reaches a constant value for very high values of x_1, corresponding to large optical thickness: all emitted radiation is re-absorbed within the downstream region of burnt gases.
High values of x_1 (of the order of meters) are not of practical meaning for semi-laboratory combustion chambers like the one retained in this study. For this reason, before proceeding to study the effect of the upstream boundary condition, the value of x_1 is fixed. The downstream boundary location is chosen to be equal to 10 cm, which is coherent with the order of magnitude of the Oxytec chamber width.

Once again, S_L and T_b are represented in Fig. 7.13 as a function of the domain extension, but this time the varied parameter is x_0.

Contrarily to the previous case where S_L decreases with x_1, when x_0 is moved further upstream, the laminar flame speed increases. Its value goes from 0.25 m/s for the case where the domain width is equal to $[-15\ cm;\ 10\ cm]$, to 0.36 m/s when x_0 is located one hundred meters far from the flame front.
Figure 7.13 indicates a very high impact of the length covered by the unburnt mixture on both S_L and T_b that, contrarily to the first case, increases with high x_0. For a better understanding, temperature profiles are shown in Fig. 7.14 for 1D flames considering x_0 = -0.5 cm, -10 m and -100 m. It can be seen that when x_0 is very far from the flame front, temperature in pre-heating zone increases because more absorption occurs. For this reason x_0 strongly impact S_L. As the pre-heating temperature increases, the flame speed also increases through the higher chemical rates and thermal and mass diffusivities.
The increasing of T^* due to higher temperature in the pre-heating zone when

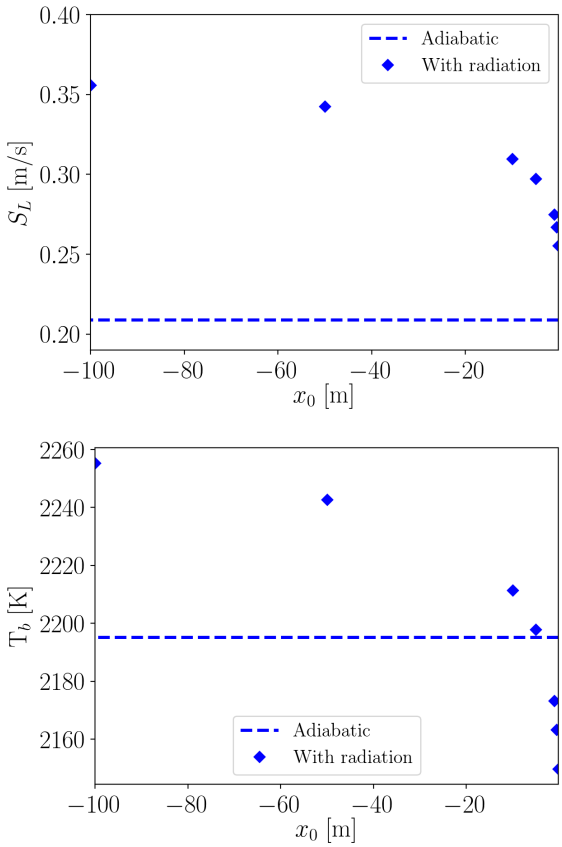

Figure 7.13: *Laminar flame speed (top) and burnt gas temperature (bottom) as a function of the upstream boundary position in adiabatic conditions (dashed line) and with radiative heat losses (diamonds) for the Flame B.*

longer mesh are considered, makes the burnt gases temperature increase on the downstream boundary.

Asymptotic behaviors do not provide practical information: flames with an infinite domain of fresh and/or burnt gases do not exist. Consequently, the domain length has to be imposed in order to obtain a realistic value for the laminar flame speed in 1-D DNS simulations. Such length is case-dependent and it has to be chosen accordingly to the retained configuration.
For a domain size coherent with the Oxytec chamber length, i.e. x_0 = -0.1 m and x_1 = 0.1 m, the variation observed on the laminar flame speed compared to the adiabatic case is 16%: 0.25 m/s against 0.21 m/s of the adiabatic conditions.

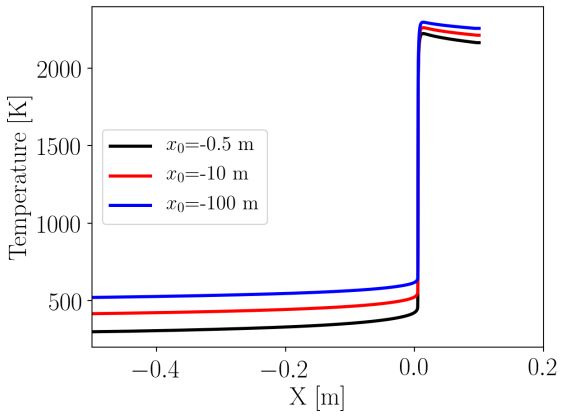

Figure 7.14: *Temperature profiles of 1D flames for three values of the upstream boundary condition x_0: -0.5, -10 and -100 m.*

Conclusions and perspectives

The impact of reabsorption on laminar flame speed in CO_2-diluted flames is discussed in the context of a CO_2-diluted oxy-methane flame (Flame B). The analysis provides a quantification of such an impact for the investigated configuration.

Results show that when accounting for radiation, the laminar flame speed is increased by 16% compared to the value obtained in adiabatic simulations (S_L = 0.25 m/s instead of 0.21 m/s). Spectral radiative properties, obtained with the narrow band model used in this study, provide interesting information about the origin of such an impact. The main mechanism responsible of the change in S_L is the absorption of thermal radiation operated from carbon dioxide, present in the fresh mixture.

However, the variation observed in the laminar flame speed value strongly depends on the domain size.

The effect of the mesh extension has been analyzed by varying the position of the hot side boundary first, and then by imposing this last one and varying the upstream boundary location. As already observed by Ju et al. (1998), the effect of the downstream domain position vanishes for domain length of the order of the meter (x = 1-3 m in the present study), while the upstream boundary location affects the laminar flame even after one hundred meter.

Concerning the future perspectives, it could be interesting to include these radiation effects in coupled simulations. In coupled DNS simulations, since the flame front is totally resolved, radiation effects on laminar flame speed can be faithfully predicted. However, reproducing such effects in a coupled LES simulation may be more complicated, because the flame thickness in LES does not correspond to the real one and this may lead to wrong information about the impact on flame speed.

In literature, the works investigating radiation impact on flame speed do not consider the possibility to extend the study in an LES context. Then, a solution would be needed for coupled LES simulation of flames diluted with radiative absorbers.
In this context, it might be necessary to study the effect of radiation on laminar flame speed of 1D thickened flames; such an analysis would allow to quantify the error made on the predicted laminar flame speed with the goal to correct it in coupled LES simulations. However, some complications could arise from the observation that the radiative environment in 1D flames is not the same as the one found in real configurations, making the study more challenging.

7.4 Towards LES of the CO2-diluted oxy-methane flame

First numerical simulations of the CO_2-diluted oxy-methane flame (Flame B), investigated during the Oxytec experimental campaign, are started in this thesis.
Non-coupled LES accounting for wall heat losses have been implemented. However, given the high computational demand of the simulations of the Oxytec chamber, only 460 ms of such computation have been simulated. These first results represent a starting point for a future study.

7.4.1 Numerical set-up of LES of Flame B

The set-up of Large Eddy Simulation of the Flame B, which is very similar to the one retained for Flame A, is described in this section.

Configuration

Switching for Flame A to B in the Oxytec chamber does not require any modification to the chamber design, then the geometrical domain is the same for both the flames.
As a consequence, the same computational domain used in LES of Chapter 4 is retained.

Procedure

The simulation procedure followed for the Flame B simulation is the following:

- LES of the non-reacting flow are first performed: CH_4-O_2-CO_2 mixture at 300 K and atmospheric pressure is injected in the burner characterized by adiabatic walls. 100 ms have been simulated in order to retrieve a

swirled flow inside the chamber.

- When the chamber is partially filled by fresh mixture, ignition is simulated through the introduction of a kernel sphere inside the chamber, placed at 60 mm far from the axis chamber to keep the same distance of the experimental ignition electrode from the axis.

- At the moment of the ignition the boundary conditions of the chamber walls are switched from adiabatic to iso-thermal.

Boundary conditions for the reacting flow

As for Flame A simulations, the boundary conditions are standard Navier-Stokes characteristic boundary conditions (NSCBC, Poinsot and Lelef (1992)) and are set according to the experimental data.
Boundary conditions imposed for the reacting flow of Flame B with iso-thermal walls are summarized in Tab. 7.2.

Boundary Condition	Physical variables	Relax coefficients
Fresh mixture Inlet	$\dot{m} = 0.00510\ kg.s^{-1}$ $T = 300$ K $Y_{CH_4} = 0.057176$, $Y_{O_2} = 0.240422$ $Y_{CO_2} = 0.702402$	50 000 s^{-1}
Atmo Inlet	$\dot{m} = 0.1\ kg.s^{-1}$ T = 300 K $Y_{O_2} = 0.233$ $Y_{N_2} = 0.767$	50 000 s^{-1}
Outlet	$P = 101325$ Pa	500 s^{-1}
Walls	Isothermal wall law	-

Table 7.2: *NSCBC conditions imposed on the boundary in the reacting flow simulation.*

The temperature field imposed on the chamber walls (bottom chamber, quartz and convergent) is extrapolated from experimental data obtained from LIP measurements of Degenève et al. (2019a).

Combustion model

The combustion model used in Non-Adiabatic LES of Flame B, as for the Flame A, is the Thickened Flame model (TFLES, Colin et al. (2000)).
A global two step reaction mechanism, named 2S-CM2-JB2 (Bibrzycki and Poinsot 2010b), developed for methane flames in O_2/CO_2 atmosphere, is used. The 2S-CM2-JB2 is obtained from the 2S-CM2 (Bibrzycki and Poinsot 2010a),

used in LES of Flame A, by readjusting the Arrhenius parameters.
The reduced mechanism is validated for Φ in $[0.6, 1.4]$, T= 300 K and P = 1 atm, and for a CO_2 mole fraction in the oxidizer up to 70 %. The operating conditions of Flame B are then comprised in the validation range of the mechanism.
The global two step mechanism retained in this study, that will be named JB2 in the following, is compared to Aramco 1.3 mechanism (Metcalfe et al. 2013), an accurate chemical kinetic mechanism including 253 species and 1542 elementary reactions, which has been shown to well predicted experimental data in flames of oxy-methane mixtures diluted with CO_2 (Almansour et al. 2015). A comparison between temperature predictions obtained with JB2 and Aramco 1.3 is shown in Fig. 7.15. Adiabatic temperature predicted by JB2 is slightly over-predicted (15 K), in comparison to results for the detailed mechanism. Also the laminar flame speed is slightly higher in JB2 (0.226 m/s) compared to Aramco (0.215 m/s).

As concerning CO_2 mass fraction in burnt gases, shown in Fig. 7.16, it is

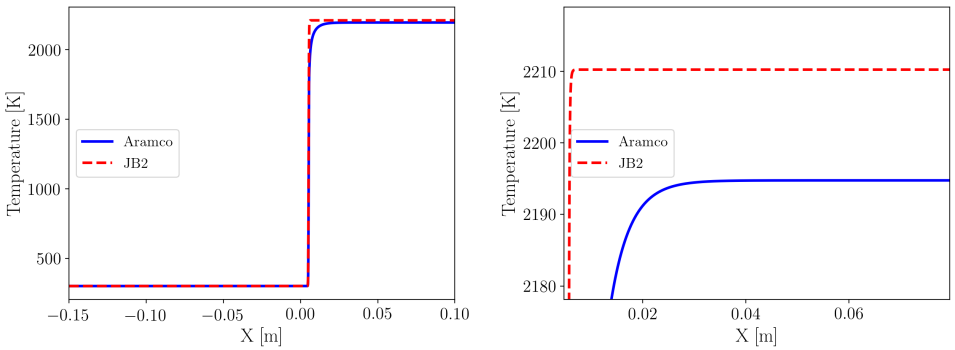

Figure 7.15: *Temperature profile of 1D simulation of Flame B obtained with 2S-CM2-JB2 (red dashed line) and Aramco 1.3 (blue solid line).*

slightly under-predicted in JB2 compared to the detailed mechanism (0.827 instead of 0.829).

Small discrepancies are finally observed in the comparison between the two step and the detailed mechanism: an error of 5% is obtained on the laminar flame speed, while errors lower than 1% are found on adiabatic temperature and CO_2.

7.4.2 Preliminary results

A physical time equal to 460 ms has been simulated for the reacting flow simulation of Flame B with iso-thermal wall.
Since the Flame B configuration is characterized by a bulk velocity which is 1.5 times lower than Flame A, its residence time is even larger than A configuration. This means that the convergence time, equal to 4τ = 1.5 s in Flame A,

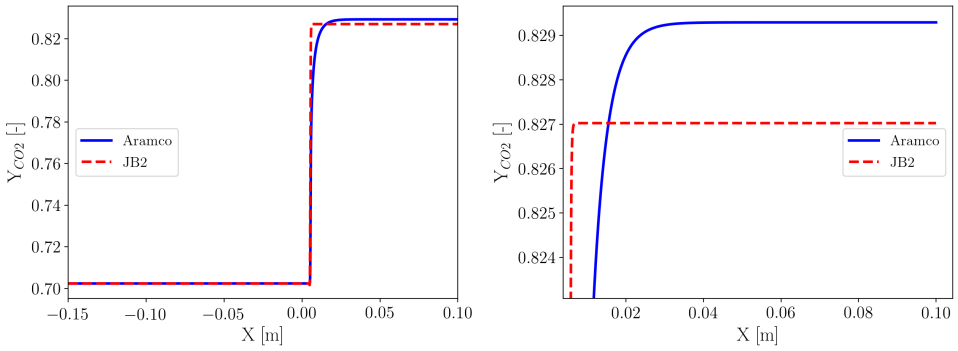

Figure 7.16: *CO_2 mass fraction profile of 1D simulation of Flame B obtained with 2S-CM2-JB2 (red dashed line) and Aramco (blue solid line)*

will be very long in this last investigated case.
However first results, even if still not converged, appear encouraging: Figure 7.17 shows the mean axial velocity field averaged on 80 ms (on the left) and axial and radial velocity profiles (on the right) for three different heights along the chamber. The flame position is highlighted by the iso-surface of the heat release rate at $4 \times 10^7\ W\ /m^3$.
Velocity profiles show a very good agreement with experimental data, both at the burner exit ($x = 5$ mm) and in the flame region ($x = 40$ mm). This comparison is striking, since only slight mismatch appears between numerical results and experimental data of Flame B, while, in the simulations of the Flame A, more discrepancies are found. Indeed the axial velocity peaks extracted from LES of Flame A are overestimated compared to experiments, while it is not the case for Flame B.
This difference is surprising since Flame A and B, as already specified, are characterized by the same computational domain and same numerical models.

7.4.3 Preliminary quantification of radiative heat transfer in Flame B

In order to estimate the radiative role of the high concentration of carbon dioxide in burnt gases of Flame B, a non-coupled radiative transfer simulation has been performed with the solver Rainier.
However, preliminary results are not converged because, as already seen for Flame A, enthalpy losses inside the combustor take several hundreds of milliseconds before converging. As a consequence, gas temperature inside the chamber is still too high compared to the one expected at the steady state.
Rather than performing a radiative simulation of a solution which is still far from the real one, an alternative way to obtain a more realistic quantification of the radiative heat flux in the configuration B is considered. It is based on the observation that A and B flames are very similar in terms of flame topology,

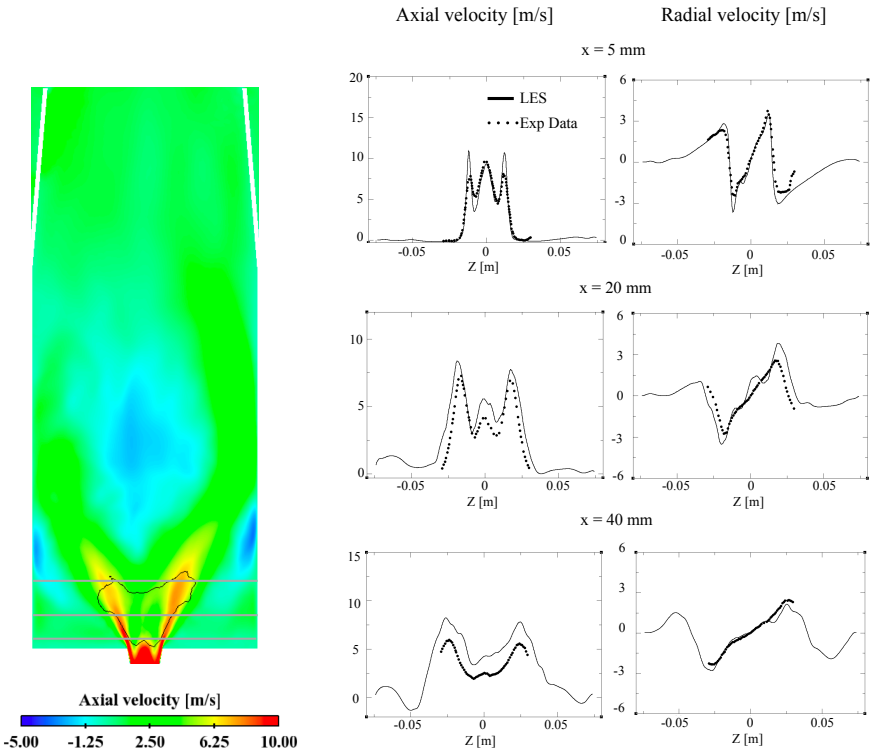

Figure 7.17: *On the left: mean axial velocity field. Black line is the iso-contour of mean heat release equal to* 4×10^7 *W* m^3*. On the right: axial and radial velocity profiles for three heights along the chamber:* $x = 5$ *mm,* $x = 20$ *mm ,* $x = 40$ *mm.*

temperatures and wall fluxes.
Then, the temperature field retained for the radiative simulation of Flame B is taken from an instantaneous converged solution of Flame A, assuming that this is very similar to the gas temperature field corresponding to the Flame B. Also the distribution of CO_2 and H_2O fields is taken from a converged solution of Flame A, but their values are replaced by the ones corresponding to the burnt gases concentration of the Flame B.
Figure 7.18 shows the instantaneous CO_2 field extracted from non-converged LES of Flame B (top) and the CO_2 field retained for the presented simulation (bottom) which is characterized by the same spatial distribution of CO_2 field in Flame A but with values coming from Flame B.

Starting from the two instantaneous solutions of Flames A and B, radiative transfer simulations have been performed and their results are summarized in Tab. 7.3. The Flame B is characterized by a molar fraction of CO_2 in burnt gases around 7 times higher than Flame A. As a consequence the integrated radiative power of Flame B, $\int P^R dV$, is more important (50 % higher) than

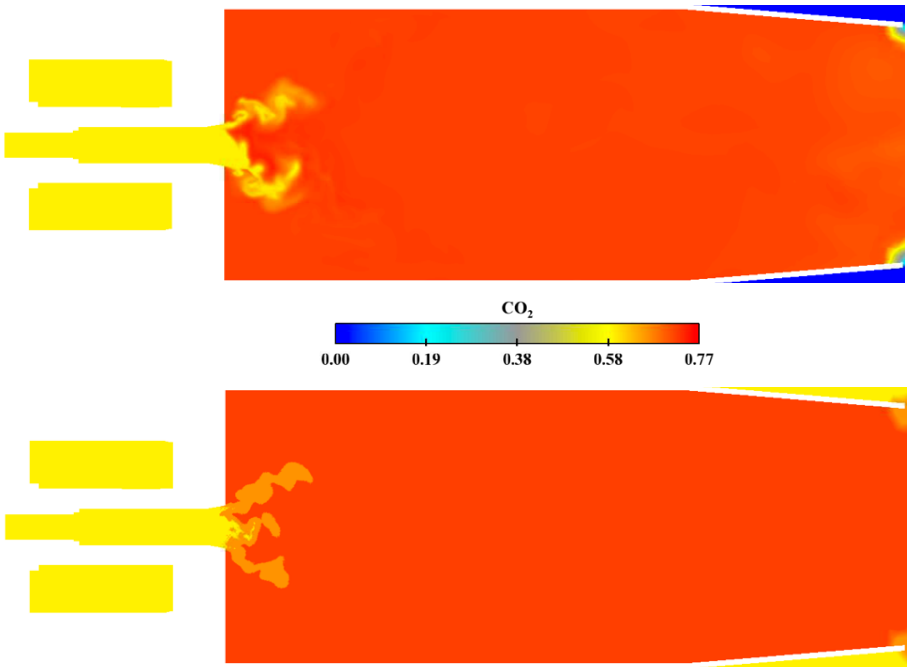

Figure 7.18: *Instantaneous field of CO_2 molar fraction taken from preliminary LES of Flame B (top) and its adaptation to the spatial distribution of CO_2 field taken from converged LES of Flame A.*

the one obtained in the configuration A.

Flame	X^b_{CO2}	X^b_{H2O}	$\int P^R dV$ $[kW]$	$\int P^e dV$	$\int P^a dV$	Wall Flux $[kW]$
A	0.09	0.19	-2.90	10.6	7.7	1.60
B	0.72	0.26	-4.35	64.3	60.0	2.51

Table 7.3: *For the two investigated Flames (A and B): burnt gases molar fraction; net, emitted and absorbed radiative power; wall radiative flux.*

Integrated values of emitted and absorbed radiative powers and radiative wall heat fluxes are also shown in Tab. 7.3. For a better understanding, instantaneous fields of radiative power are shown in Fig. 7.19 for both the configurations. Since the retained solutions are characterized by the same temperature field and same spatial distribution of participating species, absorbing and emitting regions are mostly the same for Flames A and B. However, the very high concentration of both fresh and hot CO_2 in Flame B, enhances emitted and absorbed radiative power, compared to Flame A. The integral of emitted and absorbed power in Flame B is, respectively, 6 and 8 times higher than values obtained from the methane-air flame.

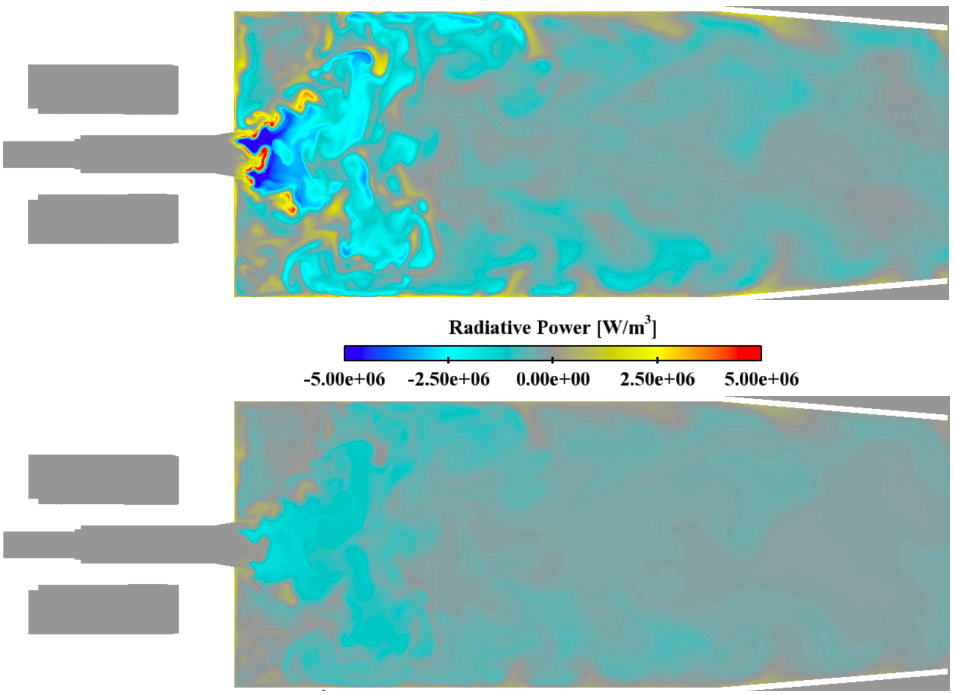

Figure 7.19: *Instantaneous fields of radiative power taken from instantaneous solutions of radiative heat transfer for Flame B (top) and Flame A (bottom).*

Degenève et al. (2019a) found that the enhancement of radiative transfer from high CO_2 concentration, surprisingly, does not increase experimental total wall heat losses when switching from A to B configuration.
The preliminary study carried out in the present work allows to quantify the radiative contribution to the wall fluxes. The numerical wall radiative fluxes, integrated on the chamber walls, appear 1.6 times higher in Flame B compared to Flame A. The active part of the radiative heat flux across the quartz windows, i.e. the part which is not transmitted through the viewing windows, is plotted along the quartz axis in Fig. 7.20 (left) for both A and B configurations. On the right, the experimental conductive flux from Degenève et al. (2019a) is shown.

For $X < 0.05$ m, corresponding to the region in proximity of the Outer Recirculation Zone (ORZ), one can observe very high radiative wall fluxes in both the configurations. Indeed, quartz mean Planck emissivity, shown in Fig. 6.2, is high in this region, because of its low temperature.
As concerning the flux repartition interesting this region, it can be seen in Fig. 7.20 (left) that radiative flux is higher in configuration B than A; besides, PIV from Jourdaine et al. (2017), show that the convective flux in this region is very low, for both configurations.

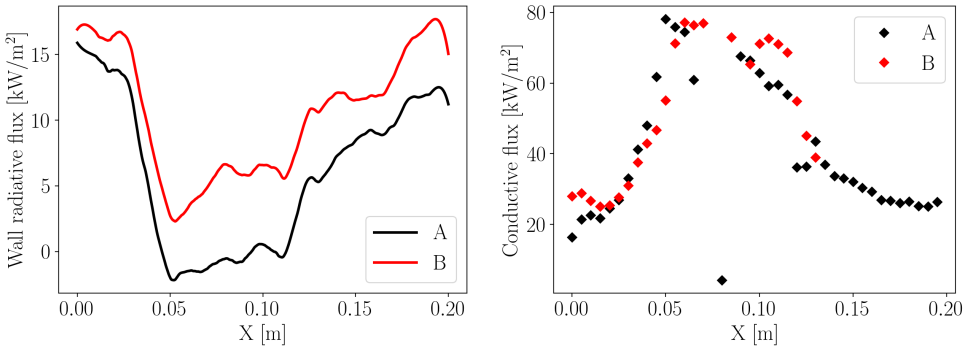

Figure 7.20: *Numerical radiative flux (on the left) and experimental conductive flux (right) along the along the quartz axis X (Y=0).*

Experimental conductive fluxes (right plot in Fig. 7.20) also show slightly higher values for Flame B in the region in proximity of ORZ. The difference between A and B experimental conductive fluxes, for $X < 0.03$ m, could be then explained through the enhanced radiative flux characterizing the Flame B compared to A, as shown in Fig. 7.20 (left).
The high temperature region of the quartz is comprised in $X = [0.05\ m; 0.12\ m]$. Here the radiative flux is close to zero for Flame A: its value is negative, meaning that this region is dominated by emission, and very small, and it is negligible compared to convective flux observed in Flame A (Fig. 4.36). As a consequence in Flame A, wall flux on this region is completely due to convective fluxes.
In the same region, for Flame B, radiative flux is higher and positive, meaning that the flux is mainly absorbed. As a consequence the radiative flux tends to increase wall thermal load. However, one should consider that Flame B is characterized by a lower convective heat transfer compared to A: indeed, injection bulk velocity is smaller in Flame B compared to A, in order to match the same thermal power. This observation may explain the similarity in experimental profiles of wall heat fluxes for this special region ($X = [0.05\ m; 0.12\ m]$): there is a counterbalance between convective and radiative wall fluxes among the two investigated flames, such that convective fluxes are higher in A than B, but radiative fluxes are smaller in A compared than B, thus making total wall fluxes close to each other.
By comparing A and B radiative fluxes, one can notice that their difference is lower in the ORZ region than in the high temperature region. Gas temperature field is assumed to be the same for the two flames in the present comparison, thus the reason can be found in the higher optical thickness of gases in ORZ of Flame B, since it is characterized by higher values of both X_{CO2} and X_{H2O}.
These preliminary results confirm the physical analysis carried out in Degenève et al. (2019a) and based on experimental measurements on Flame A and B.
However, one should remind that the observations drawn during this preliminary study are based on a strong assumption: the same temperature field is

considered for the two investigated cases. In reality, due to the high radiative fluxes encountered in Flame B, gas temperature distribution will be surely affected if radiation is coupled to LES, as seen in coupled simulations of Flame A in Chapter 6. Consequently, in order to have an accurate understanding about the heat transfer involved in the CO_2-diluted flame compared to the one taking place in the methane-air flame, a coupling of LES of Flame B with thermal radiation will be needed.

7.5 Conclusion

Experimental results performed during the Oxytec campaign showed that a methane-air flame (A) and a CO_2-diluted oxy-methane flame (B), even if very different in composition, share at the end a lot of common characteristics, such as flame topology, wall temperature and heat flux distribution.
In this chapter the first numerical study about the Flame B is started. First investigations are done in one dimension geometry by comparing an adiabatic case to another one where radiation is accounted. Significant interest is given in this study to the impact that reabsorption from fresh CO_2 has on the laminar flame speed. Results show that the laminar flame speed increases by 16% when radiation is accounted. Moreover, spectral radiative properties of participating species are considered in order to identify the origin of such phenomenon. The variations observed on S_L are mainly due to the absorption operated from fresh CO_2, which modifies the temperature profile in the radiative pre-heating zone. However, results are conditioned by the position of the upstream and downstream boundary conditions. If the effect of the downstream domain position vanishes for domain length of the order of the meter (x = 1-3 m in the present study), the upstream boundary location affects the laminar flame even after one hundred meters. Consequently, the domain length has to be imposed accordingly to the retained configuration, in order to obtain a realistic value of laminar flame speed.
In the last part of the chapter, the first steps towards the comprehension of the phenomena involved in the 3D configuration of the Flame B are illustrated. Non-adiabatic 3D LES are implemented and their numerical set-up is discussed; moreover, first results are shown and compared to experimental data. Even if the simulation is still not converged, velocity fields look in a very good agreement with experimental data.
A preliminary study of the radiative heat transfer is also carried out. In order to understand the role played by radiative heat transfer in both A and B flames, an instantaneous LES solution of Flame A is compared to a solution characterized by the same temperature field than the Flame A but with the hot gases concentration characterizing the Flame B.
Results show that the high concentration of carbon dioxide in the CO_2-diluted oxy-methane flame (B) enhances radiative power by 50% compared to the

methane-air flame (A). The analysis of radiative fluxes along the quartz axis leads to the same conclusions drawn in Degenève et al. (2019a) concerning the distribution of experimental wall fluxes. However, for a more accurate understanding, radiative heat transfer should be coupled to LES.

Conclusion

This thesis is inserted in the context of multi-physics simulations involving thermal radiation and combustion. Thermal radiation is known to play an important role in some combustion processes, such as the ones involved in the new combustion technologies. The Oxytec chamber, experimentally investigated at the EM2C laboratory by the team of Prof. Thierry Schuller and Dr. Clément Mirat, represents an interesting application to investigate one of the new combustion technologies, such as the oxy-combustion. For this reason it is retained as target application for the numerical simulations planned in this thesis work. Two swirled premixed flames have been experimentally studied during the Oxytec campaign: a methane-air flame (Flame A) and a CO_2-diluted oxy-methane flame (Flame B). Despite their different composition, such flames share a lot of common characteristics like thermal power, adiabatic temperature and wall heat fluxes distribution. The first numerical simulation of the Oxytec chamber has been performed in this study.
In order to accurately account for thermal radiation, Monte Carlo methods are retained, which, on the other hand, are known to be computationally demanding. Indeed, in coupled simulations involving MC methods, most of the computational time is consumed by the radiative solver, making such multi-physics simulations very costly.
The objective of this thesis is to make coupled simulations of real combustion systems computationally affordable, while accounting for accurate modelling of thermal radiation. For this reason, an alternative family of methods, known as Quasi-Monte Carlo methods (QMC), is investigated. QMC have been applied, in the past, only to simple 1D or 2D configurations. In this work they are, for the first time, applied to real 3D configurations.

Major achievements

Assessment of Quasi-Monte Carlo method efficiency on several 3D configurations

When 3D simulations of reactive flows are coupled with accurate methods for radiative heat transfer, such as Monte Carlo methods, the cost of a coupled simulation can be even 10 times more expensive compared to the cost of an

only-combustion simulation. Due to the increasing interest towards high-fidelity multi-physics 3D simulations, it appears necessary to reduce the computational cost of MC methods. One strategy to improve the efficiency of Monte Carlo method consists in replacing the pseudo-random sequences by an alternative sampling: the low-discrepancy sequences. The resulting method is called Quasi-Monte Carlo method (QMC). Their advantage lies in a higher convergence rate compared to MC methods; however, their deterministic feature does not make possible to get an error estimation. For this reason, a randomization of QMC (RQMC) is performed.
The low-discrepancy sequence used in this work is the Sobol sequence and the randomization technique is the *I-binomial scrambling*.
RQMC are implemented in the MC solver, Rainier. The features of the radiation solver are given in Chap 3: both MC and RQMC methods are implemented, with the possibility to use ERM and OERM formalism for each method.
The features of MC and RQMC methods are first shown on a 2-dimensional integration problem, highlighting the higher convergence rate of RQMC compared to MC. MC and RQMC are then assessed on three practical configurations (turbulent channel flow, jet flame and laboratory-scale combustion chamber) through instantaneous 3D solution fields obtained from DNS or LES. The retained cases are characterized by several degrees of complexity: high pressure, presence of soot and wall confinement. This variety of applications enables to study the impact of QMC methods in realistic cases. Simulations results show a significative improvement from RQMC compared to MC method in terms of computational efficiency, leading to a reduction of the computational time of a radiative heat transfer simulation of all the investigated cases by a factor that varies from 1.8 to 2.5, depending on the configuration.
Sometimes, to reduce the computational time of a simulation, a trade-off with accuracy has to be found. Results obtained with RQMC show that accuracy increase is simultaneously obtained with a decrease in computational cost. Such analysis anticipates the benefits of RQMC in coupled high-fidelity simulations based on LES or DNS.
In this thesis RQMC method is therefore coupled to Large Eddy Simulation of the target application: the Oxytec chamber.

Impact of radiative heat transfer in the Oxytec application target

Flame A

Radiation is one of the heat transfer mechanisms taking place in combustion chambers, and, in some configurations, it plays an important role in the prediction of wall thermal loads. In this study, the role of thermal radiation is assessed in one of the flame configurations investigated during the Oxytec experimental campaign, the Flame A.

First, Large Eddy Simulations (LES) of Flame A has been performed, imposing the measured wall temperature and without accounting for radiation. LES have highlighted two main challenges in the simulations of the Flame A.
The first challenge is the high computational cost of the simulation due to the large residence time characterizing the Oxytec chamber. This issue required the definition of convergence criteria in order to check the convergence status of the computation. The second challenge, emerged from the simulation of the Oxytec chamber, is the difficulty to numerically predict the recirculation zones, typical characteristics of a swirling flow. Both non-reacting and reacting flow simulations of the Flame A show that retrieving the position of the stagnation point is challenging. The stagnation point is the location on the chamber axis where the axial velocity becomes null and it marks the beginning of the inner recirculation zone (IRZ) in the investigated configuration. Retrieving the good position of the stagnation point is fundamental in swirled premixed flames, since the flame stabilizes just upstream the IRZ in the studied configuration.

As concerning the numerical results obtained from LES, non-reacting flow simulation show good velocity profiles compared to experimental data, however a discrepancy appears in the prediction of the stagnation point position.
When passing to the reacting flow simulation, velocity profiles get closer to experimental ones, compared to non-reacting flow. However, still a slight discrepancy appears in the prediction of the stagnation point.
As concerning the flame topology, LES correctly predict quenching effects in the outer shear layers due to heat losses, yielding a V-shape which is very similar to experimental OH* chemiluminescence; however, in LES, the flame appears more compact than the experimental one and its height is under-estimated.
A comparison on wall heat flux distribution is also carried out. The experimental trend of conductive flux is very well retrieved, the discrepancy found in the quantitative comparison is associated to the neglect of radiative heat transfer.

Radiative heat transfer is then taken into account by coupling the MC solver, Rainier, with the LES solver, AVBP. RQMC method is used for radiation, as well as the correlated-k distribution model to include spectral radiative properties of gases. Due to high computational cost of such simulation, a trade-off between accuracy and CPU cost is found, by using a computational grid for Rainier 1.5 times coarser than the one used for LES, and by coupling AVBP and Rainier every 54 μs of physical time.
Compared to non-coupled simulations, velocity profiles, flame topology and gas temperature measurements are better predicted. Results let think that the stabilisation of the IRZ is highly sensitive to the temperature field.An impact on wall fluxes is also highlighted. Radiative contribution to wall flux is predominant in the lower and upper regions of the quartz windows, characterized by higher absorption. The comparison with experimental wall flux shows that the performed coupled simulations are quite promising for predicting thermal loads

on combustor walls. A sensible enthalpy balance confirms the importance of accounting for radiative fluxes; indeed, 20% of the flame thermal power is lost through radiative fluxes. Accounting for semi-transparent properties of quartz is significant in the Oxytec configuration, since almost 35% of radiative flux is transmitted to the exterior. However, during the last milliseconds of simulation it is observed that the analyzed steady state is followed by a second transient, which is not a thermal one. In this phase, flow topology completely changes, despite position and shape of the flame remain unchanged. Such variations are attributed to the numerical pressure oscillations arising in the computations during this second transient or to bifurcating behavior that some highly swirling flow may show.

Flame B

The presence of CO_2 in the fresh mixture of Flame B has thermal, chemical and radiative effects in a combustion process. Radiation effects are investigated in this study by coupling the radiation solver, Rainier, with AGATH, a code solving the 1D equations for reacting flows. The analysis show that the presence of carbon dioxide in the fresh mixture has a great impact on the laminar flame speed, S_L. Because of the re-absorption of thermal radiation operated from CO_2, the laminar flame speed is increased by 16% compared to the value obtained in adiabatic conditions: 0.25 m/s instead of 0.21 m/s.
Moreover, the variation observed in S_L strongly depends on the domain size, making then necessary to impose the numerical domain length accordingly to the experimental configuration.

First Large Eddy Simulation of the 3D configuration of Flame B have also been implemented, by imposing measured wall temperature on the solid parts of the combustor. A comparison of the preliminary (non-converged) results with experimental data seems encouraging. A preliminary study of radiative heat transfer in Flame B is performed through a non-coupled simulation in Rainier. Results show that the high concentration of carbon dioxide in the burnt gases of Flame B enhances radiative power by 50% compared to the methane-air flame (Flame A). The analysis of radiative fluxes along the quartz axis leads to the same conclusions drawn in Degenève et al. (2019a) concerning the distribution of experimental wall fluxes and the heat transfer mechanisms taking place in both investigated configurations. However, for a more accurate understanding, a coupling of LES of Flame B with thermal radiation will be needed.

Perspectives

The non-adiabatic LES of Flame B, which have been started in this thesis work, are pursued in the PhD thesis of A. Degenève.
The Flame B represents a very interesting configuration since the high carbon

dioxide concentration characterizing burnt gases enhances radiative heat transfer. In this context the effect of radiation will be further investigated in the future by coupling LES with accurate MC methods, while adopting the numerical set-up implemented in this work and described in Chapter 5.
This study will also allow to perform a more detailed comparison between Flames A and B and to understand the mechanisms responsible of the similarity in wall temperature and heat fluxes distribution, experimentally observed in Degenève et al. (2019a), although the radiative contribution is strongly impacted by the different level of CO_2 in the gaseous mixture.

References

Adams, B. and P. Smith (1995). Modeling effects of soot and turbulence-radiation coupling on radiative transfer in turbulent gaseous combustion. *Combustion Science and technology 109*(1-6), 121–140. *(p. 18)*

Adams, C. N. and G. W. Kattawar (1978). Radiative transfer in spherical shell atmospheres: I. rayleigh scattering. *Icarus 35*(1), 139–151. *(p. 44)*

Almansour, B., L. Thompson, J. Lopez, G. Barari, and S. S. Vasu (2015). Ignition and flame propagation in oxy-methane mixtures diluted with co2. In *ASME Turbo Expo 2015: Turbine Technical Conference and Exposition*. American Society of Mechanical Engineers. *(p. 219)*

Baes, M., K. D. Gordon, T. Lunttila, S. Bianchi, P. Camps, M. Juvela, and R. Kuiper (2016). Composite biasing in monte carlo radiative transfer. *Astronomy & Astrophysics 590*, A55. *(p. 53, 56)*

Barber, R., J. Tennyson, G. J. Harris, and R. Tolchenov (2006). A high-accuracy computed water line list. *Monthly Notices of the Royal Astronomical Society 368*(3), 1087–1094. *(p. 5)*

Berger, S., S. Richard, F. Duchaine, G. Staffelbach, and L. Gicquel (2016). On the sensitivity of a helicopter combustor wall temperature to convective and radiative thermal loads. *Applied Thermal Engineering 103*, 1450–1459. *(p. 18, 19)*

Bertini, D., L. Mazzei, S. Puggelli, A. Andreini, B. Facchini, L. Bellocci, and A. Santoriello (2018). Numerical and experimental investigation on an effusion-cooled lean burn aeronautical combustor: Aerothermal field and metal temperature. In *ASME Turbo Expo 2018: Turbomachinery Technical Conference and Exposition*, pp. V05CT17A010–V05CT17A010. American Society of Mechanical Engineers. *(p. 18, 19)*

Bibrzycki, J. and T. Poinsot (2010a). Investigation of laminar flame speed of ch4/n2/o2 and ch4/co2/o2 mixtures using reduced chemical kinetic mechanisms. *Archivum combustionis 30*(4), 287–296. *(p. 118, 218)*

Bibrzycki, J. and T. Poinsot (2010b). Reduced chemical kinetic mechanisms for methane combustion in o2/n2 and o2/co2 atmosphere. *Working note ECCOMET WN/CFD/10 17*. *(p. 218)*

Blättner, W. G., H. G. Horak, D. G. Collins, and M. B. Wells (1974). Monte carlo studies of the sky radiation at twilight. *Applied optics 13*(3), 534–547. *(p. 44)*

Booth, T. E. (1983). Weight window/importance generator for monte carlo streaming problems. Technical report, Los Alamos National Lab., NM (USA). *(p. 52, 56)*

Boulet, P., J. Gerardin, Z. Acem, G. Parent, A. Collin, Y. Pizzo, and B. Porterie (2014). Optical and radiative properties of clear pmma samples exposed to a radiant heat flux. *International Journal of Thermal Sciences 82*, 1–8. *(p. 48)*

Boyle, P., M. Broadie, and P. Glasserman (2001). Monte carlo methods for security pricing. *Option pricing, interest rates and risk management*, 185–238. *(p. 70)*

Buis, S., A. Piacentini, and D. Déclat (2006). Palm: a computational framework for assembling high-performance computing applications. *Concurrency and Computation: Practice and experience 18*(2), 231–245. *(p. 152)*

Buras, R. and B. Mayer (2011). Efficient unbiased variance reduction techniques for monte carlo simulations of radiative transfer in cloudy atmospheres: The solution. *Journal of quantitative spectroscopy and radiative transfer 112*(3), 434–447. *(p. 56)*

Butler, T. and P. O'rourke (1977). A numerical method for two dimensional unsteady reacting flows. In *Symposium (International) on Combustion*, Volume 16, pp. 1503–1515. Elsevier. *(p. 117)*

Case, K. (1957). Transfer problems and the reciprocity principle. *Reviews of Modern Physics 29*(4), 651. *(p. 42, 79)*

Cashwell, E. D. and C. J. Everett (1959). A practical manual on the monte carlo method for random walk problems. *(p. 55)*

Chan, Y., M. Zhu, Z. Zhang, P. Liu, and D. Zhang (2015). The effect of co2 dilution on the laminar burning velocity of premixed methane/air flames. *Energy Procedia 75*, 3048–3053. *(p. 203)*

Charlette, F., C. Meneveau, and D. Veynante (2002). A power-law flame wrinkling model for les of premixed turbulent combustion part i: non-dynamic formulation and initial tests. *Combustion and Flame 131*(1-2), 159–180. *(p. 118)*

Chen, Z., X. Qin, B. Xu, Y. Ju, and F. Liu (2007). Studies of radiation absorption on flame speed and flammability limit of co2 diluted methane flames at elevated pressures. *Proceedings of the Combustion Institute 31*(2), 2693–2700. *(p. 205)*

Cherkaoui, M., J.-L. Dufresne, R. Fournier, J.-Y. Grandpeix, and A. Lahellec (1996). Monte carlo simulation of radiation in gases with a narrow-band model and a net-exchange formulation. *Journal of Heat Transfer 118*(2), 401–407. *(p. 45, 46, 60)*

Coelho, P. (2001). The role of ray effects and false scattering on the accuracy of the standard and modified discrete ordinates methods. In *ICHMT DIGITAL LIBRARY ONLINE*. Begel House Inc. *(p. 12)*

Coelho, P., O. Teerling, and D. Roekaerts (2003). Spectral radiative effects

and turbulence/radiation interaction in a non-luminous turbulent jet diffusion flame. *Combustion and Flame 133*(1-2), 75–91. *(p. 18, 19)*

Coelho, P. J. (2007). Numerical simulation of the interaction between turbulence and radiation in reactive flows. *Progress in energy and combustion science 33*(4), 311–383. *(p. 17, 27)*

Coelho, P. J. (2012). Turbulence–radiation interaction: from theory to application in numerical simulations. *Journal of Heat Transfer 134*(3). *(p. 27)*

Coelho, P. J., P. Perez, and M. El Hafi (2003). Benchmark numerical solutions for radiative heat transfer in two-dimensional axisymmetric enclosures with nongray sooting media. *Numerical Heat Transfer: Part B: Fundamentals 43*(5), 425–444. *(p. 60)*

Colin, O., F. Ducros, D. Veynante, and T. Poinsot (2000). A thickened flame model for large eddy simulations of turbulent premixed combustion. *Physics of fluids 12*(7), 1843–1863. *(p. 117, 118, 218)*

Colin, O. and M. Rudgyard (2000). Development of high-order taylor–galerkin schemes for les. *Journal of Computational Physics 162*(2), 338–371. *(p. 106)*

Collins, D. G., W. G. Blättner, M. B. Wells, and H. G. Horak (1972). Backward monte carlo calculations of the polarization characteristics of the radiation emerging from spherical-shell atmospheres. *Applied Optics 11*(11), 2684–2696. *(p. 42)*

Combis, P., P. Cormont, L. Gallais, D. Hebert, L. Robin, and J.-L. Rullier (2012). Evaluation of the fused silica thermal conductivity by comparing infrared thermometry measurements with two-dimensional simulations. *Applied Physics Letters 101*(21), 211908. *(p. 139)*

Cong, T. L. and P. Dagaut (2008). Experimental and detailed kinetic modeling of the oxidation of methane and methane/syngas mixtures and effect of carbon dioxide addition. *Combustion Science and Technology 180*(10-11), 2046–2091. *(p. 203, 204)*

Cranley, R. and T. N. Patterson (1976). Randomization of number theoretic methods for multiple integration. *SIAM Journal on Numerical Analysis 13*(6), 904–914. *(p. 71)*

De Lataillade, A., J. Dufresne, M. El Hafi, V. Eymet, and R. Fournier (2002). A net-exchange monte carlo approach to radiation in optically thick systems. *Journal of Quantitative Spectroscopy and Radiative Transfer 74*(5), 563–584. *(p. 46, 55)*

De Persis, S., F. Foucher, L. Pillier, V. Osorio, and I. Gökalp (2013). Effects of o2 enrichment and co2 dilution on laminar methane flames. *Energy 55*, 1055–1066. *(p. 203)*

Degenève, A., P. Jourdaine, C. Mirat, J. Caudal, R. Vicquelin, and T. Schuller (2019a). Analysis of wall temperature and heat flux distributions in a swirled combustor powered by a methane-air and a co2-diluted oxyflame. *Fuel 236*, 1540–1547. *(p. xvii, xviii, 101, 104, 106, 120, 138, 139, 140, 155, 200, 201, 218, 223, 224, 226, 230, 231)*

Degenève, A., P. Jourdaine, C. Mirat, J. Caudal, R. Vicquelin, and T. Schuller (2019b). Effects of a diverging cup on swirl number, flow pattern, and topology of premixed flames. *Journal of Engineering for Gas Turbines and Power 141*(3), 031022. *(p. 109)*

Delatorre, J., G. Baud, J.-J. Bézian, S. Blanco, C. Caliot, J.-F. Cornet, C. Coustet, J. Dauchet, M. El Hafi, V. Eymet, et al. (2014). Monte carlo advances and concentrated solar applications. *Solar Energy 103*, 653–681. *(p. 56)*

Denison, M. and B. Webb (1995a). The spectral line-based weighted-sum-of-gray-gases model in nonisothermal nonhomogeneous media. *Journal of Heat Transfer 117*(2), 359–365. *(p. 9)*

Denison, M. and B. W. Webb (1995b). Development and application of an absorptionline blackbody distribution function for co2. *International Journal of Heat and Mass Transfer 38*(10), 1813–1821. *(p. 9)*

Denison, M. K. and B. W. Webb (1993). A spectral line-based weighted-sum-of-gray-gases model for arbitrary rte solvers. *Journal of Heat Transfer 115*(4), 1004–1012. *(p. 9)*

dos Santos, R. G., M. Lecanu, S. Ducruix, O. Gicquel, E. Iacona, and D. Veynante (2008). Coupled large eddy simulations of turbulent combustion and radiative heat transfer. *Combustion and Flame 152*(3), 387–400. *(p. 18, 19)*

Duchaine, F., S. Jauré, D. Poitou, E. Quémerais, G. Staffelbach, T. Morel, and L. Gicquel (2015). Analysis of high performance conjugate heat transfer with the openpalm coupler. *Computational Science & Discovery 8*(1), 015003. *(p. 152)*

Dupoirieux, F., L. Tessé, S. Avila, and J. Taine (2006). An optimized reciprocity monte carlo method for the calculation of radiative transfer in media of various optical thicknesses. *International Journal of Heat and Mass Transfer 49*(7), 1310–1319. *(p. 44, 48)*

Dupree, S. A. and S. K. Fraley (2012). *A Monte Carlo Primer: A Practical Approach to Radiation Transport*. Springer Science & Business Media. *(p. 51, 53)*

Edwards, D. (1976). Molecular gas band radiation. In *Advances in heat transfer*, Volume 12, pp. 115–193. Elsevier. *(p. 59)*

Edwards, D. (1983). Numerical methods in radiation heat transfer. *Numerical Properties and Methodologies in Heat Transfer*, 479–496. *(p. 44)*

Evans, K. F. (1998). The spherical harmonics discrete ordinate method for three-dimensional atmospheric radiative transfer. *Journal of the Atmospheric Sciences 55*(3), 429–446. *(p. 61)*

Falese, M., L. Y. Gicquel, and T. Poinsot (2014). Les of bifurcation and hysteresis in confined annular swirling flows. *Computers & Fluids 89*, 167–178. *(p. 194)*

Farmer, J. T. and J. R. Howell (1998). Comparison of monte carlo strategies for radiative transfer in participating media. In *Advances in heat transfer*,

Volume 31, pp. 333–429. Elsevier. *(p. 50)*

Faure, H. (1982). Discrepancy of sequences associated with a numeration system (in s-dimension). *Acta Arithmetica 41*(4), 337–351. *(p. 39, 70)*

Favre, A. (1965). The equations of compressible turbulent gases. Technical report, Technical Institut de mecanique statistique de la turbulence. *(p. 16)*

Feldick, A., A. Bansal, and M. Modest (2011). Variance reduction techniques for monte carlo solution of radiative transfer in hypersonic flows: Hybrid p-1-monte carlo. In *49th AIAA Aerospace Sciences Conference, AIAA Paper 2011*, Volume 249. *(p. 55)*

Ferrarotti, M., D. Lupant, and A. Parente (2017). Analysis of a 20 kw flameless furnace fired with natural gas. *Energy Procedia 120*, 104–111. *(p. 20, 22, 23)*

Galanti, S. and A. R. Jung (1997). Low-discrepancy sequences: Monte carlo simulation of option prices. *(p. 70)*

Glarborg, P. and L. L. Bentzen (2007). Chemical effects of a high co2 concentration in oxy-fuel combustion of methane. *Energy & Fuels 22*(1), 291–296. *(p. 203, 204)*

Goody, R., R. West, L. Chen, and D. Crisp (1989). The correlated-k method for radiation calculations in nonhomogeneous atmospheres. *Journal of Quantitative Spectroscopy and Radiative Transfer 42*(6), 539–550. *(p. 6, 8, 59, 60, 152, 206)*

Goody, R. M. and Y. L. Yung (1995). *Atmospheric radiation: theoretical basis*. Oxford University Press. *(p. 81)*

Gordon, H. R. (1985). Ship perturbation of irradiance measurements at sea. 1: Monte carlo simulations. *Applied optics 24*(23), 4172–4182. *(p. 44)*

Guiberti, T. F., D. Durox, P. Scouflaire, and T. Schuller (2015). Impact of heat loss and hydrogen enrichment on the shape of confined swirling flames. *Proceedings of the Combustion Institute 35*(2), 1385–1392. *(p. 20, 85)*

Guiberti, T. F., D. Durox, L. Zimmer, and T. Schuller (2015). Analysis of topology transitions of swirl flames interacting with the combustor side wall. *Combustion and Flame 162*(11), 4342–4357. *(p. 85)*

Gupta, A., D. Haworth, and M. Modest (2013). Turbulence-radiation interactions in large-eddy simulations of luminous and nonluminous nonpremixed flames. *Proceedings of the Combustion Institute 34*(1), 1281–1288. *(p. 18, 19, 27)*

Habibi, A., B. Merci, and D. Roekaerts (2007). The importance of turbulence–radiation interaction in rans simulations of a turbulent nonpremixed laboratory-scale bluff-body flame. In *3rd European combustion meeting*. *(p. 18, 19)*

Haghighat, A. and J. C. Wagner (2003). Monte carlo variance reduction with deterministic importance functions. *Progress in Nuclear Energy 42*(1), 25–53. *(p. 51)*

Haji-Sheikh, A. and J. Howell (1988). Monte carlo methods. *Handbook of Numerical Heat Transfer, Second Edition*, 249–295. *(p. 55)*

Haji-Sheikh, A. and E. Sparrow (1969). Probability distributions and error estimates for monte carlo solutions of radiation problems. *(p. 51)*

Halter, F., F. Foucher, L. Landry, and C. Mounaïm-Rousselle (2009). Effect of dilution by nitrogen and/or carbon dioxide on methane and iso-octane air flames. *Combustion Science and Technology 181*(6), 813–827. *(p. 203)*

Halton, J. H. (1960). On the efficiency of certain quasi-random sequences of points in evaluating multi-dimensional integrals. *Numerische Mathematik 2*(1), 84–90. *(p. 39, 70)*

Heraeus. Heraeus, quartz glass for optics data and properties quartz glass for optics data and properties (2013) 8. *(p. 138)*

Hlawka, E. (1961). Funktionen von beschränkter variatiou in der theorie der gleichverteilung. *Annali di Matematica Pura ed Applicata 54*(1), 325–333. *(p. 38, 69)*

Hottel, H. and A. Sarofim (1965). Radiative transport. *McCravv Hill, New York*. *(p. 58)*

Hottel, H. and A. Sarofim (1972). Radiative transfer, mcgraw-hill, new york, 1967. *ed: Siegel, R. and Howell, JR, Thermal Radiation Heat Transfer, Me Graw-Hill Kogakusha, Tokyo*. *(p. 8, 59)*

House, L. and L. Avery (1969). The monte carlo technique applied to radiative transfer. *Journal of Quantitative Spectroscopy and Radiative Transfer 9*(12), 1579–1591. *(p. 54)*

Howell, J. R., M. P. Menguc, and R. Siegel (2010). *Thermal radiation heat transfer*. CRC press. *(p. 9, 11, 158)*

Howell, J. R. and M. Perlmutter (1964). Monte carlo solution of thermal transfer through radiant media between gray walls. *Journal of heat transfer 86*(1), 116–122. *(p. 58)*

Hunnewell, T. S., K. L. Walton, S. Sharma, T. K. Ghosh, R. V. Tompson, D. S. Viswanath, and S. K. Loyalka (2017). Total hemispherical emissivity of ss 316l with simulated very high temperature reactor surface conditions. *Nuclear Technology 198*(3), 293–305. *(p. 155)*

Iwabuchi, H. (2006). Efficient monte carlo methods for radiative transfer modeling. *Journal of the atmospheric sciences 63*(9), 2324–2339. *(p. 49, 55, 56)*

Joe, S. and F. Y. Kuo (2008). Constructing sobol sequences with better two-dimensional projections. *SIAM Journal on Scientific Computing 30*(5), 2635–2654. *(p. 70, 152)*

Johansson, R., K. Andersson, B. Leckner, and H. Thunman (2010). Models for gaseous radiative heat transfer applied to oxy-fuel conditions in boilers. *International Journal of Heat and Mass Transfer 53*(1-3), 220–230. *(p. 58)*

Jones, W. and M. Paul (2005). Combination of dom with les in a gas turbine combustor. *International journal of engineering science 43*(5-6), 379–397.

(p. 18, 19)

Jonsson, P. (2006). Sunrise: polychromatic dust radiative transfer in arbitrary geometries. *Monthly Notices of the Royal Astronomical Society 372*(1), 2–20. *(p. 55)*

Jørgensen, U. G., P. Jensen, G. O. Sørensen, and B. Aringer (2001). H2o in stellar atmospheres. *Astronomy & Astrophysics 372*(1), 249–259. *(p. 5)*

Jourdaine, P. (2017). *Analyse des mécanismes de stabilisation d'oxy-flammes prémélangées swirlées*. Ph. D. thesis, CentraleSupélec, Université Paris Saclay, France. *(p. xxii, 103, 105, 128, 134, 202)*

Jourdaine, P., C. Mirat, J. Beaunier, J. Caudal, Y. Joumani, and T. Schuller (2016). Effect of quarl on n2-and co2-diluted methane oxy-flames stabilized by an axial-plus-tangential swirler. In *ASME Turbo Expo 2016: Turbomachinery Technical Conference and Exposition*. American Society of Mechanical Engineers. *(p. 103)*

Jourdaine, P., C. Mirat, J. Caudal, A. Lo, and T. Schuller (2017). A comparison between the stabilization of premixed swirling co2-diluted methane oxy-flames and methane/air flames. *Fuel 201*, 156–164. *(p. xvii, 24, 103, 104, 200, 223)*

Jourdaine, P., C. Mirat, J. Caudal, and T. Schuller (2018). Stabilization mechanisms of swirling premixed flames with an axial-plus-tangential swirler. *Journal of Engineering for Gas Turbines and Power 140*(8), 081502. *(p. 103, 112)*

Joy, C., P. P. Boyle, and K. S. Tan (1996). Quasi-monte carlo methods in numerical finance. *Management Science 42*(6), 926–938. *(p. 70)*

Ju, Y., G. Masuya, and P. D. Ronney (1998). Effects of radiative emission and absorption on the propagation and extinction of premixed gas flames. *(p. 205, 209, 211, 216)*

Juvela, M. (2005). Efficient monte carlo methods for continuum radiative transfer. *Astronomy & Astrophysics 440*(2), 531–546. *(p. 55, 56)*

Kahn, H. and T. E. Harris (1951). Estimation of particle transmission by random sampling. *National Bureau of Standards applied mathematics series 12*, 27–30. *(p. 51)*

Kersch, A., W. Morokoff, and A. Schuster (1994). Radiative heat transfer with quasi-monte carlo methods. *Transport Theory and Statistical Physics 23*(7), 1001–1021. *(p. 61)*

Koren, C., R. Vicquelin, and O. Gicquel (2017). High-fidelity multiphysics simulation of a confined premixed swirling flame combining large-eddy simulation, wall heat conduction and radiative energy transfer. In *ASME Turbo Expo 2017: Turbomachinery Technical Conference and Exposition*. American Society of Mechanical Engineers. *(p. xiii, 18, 19, 20, 21, 60, 85)*

Koren, C., R. Vicquelin, and O. Gicquel (2018). Multiphysics simulation combining large-eddy simulation, wall heat conduction and radiative energy transfer to predict wall temperature induced by a confined premixed

swirling flame. *Flow, Turbulence and Combustion 101*(1), 77–102. *(p. 77, 85)*

Lacis, A. A. and V. Oinas (1991). A description of the correlated k distribution method for modeling nongray gaseous absorption, thermal emission, and multiple scattering in vertically inhomogeneous atmospheres. *Journal of Geophysical Research: Atmospheres 96*(D5), 9027–9063. *(p. 59)*

Lauer, M. and T. Sattelmayer (2010). On the adequacy of chemiluminescence as a measure for heat release in turbulent flames with mixture gradients. *Journal of Engineering for Gas Turbines and Power 132*(6), 061502. *(p. 134)*

Lauer, M. R. W. (2011). *Determination of the heat release distribution in turbulent flames by chemiluminescence imaging*. Ph. D. thesis, Technische Universität München. *(p. 134)*

Le Corre, B., A. Collin, L. Soudre-Bau, Y. Meshaka, and G. Jeandel (2014). Glass sagging simulation with improved calculation of radiative heat transfer by the optimized reciprocity monte carlo method. *International Journal of Heat and Mass Transfer 70*, 215–223. *(p. 48)*

Leckner, B. (1972). Spectral and total emissivity of water vapor and carbon dioxide. *Combustion and flame 19*(1), 33–48. *(p. 58)*

L'ecuyer, P. (1999). Good parameters and implementations for combined multiple recursive random number generators. *Operations Research 47*(1), 159–164. *(p. 36, 77)*

L'Ecuyer, P. and C. Lemieux (2005). Recent advances in randomized quasi-monte carlo methods. In *Modeling uncertainty*, pp. 419–474. Springer. *(p. 70)*

Legier, J.-P., T. Poinsot, and D. Veynante (2000). Dynamically thickened flame les model for premixed and non-premixed turbulent combustion. In *Proc. of the summer program*, pp. 157–168. Center for Turbulence Research, NASA Ames/Stanford Univ. *(p. 118)*

Lemieux, C. (2009). *Monte carlo and quasi-monte carlo sampling*. Springer Science & Business Media. *(p. 37, 39, 67, 69, 71, 74, 93, 152)*

Liu, F., H. Guo, and G. J. Smallwood (2003). The chemical effect of co2 replacement of n2 in air on the burning velocity of ch4 and h2 premixed flames. *Combustion and Flame 133*(4), 495–497. *(p. 203)*

Liu, J. and S. Tiwari (1994). Investigation of radiative transfer in nongray gases using a narrow band model and monte carlo simulation. *Journal of heat transfer 116*(1), 160–166. *(p. 59)*

Liua, F., H. Becker, and Y. Bindar (1998). A comparative study of radiative heat transfer modelling in gas-fired furnaces using the simple grey gas and the weighted-sum-of-grey-gases models. *International Journal of Heat and Mass Transfer 41*(22), 3357–3371. *(p. 58)*

Lu, X. and P.-f. Hsu (2005). Reverse monte carlo simulations of light pulse propagation in nonhomogeneous media. *Journal of Quantitative Spectroscopy and Radiative Transfer 93*(1), 349–367. *(p. 44)*

Lucca-Negro, O. and T. O'doherty (2001). Vortex breakdown: a review. *Progress in energy and combustion science 27*(4), 431–481. *(p. 109, 110)*

Malkmus, W. (1967). Random lorentz band model with exponential-tailed s- 1 line-intensity distribution function. *Journal of the Optical Society of America 57*(3), 323–329. *(p. 59)*

Mattila, K. (1970). Interpretation of the surface brightness of dark nebulae. *Astronomy and Astrophysics 9*, 53–63. *(p. 55)*

Maurente, A., H. Vielmo, and F. França (2008). Comparison of the standard weighted-sum-of-gray-gases with the absorption-line blackbody distribution function for the computation of radiative heat transfer in h 2 o/co 2 mixtures. *Journal of Quantitative Spectroscopy and Radiative Transfer 109*(10), 1758–1770. *(p. 44, 60)*

Mazas, A., D. Lacoste, and T. Schuller (2010). Experimental and numerical investigation on the laminar flame speed of ch4/o2 mixtures diluted with co2 and h2o. In *ASME Turbo Expo 2010: Power for Land, Sea, and Air*, pp. 411–421. American Society of Mechanical Engineers. *(p. 203)*

Mehta, R. S., A. Wang, M. F. Modest, and D. C. Haworth (2009). Modeling of a turbulent ethylene/air jet flame using hybrid finite volume/monte carlo methods. *Computational Thermal Sciences: An International Journal 1*(1). *(p. 18)*

Mercier, R., T. Guiberti, A. Chatelier, D. Durox, O. Gicquel, N. Darabiha, T. Schuller, and B. Fiorina (2016). Experimental and numerical investigation of the influence of thermal boundary conditions on premixed swirling flame stabilization. *Combustion and Flame 171*, 42–58. *(p. xiii, 20, 21, 85)*

Metcalfe, W. K., S. M. Burke, S. S. Ahmed, and H. J. Curran (2013). A hierarchical and comparative kinetic modeling study of c1- c2 hydrocarbon and oxygenated fuels. *International Journal of Chemical Kinetics 45*(10), 638–675. *(p. 219)*

Metropolis, N. and S. Ulam (1949). The monte carlo method. *Journal of the American statistical association 44*(247), 335–341. *(p. 34)*

Meulemans, J. (2016). An assessment of some non-gray global radiation models in enclosures. In *Journal of Physics: Conference Series*, Volume 676, pp. 012017. IOP Publishing. *(p. 58)*

Modest, M. F. (1992). The monte carlo method applied to gases with spectral line structure. *Numerical Heat Transfer, Part B Fundamentals 22*(3), 273–284. *(p. 59)*

Modest, M. F. (2003). Backward monte carlo simulations in radiative heat transfer. *Transactions-American Society of Mechanical Engineers Journal of Heat Transfer 125*(1), 57–62. *(p. 44, 50)*

Modest, M. F. (2013). *Radiative heat transfer*. Academic press. *(p. xiii, xiv, 6, 7, 10, 11, 35, 37, 67, 81, 84, 156, 206)*

Modest, M. F. and D. C. Haworth (2016). *Radiative heat transfer in turbulent combustion systems: theory and applications*. Springer. *(p. 20)*

Modest, M. F. and H. Zhang (2000). The full-spectrum correlated-k distribution and its relationship to the weighted-sum-of-gray-gases method. *ASME-PUBLICATIONS-HTD 366*, 75–84. *(p. 10)*

Modest, M. F. and H. Zhang (2002). The full-spectrum correlated-k distribution for thermal radiation from molecular gas-particulate mixtures. *Journal of heat transfer 124*(1), 30–38. *(p. 10, 60)*

Morokoff, W. J. and R. E. Caflisch (1995). Quasi-monte carlo integration. *Journal of computational physics 122*(2), 218–230. *(p. 39, 61, 70)*

Nguyen, P. D., G. Ghazal, V. C. Piñera, V. Battaglia, A. Rensgard, T. Ekman, and M. Gazdallah (2017). Modelling of flameless oxy-fuel combustion with emphasis on radiative heat transfer for low calorific value blast furnace gas. *Energy Procedia 120*, 492–499. *(p. 58)*

Nicoud, F., H. B. Toda, O. Cabrit, S. Bose, and J. Lee (2011). Using singular values to build a subgrid-scale model for large eddy simulations. *Physics of Fluids 23*(8), 085106. *(p. 106)*

Niederreiter, H. (1992). *Random number generation and quasi-Monte Carlo methods*, Volume 63. Siam. *(p. 39)*

Nishita, T., Y. Miyawaki, and E. Nakamae (1987). A shading model for atmospheric scattering considering luminous intensity distribution of light sources. *Acm Siggraph Computer Graphics 21*(4), 303–310. *(p. 44)*

O'Brien, D. (1992). Accelerated quasi monte carlo integration of the radiative transfer equation. *Journal of Quantitative Spectroscopy and Radiative Transfer 48*(1), 41–59. *(p. 61)*

Owen, A. B. et al. (1997). Scrambled net variance for integrals of smooth functions. *The Annals of Statistics 25*(4), 1541–1562. *(p. 71)*

Palluotto, L., N. Dumont, P. Rodrigues, C. Koren, R. Vicquelin, and O. Gicquel (2017). Comparison of monte carlo methods efficiency to solve radiative energy transfer in high fidelity unsteady 3d simulations. In *ASME Turbo Expo 2017: Turbomachinery Technical Conference and Exposition*. American Society of Mechanical Engineers. *(p. 77, 152)*

Partridge, H. and D. W. Schwenke (1997). The determination of an accurate isotope dependent potential energy surface for water from extensive ab initio calculations and experimental data. *The Journal of Chemical Physics 106*(11), 4618–4639. *(p. 5)*

Pierrot, L., P. Rivière, A. Soufiani, and J. Taine (1999). A fictitious-gas-based absorption distribution function global model for radiative transfer in hot gases. *Journal of Quantitative Spectroscopy and Radiative Transfer 62*(5), 609–624. *(p. 10)*

Pierrot, L., A. Soufiani, and J. Taine (1999). Accuracy of narrow-band and global models for radiative transfer in h2o, co2, and h2oî—¸ co2 mixtures at high temperature. *Journal of Quantitative Spectroscopy and Radiative Transfer 62*(5), 523–548. *(p. 10)*

Poinsot, T. and D. Veynante (2005). *Theoretical and numerical combustion*. RT Edwards, Inc. *(p. 16, 210)*

Poinsot, T. J. and S. Lelef (1992). Boundary conditions for direct simulations of compressible viscous flows. *Journal of computational physics 101*(1), 104–129. *(p. 107, 118, 218)*

Poitou, D., J. Amaya, M. El Hafi, and B. Cuenot (2012). Analysis of the interaction between turbulent combustion and thermal radiation using unsteady coupled les/dom simulations. *Combustion and Flame 159*(4), 1605–1618. *(p. 18, 19)*

Qiao, L., Y. Gan, T. Nishiie, W. Dahm, and E. Oran (2010). Extinction of premixed methane/air flames in microgravity by diluents: Effects of radiation and lewis number. *Combustion and Flame 157*(8), 1446–1455. *(p. 205)*

Refloch, A., B. Courbet, A. Murrone, P. Villedieu, C. Laurent, P. Gilbank, J. Troyes, L. Tessé, G. Chaineray, J. Dargaud, et al. (2011). Cedre software. *AerospaceLab* (2), p–1. *(p. 152)*

Ren, T. and M. F. Modest (2019). Line-by-line random-number database for monte carlo simulations of radiation in combustion system. *Journal of Heat Transfer 141*(2), 022701. *(p. 59)*

Rivière, P. and A. Soufiani (2012). Updated band model parameters for h2o, co2, ch4 and co radiation at high temperature. *International Journal of Heat and Mass Transfer 55*(13-14), 3349–3358. *(p. 8, 81, 152)*

Riviere, P., A. Soufiani, M. Perrin, H. Riad, and A. Gleizes (1996). Air mixture radiative property modelling in the temperature range 10,000–40,000 k. *Journal of Quantitative Spectroscopy and Radiative Transfer 56*(1), 29–45. *(p. 10)*

Riviere, P., A. Soufiani, and J. Taine (1992). Correlated-k and fictitious gas methods for h2o near 2.7 μm. *Journal of Quantitative Spectroscopy and Radiative Transfer 48*(2), 187–203. *(p. 59)*

Riviere, P., A. Soufiani, and J. Taine (1995). Correlated-k fictitious gas model for h2o infrared radiation in the voigt regime. *Journal of Quantitative Spectroscopy and Radiative Transfer 53*(3), 335–346. *(p. 5, 59)*

Rodrigues, P., B. Franzelli, R. Vicquelin, O. Gicquel, and N. Darabiha (2018). Coupling an les approach and a soot sectional model for the study of sooting turbulent non-premixed flames. *Combustion and Flame 190*, 477–499. *(p. 84)*

Rodrigues, P., O. Gicquel, N. Darabiha, K. Geigle, and R. Vicquelin (2018). Assessment of external heat transfer modeling of a laboratory-scale combustor inside a pressure-housing environment. In *ASME Turbo Expo 2018: Turbomachinery Technical Conference and Exposition*. American Society of Mechanical Engineers. *(p. 18, 19, 60, 147, 155, 157)*

Rothman, L., I. Gordon, R. Barber, H. Dothe, R. Gamache, A. Goldman, V. Perevalov, S. Tashkun, and J. Tennyson (2010). Hitemp, the high-temperature molecular spectroscopic database. *Journal of Quantitative Spectroscopy and Radiative Transfer 111*(15), 2139–2150. *(p. 5, 8, 81)*

Rothman, L. S., I. E. Gordon, A. Barbe, D. C. Benner, P. F. Bernath,

M. Birk, V. Boudon, L. R. Brown, A. Campargue, J.-P. Champion, et al. (2009). The hitran 2008 molecular spectroscopic database. *Journal of Quantitative Spectroscopy and Radiative Transfer 110*(9-10), 533–572. *(p. 5, 58)*

Ruan, J., H. Kobayashi, T. Niioka, and Y. Ju (2001). Combined effects of nongray radiation and pressure on premixed ch4/o2/co2 flames. *Combustion and Flame 124*(1-2), 225–230. *(p. 205)*

Ruan, L., H. Tan, and Y. Yan (2002). A monte carlo (mc) method applied to the medium with nongray absorbing-emitting-anisotropic scattering particles and gray approximation. *Numerical Heat Transfer: Part A: Applications 42*(3), 253–268. *(p. 44)*

Sabella, P. (1988). A rendering algorithm for visualizing 3d scalar fields. *ACM SIGGRAPH computer graphics 22*(4), 51–58. *(p. 44)*

Sarkar, P. and M. Prasad (1987). A comparative study of pseudo and quasi random sequences for the solution of integral equations. *Journal of Computational Physics 68*(1), 66–88. *(p. 61)*

Sarpkaya, T. (1974). Effect of the adverse pressure gradient on vortex breakdown. *AIAA Journal 12*(5), 602–607. *(p. 109)*

Schoenfeld, T. (2008). The avbp handbook. *(p. 106)*

Scutaru, D., L. Rosenmann, J. Taine, R. Wattson, and L. Rothman (1993). Measurements and calculations of co2 absorption at high temperature in the 4.3 and 2.7 μm regions. *Journal of Quantitative Spectroscopy and Radiative Transfer 50*(2), 179–191. *(p. 5)*

Shamsundar, N., E. Sparrow, and R. Heinisch (1973). Monte carlo radiation solutions—effect of energy partitioning and number of rays. *International Journal of Heat and Mass Transfer 16*(3), 690–694. *(p. 50)*

Shuai, Y., S. Dong, and H. Tan (2005). Simulation of the infrared radiation characteristics of high-temperature exhaust plume including particles using the backward monte carlo method. *Journal of Quantitative Spectroscopy and Radiative Transfer 95*(2), 231–240. *(p. 44)*

Sloan, D. G., P. J. Smith, and L. D. Smoot (1986). Modeling of swirl in turbulent flow systems. *Progress in Energy and Combustion Science 12*(3), 163–250. *(p. 112)*

Smith, G. P., D. M. Golden, M. Frenklach, B. Eiteener, M. Goldenberg, C. T. Bowman, R. K. Hanson, W. C. Gardiner, V. V. Lissianski, and Z. W. Qin (2011). *http://www.me.berkeley.edu/gri_mech*. *(p. xii, 202, 204, 206, 207)*

Smith, T., Z. Shen, and J. Friedman (1982). Evaluation of coefficients for the weighted sum of gray gases model. *Journal of heat transfer 104*(4), 602–608. *(p. 60)*

Smyth, K. C. and C. R. Shaddix (1996). The elusive history of m = 1.57–0.56 i for the refractive index of soot. *Combustion and Flame 107*(3), 314–320. *(p. 84)*

Snegirev, A. Y. (2004). Statistical modeling of thermal radiation transfer

in buoyant turbulent diffusion flames. *Combustion and Flame 136*(1-2), 51–71. *(p. 18, 60)*

Soboĺ, I. (1976). Uniformly distributed sequences with additional uniformity properties. *USSR Comput. Math. and Math. Phy 16*, 236–242. *(p. 39, 70)*

Solovjov, V. and B. Webb (2011). Global spectral methods in gas radiation: the exact limit of the slw model and its relationship to the adf and fsk methods. *Journal of Heat Transfer 133*(4), 042701. *(p. 10)*

Soucasse, L., P. Rivière, and A. Soufiani (2013). Monte carlo methods for radiative transfer in quasi-isothermal participating media. *Journal of Quantitative Spectroscopy and Radiative Transfer 128*, 34–42. *(p. 59)*

Soucasse, L., P. Rivière, and A. Soufiani (2014). Subgrid-scale model for radiative transfer in turbulent participating media. *Journal of Computational Physics 257*, 442–459. *(p. 27)*

Steward, F. and P. Cannon (1971). The calculation of radiative heat flux in a cylindrical furnace using the monte carlo method. *International Journal of Heat and Mass Transfer 14*(2), 245–262. *(p. 58)*

Sun, X. and P. J. Smith (2010). A parametric case study in radiative heat transfer using the reverse monte-carlo ray-tracing with full-spectrum k-distribution method. *Journal of Heat Transfer 132*(2), 024501. *(p. 44)*

Surzhikov, S. T. and J. R. Howell (1998). Monte carlo simulation of radiation in scattering volumes with line structure. *Journal of thermophysics and heat transfer 12*(2), 278–281. *(p. 59)*

Taine, J., F. Enguehard, and E. Iacona (2014). *Transferts thermiques-Introduction aux transferts d'énergie-5e édition*. Dunod. *(p. 206)*

Tang, K. and M. Brewster (1999). Analysis of molecular gas radiation: real gas property effects. *Journal of thermophysics and heat transfer 13*(4), 460–466. *(p. 59)*

Tashkun, S. and V. Perevalov (2011). Cdsd-4000: High-resolution, high-temperature carbon dioxide spectroscopic databank. *Journal of Quantitative Spectroscopy and Radiative Transfer 112*(9), 1403–1410. *(p. 5, 8, 81)*

Tessé, L., F. Dupoirieux, and J. Taine (2004). Monte carlo modeling of radiative transfer in a turbulent sooty flame. *International journal of heat and mass transfer 47*(3), 555–572. *(p. 18, 46, 60)*

Tessé, L., F. Dupoirieux, B. Zamuner, and J. Taine (2002). Radiative transfer in real gases using reciprocal and forward monte carlo methods and a correlated-k approach. *International Journal of Heat and Mass Transfer 45*(13), 2797–2814. *(p. 44, 46, 47, 48, 60, 78, 80, 86, 152)*

Tezuka, S. and H. Faure (2003). I-binomial scrambling of digital nets and sequences. *Journal of complexity 19*(6), 744–757. *(p. 71)*

Tien, C. and J. Lowder (1966). A correlation for total band absorptance of radiating gases. *International Journal of Heat and Mass Transfer 9*(7), 698–701. *(p. 59)*

Tien, C.-L. (1969). Thermal radiation properties of gases. In *Advances in heat transfer*, Volume 5, pp. 253–324. Elsevier. *(p. 59)*

Vanierschot, M. and E. Van den Bulck (2007). Hysteresis in flow patterns in annular swirling jets. *Experimental Thermal and Fluid Science 31*(6), 513–524. *(p. 194)*

Viskanta, R. and M. Mengüç (1987). Radiation heat transfer in combustion systems. *Progress in Energy and Combustion Science 13*(2), 97–160. *(p. 19)*

Walters, D. V. and R. O. Buckius (1992). Rigorous development for radiation heat transfer in nonhomogeneous absorbing, emitting and scattering media. *International Journal of Heat and Mass Transfer 35*(12), 3323–3333. *(p. 42, 44)*

Walters, D. V. and R. O. Buckius (1994). Monte carlo methods for radiative heat transfer in scattering media. *Annual review of heat transfer 5*(5). *(p. 42, 49, 50)*

Wang, A. and M. F. Modest (2007). Spectral monte carlo models for nongray radiation analyses in inhomogeneous participating media. *International Journal of Heat and Mass Transfer 50*(19-20), 3877–3889. *(p. 59)*

Wang, A., M. F. Modest, D. C. Haworth, and L. Wang (2008). Monte carlo simulation of radiative heat transfer and turbulence interactions in methane/air jet flames. *Journal of Quantitative Spectroscopy and Radiative Transfer 109*(2), 269–279. *(p. 18, 19, 44)*

Wang, L., J. Yang, M. Modest, and D. Haworth (2007). Application of the full-spectrum k-distribution method to photon monte carlo solvers. *Journal of Quantitative Spectroscopy and Radiative Transfer 104*(2), 297–304. *(p. 60)*

Wang, P., F. Fan, and Q. Li (2014). Accuracy evaluation of the gray gas radiation model in cfd simulation. *Case Studies in Thermal Engineering 3*, 51–58. *(p. 58)*

Witt, A. N. (1977). Multiple scattering in reflection nebulae. ii. uniform plane-parallel nebulae with foreground stars. *The Astrophysical Journal Supplement Series 35*, 7–19. *(p. 55)*

Wong, B. T. and M. P. Mengüç (2002). Comparison of monte carlo techniques to predict the propagation of a collimated beam in participating media. *Numerical Heat Transfer: Part B: Fundamentals 42*(2), 119–140. *(p. 44)*

Wu, Y., D. Haworth, M. Modest, and B. Cuenot (2005). Direct numerical simulation of turbulence/radiation interaction in premixed combustion systems. *Proceedings of the Combustion Institute 30*(1), 639–646. *(p. 18, 19)*

Xie, Y., J. Wang, M. Zhang, J. Gong, W. Jin, and Z. Huang (2013). Experimental and numerical study on laminar flame characteristics of methane oxy-fuel mixtures highly diluted with co2. *Energy & Fuels 27*(10), 6231–6237. *(p. 203, 204)*

Zhang, J., C. R. Shaddix, and R. W. Schefer (2011). Design of "model-

friendly" turbulent non-premixed jet burners for c2+ hydrocarbon fuels. *Review of Scientific Instruments 82*(7), 074101. *(p. 83)*

Zhang, Y., O. Gicquel, and J. Taine (2012). Optimized emission-based reciprocity monte carlo method to speed up computation in complex systems. *International Journal of Heat and Mass Transfer 55*(25-26), 8172–8177. *(p. 56, 57, 58, 77, 78, 96)*

Zhang, Y., R. Vicquelin, O. Gicquel, and J. Taine (2013). Physical study of radiation effects on the boundary layer structure in a turbulent channel flow. *International Journal of Heat and Mass Transfer 61*, 654–666. *(p. 18, 19, 60, 77, 83)*

Zhao, X., D. Haworth, T. Ren, and M. Modest (2013). A transported probability density function/photon monte carlo method for high-temperature oxy–natural gas combustion with spectral gas and wall radiation. *Combustion Theory and Modelling 17*(2), 354–381. *(p. 18)*

université PARIS-SACLAY

ÉCOLE DOCTORALE
Sciences mécaniques et énergétiques, matériaux et géosciences (SMEMAG)

Titre: Prédiction du transfert radiatif au sein d'une flamme prémélangée swirlée à l'aide d'une méthode Quasi-Monte Carlo couplée à la simulation aux grandes échelles
Mots-clés: Quasi-Monte Carlo, Rayonnement, Combustion, Simulation aux grandes échelles

Résumé: La prédiction des flux aux parois joue un rôle déterminant dans le cycle de vie des chambres de combustion. Le transfert de chaleur de la flamme aux parois est entraîné, outre la convection, également par le rayonnement des gaz chauds au sein de la chambre. Afin d'intégrer les contributions convectives et radiatives au flux pariétal il est nécessaire de résoudre simultanément l'équation de transfert radiatif et les équations régissant l'écoulement réactif. Quand les méthodes de Monte Carlo sont couplées aux simulations aux grandes échelles (LES), de telles simulations deviennent très coûteuses. L'objectif de cette thèse est donc d'investiguer une technique pour améliorer l'efficacité de la méthode MC, basée sur un mécanisme alternatif d'échantillonnage appelée intégration Quasi-Monte Carlo (QMC). Au cours de cette thèse, la méthode QMC a été couplée à une simulation LES dans une configuration où le rayonnement joue un rôle très important : la flamme méthane-air de la chambre Oxytec. La comparaison entre les simulations couplées et non couplées avec les données expérimentales montre que le rayonnement thermique a un impact sur la topologie de l'écoulement et de la flamme. Enfin, un bon accord est trouvé entre le flux de chaleur pariétal prédit par la simulation et les données expérimentales.

Title: Quasi-Monte Carlo computation of radiative heat transfer in coupled Large Eddy Simulation of a swirled premixed flame
Keywords: Quasi-Monte Carlo, Radiation, Combustion, Large Eddy Simulation

Abstract: The prediction of wall fluxes is a significant aspect in the life cycle of combustors, since it allows to prevent eventual wall damages. Heat transfer from flame to the walls is driven, apart from convection, also by radiation of burnt gases inside the chamber. In order to correctly account for both convective and radiative contributions to wall fluxes, the simultaneous solution of the radiative transfer equation (RTE) and the governing equations for reactive flows is required. However, multi-physics simulations where MC methods are coupled to Large Eddy Simulation (LES), remain very costly. The purpose of this study is then to investigate improvements of MC methods, by using an alternative sampling mechanism for numerical integration usually referred to as Quasi-Monte Carlo (QMC) integration. In this study, QMC method is coupled to Large Eddy Simulation (LES) of a configuration where the radiation plays an important role: the methane-air flame investigated during the experimental campaign Oxytec. Coupled and non-coupled simulations are compared and their comparison with experimental data shows that thermal radiation has an impact on both flow and flame topology. Finally a good agreement is found between numerical wall fluxes and experimental conductive fluxes.